From Desktop to Benchtop – Developing Computational Tools for Organic and Medicinal Chemistry

Mihai Burai-Patrascu

A thesis submitted to McGill University in partial fulfillment of the requirements for the degree of Doctor of Philosophy.

Department of Chemistry

McGill University

Montréal, Québec, Canada

April 2020

Abstract

Organic and medicinal chemistry research contribute extensively to the discovery, optimization, and ton-scale production of numerous small molecules, such as novel drugs that treat life-threatening diseases. This research can be put in the context of the COVID-19 global pandemic, which has claimed many lives, shut down the entire planet, and made humanity reliant on chemistry (amongst which organic and medicinal chemistry play a key role) and biochemistry research to come up with innovative solutions in a short amount of time. A major hurdle in organic and medicinal chemistry research is the production of these complex life-saving small molecules and the tedious and time-consuming syntheses they require. To offset this, these two fields of chemistry make use of a different branch of chemistry, namely computational chemistry. Over the years, computational chemistry has become a trusted partner of experimental chemistry and has significantly contributed to the discovery of novel drugs. However, computational chemistry often requires expertise in both chemistry and coding, the latter of which most experimentalists do not possess. As such, in this thesis I seek to develop and interface computational tools with organic and medicinal chemistry to improve the molecular discovery rate. The majority of the tools that we have developed have been implemented in our drug discovery platform FORECASTER and in our asymmetric catalyst design platform VIRTUAL CHEMIST, to enable chemists to use powerful software developed by chemists for chemists. In only a few clicks, the user can interact with our platforms without the need for expertise in computational chemistry.

This thesis begins with a short but comprehensive introduction (Chapter 1) into computational chemistry and its various applications. Following this, I developed a computational protocol that allows the accurate modeling of nucleoside conformations (Chapter 2), which in turn

enables the synthesis of only those nucleosides that exhibit desirable properties. This work was done in relation to the current methodology of developing nucleosides, which entails the synthesis of multiple analogues until one with desirable properties is found, since this contributes to an increased cost, waste production and energy expenditure. Then, using this protocol, I quantified the various effects that contribute to the different nucleoside conformations, and we were able to provide plausible explanations of why non-natural nucleosides behave in certain ways (Chapter 3). As a change of pace, I turned my attention to Cytochrome P450-mediated drug metabolism and toxicity, which constitutes one of the main interests of medicinal chemists (Chapter 4). In this chapter I developed a novel tool based on quantum mechanics, docking and machine learning that enables the identification of Cytochrome P450 inhibitors *in silico*. This allows medicinal chemists to test whether a compound or drug of interest presents inhibitory activity against a Cytochrome P450 isoform before attempting synthesis. Finally, we provided organic chemists with a computational platform – VIRTUAL CHEMIST – that allows them to undertake an asymmetric synthesis project virtually from A-Z (Chapter 5). Such a platform facilitates organic chemists to test thousands of molecules at the click of a button and to select only those catalysts that show excellent stereoselectivity and reactivity. The thesis then concludes with the overall obstacles I have overcome in my research, as well as possible future avenues for research.

Résumé

La recherche en chimie organique et médicinale contribue largement à la découverte, à l'optimisation et à la production à l'échelle de la tonne de nombreuses petites molécules, telles que les nouveaux médicaments qui traitent des maladies mortelles. Cette recherche peut être placée dans le contexte de la pandémie mondiale COVID-19, qui a fait de nombreuses victimes, a fermé la planète entière et a rendu l'humanité dépendante de la capacité de la recherche en chimie (organique et médicinale) et biochimie à trouver des solutions innovantes en peu de temps pour ceux qui en ont besoin. L'un des principaux obstacles à la recherche en chimie organique et médicinale est la production de ces petites molécules complexes qui sauvent des vies et le développement des synthèses fastidieuse qu'elles nécessitent souvent. Pour y remédier, ces deux domaines de la chimie font appel à une branche différente de la chimie, à savoir la chimie computationnelle. Au fil des ans, la chimie computationnelle est devenue un partenaire de confiance de la chimie expérimentale et a contribué de manière significative à la découverte de nouveaux médicaments. Cependant, la chimie computationnelle requiert souvent une expertise à la fois en chimie et en programmation, cette dernière n'étant pas du ressort de la plupart des expérimentateurs. C'est pourquoi, dans cette thèse, nous cherchons à développer et interfacer les outils informatiques avec la chimie organique et médicinale afin d'améliorer le taux de découverte moléculaire. La majorité des outils que nous avons développés ont été intégrés dans notre plateforme de découverte de médicaments FORECASTER, et dans notre plateforme de conception de catalyseurs asymétriques VIRTUAL CHEMIST, pour permettre aux chimistes d'utiliser des logiciels puissants développés par des chimistes pour des chimistes, qui peuvent être utilisés en quelques clics seulement, sans avoir besoin d'une expertise en chimie computationnelle.

Dans l'ensemble, cette thèse commence par une introduction complète mais concise (Chapitre 1) à la chimie computationnelle et à ses diverses applications. Ensuite, nous présentons un protocole de calcul que nous avons développé et qui permet la modélisation précise des conformations de nucléosides (Chapitre 2), qui à son tour permet la synthèse des seuls nucléosides qui présentent des propriétés souhaitables. Ce travail a été effectué en relation avec la méthodologie actuelle de développement des nucléosides, qui implique la synthèse de multiples analogues jusqu'à ce qu'un seul présentant des propriétés souhaitables soit trouvé. La synthèse d'analogues multiples contribue à augmenter les coûts, la production de déchets et la dépense énergétique. Ensuite, grâce à ce protocole, nous avons quantifié les divers effets qui contribuent aux différentes conformations des nucléosides, et nous avons pu fournir des explications plausibles sur les raisons pour lesquelles des nucléosides non naturels se comportent de certaines manières (Chapitre 3). Par la suite, nous avons porté notre attention sur le métabolisme et la toxicité des médicaments par les cytochromes P450, qui constituent l'un des principaux intérêts des chimistes médicinaux (Chapitre 4). Dans ce chapitre, nous avons développé un nouvel outil basé sur la mécanique quantique, l'arrimage et l'apprentissage machine qui permet l'identification *in silico* des inhibiteurs de cytochromes P450. Cela permet aux chimistes de tester si un composé ou un médicament d'intérêt présente une activité inhibitrice contre une isoforme des cytochromes P450, sans avoir besoin de synthèses coûteuses ou d'acheter des kits de test. Enfin, nous nous efforçons de fournir aux chimistes organiciens une plateforme de calcul - VIRTUAL CHEMIST - qui leur permet d'entreprendre un projet de synthèse asymétrique virtuellement de A à Z (Chapitre 5). Une telle plateforme permet aux chimistes organiciens de tester des milliers de molécules en un clic et de ne sélectionner que les catalyseurs qui présentent une excellente stéréosélectivité et réactivité. La

thèse se termine ensuite par les obstacles que nous avons surmontés dans nos recherches, ainsi que les développements futurs de nos travaux.

Acknowledgements

First of all, I would like to thank my supervisor**, Dr. Nicolas Moitessier,** for his unwavering support, mentorship and friendship during my PhD. Brainstorming sessions, code implementations, fixing memory leaks, petting dogs in the office, Zoom meetings, getting overpriced and tasteless Tim Horton's coffee, you name it, we did it. Also, lest we forget – backing up your code is essential, if you do not want to spend thousands of $$$ to recover it from a 15-year old HDD. I would also like to thank **my family** – you were always there for me and I couldn't have done it without you. Mulţumesc! I would also like to thank **my roommate and BFF Patrick Outhwaite** for putting up with me for 4 years – I have no idea how I would have stayed sane during my PhD without watching the Premier League and supporting Crystal Palace (which you made me a fan of). Also ordering food, taking care of dogs together and watching Impractical Jokers and laughing so much that I would stop breathing … also of course being **QUARANTINED** together during a pandemic. I want to thank **Sharon Pinus** – I have to admit, I didn't really like you at the beginning, but you soon turned into one of my favorite people ever. You made my days in the office so much better, including but not limited to Haribo, cookies, Hamantaschen and stories of Israel and Germany. Our daily ritual of looking at the "Rate My Dogs" dog of the day was something I always looked forward to. Thank you! I also want to thank **Julia Stille and Anne Labarre**. Our lengthy discussions of what constitutes a sandwich, camping trip(s), mojito nights and asking me to provide you with the admin password to install software on your PC kept me sane during this degree. I'm lucky to have you and Sharon as such good friends – thank you! Another major thank you goes to the **Moitessier Research Group** – past and present. I learnt so much from y'all and I hope I was able to impart some of my knowledge and passion on you. I couldn't have asked for a better environment to do my PhD in, thank you! Last, I would like

to thank **Ginger, Darcy, Jack, Leia and Gaia** (and their owners) **–** amazing dogs I had the opportunity and pleasure to spend time with and take care of. You hold a special place in my heart. For those of you I haven't mentioned in this short acknowledgment section – I haven't forgotten you - you are forever in my heart!

Table of Contents

List of Figures

List of Schemes and Charts

List of Tables

List of Equations

List of Abbreviations

- listed alphabetically -

%ee – enantiomeric excess

AC_{50} – half maximal activity

ACE – Asymmetric Catalyst Evaluation software

ADMET – absorption, distribution, metabolism, excretion and toxicity

AMBER - assisted model building with energy refinement

AMOEBA - atomic multipole optimized energetics for biomolecular applications

ANN – artificial neural network

AO – atomic orbitals

ASO - antisense oligonucleotides

AUROC - area under receiver operating curve

B3LYP – Becke 3-parameter Lee-Yang-Parr exchange-correlation functional

BCP – bond critical point

BP – bond path

BPTI – bovine pancreatic trypsin inhibitor

BSSE – basis set superposition error

CADD – computer-aided drug design

cDFT – conceptual DFT

CI – configuration interaction

CoMFA – comparative molecular field analysis

CoMSIA – comparative molecular similarity indices

CPU – central processing unit

CYP450 – cytochrome P450

D3BJ – Grimme's D3 dispersion using a Becke-Johnson damping function

def2-SVP – Karlsruhe split-valence potential double zeta basis set

DDI – drug-drug interactions

DFT – density functional theory

DNA - deoxyribonucleic acid

FC – Fukui coefficients

FF – force field

FITTED – Flexibility Induced Through Targeted Evolutionary Description – docking software

FMO – Frontier molecular orbital theory

gCP – geometrical counterpoise correction

gRNA - guide RNA

GUI – graphics user interface

GUI/UI - graphics user interface / user interface

HF – Hartree-Fock

HMBC - heteronuclear multiple bond correlation

HOMO – highest occupied molecular orbital

HSAB – hard-soft acid-base theory

HTS - high throughput screening

IAS – interatomic surfaces

IC_{50} – half maximal inhibitory concentration

IUPAC – International Union of Pure and Applied Chemistry

LANLDZ – Los Alamos National Laboratory Double-Zeta Basis Set

LARI – local atomic reactivity indices

LBDD – ligand-based drug design

LCAO – linear combination of atomic orbitals

LJ – Lennard-Jones potential

LNA - locked nucleic acid

logP – molecular octanol/water partition coefficient

LUMO – lowest unoccupied molecular orbital

MC – metabolic intermediate complex

MD – molecular dynamics

MIC – minimum inhibitory concentration

ML – machine learning

MM – molecular mechanics

MO – molecular orbitals

MOE - 2'-methoxy-ethyl

MPn – Moller-Plesset perturbation theory (n = 1,2,3,4)

MS - mass spectrometry

MUE – mean unsigned error

NBO - natural bond orbitals

NMR - nuclear magnetic resonance

NOE – nuclear Overhauser effect

NPV – negative predicted value

NRTIs - nucleoside reverse transcriptase inhibitors

OLEDs - organic light emitting diodes

OOP – out-of-plane angle

PBE0 – Perdew–Burke-Ernzerhof hybrid exchange-correlation functional

PES – potential energy surface

PME - particle mesh Ewald

PMF - potential of mean force

PPV – positive predicted value

Q2MM – quantum guided molecular mechanics

QCISD – quadratic configuration interaction including single and double excitations

QCSID(T) – quadratic configuration interaction including single and double excitations and an estimate of triplet excitations

QM – quantum mechanics

QM/MM – quantum mechanics/molecular mechanics

QSAR – quantitative structure-activity relationships

QTAIM – quantum theory of atoms in molecules

RESP - restricted electrostatic potential

RF – random forest

RM – reactive metabolites

RMSD - root mean square deviation

RNA - ribonucleic acid

SASA – solvent accessible surface area

SBDD – structure-based drug design

SCC-DFTB - self-consistent charge density functional tight-binding

SCF – self-consistent field

SE-QM – semiempirical quantum mechanical methods

SIE – self-interaction error

siRNA - small interfering RNA

SMILES – simplified molecular-input line-entry system

SoM – sites of metabolism

SVM – support vector machine

TS – transition state

TSFF – transition state force field

vdW – van der Waals

VS – virtual screening

WHAM - weighted histogram analysis method

ZPE – zero-point energy

List of Author Contributions

During the course of my PhD I have co-authored 7 published manuscripts and 3 manuscripts in preparation, listed below:

Publications (chronological order). ‡ denotes first author or co-first-author

1. **Burai Patrascu, M.;**‡ Pottel, J.; Pinus, S.; Bezanson, M.; Norrby, P.O.; and Moitessier, N. *Nat. Catal*. **2020**, 3, 574-584. https://doi.org/10.1038/s41929-020-0468-3
2. **Burai Patrascu, M.;**‡ Plescia, J.; Kalgutkar, A.; Mascitti, V.; and Moitessier, N. *Arkivoc*, **2019**, part IV, 280-298. https://doi.org/10.24820/ark.5550190.p010.970
3. Plescia, J. ‡ De Cesco, S.;‡ **Burai Patrascu, M.;**‡ Kurian, J.; Dufresne, C.; Wahba, A.S.; Janmamode, N.; Mittermaier, A.K.; and Moitessier, N. *J. Med. Chem.* **2019**, 62, 17, 7874-7884
4. O'Reilly, D.;‡ Stein, R.; **Burai Patrascu, M.;** Jana, S.; Kurrian, J.; Moitessier, N.; and Damha M.J. *Chem. Eur. J.*, **2018**, 24, 61, 16432-16439. https://doi.org/10.1021/acs.jmedchem.9b00642
5. Malek-Adamian, E.,‡ **Burai Patrascu, M.;** Jana, S.; Montero-Martinez, S.; Moitessier, N.; and Damha M.J. *J. Org. Chem.*, **2018**, 83, 17, 9839-9849. https://doi.org/10.1021/acs.joc.8b01329
6. **Burai Patrascu, M.;** ‡ Malek-Adamian, E.; Damha, M.J.; and Moitessier, N. *J. Am. Chem. Soc.*, **2017**, 139, 39, 13620-13623. https://doi.org/10.1021/jacs.7b07436
7. Malek-Adamian, E.;‡ Guenther, C.; Matsuda, S.; Montero-Martinez, S.; Zlatev, I.; Harp, J.; **Burai Patrascu, M.;** Foster, D.J.; Fakhoury, J.; Perkins, L.; Moitessier, N.; Manoharan, R.M.; Taneja, N.; Bisbe, A.; Charisse, K.; Maier, M.; Rajeev, K.G.; Egli, M.; Manoharan M.; and Damha M.J. *J. Am. Chem. Soc.*, **2017**, 139 , 41, 14542-14555. https://doi.org/10.1021/jacs.7b07582

Manuscripts in Preparation. ‡ denotes first author or co-first-author

8. **Burai Patrascu, M.;**‡ and Moitessier, N. **2020**, Improvement of the IMPACTS Drug Metabolism Tool.
9. Pinus, S.;‡ **Burai Patrascu, M.;** and Moitessier, N., **2020**, Organocatalyzed Diels-Alder Cycloaddition – A Comprehensive Experimental and Computational Study.
10. Labarre, A.;‡ **Burai Patrascu, M.;** Wei, W.; Luo, J. ; Martins, A.; Pottel, J.; Liu, Z.; and Moitessier, N., **2020**, Docking Ligands into Flexible and Solvated Macromolecules. 8. Beyond Non-Covalent Enzyme Inhibitors.

This page intentionally left blank

Chapter 1 – Introduction

1.1. Computational Chemistry – A Brief History.

Computational chemistry is a branch of chemistry that uses computer simulations to solve complex chemical problems. Rooted in quantum mechanics theories developed since the 1920s, computational chemistry rose to prominence only in the 1950s when chemists became interested in obtaining quantitative information about molecular systems.[1] The first journal specifically dedicated to computer-aided chemistry was the *Journal of Chemical Information and Computer Sciences*, which launched in 1960.[2] Nevertheless, it was not until the late 1960s and 1970s that the field of computational chemistry started expanding at a rapid rate. During those formative years several breakthroughs were made in terms of hardware (reasonably fast computers accessible to chemists) and software (accurate basis sets and efficient quantum chemistry packages such as Gaussian70[3]). These improvements gave rise to a plethora of applications that quickly became of interest to chemists and non-chemists alike. Among these applications is the rationalizing of reaction mechanisms, of which a famous example is the [3+2] cycloaddition step in the Sharpless asymmetric dihydroxylation,[4] as well as the first protein dynamics simulation (bovine pancreatic trypsin inhibitor – BPTI), which revealed its fluid-like interior.[5] The impact of such applications and of computational chemistry as a whole has not gone unseen; in fact, two Nobel Prizes have been awarded to computational chemists: in 1998 (Walter Kohn and John Pople)[6] for fundamental developments of computational chemistry and in 2013 (Martin Karplus, Michael Levitt and Arieh Warshel) for the development of multiscale methods for characterizing complex systems.[7]

1.2. Computational Techniques – An Overview.

To understand how computational means can be applied to complex chemical problems, we must first take an in-depth look into the different available computational methods. Depending on the system under scrutiny, as well as on the desired accuracy, several methods can be used. For example, one can use methods that only describe the positions of the nuclei but not of the electrons (i.e. molecular mechanics), those that depict both nuclei and electrons with various degrees of accuracy (i.e. quantum mechanics) or those that encode molecules as a series of numbers (machine learning). In this chapter we will take a closer look at these available techniques and will discuss their applications in various fields of chemistry, including organic and medicinal chemistry.

1.2.1. Molecular Mechanics (MM).

The simplest way to describe a chemical system consists of only considering nuclei and disregarding electrons. In this method, termed molecular mechanics (MM), the atoms are treated as "points" interconnected through "springs" (covalent bonds), which contain partial charges (for Coulombic interactions) and resemble soft spheres (for van der Waals interactions). This approximation is essential since MM uses classical mechanics to compute the potential energy of a system. To aid in the evaluation of this energy, MM uses sets of pre-computed parameters (atomic masses and charges, atom types, equilibrium bond lengths etc.) and energy functions that comprise a *force field* (FF). Amongst the common FFs are the AMBER,[8] GAFF[9] and OPLS3[10] FFs, which are used in most simulation programs that employ MM methods. Since FFs are an integral part of any MM method, we shall take a closer look at their particularities and inner workings.

1.2.1.1. MM – Force Field Energy Terms.

In modern FFs, in order to evaluate the energy of a system, contributions from both covalent (bonds, angles, torsions and out-of-plane (oop) angles) and non-covalent (van der Waals (vdW) and electrostatic) terms must be accounted for (Eqs. 1.1 – 1.9 and Figure 1.1).[11,12]

$$E_{total} = E_{covalent} + E_{non-covalent} \quad \text{Eq. (1.1)}$$

$$E_{covalent} = E_{bonds} + E_{angles} + E_{torsions} + E_{oop} \quad \text{Eq. (1.2)}$$

$$E_{non-covalent} = E_{vdW} + E_{electrostatics} \quad \text{Eq. (1.3)}$$

$$E_{bonds} = k_r (r - r_{eq}) \quad \text{Eq. (1.4)}$$

$$E_{angles} = k_\theta (\theta - \theta_{eq}) \quad \text{Eq. (1.5)}$$

$$E_{torsions} = \sum_{n=1}^{N} \frac{V_n}{2} [1 + \cos n(\varphi - \delta)] \quad \text{Eq. (1.6)}$$

$$E_{oop} = k_\omega (\omega - \omega_{eq}) \quad \text{Eq. (1.7)}$$

$$E_{vdW} = \sum_{pairs\ i,j} \varepsilon_{ij} \left[\left(\frac{R_{min,ij}}{r_{ij}} \right)^{12} - \left(\frac{R_{min,ij}}{r_{ij}} \right)^{6} \right] \quad \text{Eq. (1.8)}$$

$$E_{electrostatics} = \sum_{pairs\ i,j} \frac{q_i q_j}{4\pi\varepsilon_0 r_{ij}} \quad \text{Eq. (1.9)}$$

Equations 1.1-1.9: k_r – bond stretching force constant; r_{eq} – equilibrium bond length; k_θ – angle bending force constant; θ_{eq} – equilibrium angle value; V_n – amplitude of cosine function; φ – torsional angle value; δ – torsional angle phase; k_ω – oop angle bending force constant; ω_{eq} – equilibrium oop angle value; ε_{ij} – energy well depth; $R_{min,ij}$ – radius at which interatomic potential is 0; r_{ij} – distance between atoms; q_i – point charge on atom i; ε_0 – vacuum electric permittivity.

As can be seen in Eqs. 1.1, 1.4 and 1.7 the bond and angle contributions to the potential energy are approximated as harmonic oscillators that depend on only two terms: bond stretching/angle bending force constants and the equilibrium bond length/angle value. It is essential to note that these terms control the local covalent atomic environment.[12] In the case of the torsional terms (Eq. 1.6), the harmonic oscillator approximation cannot be used due to the presence of several minima on the potential energy surface (PES).

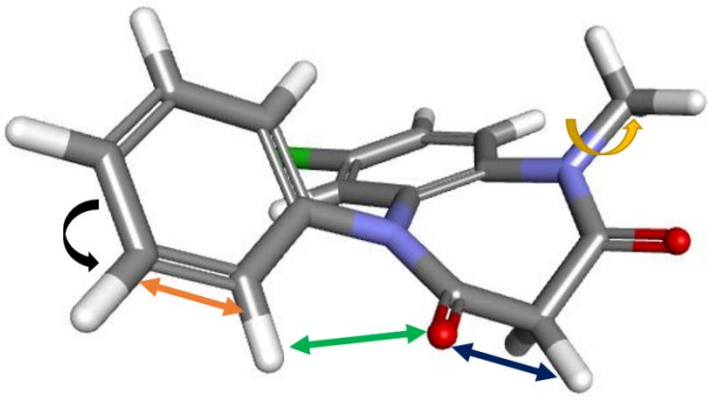

Figure 1.1. Molecular structure: Clobazam.[13] Arrows: orange – bond stretching; black – angle bending; yellow – torsional rotation; green – electrostatic interactions; blue – vdW interactions; oop angle bending not shown for clarity.

As such, these terms are modeled as a sum of cosine functions with different multiplicities (n) and phases (δ). Generally, the phases δ are constrained to either 0° or 180° to ensure that the PES of achiral molecules is symmetric.[12] The change in energy of a system is highly sensitive to rotations around the central bond in a torsion, and as such it highly influences the conformational energetics of the system. Therefore, having an accurate description of torsional terms is paramount for the usability of a FF.

When considering non-covalent terms, both the vdW and electrostatic terms are functions of distance between atoms. In the case of the vdW interactions (Eq. 1.8) the energy contribution is described as a Lennard-Jones (LJ) 12-6 potential, with the atomic repulsion term decaying as $1/r^{12}$ and the atomic attraction term decaying as $1/r^{6}$. The electrostatic terms (Eq. 1.9) are treated in terms of interactions between fixed atomic partial charges i.e. through a Coulomb potential. The usage of fixed partial charges brings about an important caveat of using the Coulomb potential for assessing electrostatic interactions, namely it precludes the introduction of polarizability into the system. Moreover, the Coulomb potential is known to be problematic due to the decay of the Coulomb function (1/r) that makes the calculation of the Coulomb contribution computationally expensive.[12]

While the descriptions above refer to fairly simple FFs, it is also worth mentioning that more complex terms (e.g., Taylor series approximation of a Morse function in MM3) or additional terms (cross-terms in MM3) may be used by more advanced, though more time consuming FFs (e.g., MMFF94, MM3, CFF). These FFs may also use complex terms to describe non-covalent interactions, such as a buffered LJ 14-6 potential in MMFF94 and dipole-dipole interactions in MM3.

1.2.1.2. MM – Force Field Atom Types.

In order to distinguish between atoms in different chemical environments, the most common FFs (including the ones described in section 1.2.1.) rely on so-called “atom types”. For example, a sp^3 hybridized oxygen atom (i.e. in a hydroxyl group) would have a different atom type than a sp^2 hybridized oxygen (i.e. in a carbonyl group). Each atom type has a different set of parameters associated with it to better describe the chemical system under scrutiny. Nonetheless, it is important to understand that, due to the relative size of the entire chemical space, it is

impossible to cover all the possible atom types. As such, the currently used atom types are valid only for local environments but do not consider distant functional groups. Such an example would be an aromatic carbon atom (e.g. in benzene), where irrespective of the nature of the substituent attached to it (i.e. electron-withdrawing or electron-donating) the atom type would be the same as for an unsubstituted aromatic carbon (Figure 1.2).[11]

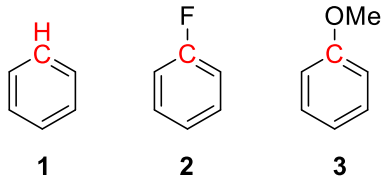

Figure 1.2. The atom type assigned to the aromatic carbon depicted in red would be the same for all three cases, irrespective of the substituent nature.

One way to avoid the pitfalls of using atom types is to discard them entirely. This is the philosophy behind two novel methods – H-TEQ[11] and SMIRNOFF[14] – that use basic chemical principles (i.e. electronegativity and hyperconjugation) and direct chemical perception to develop generic parameters for any molecule. While these methods are fairly new and still in the development phase, they have been shown to reach accuracies comparable to GAFF (a widely used, AMBER-compatible FF for small molecules) which has been parametrized on thousands of molecules.[11,14]

1.2.1.3. MM - Applications.

MM methods have been widely used to assess the properties of systems ranging from small organic molecules to proteins and large materials (e.g. zeolites). For example, MM is the basis of some docking programs, which are essential tools in drug discovery. Docking predicts the preferred orientation of a ligand inside the active site of a target molecule and as such can be used to distinguish good or weak binders from non-binders in the search for new drugs.[15] MM is also the basis of molecular dynamics (MD) simulations, which are used to observe how atoms interact

with each other over time.[16] For example, MD simulations have been used to describe protein folding[17] or to assess the stability of complexes obtained after docking.[16] Docking and MD will be discussed in-depth in section 1.3. In addition to these examples and to many others, as will be described in Chapter 5, MM methods have also been used in asymmetric catalysis to predict stereoselectivities with excellent results.[18]

1.2.1.4. MM - Limitations.

Despite the widespread use of MM methods, there are several limitations that must be considered. First, as described in section 1.2.1, MM methods rely on FFs to compute the potential energy of a system. The FFs are usually parametrized using high-level quantum chemical data or experimental data (i.e. ^{1}H nuclear magnetic resonance - NMR) on a representative set of molecules. Importantly, metals are notoriously hard to parametrize due to the difficulty of accounting for oxidation and spin states, which affect the energetics of metal-bound complexes significantly. As such, metals are not extensively described in most common FFs. Moreover, even though a representative molecule set is used for parametrization, it will not be enough to cover the entirety of the chemical space. As described in section 1.2.1.2, FFs rely on atom types to distinguish between atoms in different environments. It is generally accepted that the more atom types a FF contains, the more accurate it is.[12] Nevertheless, combined with limited parametrization, the usage of atom types restricts the transferability of parameters between molecules within a FF.[12] Thus, there will be molecular systems that will not be properly described with the existent parametrizations.

Second, as mentioned in section 1.2.1.1., the electrostatic terms are described by a Coulombic potential that does not account for polarizability. There have been several attempts to correct this behaviour. For example, the Atomic Multipole Optimized Energetics for Biomolecular

Applications (AMOEBA)[19] FF has been specifically designed to include polarizability in its treatment of electrostatic interactions through computed atomic multipole moments and an empirical atomic dipole induction model. While initially developed for water, AMOEBA was extended for small organic molecules, proteins, and nucleic acids. Nonetheless, the majority of commonly used force fields do not account for polarizability.

1.2.2. Quantum Mechanics (QM).

To improve on the limitations of MM and to obtain more accurate chemical results, it is important to use methodologies that concomitantly describe both nuclei and electrons. Amongst these methodologies is quantum mechanics (QM), which has seen widespread use in computational chemistry, especially for small organic molecules. It is important to note that through the treatment of electrons, QM methods are several orders of magnitude more computationally expensive than MM methods. Some of the most important milestones in QM method advancement were the development of the Roothaan-Hall equations (1951),[20] the Kohn-Sham equations (1965),[21] and the intermediate neglect of differential overlap (INDO) method developed by Pople (1970),[22] which gave rise to a plethora of QM techniques currently in use today. Amongst these, the most important are Hartree-Fock methods (section 1.2.2.1), semiempirical methods (section 1.2.2.2), and density functional theory (section 1.2.2.3).

1.2.2.1. Hartree-Fock (HF).

1.2.2.1.1. HF - Background.

Experimental chemists have found it useful to describe the behaviour of electrons in relation to orbiting nuclei and residing in orbitals. In computational chemistry, this concept is known as the Hartree-Fock (HF) approximation.[23] Developed in the 1920s, HF became popular in the 1950s with the advent of powerful computing methods. In short, HF is an *ab initio* (i.e. from

first principles) method that aims to determine the wavefunction of a system and its ground state energy by using several approximations including the Born-Oppenheimer approximation (i.e. nuclei are fixed and only electrons are moving). HF computes the molecular orbitals (MOs) of a molecule in terms of a linear combination of atomic orbitals (LCAO). Atomic orbitals (AOs) can routinely be built using the numerous basis sets available in the literature.[24]

To determine the ground state MOs, HF makes use of the self-consistent field (SCF) algorithm. In this algorithm, the Roothan-Hall equation (Eq. 1.10) is used as a substitute for the time-independent Schrödinger equation and is solved iteratively until self-consistency is achieved and the energy has converged (i.e. the change in energy between two consecutive iterations is smaller than a predetermined threshold).

$$FC = \varepsilon SC \qquad \text{Eq. (1.10)}$$

Equation 1.10: Roothan-Hall equation used for solving the SCF algorithm. F – Fock matrix; C – MO coefficient matrix; ε – diagonal matrix containing orbital energies; S – overlap matrix.

The Fock matrix in Eq. 1.10 is built at every iteration using the one-electron core Hamiltonian (containing the nuclear attraction and kinetic one-electron integrals) matrix and the Coulomb (electron repulsion) and exchange matrices obtained from calculating the two-electron integrals (Eq. 1.11).

$$F = H + 2J - K \qquad \text{Eq. (1.11)}$$

Equation 1.11: Obtaining the Fock matrix. H = Hamiltonian; J – Coulomb contribution of two-electrons integrals; K – exchange contribution of two-electron integrals.

The computation of the J and K matrices used to build the Fock matrix represents the most computationally intensive step of calculating the Roothan-Hall equation. The Fock matrix is diagonalized and a new set of MOs is obtained at every iteration. Once convergence is achieved,

the MOs represent an accurate description of the wavefunction and can be used to calculate any molecular property within the HF framework. Because the computational cost associated with HF is relatively high for standard desktop PCs, this method has been routinely used only for relatively small systems (< 200 atoms).

1.2.2.1.2. HF - Limitations.

While HF represented a major breakthrough for quantum chemists, it soon became apparent that a major pitfall of the method involved the neglect of electronic correlation. In brief, electron correlation measures how much the movement of one electron is influenced by all the others. This neglect is one of the major reasons why HF is incapable of describing dispersion interactions (London forces contributing to vdW interactions), which are of paramount importance in biomacromolecules and biological systems. Nonetheless, it is important to mention that several methods have been developed based on the HF formalism (post-HF methods) that account for dynamic electron correlation (i.e. Møller-Plesset perturbation theory (MPn, n=1-4), configuration interaction (CI), quadratic configuration interaction using single and double excitations (QCISD), QCISD including an estimate of triplet excitations (QCISD(T)), etc. However, these methods are even more computationally intensive than HF and are thus only applicable to small organic molecules.

1.2.2.1.3. HF - Applications.

Despite these drawbacks, HF and post-HF methods have been successfully used in the determination of barrier heights in reaction mechanisms i.e. Diels-Alder reactions[25] and intramolecular hydrogen transfers, of which we mention the case of 2-pyridone (Schemes 1.1-1.2)[26], to name a few.

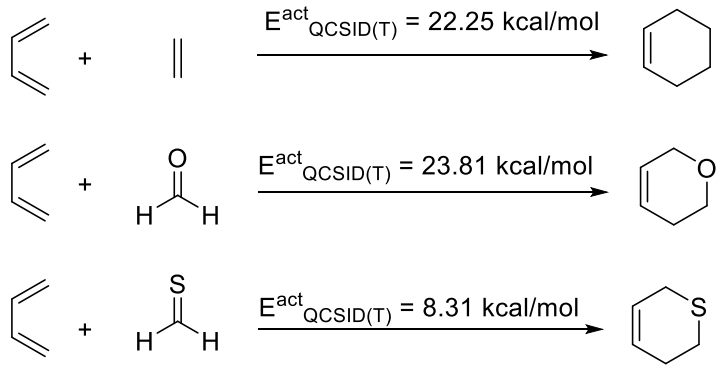

Scheme 1.1. Diels-Alder reaction between butadiene and ethylene, formaldehyde and thioformaldehyde. Activation energies show that these reactions can take place at room temperature, with the thioformaldehyde addition being the fastest.[25]

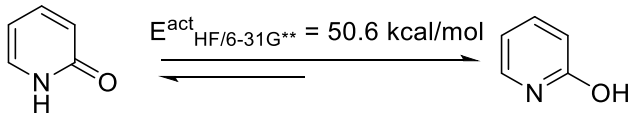

Scheme 1.2. Keto-enol tautomerism of 2-pyridone in the ground state. The major tautomer was computed to be the enol tautomer, with a barrier of tautomerization of ~ 50 kcal/mol at the HF/6-31G** level of theory.[26]

1.2.2.2. Semiempirical Methods (SE-QM).

1.2.2.2.1. SE-QM - Background.

Since even two decades ago HF methods were too computationally expensive to apply on large systems (i.e. biomacromolecules and proteins), chemists started looking into alternatives that would be more accurate than MM but computationally cheaper than HF methods. One answer to this problem was the development of semiempirical QM (SE-QM) methods. Based on the HF formalism, SE-QM methods are less computationally expensive than HF through their approximation or omission of electronic interactions (J and K matrices in Eq. 1.11). To account

for the electronic interactions, SE-QM use empirical parameters that are fitted to reproduce experimental data.[27] Moreover, the most common SE-QM methodologies use specially optimized Slater-type minimal basis set approximations to ensure fast and relatively reliable calculations. Several SE-QM have been developed, such as AM1,[28] PM3,[29] PM6,[30] and RM1,[31] which have been extensively used in conjunction with large systems (i.e. water clusters, nucleic acids, proteins).[24,32] Several important developments to SE-QM methods have been made to accurately depict the non-covalent interactions found in biological systems, including dispersion, hydrogen-bonding, and halogen-bonding corrections.[24]

1.2.2.2.2. SE-QM - Limitations.

Several limitations plague SE-QM methods, as they did in the case of the "parent" approach (HF). First, as was the case with HF, correlation is generally not described. Moreover, when using SE-QM methods on small organic molecules one must be careful, as qualitatively and quantitatively wrong results will be obtained for molecules that are dissimilar from the molecules used to parametrize the methods.[24] Another limitation stems from the use of the minimal basis set, which leads to the underestimation of intermolecular polarization and affects non-covalent interactions.[33] In addition to this, the majority of SE-QM methods only consider valence electrons.

1.2.2.2.3. SE-QM - Applications.

One of the most widely used SE-QM methods is PM6, which has been successfully used in generating optimized protein structures and determining several protein properties, such as secondary and tertiary structures. Moreover, PM6 has been used to model the formation of a tetrahedral intermediate in chymotrypsin (Scheme 1.3).[34]

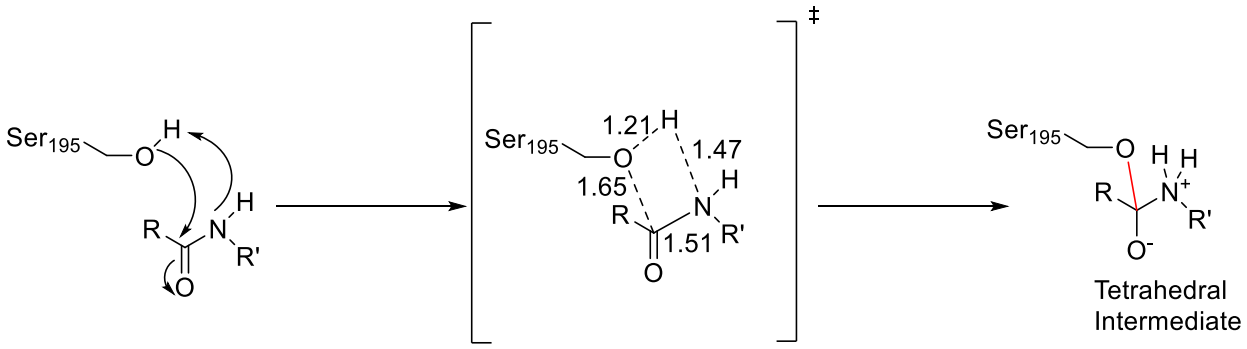

Scheme 1.3. Formation of a tetrahedral intermediate in chymotrypsin.[34] Distances for the transition state (TS) are given in Ångstrom. New covalent bond between O-C in the tetrahedral intermediate is shown in red. R and R' can be any substituent. The TS was verified to contain only one negative frequency.[34]

Another interesting application of SE-QM methods is the prediction of host-guest binding affinities in supramolecular chemistry. In a study by Muddana and Gilson,[35] the PM6-DH+ method developed by Korth[36] (DH+ represents dispersion and hydrogen bonding corrections to the PM6 method) was used to calculate the binding affinities of 29 guest complexes in conjunction with cucurbit[7]uril. The authors found a strong correlation between computed and experimentally determined binding free energies, showcasing the versatility of SE-QM methods.

1.2.2.3. Density Functional Theory (DFT).

1.2.2.3.1. DFT - Background.

While HF and SE-QM methods are useful in certain circumstances, there are times when the system under scrutiny requires computing with a high degree of accuracy, such is the case for predicting molecular properties of organic molecules, breaking/forming covalent bonds or computation of stereoselectivities. For these purposes, density functional theory (DFT) was developed in the 1960s by Kohn and Hohenberg and later by Kohn and Sham. DFT differs

fundamentally from HF and SE-QM methods by only requiring the electron density to determine the molecular properties of chemical systems. Moreover, unlike HF methods, DFT uses functionals (i.e. a function of another function) to approximate the exchange-correlation energy, thus providing more accurate results than HF methods. It is interesting to note that although DFT has been used in computational physics since the 1970s, it only gained traction in computational chemistry in the 1990s through the seminal work of Becke and others in the area of computing the exchange-correlation term, which led to the creation of the famous B3LYP functional.[37-39] Ever since, functional development has become one of the most active areas in computational chemistry, along with the development of several highly efficient quantum chemistry packages such as ORCA[40] and GAMESS.[41,42]

To obtain the DFT ground state energy, one must follow the same path as for HF methods, i.e. solving Eq. 1.10 through the SCF algorithm. The Fock matrix, by contrast, described in Eq. 1.11 has a different form, which includes the exchange-correlation term – Eq. 1.12.

$$F = H + 2J - \alpha K + V_{XC} \qquad \text{Eq. (1.12)}$$

Equation 1.12: Obtaining the Fock matrix in DFT. H = Hamiltonian; J – Coulomb contribution of two-electrons integrals; K – exchange contribution of two-electron integrals; V_{XC} – exchange-correlation matrix.

It is important to note that the exchange-correlation matrix V_{XC} in Eq. 1.12 is computed using numerical integration on a grid. Moreover, the α scaling factor in Eq. 1.12 is functional dependent (i.e. some functionals use exact exchange from HF theory in addition to the exchange-correlation computed with DFT in their formulation. As such $\alpha \neq 0$ in the case of these functionals.).

1.2.2.3.2. DFT - Limitations.

Although DFT methods account for the correlation term, they still suffer from the same inability as HF methods to describe intermolecular interactions, especially vdW forces.[43] Nevertheless, major advancements have been made in this area through the work of Grimme with his DFT-Dn(n=1,2,3,4) schemes[44] that allow a correct treatment of long-range interactions. Most importantly, these schemes are easy to implement and very fast to compute, making them a must-have for any DFT calculation. Grimme has also been the proponent of several low-cost composite methods for the accurate description of large systems (i.e. biomacromolecules or proteins) including the PBEh-3c and B97-3c methods.[45,46] These methods use relatively small basis sets but include corrections for basis set superposition error (BSSE) and long-range dispersion interactions, which makes them highly appealing for biological systems.

Another major limitation of DFT is the self-interaction error (SIE). When describing the correlation energy using an exchange-correlation functional, the interaction of an electron with itself is taken into account. This behavior is wrong and is evident primarily in systems with unpaired electrons. This leads to quantitively and qualitatively wrong results, as is the case for the dissociation of carbocation radicals, which often give large errors when computing binding energies.[47] Moreover, due to the SIE, DFT encounters issues with describing some transition metal complexes, including spin states and binding free energies.[48]

1.2.2.3.3. DFT - Applications.

As outlined above, DFT is highly useful for describing properties of organic molecules and chemical phenomena such as breaking/forming of covalent bonds and computing enantioselectivities. These will be discussed in depth in section 1.4 but we will highlight some examples in this section as well. For instance, DFT (B3LYP/6-31+G** level of theory) has been

successfully used to assign vibrational frequencies and normal modes of flavonoid derriobtusone A using predicted and experimental IR and Raman spectra (Figure 1.3).[49]

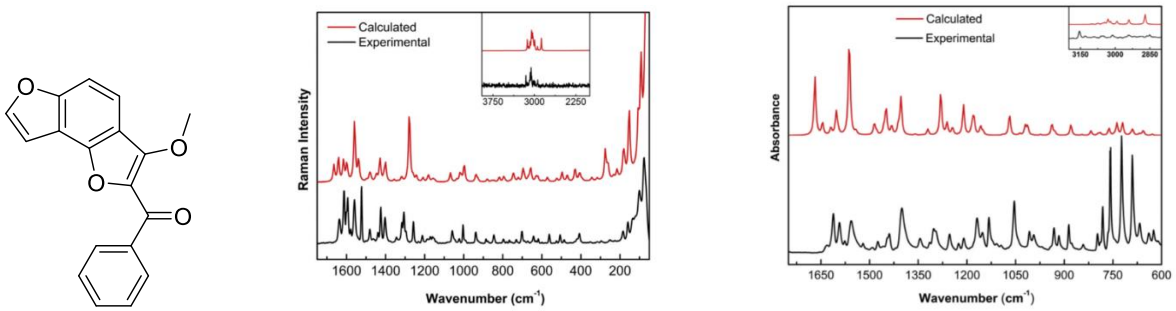

Figure 1.3. Structure of derriobtusone A (left). Comparison between the experimental and predicted Raman spectra (middle) and IR spectra (right) for derriobtusone A. Spectra taken from reference 49.

In addition to molecular properties and vibrational spectra, DFT has been used to rationalize numerous reaction mechanisms. Among the most interesting ones we mention the mechanism of the first selenium organocatalyzed *syn*-dichlorination of alkenes.[50] In the original paper, Cresswell *et al.*[50] proposed PhSeCl as the active catalyst. However, a DFT study by Fu *et al.*[51] at the B3LYP/6-311++G** level of theory showed that using PhSeCl as the catalyst leads to an endergonic reaction (Figure 1.4), while using $PhSeCl_3$ as the active catalyst led to a very favourable exergonic reaction (Figure 1.5).

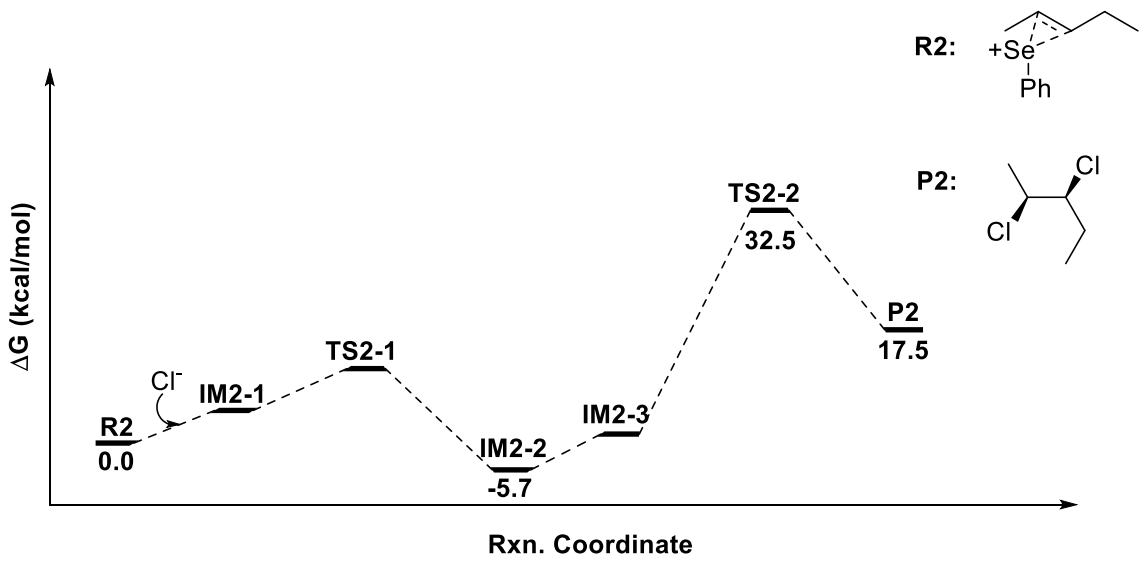

Figure 1.4. Reaction mechanism in acetonitrile of the selenium organocatalyzed *syn*-dichlorination of 2-pentene using PhSeCl as the active catalytic species. The reaction is endergonic by ~ 17 kcal/mol. Figure reproduced from reference 51.

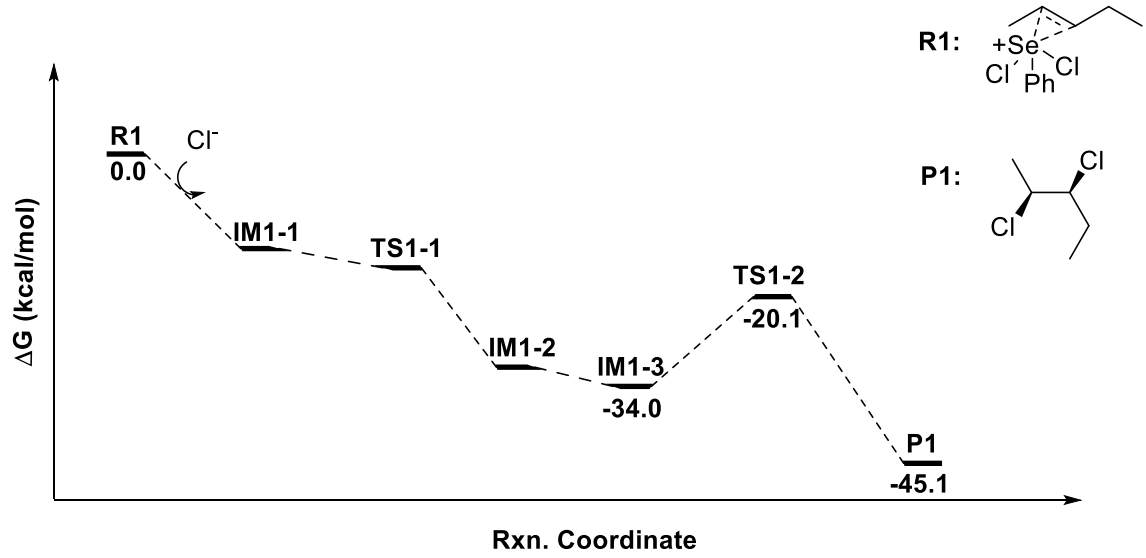

Figure 1.5. Reaction mechanism in acetonitrile of the selenium organocatalyzed *syn*-dichlorination of 2-pentene using $PhSeCl_3$ as the active catalytic species. The reaction is exergonic by ~ 45 kcal/mol. Figure reproduced from reference 51.

Fu *et al.* also showed that the rate-limiting step of the reaction has a barrier of only 13.9 kcal/mol for $PhSeCl_3$ (TS1-2, Figure 1.5), which agrees with the experimental data that the reaction happens readily.

Beyond the ability of rationalizing reactions mechanisms, DFT has also been used to develop new organocatalysts. In a study by Fleming *et al.*[52] a highly active urea catalyst was developed for addition reactions to epoxides (Scheme 1.4).

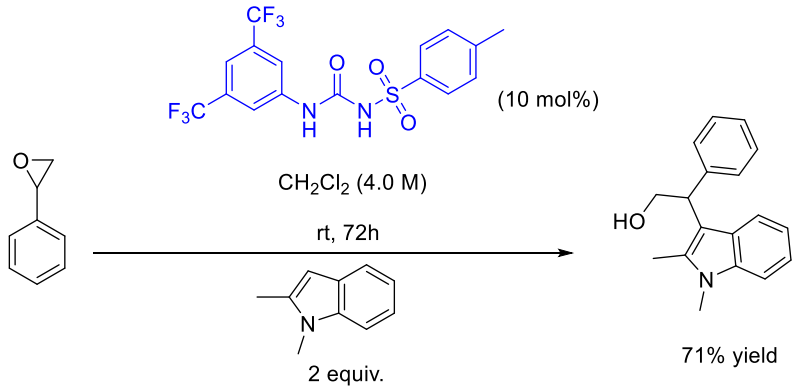

Scheme 1.4. Reaction scheme for the indole addition to styrene oxide in the presence of a urea catalyst. Scheme reproduced from reference 52. Catalyst shown in blue.

This catalyst was selected based on structural optimization at the B3LYP/6-31G* level of theory in the presence of the styrene oxide. The hydrogen-bonding interactions between the catalyst and epoxide were deemed crucial for the catalyst reactivity (Figure 1.6).

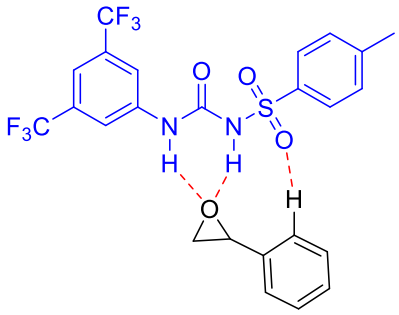

Figure 1.6. Hydrogen bonding interactions between the urea catalyst and styrene oxide. Key interactions are shown with dashed red lines. Figure reproduced from reference 52.

1.2.3. Quantum Mechanics/Molecular Mechanics (QM/MM).

As outlined in the previous sections, MM methods are very useful at describing entire proteins or large biomacromolecules, while QM methods are useful at describing organic molecules with the occasional application to larger systems. However, in some cases, it is highly desirable to combine the two methods – QM and MM – to study important aspects of chemistry, such as stereoselective and/or regioselective protein catalysis. The main idea behind this hybrid approach – QM/MM – is the treatment of a small number of atoms using highly accurate QM methods (generally the ligand of interest and key amino acids in the active site of the protein) while treating all the other atoms with MM methods. This approach allows the computation of long-range electrostatic terms and steric effects that contribute to enzyme reactivity while accurately describing the bond breaking/formation process between the ligand and active site residues.[53] The QM/MM approach has been used, for example, to propose a credible mechanism for the regioselective chlorination of tryptophan (Trp) in the biosynthesis of pyrrolnitrin (Scheme 1.5), an antifungal antibiotic, by the Trp-7-halogenase.[54]

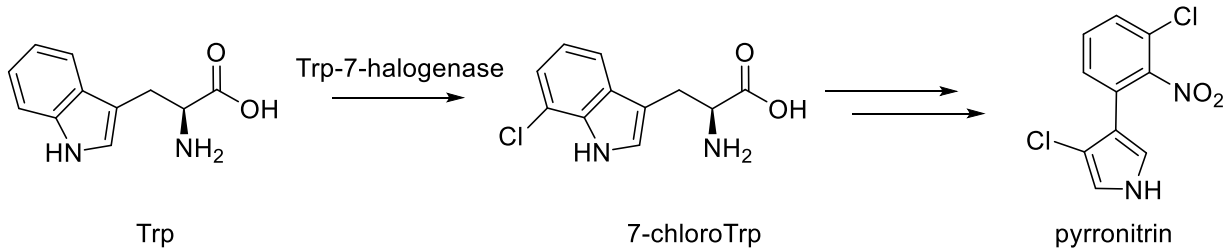

Scheme 1.5. Transformation of Trp to pyrronitrin.

The QM/MM study showed that two aminoacids, K49 and E346, played a major role in stabilizing the intermediate products formed during the reaction between hypochlorous acid (HOCl) and Trp (Scheme 1.6).

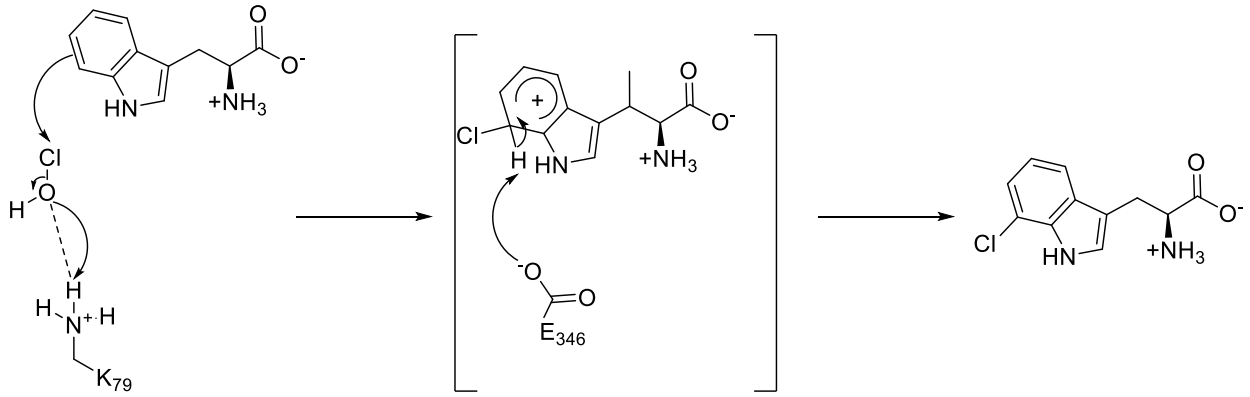

Scheme 1.6. Proposed regioselective mechanism from reference 54.

In addition to studying stereoselective protein catalysis, QM/MM methods have also been used for docking. For example, a QM/MM algorithm developed by Chaskar *et al.*[55] overcomes some of the FF limitations described in section 1.2.1.4. (polarization effects and metal-bound complexes). This algorithm was tested on three different sets that included zinc and iron metalloproteins and compared to classical docking studies. As expected, compared to classical docking, the QM/MM algorithm showed a significant improvement due to accounting for polarization and correctly treating oxidation and spin states using QM.

While QM/MM methods are extremely valuable tools and provide accurate results when used correctly, it must be emphasized that they too suffer from drawbacks, some more serious than others. First, QM/MM calculations are computationally demanding, and as such extended simulations on large systems can be performed routinely on standard desktop PCs only using SE-QM methods for the QM region. If computational resources allow (i.e. access to supercomputers and parallel computing), QM/MM calculations can employ either HF or DFT for the QM region.

Second, QM/MM simulations are not "black box" calculations – significant work must be put into generating a correct starting system. As is the case for any molecular dynamics simulation, several important steps must be undertaken before the simulations can be run: the correct protonation state must be assigned to all ionizable amino acids in the active site, MM parameters have to be generated in case they are missing from the FF used in the simulations, and the number and placement of water molecules near and around the active site must be carefully assessed.[56] Third, when performing a QM/MM calculation, a decision has to be made with regards to counter ions and charge neutralization. Currently, there is no consensus as to whether to add counter ions to the system to neutralize the charge due to charged buried groups.[56] However, a popular approach is that after deciding on a pH at which to run the simulation and assignment of protonation states, the total charge of the system is kept as is, while others propose that the decision to add counter ions should be made depending on the system at hand.[57]

1.2.4. Machine Learning (ML).

In the previous sections we have described how computational methods use the information from nuclei and electrons to compute properties and rationalize various chemical principles. In this section we will focus on methods that use chemical patterns, including complex combinations of functional groups and patterns that govern molecular properties to describe and rationalize various aspects of chemistry.[58] Among these methods we will mainly focus on machine learning (ML), a field of artificial intelligence that uses extensive training sets to gain knowledge from them and use it for predicting properties of new data.

1.2.4.1. ML – Background.

ML has seen an impressive surge of interest in chemistry in the past decade due to several factors: **1)** increased computational power available even for a non-specialist user, **2)** availability

of open-source data sets necessary to create predictive models and **3)** development of several easy-to-use software packages and libraries used to create ML models. A recent review by Cova and Pais[58] explored the exponential growth of publications involving ML models in chemistry over a 10-year timeframe (2008-2018), and showed that the number of publications skyrocketed from a few hundred in 2008 (counted from 1970 onward) to over 8000 in 2018. This significant increase was prevalent in fields such as quantum, organic and medicinal chemistry, where ML methods were used to improved existing methodologies and to aid in the design and synthesis of new molecules.[58] To better understand ML techniques and their applications, we will take a closer look at the most popular models that have had widespread success in chemistry applications: artificial neural networks (ANNs) and Random Forest (RF) models.

1.2.4.2. ML - Artificial Neural Networks.

Artificial neural networks (ANNs) are ML models that can fall under two categories. The first category is that of supervised learning, meaning they require training data in order to learn and infer the parameters of the function described by the ANN architecture. These parameters are then used to describe novel data (or testing set). The second category is that of unsupervised learning, meaning that the ANNs look for patterns in non-labeled input data. ANNs resemble a biological neural network (Figure 1.7), with the basic unit being the artificial "neuron" connected to other "neurons" through "synapses". Neurons (or nodes) can be of three types: input nodes (which takes numerical data presented as input), hidden nodes, and output nodes. The input data is presented in the form of activation values i.e. each node has an input value made of a series of numbers (often normalized in the [0,1] range) that describe molecules. As such, the ANN must understand the molecular description (i.e. its simplified molecular-input line-entry system (SMILES) classification),[59] and molecular properties and convert them to usable numbers. It is

important to mention that the higher the input number, the greater the activation. As can be seen in Figure 1.7, the activation values are passed through the neural network by the means of hidden nodes. The activation values are weighted before reaching the hidden nodes. Each hidden node can receive several activation values, which it then sums up. However, before a meaningful output can be delivered by the ANN, the information passing through the network must be translated by a transfer function. This is done at each node that receives activation values by the means of common transfer functions such as sigmoid or Gaussian. Depending on the task at hand, several layers of neurons may be required to produce the required output. The first application of ANNs in chemistry dates back to 1973, when Hiller *et al*.[60] used an ANN to predict the bioactivity of 1,3-dioxanes. Ever since, pharmaceutical companies and academic groups alike have used ANNs to improve the drug discovery rate. For example, Jaen-Oltra *et al*.[61] used ANNs on a series of 111 quinolones (molecules with antibacterial activity) in order to build a model that would predict the minimum inhibitory concentration (MIC) of quinolones.

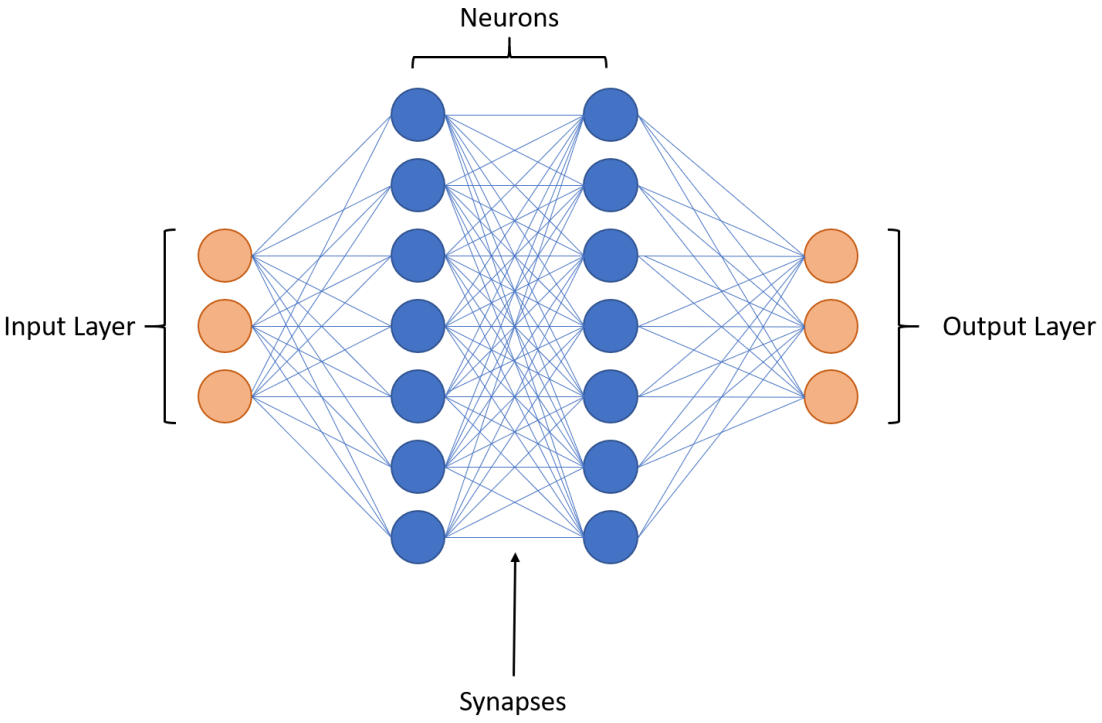

Figure 1.7. Description of a simple ANN containing an input and output layer along with neurons and synapses.

Out of the 111 quinolones with experimentally determined MICs, 70% were randomly selected as the training set with the remaining 30% as testing set. As inputs for their ANN, the authors used a series of 62 descriptors, including the number of heavy atoms, double and triple bonds and carbon atom type (primary, secondary etc). The correctness results obtained for three categories of MICs (≤ 0.05, ≤ 0.10 and ≤ 0.20 μg/ml) were ~ 100% for the training set and > 80% for the testing set, which shows the predictive power of the ANN. In addition to being used for quantitative structure-activity relationships (QSAR) studies, ANNs have been extensively used in predicting absorption, distribution, metabolism, excretion and toxicity (ADMET) properties of drug molecules.[62] For example, a highly accurate software package using ANNs to predict cytochrome P450 (CYP450)-mediated sites of metabolism (SoMs) is XenoSite,[63] which was trained using quantum, atomic and molecular descriptors and applied to 680 CYP450 substrates across 9 isoforms. The results showed that XenoSite is extremely accurate across all isoforms, with an average accuracy of 87% using the top2-metric (predicted metabolite is correct if it is ranked in the top 2 predictions).[63]

1.2.4.3. ML - Random Forest Models.

RF models are part of the supervised learning category of ML. More specifically, RFs are classification models that contain an ensemble of *N* decision trees trained on different randomly selected subsets of the training set. The decision trees will then provide *N* predictions that will be counted towards the final prediction, which will be made using the "majority rule" (i.e. the most frequent prediction made by the *N* decision trees will be selected as the final prediction). Decision trees have several advantages over ANNs and SVM models: they can be used to describe highly

dimensional data, they can discard irrelevant descriptors, and can be interpreted easily by chemists.[64] As such, RF models have been highly sought after in the drug discovery field. For example, an essential molecular lipophilicity descriptor used in drug discovery is the octanol/water partition coefficient logP. A highly lipophilic molecule (logP > 5) will be poorly soluble, and as such will have low bioavailability. In contrast, a lightly lipophilic molecule (logP < 2) will be soluble and highly bioavailable.

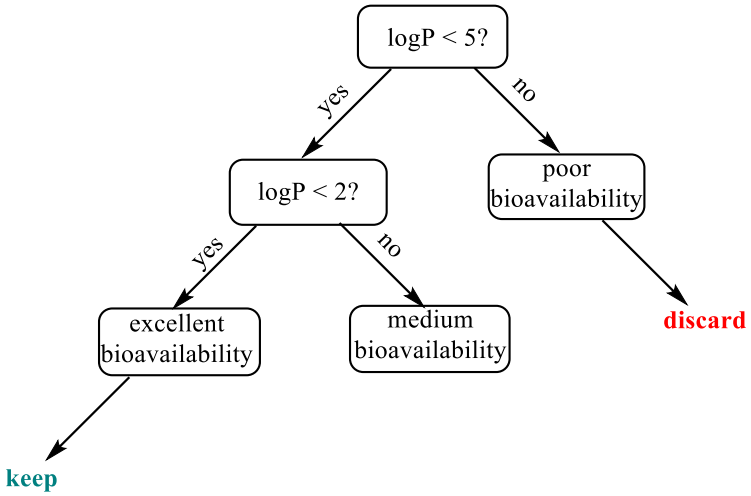

Figure 1.8. Decision tree describing whether a drug candidate would be kept or discarded based on its logP value.

During QSAR or virtual screening (VS) studies, a decision tree like the one in Figure 1.8 can be built and integrated into a larger RF model to determine whether a molecule would be suitable for synthesis and testing. In addition to QSAR and VS studies, RF models have also been used in docking to improve scoring functions. For example, Wang and Zhang[65] developed a new protein-ligand binding scoring function based on RF using a highly accurate training set containing over 3000 experimentally-determined binding affinities and over 3000 computer-generated decoys. Their RF model was built using 20 descriptors and exhibited a Pearson coefficient R = 0.73, which was shown to be superior to the best classical scoring function tested (R = 0.64).

Moreover, as was the case with ANNs, RF models can be used to accurately predict SoMs. Recently, a method developed by Finkelmann *et al.*[66] used an RF model built with atomic descriptors related to both the electronic and steric environments of atoms in molecules. The model was tested on the XenoSite dataset and led to an average accuracy of 90.9% using the top2-metric.

1.2.4.4. ML – Limitations.

While ML models are generally robust and provide accurate results, they are not without drawbacks. First, ML models are only as accurate as the data used for training them. While several datasets (SoMs, protein-ligand binding affinities etc.) have recently been made available for QSAR and VS studies, the data might not necessarily be uniform. For example, when it comes to SoM determination, there are several assays that can be used to determine which CYP isoform is responsible for substrate oxidation. Depending on the assay and conditions employed (which might differ between laboratories) non-uniform data will be collected, which will ultimately impact the ML models that predict SoMs.[27] Second, a high-quality dataset must also be large enough for training as well as highly diverse. If the dataset is small the model will be poorly predictive due to overfitting of parameters. Moreover, if the dataset is not diverse enough, the RF model can only be used to predict properties of similar molecules (similar to SE-QM methods discussed in section 1.2.2.2).[27]

1.3. Computational Tools in the Context of Medicinal Chemistry and Drug Discovery.

In the previous sections we have discussed the background of the most important computational methods currently in use in chemistry and some applications and drawbacks of each. In this section we will expand on the usage of these methods in drug discovery and development, a field tightly entwined to medicinal chemistry. Moreover, we will highlight the

requirements that medicinal chemists have when it comes to the application of these methods in terms of usability and underlying methodologies.

1.3.1. Computer-Aided Drug Design (CADD).

It is well known that drug discovery is a highly tedious and expensive endeavour. Overall it takes approximately 9 years on average to bring a drug to the market with a total development cost of ~$2 billion.[67,68] To shorten the required time to bring a drug to the market and to reduce the associated costs, medicinal chemists have advocated for the introduction of computer-aided drug design (CADD) techniques in the drug discovery pipeline. Indeed, it has been proposed that using CADD tools in this process could lead to an overall cost reduction of 50%.[69] However, to streamline the usage of CADD tools in drug design, medicinal chemists require **1)** user-friendly software in a "black box" environment, **2)** accurate and reliable software that is ideally contained within one drug design platform and **3)** simple and easy to read output that can be visualized if necessary (i.e. protein-ligand interactions). These requirements are paramount because medicinal chemists often have no expertise in computational chemistry. Moreover, to complement the experimental tools that medicinal chemists have at their disposal and to ensure that the correct computational tool is used in the drug discovery process, CADD methods have been divided into two subcategories: structure-based drug design (SBDD) and ligand-based drug design (LBDD).

1.3.1.1. Structure-Based Drug Design (SBDD).

SBDD is a category of CADD that uses the 3D structure of a validated biological target (enzyme or receptor) in order to develop high-affinity ligands or inhibitors.[70] In this method, the emphasis is put on the interactions between the target and ligand, including binding poses, conformational preferences and reaction mechanisms.[27] Generally, the target structure is

determined through either NMR, X-ray crystallography or homology modelling. Amongst the most important techniques in SBDD are molecular docking, VS and MD simulations.

1.3.1.1.1. SBDD - Molecular Docking.

Molecular docking is an essential tool in the repertoire of medicinal chemists. In short, docking is a method that explores the behaviour of a ligand inside the active site of a target. Often the underlying theory behind docking is MM-based, although rule-based docking methods exist as well. The docking procedure consists of two distinct steps: conformational search and scoring.

To perform the conformational search, several algorithms can be employed. For example, the docking program FITTED[71] uses a highly efficient genetic algorithm to find the best ligand poses inside the active site of the target. If during the conformational search the parameters of the ligand and protein (bond lengths, angles, and torsions) do not change, the docking technique is called rigid-body docking. This technique is a direct consequence of the "lock and key" mechanism of enzyme-ligand interactions, which assumes that only the right ligand will fit inside the active site of a target enzyme. It has been shown that rigid body docking has a far greater accuracy if the crystal structure was co-crystallized with a ligand rather than in its apo structure.[72] If the parameters change during the docking process to account for variations in the ligand and protein conformations, the technique is called flexible docking. Flexible docking was developed as a consequence of the "induced-fit" theory introduced by Koshland,[73] where an enzyme can change conformations to accommodate an incoming ligand. It is worth noting that flexible docking is more computationally demanding than rigid body docking due to the sampling of different side chain and/or backbone and ligand conformations.

When the conformational search is complete, the binding poses are scored to determine the most likely conformation of the ligand inside the active site. While scoring functions differ

between docking programs, they generally involve MM-based energy terms such as electrostatics and vdW interactions between ligands and target along with more complex terms.

Over time several docking programs have been developed – AutoDock,[74] Glide,[75] GOLD,[76] FITTED – and successfully used in the drug discovery process. Importantly, these docking programs all have somewhat easy-to-use interfaces that allow medicinal chemists to undertake their own docking studies. Moreover, at the end of a docking run, it is possible to visualize the preferred binding poses inside the active site of the enzyme target. This visualization is important because it gives medicinal chemists the opportunity to assess the structural integrity of the protein-ligand complex, as well as to visually assess if the desired interactions between enzyme and ligand are fulfilled. In addition, a medicinal chemist could use their chemical intuition to elicit changes in the ligand to improve the binding affinity and then dock the improved compound and compare to the original to test their hypothesis. Success stories that involved molecular docking include the *in silico* development of Zanamivir (influenza drug),[77] the first neuraminidase inhibitor to be commercially developed, and the rationalization of nelfinavir HIV-1 protease resistance, which lead to the development of more potent analogues.[78]

1.3.1.1.2. SBDD - Virtual Screening.

At the onset of any drug development project a decision must be made with respect to which type of compounds should be pursued. Knowledge and information about the biological target are paramount, as well as that of key interactions in the active site of the target that should be fulfilled by a possible drug. Therefore, the question is: what is the starting point for developing a new drug?

Thankfully, sustained efforts by several pharmaceutical companies and academic groups have led to the creation of large commercially available small-molecule libraries that cover a large

area of the available chemical space. Databases such as ZINC[79] and Chemspace[80] have proven to be invaluable when it comes to providing a suitable starting point for a drug design project. These databases can then be screened to obtain a series of drug-like molecules that can be docked into the target enzyme to assess their suitability as ligands or inhibitors or used in LBDD methods. The top compounds can then be selected as lead compounds, synthesized, or purchased and biologically tested. As such, obtaining a hit compound can be done exclusively *in silico* and the first stage of the drug development process (i.e. hit discovery) can be resolved in a matter of days or weeks. This entire approach is known as virtual screening. To enable medicinal chemists to undertake their own VS studies without proficiency in software development or command line environments, drug discovery platforms such as FORECASTER[81] have been developed. FORECASTER was developed by chemists for chemists, and it provides inexperienced users with a graphics user interface (GUI) that automates the process of running a VS study without the need to know the underlying theories. VS has become standard for drug design and has led to several success stories, such as finding novel inhibitors for DNA methyltransferase (involved in cancer)[82] and a potent drug candidate against tyrosine phosphorylation regulated kinase 1A (involved in Down Syndrome).[83]

1.3.1.1.3. SBDD - MD Simulations.

As described in section 1.3.1.1.1, docking is an essential tool in drug discovery. However, docking only provides a static picture of ligand-enzyme interactions. At times, it is desirable to observe the effects of these ligand-enzyme interactions over time to better understand the processes that take place while the enzyme is performing its biological function. One method of tracking these interactions and changes in enzyme structure is through MM-based MD simulations. Through the usage of modern computing facilities, simulations of more than 100000 atoms are

now routine[84] and the timescales on which MD simulations can be run range from picoseconds to milliseconds.[17] Moreover, depending on the level of detail required for the simulations, MD can be performed at either the atomistic level (each atom is represented individually) or using coarse-grained representations. For example, if one is interested in observing bond breaking/formation during protein catalysis, it would be advisable to use MD simulations at the atomistic level. This approach is, however, computationally demanding, and it should only be employed if the protein of interest is relatively small and the timescale of simulation relatively short. On the other hand, if one is interested in protein folding, which occurs on a long timescale (micro to milliseconds), a coarse-grained MD simulation can be undertaken. In the coarse-grained representation, entire functional groups or amino acid residues are represented by "beads" in order to speed up the simulations and to reduce the computational cost.[85]

To perform an MD simulation, several steps must be undertaken prior to starting the simulation. First, a good initial structure for the enzyme is required. This structure can either be taken from X-ray crystallography, NMR, homology modeling, or cryogenic electron microscopy (Cryo-EM). Then, hydrogen atoms must be added to the crystal structure to prepare it for the simulation and the correct protonation state must be assigned to the ionizable amino acids. Once the structure is ready for simulation, the overall enzyme charge may be neutralized through the addition of counter ions, followed by the placement of the enzyme in a box of solvent (water, methanol etc.) to obtain a realistic solvent effect. While this adds complexity to the system, it allows a more accurate description of entropic effects (i.e. hydrophobic effects).[84] Next, as described in section 1.2.3, a decision has to be made whether charge equilibration should be performed or not. Once all these steps have been fulfilled, the simulation can be run. The steps described above are non-trivial and are in fact largely inaccessible to medicinal chemists.[84] As

such, developers of MD software packages such as NAMD[86] have spent considerable time in providing a comprehensive and user-friendly GUI that automates these steps, hiding the underlying theory for easier use. These developments have led to several successes in the application of MD simulations to drug discovery, such as identifying cryptic binding sites.[87]

In one example, a novel trench-like binding site was identified for HIV-1 integrase, which led to the discovery of raltegravir, the first FDA-approved drug for this enzyme.[88] Another application of MD in drug discovery is the accurate computation of ligand binding energies. For instance, a series of azoles were optimized as potent anti-HIV agents starting from inactive scaffolds through free energy perturbation calculations.[89] Based on these calculations, two compounds were selected and tested *in vitro* where they exhibited high nM activity (300-800 nM range). To improve their potency, they were subsequently modified based on the ligand binding energy calculations to improved compounds with low nM (10-20 nM range) activity.

1.3.1.2. Ligand-Based Drug Design (LBDD).

In contrast to SBDD, LBDD is used when 3D information about the biological target of interest is unavailable. Active compounds such as drugs must be developed indirectly by carefully studying the known substrates and/or inhibitors of a target.[90] The most popular approaches in LBDD involve QSAR studies and pharmacophore modeling, which will be discussed below.

1.3.1.2.1. LBDD – QSAR.

When compounds (substrates or inhibitors) are known for a biological target, it is desirable to map the relevant features (key physicochemical characteristics) to understand their activity and the relation between their structure and activity (structure-activity relationship). Then, analogues with improved potency and/or drug-likeness can be designed while maintaining the core features that afford activity. This is the underlying theory behind QSAR, a computational method used for

quantifying the relationship between the structural features of a molecule and its biological activity.[90] To maximize the biological activity of subsequent analogues of a compound of interest, a mathematical model is built using molecular descriptors of these compounds (such as logP, pKa, and molecular weight) and the stability and robustness of the model is verified against biological activity. The paramount aspect of QSAR is the selection of descriptors - only those descriptors that affect biological activity should be chosen. This can be done using several statistical methods, such as linear regression, principal component analysis or partial least square analysis.[90] Some QSAR models (comparative molecular field analysis - CoMFA[91] and comparative molecular similarity indices - CoMSIA[92]) use 3D descriptors to build models that relate to biological activity. The advantage of applying such descriptors is that they use both steric and electrostatic molecular features to relate to biological activity. However, these 3D descriptors are highly dependent on the conformation of the compound of interest. Generally, such compounds are optimized using MM or QM techniques to obtain the lowest-energy conformation, which is then assumed to be the biologically active one. This assumption might not always hold, and as such a major pitfall of 3D QSAR techniques is building erroneous models based on the wrong active conformer. Nonetheless, 3D QSAR methods - CoMFA and CoMSIA - have been applied successfully to various aspects of drug design, chiefly the optimization of mercaptobenzensulfonamides as HIV-1 integrase inhibitors[93] and the design of 1,4-dihydropyridines as calcium channel blockers.[94]

1.3.1.2.2. LBDD - Pharmacophore Modeling.

While pharmacophore modeling has generated interest in drug discovery only in the past few decades, the concept of a pharmacophore was introduced as early as the beginning of the 20th century.[95] Across the decades, medicinal chemists have offered different definitions for a pharmacophore, including a highly popular one given by Schueler[96] in 1961: “a molecular

framework that carries (phoros) the essential features responsible for a drug's (pharmacon) biological activity." To unify the existing definitions, the International Union of Pure and Applied Chemistry (IUPAC) provided an updated description of a pharmacophore in 1997: "a pharmacophore is the ensemble of steric and electronic features that is necessary to ensure the optimal supramolecular interactions with a specific biological target structure and to trigger (or to block) its biological response".[97] A pharmacophore is comprised of structural features such as hydrogen-bond donors/acceptors and hydrophobic, halogen or aromatic moieties that contribute to a molecule's biological activity (Figure 1.9).

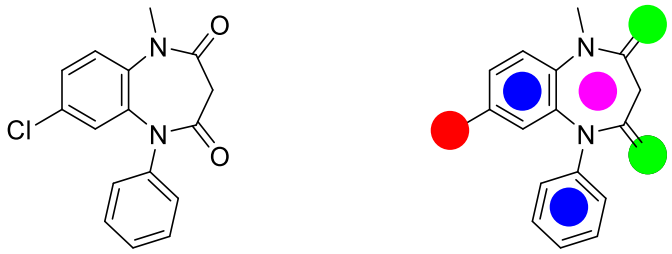

Figure 1.9. Structure of Clobazam[13] (left) and its pharmacophore (right). Red – halogen moiety; blue – aromatic moiety; green – hydrogen bond acceptor; purple – hydrophobic moiety.

In drug discovery, a pharmacophore model is usually generated on a training set made of compounds that are known to be active on a specific target. The molecules have their conformations sampled through various algorithms, followed by molecular alignment and assembly of their pharmacophore features.[98] Sampling algorithms have to account for ligand flexibility, which is one of the main challenges of pharmacophore modeling. This can be achieved by pre-generating multiple conformations for each ligand and saving them in a database, or computing them on-the-fly during the generation of the pharmacophore model. Regardless of method, the sampling of the conformational space must ensure that all biologically-relevant conformations have been considered.[98]

Apart from ligand flexibility, the alignment of various ligands represents a different challenge. Molecular alignment can be carried out in two different ways: atom-by-atom mapping and mapping based on molecular features. For structures with similar atomic environments, atom-by-atom mapping represents a good choice. However, for highly dissimilar ligands, mapping based on molecular features is more advantageous because it precludes the usage of pre-defined anchor points necessary for atom-by-atom mapping.[98] Another challenge of pharmacophore modeling is represented by the choice of training set; it has been shown that depending on the training set, completely different pharmacophore models can be generated for the same target using the same software.[99-101]

Despite these challenges, pharmacophore modeling has seen widespread use in the drug discovery community. A study by Ren *et al.*[102] used pharmacophore modeling in conjunction with VS to find potent *in vitro* and *in vivo* inhibitors of transforming growth factor-β Type I receptor. In a different example, pharmacophore modeling combined with docking led to the discovery of potent compounds against human leukotriene A_4 hydrolase and the human nonpancreatic secretory phospholipase A2.[103] In another study, successful virtual activity profiling was achieved on a set of 100 antiviral compounds and several antiviral targets using a novel pharmacophore-based parallel screening approach.[104]

1.4. Computational Tools in the Context of Organic Chemistry.

In the previous section we described how computational tools are used to improve the drug discovery process and the overall molecular discovery rate. Nevertheless, these tools have far-reaching implications in many other fields, such as organic chemistry and more specifically organic synthesis. For example, ML methods have been used with some success in retrosynthetic analyses and synthesis design.[105-107] Nonetheless, these methods have several drawbacks. One

drawback is that it does not consider stereochemistry changes during reactions, and it also provides reaction pathways that are either too long or unfeasible.[108] These current drawbacks preclude the implementation of these tools in wet labs, but do provide an important stepping stone in the overall endeavour of using computational tools in organic synthesis. Moreover, the area of reaction prediction and design is still under active development and will likely yield successful methodologies for experimentalists to use. Apart from the usage of ML methods for synthesis design, other computational tools have been widely used in organic synthesis to rationalize reaction mechanisms, chemical reactivity and stereoselectivities of various organic and metal-based catalysts. The usage of these tools, along with relevant examples and success stories will be discussed below.

1.4.1. Reaction Mechanisms.

The breaking and formation of bonds occurs on an attosecond timescale.[109] Experimental measurements of such phenomena require incredibly complex equipment, and is beyond the means of most organic chemists. As such, computational chemistry has taken over the role of explaining how chemical bonds form and break. Among the most widely used tools to explore reaction mechanisms is DFT, because of its low computational cost in comparison to post-HF methods and its relatively high accuracy. DFT is particularly well suited in describing the ground state geometries of reactants and products, as well as exploring the reaction PES, locating TS structures, and predicting side products. Increasingly, experimental chemists have collaborated with computational chemists to rationalize experimental observations. Furthermore, due to significant advancements in the development of user-friendly, highly efficient and accurate QM packages, experimental chemists have slowly started running their own DFT studies.[110]

To understand the necessity of DFT in elucidating reaction mechanisms, we will first refer to the famous example mentioned in section 1.1: the Sharpless asymmetric dihydroxylation.[4] To understand how important DFT was in this case, we will take a closer look at the possible reaction mechanisms proposed before theoretical studies were conducted, and how DFT was used to differentiate between them. The Sharpless asymmetric dihydroxylation of alkenes (Scheme 1.7) proceeds through an osmium-based catalyst and leads to the formation of chiral diols. This reaction is of exceptionally high value in organic synthesis because it allows the introduction of chirality in non-chiral compounds. Since its development, the Sharpless asymmetric dihydroxylation has been extensively used in the total synthesis of natural products.[111]

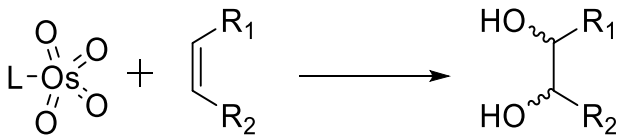

Scheme 1.7. Sharpless asymmetric dihydroxylation of alkenes.

When the reaction was first described, Sharpless proposed that the mechanism went through a [2+2] cycloaddition step that led to the formation of a 4-membered ring osmaoxetane (Scheme 1.8a), which would undergo ring expansion to convert to a 5-membered ring TS.[112] Later, Corey proposed that the mechanism actually proceeded through a [3+2] cycloaddition step that led to the direct formation of a 5-membered ring TS without proceeding through an osmaoxetane intermediate (Scheme 1.8b).[113] These proposals sparked a decade-long debate between Corey and Sharpless, with both producing experimental evidence for their respective mechanisms.

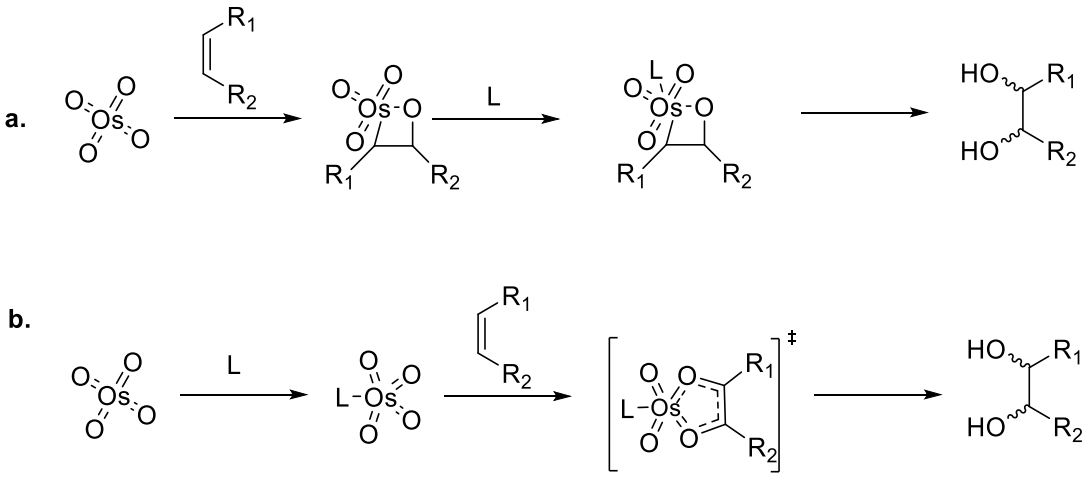

Scheme 1.8. Proposed mechanisms for the Sharpless asymmetric dihydroxylation.

It was not until 1997, 17 years after the Sharpless asymmetric dihydroxylation was first described, that the mechanism of the reaction was established. Using ammonia as the ligand to chelate osmium (L in Schemes 1.7 and 1.8), and using ethylene and propene as model alkenes, Houk and Sharpless[4] located TS structures for both mechanisms at the B3LYP/6-31G* level of theory. Importantly, they showed that the TS energy for the [3+2] cycloaddition step was in the range of 3.1-3.4 kcal/mol, while the [2+2] cycloaddition had a prohibitive barrier of ~ 40 kcal/mol for the formation of the osmaoxetane and a barrier of ~30 kcal/mol for the ring expansion. Moreover, they obtained theoretical kinetic isotope effects that could be compared to experimentally determined ones. In the case of the [3+2] cycloaddition step, 80% of the experimentally determined kinetic isotope effects matched the theoretically determined ones within one standard deviation, while the ones for the [2+2] cycloaddition step did not match at all. This data was then used to conclude that the rate limiting step of this reaction was indeed a [3+2] cycloaddition step, and that the reaction proceeded through a stepwise mechanism.

In another example that showcases the effectiveness of DFT in elucidating reaction mechanisms, Tomberg *et al.*[114] studied the formation of epoxides versus hydroxylation products

in CYP450-mediated aromatic oxidations using the PBE0 functional and a custom built basis set. This oxidation takes place through a radical mechanism. Using a simplified heme model along with bromobenzene and phenol as model substrates (Scheme 1.9a), Tomberg *et al.* showed that the nature of the intermediate (radical or cationic) played a major role in the resulting product (Scheme 1.9b). Moreover, the authors were able to show that the spin density during the reaction resides primarily on the iron if the resulting product was a hydroxide, while residing primarily on the aromatic ring if the product was an epoxide. The elucidation of this mechanism is of high importance in transition-metal catalysis, as well as in enzyme catalysis, where CYP450 have been often used.

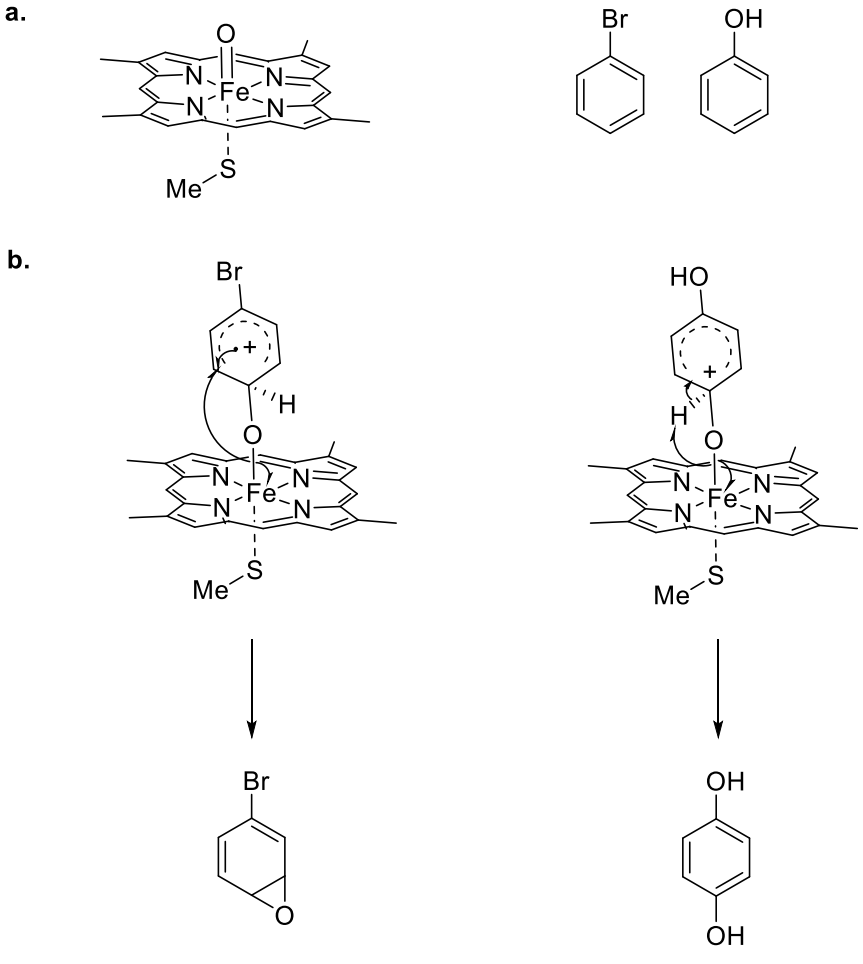

Scheme 1.9. a) Simplified heme model used as reactive species in the reaction mechanism, along with bromobenzene and phenol used as model substrates for the reaction. b) Reaction mechanisms that lead to the formation of either epoxide or hydroxide.[114]

1.4.2. Chemical Reactivity.

The effectiveness of DFT studies is not only limited to the study of reaction mechanisms. In fact, a whole new field of study built around DFT has emerged in the past few decades – conceptual DFT (cDFT). cDFT has been successfully used in providing the theoretical basis of qualitative chemical concepts, such as hardness, softness, electronegativity, chemical potential, electrophilicity, and nucleophilicity.[115] For example, the chemical potential μ of a molecule represents the tendency of electrons to escape from a system in a state of equilibrium.[116] Within the DFT framework, μ can be computed as the sum of the energy of the lowest unoccupied molecular orbital (LUMO) and highest occupied molecular orbital (HOMO) (Eq. 1.14).[115] In another example, to explain why acid-base reactions proceed in a set direction, Pearson introduced the concept of "hardness" and "softness", as well as the hard-soft acid-base (HSAB) theory.[117] The HSAB theory states that a hard nucleophile will preferentially react with a hard electrophile, while a soft nucleophile will preferentially react with a soft electrophile. Within the framework of DFT, the chemical hardness can be expressed as the difference between the energies of the LUMO and the HOMO, while the softness is just the inverse of hardness (Eqs. 1.15-1.16).

$$\mu = \frac{1}{2} \times (\varepsilon_{\mathrm{LUMO}} + \varepsilon_{\mathrm{HOMO}}) \qquad \mathrm{Eq.}\,(1.14)$$

$$\eta = \frac{1}{2} \times (\varepsilon_{\mathrm{LUMO}} - \varepsilon_{\mathrm{HOMO}}) \qquad \mathrm{Eq.}\,(1.15)$$

$$S = \frac{1}{2\eta} \qquad \mathrm{Eq.}\,(1.16)$$

Equations 1.14-1.16. Description of the global parameters chemical potential, hardness, and softness.

The softness of a molecule relates to its polarizability, with a larger molecule being softer, thus more polarizable. Once hardness and chemical potential were introduced as concepts, Parr *et al.*[118] developed an electrophilicity index ω that makes use of them (Eq. 1.17).

$$\omega = \frac{\mu^2}{2\eta} \qquad \text{Eq. (1.17)}$$

Equation 1.17. Description of the global electrophilicity ω.

This index is an excellent description of the energy stabilization obtained when the molecule receives an additional electronic charge from the environment.[115] Importantly, these indices only provide information about molecular reactivity and stability. However, sometimes it is useful to determine exactly which atom(s) within a molecule will react. To this end, local atomic reactivity indices (LARIs) have been developed to account for the reactivity of individual atoms.

Among these, the most important are the Fukui functions.[119] Based on Kenichi Fukui's seminal work on the role of the HOMO and LUMO orbitals in chemical reactions,[120] the Fukui functions (or coefficients – FC) relate the atomic electronic density in the HOMO and LUMO orbitals to the propensity of an individual atom to undergo nucleophilic (f^+), electrophilic (f^-) or radical attack (f^0) (Eq.1.18-1.20).[115]

$$f^+ = \rho_{LUMO} \qquad \text{Eq. (1.18)}$$

$$f^- = \rho_{HOMO} \qquad \text{Eq. (1.19)}$$

$$f^0 = \frac{1}{2} \times (\rho_{HOMO} + \rho_{LUMO}) \qquad \text{Eq. (1.20)}$$

Equations 1.18-1.20. Description of the Fukui functions for nucleophilic, electrophilic, and radical attacks.

The Fukui functions have been applied extensively within the cDFT framework to explain local atomic reactivity patterns. For example, the reactivity of lignin precursors *p*-coumarol, coniferol and sinapol (Figure 1.10) was investigated in order to explain the formation of lignin, an aromatic polymer present in the walls of wood cells.[121]

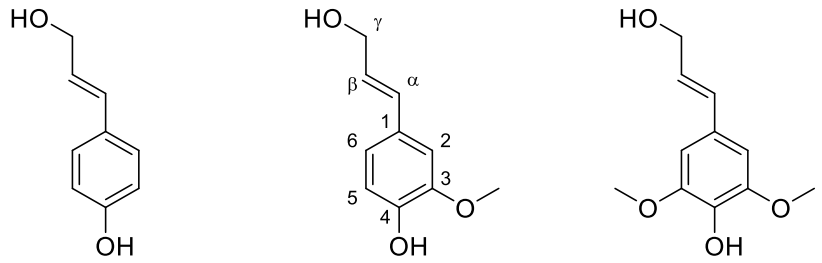

Figure 1.10. Structures of *p*-coumarol, coniferol and sinapol.

Since the formation of lignin involves a radical mechanism, the f^0 values were computed and it was shown that for *p*-coumarol and sinapol the *β*-carbon is the most reactive site, while for coniferol the most reactive site is in the carbon-oxygen bond region of the hydroxyl group attached to the γ carbon. In another example, Mendez and Gazquez[122] looked at the reactivity of three enolates: cyclohexanone, phenacyl and butyrolactone (Figure 1.11) using Fukui functions and the HSAB theory.

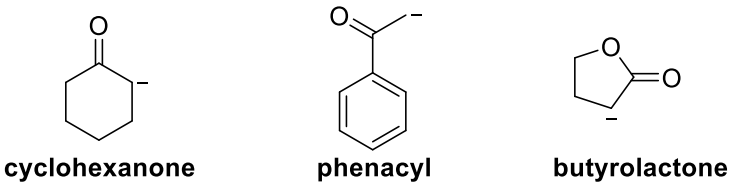

Figure 1.11. Structures of the enolate ions of cyclohexanone, phenacyl and butyrolactone.

To understand the difference in reactivity between the different reactive sites, Mendez and Gazquez computed the f^- values for the three enolates. These values showed that the highest values

for the electrophilic Fukui function resided on the carbonyl oxygen atom in all three cases, followed by the enolate carbon. Moreover, they showed that depending on the substituents on the enolate, the reactivity order can shift between the enolate carbon and carbonyl oxygen, effectively changing the reactive site. This can occur if the reagent and solvent is kept constant. However, changing the solvent can lead to a change in reactivity in the same enolate, which is supported by experimental evidence.[122] Overall, these examples serve as a validation of the usage of cDFT in organic chemistry, and as proof of the ability of cDFT to aid chemists in their understanding of chemical reactivity.

1.4.3. Catalyst Design, Screening and Enantioselectivity Computations.

Apart from rationalizing reaction mechanisms and chemical principles, computational tools can also be used to design new molecules or new reactions. For example, of high interest in organic chemistry are chiral molecules. To synthesize such molecules one could use biocatalysis or a chiral pool; however, these methods have numerous drawbacks, such as the relative stability and specificity of biocatalysts and the reduced number of chiral molecules available in the chiral pool.[18] An alternative to these methods is asymmetric synthesis, which allows one to synthesize chiral molecules in high yield and purity. To allow for efficient asymmetric syntheses, cheap, green, selective catalysts must be employed. Most commonly used catalysts in asymmetric syntheses are metal based, which suffer from poor availability, high cost, and relative toxicity. To avoid the usage of metals in catalysis, one can explore the organic catalysts for the required chemical transformations. However, these catalysts must be designed and synthesized, a tedious process if done only experimentally. Thus, screening and designing new catalysts computationally has started gaining traction in the organic chemistry field.

To enable the design of selective catalysts, one must first have an accurate method to compute the stereoselectivity of the catalysts. To this end, several methodologies for designing catalysts and computing stereoselectivities have been developed, including MM,[123,124] QM,[125-127] and QM/MM[128] techniques. For example, Du *et al.*[126] used DFT to predict the reactivity of supported metal oxide for the selective catalytic reduction of nitrogen oxides with ammonia. In their study, they used several DFT descriptors – LUMO, hydrogenation and HOMO energies – to establish the oxidizing ability and acidity of potential oxide catalysts. In their search they separated the potential catalysts in three categories: active components, promoters, and inactive components/support. Those catalysts that exhibited strongly negative hydrogenation energies (high oxidizing ability), combined with low LUMO energies (high acidity) and high HOMO energies (possibility for reoxidation) were the active components of the reaction. These were experimentally tested and found to correlate accurately with the theoretical study, providing an excellent example about the usage of DFT in obtaining new catalysts.

However, while DFT has been used in catalyst screening and design, it suffers from several drawbacks. First, the computation times of optimizing ground state geometries, finding TS structures, and computing enantioselectivities might be prohibitive for organic chemists, especially when libraries of potential catalysts must be screened. Second, it has been shown that popular integration grids used for computing the exchange-correlation energy provide quantitatively wrong results for computed stereoselectivities due to their lack of rotational invariance.[129] Thus, due to these drawbacks and to ensure a fast, efficient, and accurate screening of libraries of potential catalysts, several academic groups have been working on providing user-friendly computational platforms that use MM methods. Among the most comprehensive platforms are VIRTUAL CHEMIST[18] and CatVS.[130]

VIRTUAL CHEMIST, developed in the Moitessier research group at McGill University, is a state-of-the-art computational platform that allows an organic synthesis experiment to be simulated from start to finish. Specifically designed for asymmetric synthesis, the platform was validated on four different types of experiments: one-by-one design, library screening, hit optimization and substrate scope evaluation. The platform was designed with the necessities of organic chemists in mind and includes modular workflows that allows experimentalists to create their own experiments through a few clicks. Most importantly, the underlying methodologies are hidden from the user and using the platform does not require any computational expertise. When the platform was developed, three main aspects were given special consideration: **1)** preparation of libraries of catalysts, **2)** predicting stereoselectivities, and **3)** evaluating catalytic activity.

The most important program in the VIRTUAL CHEMIST platform is the Asymmetric Catalyst Evaluation (ACE)[123] package. Based on the MM3 FF, ACE uses the Hammond-Leffler postulate (Figure 12 top) to construct the TS as linear combination of reactants and products. The forming bonds are considered as a combination of covalent bonds, present in the products, and non-covalent interactions present in the reactants (Eq. 1.21).

$$E_{TS} = (1 - \lambda)E_R + \lambda E_P \qquad \text{Eq. (1.21)}$$

Equation 1.21. Description of the linear combination of reactants and products used by ACE to construct the TS.

To ensure that the TSs are properly described, a Lamarckian genetic algorithm to optimize and perform an exhaustive conformational space search of TS templates was implemented. After the TSs for a given reaction have been optimized, ACE computes the stereoselectivities of a given catalyst (in either vacuum or solvent) using the Curtin-Hammett principle (Figure 1.12 bottom).

Although ACE uses an MM-based FF for the conformational search, TS optimization and

stereoselectivity computation, the accuracy of the program is within 1 kcal/mol when compared to experimentally determined stereoselectivities (tested on 350 reactions from 7 reaction classes).[18] The accuracy and ease-of-use makes the overall platform highly attractive for organic chemists.

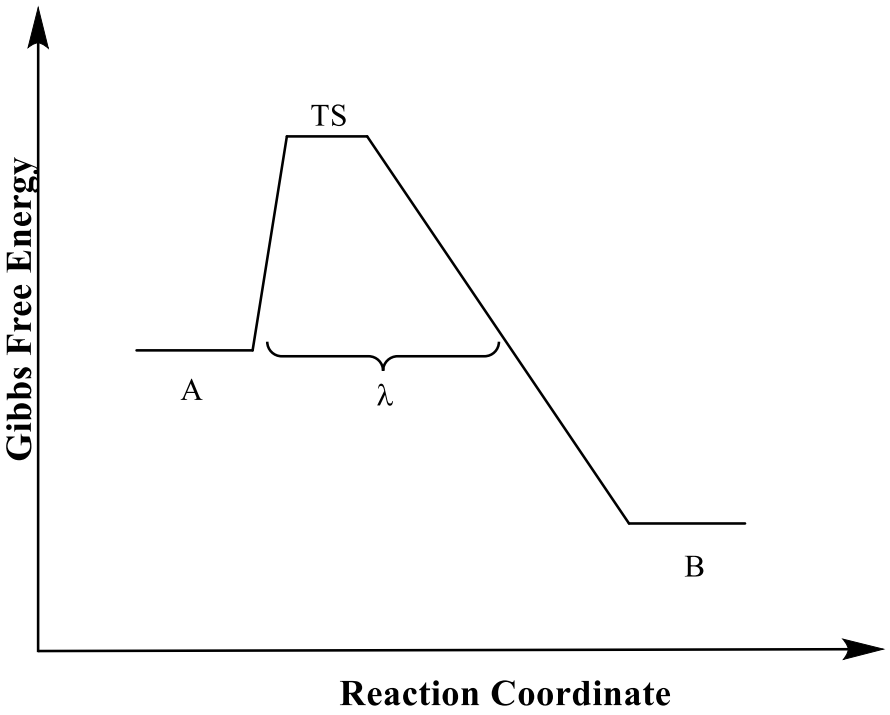

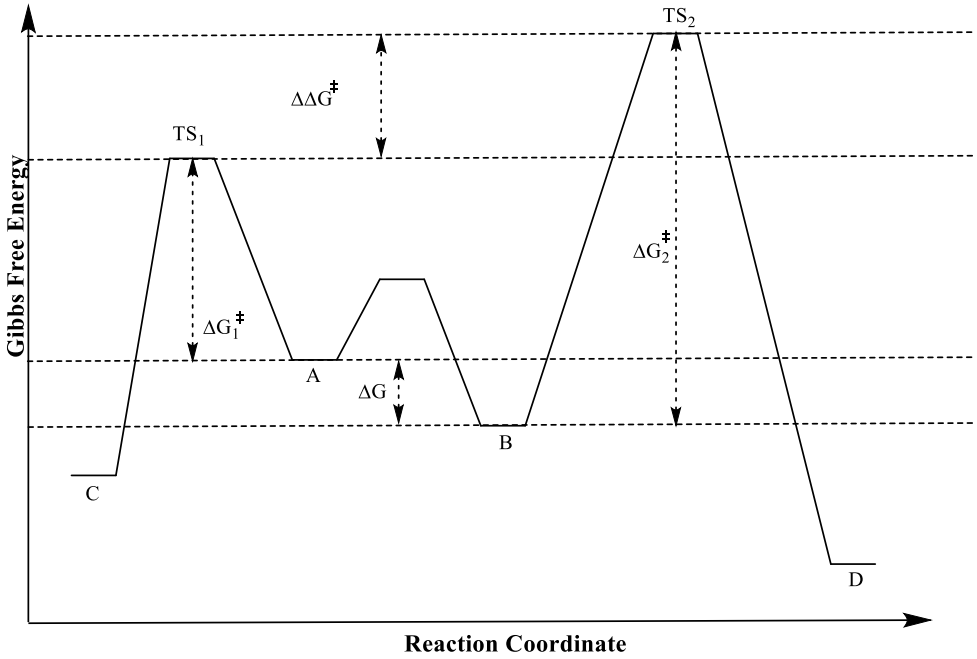

Figure 1.12. Top: Hammond-Leffler postulate: the TS resembles the reactants (A) if it is an early TS and the products (B) if it is a late TS. The step λ controls whether the TS is late or early in the ACE computations. **Bottom:** Schematic depiction of the Curtin-Hammet principle. Stereoselectivity of a catalyst can be computed by converting the difference in energy between TS_1 and TS_2 (i.e. $\Delta\Delta G^{\ddagger}$) to an enantiomeric excess (%ee) ratio.

The underlying theory, auxiliary programs, drawbacks and extensive testing and validation of VIRTUAL CHEMIST will be discussed in greater detail in Chapter 5.

Another important computational platform in the field of asymmetric synthesis is CatVS, developed by Rosales *et al.*[130] This platform is based on the quantum guided molecular mechanics method (Q2MM),[131] which allows the development of transition state force fields (TSFFs)[132] using QM data obtained for small model systems of a reaction's TS. This methodology has been validated on several reactions, such as metal-catalyzed oxidations and hydrogenations, P450 oxidations, and stereoselective additions to aldehydes.[130] To explore the conformational space of the possible TSs, CatVS uses the Monte Carlo routines available in Macromodel,[133] while the computation of stereoselectivities is done using Boltzmann-averaging of the energies of the conformations that lead to a specific stereoisomer. To explore the applicability of CatVS to a reaction of chemical interest, a library of ligands was screened for the Rh-catalyzed asymmetric hydrogenation of enamides on two substrates (Scheme 1.10).

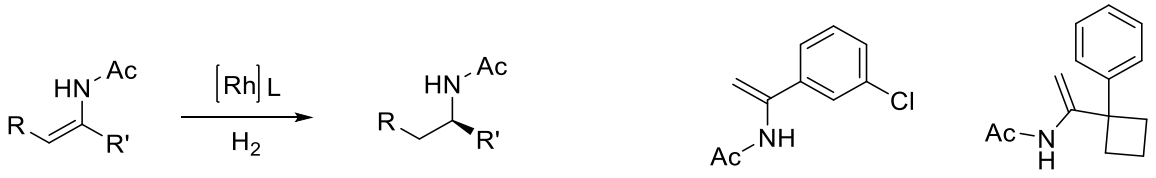

Scheme 1.10. Overall scheme for the Rh-catalyzed asymmetric hydrogenation of enamides (left).[130] Substrate with a conjugated α-substituent (middle) and substrate with a non-conjugated α-substituent (right).

To differentiate between screened ligands (L in Scheme 1.10), Rosales *et al*. set a threshold of 96% for the enantiomeric excess. In the case of the substrate with a conjugated α-substituent, CatVS was able to identify four correct ligands and one false positive. In the case of the substrate with a non-conjugated α-substituent, CatVS found two highly selective ligands and failed to identify one false negative. Despite these successes, CatVS presents drawbacks, such as the inability to consider highly flexible or highly charged TSs, as well as the inability to model solvent effects. Nonetheless, if the TSs of the reaction of interest are rigid and experimental data available to compare to predictions, CatVS can be highly useful. Moreover, the VS study presented above was performed on a standard PC in less than 12h per ligand, which makes it highly attractive to organic chemists due to low computational requirements and fast turnover rate.

1.5. Conclusions.

In this chapter, we presented several computational tools and methodologies, each with their associated background, limitations, and applications. Among the most interesting tools are MM, QM, and ML methods, which have seen widespread use in various fields of chemistry. Most importantly, we described the usage of these methods in the context of drug discovery/medicinal chemistry and organic chemistry research.

Within drug discovery, computational tools are of extreme importance due to their ability to shorten the time a drug requires to reach clinical trials, and to potentially reduce the failure rate (reduced toxicity). Using computational tools in the drug discovery pipeline enables researchers to test hypotheses much faster than they would experimentally (for example changing various

functional groups on drug candidates and observing the interactions with a biological target through docking or MD simulations), and allows them to obtain a hit compound in mere days or weeks. This compound can then be tested for toxicity *in silico.* For example, computational tools to assess the potential SoMs can be used to verify whether the lead compound could be metabolized into harmful reactive metabolites. If this is the case, *in silico* structural changes can be made to the compound to remove the possibility of reactive metabolite formation even before attempting synthesis. This process ensures that only promising molecules are synthesized, which contributes to a lower cost of the overall drug discovery process.

Within organic chemistry, computational tools can be used to rationalize reaction mechanisms and chemical reactivity, but also to design new molecules and reactions. Throughout the years, reaction mechanisms for highly synthetically relevant reactions, such as the Sharpless asymmetric dihydroxylation and P450-mediated oxidation of aromatic compounds, have been explained. Moreover, significant advancements in understanding chemical reactivity have been made through the application of cDFT to chemical principles such as hardness, softness, chemical potential, and electrophilicity. These examples showcase the power and utility of computational tools when applied to problems of organic chemistry. In addition to this, we described the ability to design and screen numerous catalysts *in silico* in a matter of days with user-friendly computational platforms. These platforms are designed especially for experimentalists to allow their manipulation with limited computational expertise. Most importantly, these tools allow organic chemists to design and perform experiments *in silico* and to make any necessary adjustments and changes to their hypotheses and reagents. Indeed, these tools enable scientists to effectively remove tedious aspects of experimental chemistry and to focus on high-level problem solving and experimental design.

1.6.Thesis Objectives.

This thesis develops computational tools and protocols to improve the molecular discovery rate in organic and medicinal chemistry. Overall, the thesis will address the advancements we have made in this field, by considering three separate but interconnected examples. **Chapters 2 and 3** will discuss the development of a computational protocol to accurately model the conformational preferences of clinically-relevant nucleosides (historically used as drugs against diseases such as HIV, cancer and herpes), and thereby enable the design and synthesis of those nucleosides with desirable properties. **Chapter 4** will present integration of QM, docking, and ML methods for CYP450 inhibition prediction in the drug discovery pipeline, while **Chapter 5** will focus on improving the current tedious, costly process of developing asymmetric catalysts by delivering a computational platform that has been experimentally validated by organic chemists for catalyst discovery.

Chapter 2 – Accurately Modeling the Conformational Preferences of Nucleosides – Methodology

Preface.

Existing computational methods are useful in enabling the synthesis of compounds with highly desirable properties, yet in some cases these methods need to be developed for special classes of molecules. This is the case of nucleosides, which have historically been used as drugs against diseases like cancer and HIV. Nucleosides are notorious for their modeling difficulty because their conformations are highly sensitive to solvent and intrinsic stereoelectronic effects. Since they owe their activity to their conformation, the ability to predict these conformations is significant. Currently, experimentalists rely only on the synthesis of various nucleoside analogues to improve on existing drugs. However, this approach is very iterative and costly, since it requires a high number of analogues to be synthesized and tested. The work presented in Chapter 2 focuses on facilitating the synthesis of only desirable nucleosides by developing a computational protocol that is able to accurately predict the conformational preferences of these nucleosides in solution. This approach will likely reduce the cost associated with developing new nucleoside-based drugs. This chapter is based on the work published in the paper:

Burai Patrascu, M.; ‡ Malek-Adamian, E.; Damha, M.J.; and Moitessier, N. *J. Am. Chem. Soc.*, **2017**, 139, 39, 13620-13623.

‡ first author

MBP developed the computational protocol, compiled the training and testing sets and performed the calculations and data analysis. EMA performed the wet lab experiments and MBP, EMA, MJD and NM contributed to writing the manuscript.

Abstract.

Sugar puckering of nucleosides impacts nucleic acid structures, hence their biological function. Similarly, nucleoside-based therapeutics may adopt different conformations affecting their binding affinity, DNA incorporation, and excision rates. As a result, significant efforts have been made to develop nucleoside analogues adopting specific conformations to improve bioactivity and pharmacokinetic profiles of the corresponding nucleoside-containing drugs. Understanding and ultimately predicting these conformational preferences would significantly help in the design of more effective structures. We developed a computational protocol based on hybrid QM/MM umbrella sampling simulations that allows the accurate prediction of the sugar conformational preferences of chemically modified nucleosides in solution. Moreover, we used these simulations in conjunction with natural bond orbital (NBO) analysis to gain key insights into the role of substituents in the conformational preferences of these nucleosides.

Chapter 2

2.1. Introduction.

2.1.1. Chemically Modified Oligonucleotides.

Chemically modified oligonucleotides have widespread biological applications: while classically used as chemical probes due to their specific binding of an intended target,[134] they have been shown in recent decades to become promising therapeutic agents following the advent of small interfering RNA (siRNA) and antisense oligonucleotide (ASO) technologies. This fact has been reinforced by the FDA approvals of three ASOs, namely Vitravene (1998), Kynamro (2013), and more recently Defitelio (2016) for the treatment of cytomegalovirus retinitis, homozygous familial hypercholesterolemia, and severe hepatic veno-occlusive disease, respectively.[135] All these therapies had to be chemically modified at the nucleotide level in order to increase their stability, bioavailability, and overall pharmacokinetic properties. Thus, despite recent successes, there is still much work to be done to improve upon the current technologies, and ideally do all this and more with intelligent design.[136]

2.1.2. Nucleoside Reverse Transcriptase Inhibitors (NRTIs).

Over the past decades, nucleoside analogues have also been successfully developed for the treatment of viral infections and cancer (Figure 2.1). Examples are Zidovudine (AZT),[137] Lamivudine (3TC),[138] and Emtricitabine (FTC),[139] three inhibitors of the HIV's reverse transcriptase. Other viruses have been targeted by structurally similar inhibitors including hepatitis B virus (Telbivudine[140]), Ebola virus (BCX4430[141]), and herpes simplex virus (Vidarabine[142]). Cancer has also been targeted by nucleosides such as Gemcitabine, which, when incorporated into DNA, leads to a DNA strand that can no longer be processed by the DNA polymerase.[143]

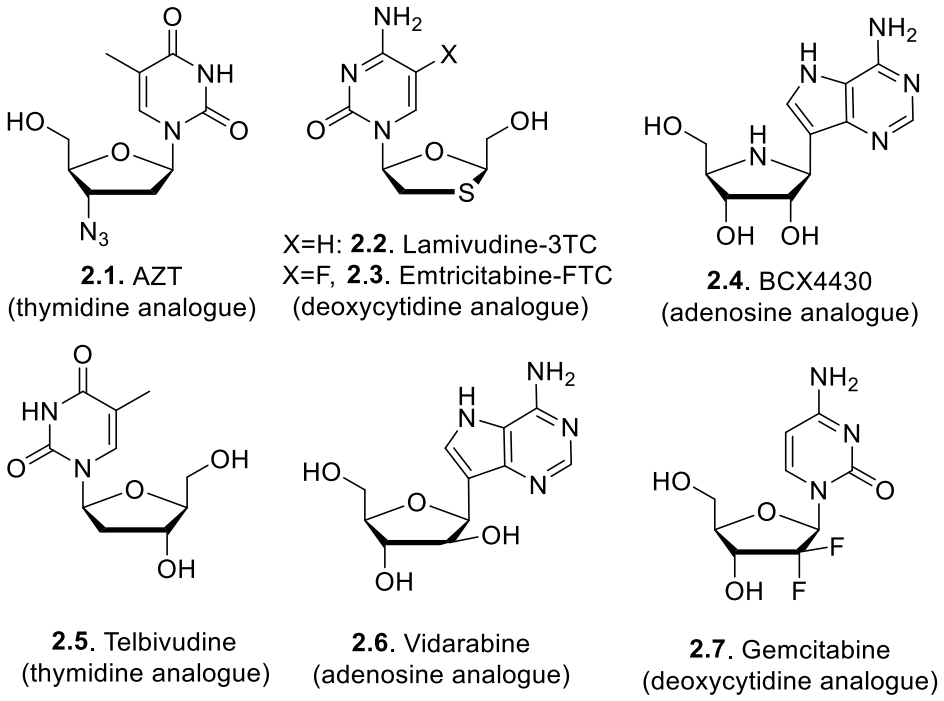

Figure 2.1. Nucleoside analogues used as drugs.

2.1.3. Nucleoside Conformation.

It is well established that enzyme inhibitors and other small molecule drugs often owe their activity to their shape (i.e. conformation) and chemical features (e.g., hydrogen-bond donor, hydrophobicity). In the field of inhibitor design, high throughput computational methods to investigate and/or guide the design of this class of small molecule drugs, such as docking methods,[144] are often considering drug flexibility. In the field of chemically modified oligonucleotides, the problem is much more complex since a subtle structural change in a nucleotide may have a profound effect on duplexes' shape and stability. In addition, the size of the systems is such that identifying the preferred conformations requires significantly more time-consuming methods.[145] Nucleoside building blocks can be tailored to adopt different sugar conformations (often referred to as the sugar pucker), which, in turn, affect duplex structure, pairing affinity, and, ultimately, biological activity.[146] The puckering can be described with the

pseudorotational circle (Figure 2.2a), the pseudorotational angle P, and the puckering amplitude Φ_m (Figure 2.3 and Equations 2.1 and 2.2).[147]

In general, sugars that adopt the C3'-*endo* conformation (also referred to as *North*, Figure 2.a) demonstrate increased binding affinity towards complementary RNA strands.[148] For example, the substitution of a natural nucleoside by a conformationally restricted nucleoside such as locked nucleic acid (LNA, Figure 2.c)[149,150] dramatically improves binding affinity within duplexes due to the increased pre-organization and resulting reduced entropic cost for duplex formation. There are, however, synthetically fewer challenging approaches to favor a desired conformation. Electronegative 2′-substituents, such as 2′-OMe, 2′-methoxy-ethyl (MOE), 2′-F (Figure 2.b), impart stereoelectronic effects that favor the *North* conformation.[146]

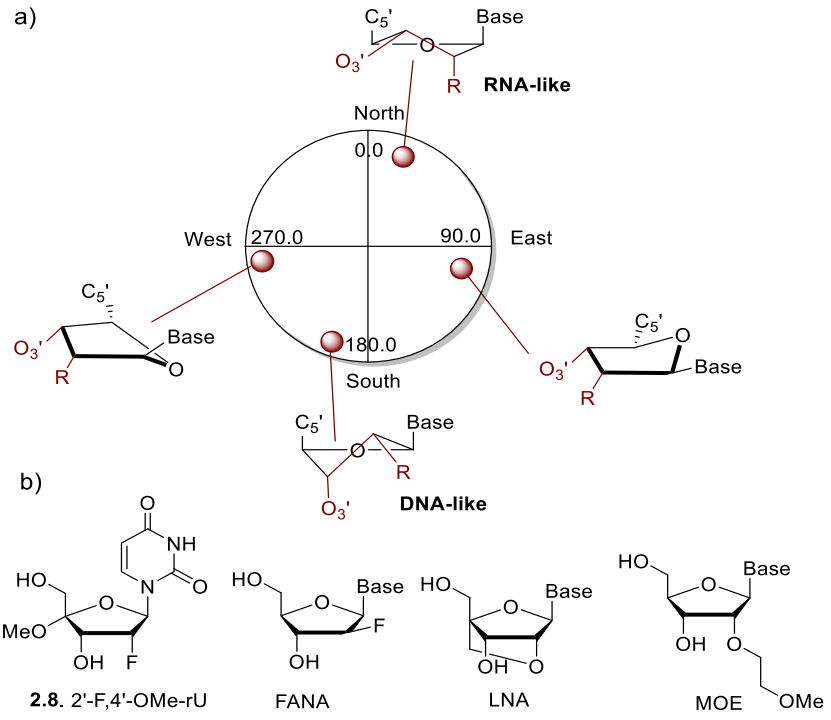

Figure 2.2. a) Conformational characterization of the ribose puckering;[151] b) 2′-F,4′-OMe-rU (**2.8**)[152] and clinically-relevant nucleoside analogues.

These specificities render these structural modifications attractive for use not only in ASO and siRNA, but also for modification of the guide RNA (gRNA) in the CRISPR/Cas9 system due their ability to resemble RNA structure.[153,154] In contrast, the 2′-FANA modification has been shown to favor the *South/East* conformation, but it has still been shown to increase binding to complementary RNA targets, confer nuclease resistance, and is well tolerated by the cellular machinery needed for gene knockdown.[155-157] Notably, the *North* and *South* preference of a nucleoside analogue can also be harnessed to design more effective antivirals and chemotherapeutics: nucleosides with a sugar pucker in the *South* range of the pseudorotational circle are preferentially phosphorylated by kinases, while *North* type nucleosides are preferentially incorporated by polymerases.[158-160] These conformational considerations allow for more effective designs with an intended target in mind.

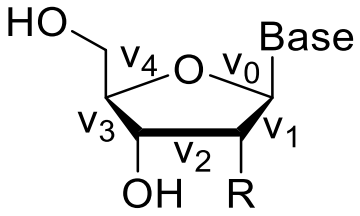

Figure 2.3. Definition of dihedral angles used to calculate the pseudorotational phase angle P in Eqs. 2.1 and 2.2. R = any substituent.

$$\tan P = \frac{(v_4 + v_1) - (v_3 + v_0)}{2v_2(\sin 36 + \sin 72)} \qquad \text{Eq. (2.1)}$$

$$\phi_m = \frac{v_2}{\cos P} \qquad \text{Eq. (2.2)}$$

Equations 2.1-2.2. Description of the formulas used to compute the pseudorotational phase angle P and the puckering amplitude Φ_m.

2.1.4. Computational Methods.

Nowadays, several computational methods are available at the drug design and discovery stage, from ligand-based (e.g., QSAR) to structure-based (e.g., docking). However, while these methods are commonly used (and validated) with enzymes or receptors as drug targets, the problem at hand with nucleic acids as described herein, are very different. Current methods developed for small drug molecules binding to proteins can be retrained (and validated) with nucleic acids or new strategies can be envisioned. In the field of nucleosidic building blocks or drugs, the biological activity is directly related to the puckering of the ribose (or deoxyribose) ring. This puckering is, for a large part, controlled by hyperconjugation effects.

On one side, one can consider MM-derived methods, although their accuracy for this class of molecules must be demonstrated and/or improved.[161] On the other side, one can envision QM techniques, although, investigating the dynamic equilibrium between the different conformations and the conformational ensemble may be time-consuming. With this in mind, we set out to filter through all the existing methods and find a suitable computational technique that would accurately and quickly describe the conformation of nucleosides such as the ones in Figures 2.1-2.2 in solution. Ideally, the method would properly describe the hyperconjugation effects including the anomeric effect and potential intramolecular hydrogen bonding effects governing the sugar puckering and would be able to assign *North/South* ratios consistent with experimental data e.g. derived from ^{1}H NMR spectroscopy. Such a method would be an asset since it would allow the design of numerous nucleosides and nucleoside analogues that can be tested computationally prior to synthesis, with the only cost being central processing unit (CPU) time.

2.2. Benchmark Study.

Many computational methods have been used to determine the sugar puckering of furanosides, from QM (primarily DFT) to more time-efficient MM approaches. A close look at the reports revealed somewhat conflicting information. On one side, pure DFT calculations were used to determine the sugar puckering of α- and β-D-aldopentofuranosides.[162] On the other hand, Roy and co-workers[163,164] reported the use of a special MD technique - umbrella sampling – used in a pure MM fashion along with the GLYCAM parameter set[165] for carbohydrates, advocating for its use as a principal method of investigation of sugar puckering in mono- and oligosaccharides. Another report by Roy and co-workers[164] on mono- and oligosaccharides showed that when compared to a QM/MM approach using semi-empirical methods such as SCC-DFTB, the GLYCAM approach yielded results close to experimental data, while SCC-DFTB did not. By contrast, Naidoo and Barnett[166] showed that between various semi-empirical QM methods tested on ribose and glucose, SCC-DFTB was the one that produced sugar (ribose and glucose) puckers close to those obtained by high-level calculations. Moreover, a study by Huang *et al.*[167] claimed that commonly employed semi-empirical methods such as SCC-DFTB fail to properly describe sugar puckering, while proposing their own method of correcting their flaws. While some methods arrive to contradictory results, the system under scrutiny plays a major role in the effectiveness of these methods. For example, electron-withdrawing substituents on sugar rings such as fluorine affect sugar puckering due to hyperconjugation effects. While these effects can be described by QM methods, MM methods are not properly parametrized to take them into account.[161] In this sea of possibilities, one can only make an informed decision by testing all possibilities and choosing the one that yields the most accurate results for that particular system, especially when

experimental data is available. Therefore, we decided to run our own benchmark study to assess the suitability of various methods.

2.2.1. DFT Calculations.

To start off our benchmark study we set our sights on nucleoside **2.8** (Figure 2.2)[152] for several key reasons:

1. we had access to high quality experimental data to which we could compare our predictions;
2. the methoxy substituent at C-4′ alters the stereoelectronics and subsequently the sugar conformation; and
3. oligonucleotides containing this nucleoside analogue exhibit favorable binding properties, increased nuclease resistance, and perform well in RNAi gene knockdown experiments.

Therefore, we decided to start our benchmark study with DFT calculations focused on several envelope conformations that **2.8** could adopt in solution. We optimized these conformations using an implicit solvent and the energies we obtained for each conformation are given in Table 2.1. As seen in Table 2.1. our computed data suggested a significantly large *North (N)* preference with an energy difference well above 3.5 kcal/mol relative to the *South (S)* conformer, hence a *N/S* ratio greater than 100:1. However, the experimental *N/S* ratio obtained by NMR experiments at 303K for **2.8**[152] revealed a preference for the *N* conformation in the ratio 87:13 ($\Delta E_{(N/S)}$ = 1.15 kcal/mol).

To explain such a deviation, one must look at the underpinnings of DFT. First, although DFT can describe the hyperconjugation effects, it only provides static conformations of the molecule, meaning that the dynamic behavior of sugar puckering would not be described fully. Moreover, the solvent (water) used in DFT-solution phase calculations is implicit.

Table 2.1. Data obtained for different envelope conformations of **2.8** at the M06/def2-TZVP level of theory.

Envelope Conformation	P* (°)	ϕ_m**(°)	Pucker Type	Energy (kcal/mol)
^{1}E	303	26.11	C1'-endo	7.40
^{2}E	168	38.20	C2'-endo	3.64
^{3}E	23	33.71	C3'-endo	0.00
^{4}E	234	41.90	C4'-endo	10.42
$_1$E	124	43.88	C1'-exo	5.84
$_2$E	350	34.59	C2'-exo	7.66
$_3$E	199	32.51	C3'-exo	5.77
$_4$E	56	45.37	C4'-exo	6.65

*P = pseudorotational phase angle; **ϕ_m = puckering amplitude

As continuum solvation does not consider individual water molecules, the possibility of hydrogen-bonding between the sugar hydroxyls and water is non-existent. Utilizing explicit water molecules would add a high degree of complexity (e.g., location, number, placement and orientation of water molecules), and CPU time to the calculations, thus making the calculations intractable. Poor placement (and estimate on the number) of water molecules will likely yield incorrect results. Therefore, we reasoned that the cause of this inaccurate prediction of the *N/S* ratio likely resides in the improper computation of intermolecular hydrogen bond strengths, as well as the lack of explicit waters which would modulate the stereoelectronic effects.

2.2.2. MM Study.

Recently, Roy and co-workers[163] suggested umbrella sampling simulations with the GLYCAM parameter set were suitable for describing furanosides, and thus we turned our attention to this approach in our study as well. Such simulations allow the description of the system of interest in a dynamic fashion, at a desired temperature and pressure. However, the major advantage

of using umbrella sampling simulations is that it allows one to overcome high free energy barriers for conformational changes, thus effectively ensuring that the full conformational landscape is evenly (or nearly evenly) explored. Nonetheless, such a simulation requires a specific reaction coordinate in the context of which sugar puckering can be analyzed. Roy and co-workers showed that the rotation about the exocyclic C4-C5 bond (Figure 2.4c) occurs on a faster time scale than sugar puckering, thus making the analysis of puckering in the context of an exocyclic torsion reasonable. We decided to use the same exocyclic torsion as our reaction coordinate. Another advantage of using umbrella sampling simulations was the significantly lower CPU-time requirement (since they rely on MM), which enabled the use of explicit solvents that we believe may be critical for optimal predictions. The free energy (also known as Potential of Mean Force – PMF) of sugar puckering as well as average sugar pucker population distributions could be easily obtained from our simulations and the data is shown in Figure 2.4a.

Although this method was able to identify two distinct minima, it assigned the global energy minimum for **2.8** (and the most populated conformation) to the *S* conformation. This is contradicted by experiment, which assigns the *N* region as the most populated one, thus rendering the pure MM approach with the GLYCAM parameter set unviable. A closer look at the previous study shows that the systems previously treated with the AMBER/GLYCAM approach focuses on mono- and oligosaccharides lacking strong electron-withdrawing substituents in the 2′ and 4′ positions (such as -F and –OMe present in **2.8**). It is known that MM methods are not explicitly parametrized to describe strong hyperconjugation effects such as the anomeric or gauche effect; because the GLYCAM parameter set does not have specific fluorine parameters, generic parameters (the ff99SB force field) were applied to our system. Since these electronic effects play a major role in determining sugar puckering, it is reasonable to assume that the failure of this

method stems from this improper description of these effects. As an additional limitation, since MM methods explicitly consider nuclei but not electrons, most commonly used force fields used in MM (including the ff99SB force field used for these calculations) are non-polarizable and thus molecular polarizability is not taken into account for any given system.

a)

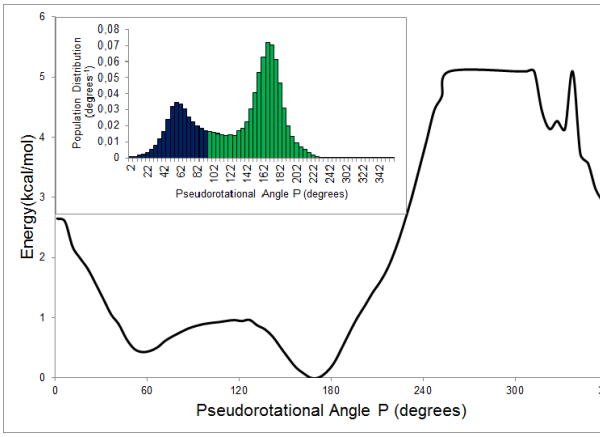

b)

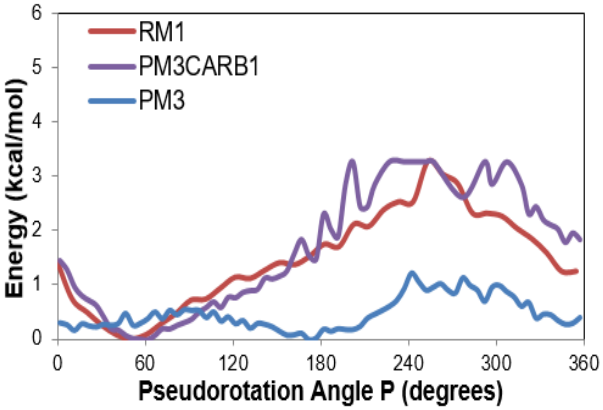

c)

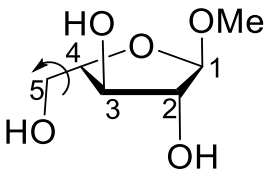

d)

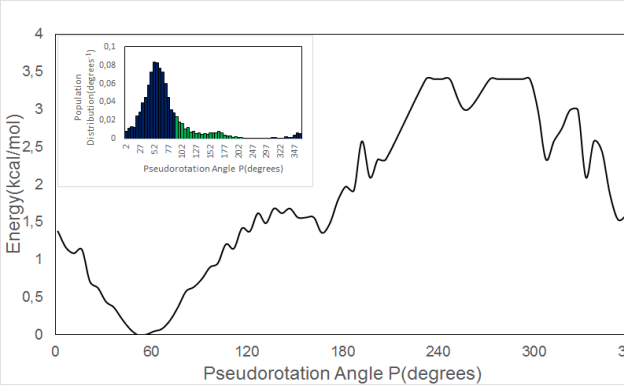

Figure 2.4. a) PMF curve along the pseudorotational phase angle for **2.8** using GLYCAM. Inset shows the sugar pucker distribution. (blue – *N*, green – *S*). b) PMF curves obtained using the RM1, PM3 and PM3CARB1 semi-empirical methods. c) Exocylic C4-C5 bond rotation was shown to be on a faster time scale than sugar puckering.[163] d) PMF curve of **2.8** using SCC-DFTB. Inset shows the sugar pucker distribution (blue – *N*, green – *S*).

2.2.3. QM/MM Calculations.

Since DFT and MM calculations proved to be unsuitable for this type of system, we turned our attention to hybrid QM/MM umbrella sampling simulations. The main advantage of using such methods is that they give the possibility of analyzing the system of interest in a QM fashion, while the explicit solvent is treated with MM. We decided to test various semi-empirical methods for the QM region, namely RM1,[31] PM3,[29] PM3CARB1,[168] and SCC-DFTB.[169] Time-wise, this approach performed similarly as the pure MM approach while employing the same computational resources.

A comparison between the PMF curves obtained with RM1, PM3, and PM3CARB1 is provided in Figure 2.4b. Interestingly, none of these first three semi-empirical methods correctly distinguished between two distinct minima. Moreover, while RM1 and PM3CARB1 correctly described the global minimum in the *N* region, PM3 failed to describe this minimum altogether. The inability of these methods to model the dynamics of these sugar structures has also been described by Naidoo and Barnett,[166] who argued that these semi-empirical methods produce sugar rings having inaccurately low conformational free energy barriers. However, this is not the case when using SCC-DFTB (Figure 2.4d). In the past few years, this method has proven to be fast, reliable, and accurate when describing various systems, including sugar-containing molecules.[166]

As can be seen in Figure 2.4d, SCC-DFTB correctly assigned the global minimum in the *N* region, while simultaneously finding a local minimum in the *S* conformation. As we reported in a previous study[152] the calculations yielded two distinct energy minima, one at a pseudorotational phase angle P_N=58.5° (puckering amplitude ϕ_m = 42.9), corresponding to the global minimum in the *N/E* conformation and one at P_S=168.5° (puckering amplitude ϕ_m = 31.2), corresponding to a local minimum in the *S* conformation (Figure 2.5). The difference in energy between the *N* and *S* conformation was computed to be ~1.15 kcal/mol, and the integration of the distribution in Figure

2.4d lead to a *N/S* ratio of 84:16, which is remarkably similar to the experimental *N/S* ratio of 87:13 (Figure 2.5).

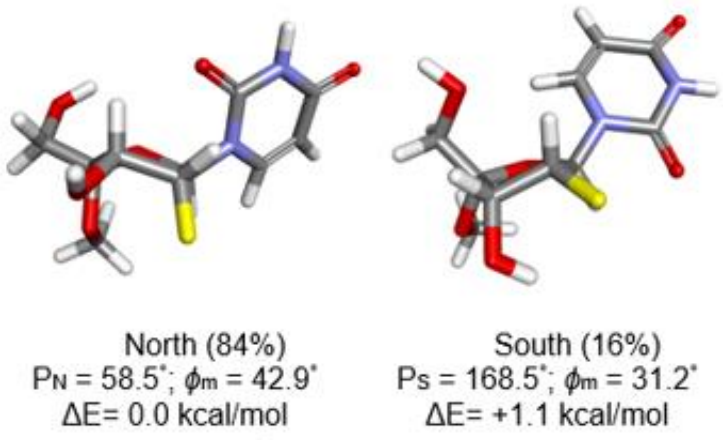

Figure 2.5. Structural information for the *N* and *S* minima obtained for **2.8.**[152]

These accurate *N/S* ratios provided us with confidence in the computed structural information using this approach. However, testing this method on one compound was not enough to make assertions about its accuracy, thus we assembled a set of various nucleosides published in the literature that could serve as a validation set (Chart 2.1). Moreover, we also assembled a set of modified monosaccharides (Chart 2.1) to perform a comparative study between the method used here and the various methods used in the literature.

2.3. Validation of the Method on a Set of Nucleosides and Monosaccharides.

Our literature search focused on a variety of monosaccharides,[162-164] as well as on nucleosides with various substituents (or lack thereof) affecting the sugar puckering; moreover, we decided to include in our set well-known nucleosides, such as AZT.[170] Obviously, we restricted our set to compounds which have an experimentally determined *N/S* ratio to which we could compare our theoretical predictions. Furthermore, we chose only those nucleosides that had their *N/S* ratios determined in D_2O, since our method uses water as a computational solvent. Although

isotope effects might play a very subtle role in sugar puckering, we believe that choosing water as our solvent would not affect our predictions. Following our search, we settled on the compounds presented in Chart 2.1, as well as on some of the nucleosides in Figures 2.1 and 2.2.

2.3.1. Application to Monosaccharides Investigations.

We first focused our efforts on monosaccharides **2.9**-**2.17** (Chart 2.1). Since various methods have been proposed to study such systems, we thought to verify if the QM/MM approach using SCC-DFTB would yield *N/S* ratios and conformers close to experimental ones. The data computed for monosaccharides **2.9**-**2.17** is presented in Table 2.2. Crystal structure data[171-173] was available for some monosaccharides and thus we were also able to compare our lowest-energy conformations to those found in the crystal structures. Before any claims about the accuracy of SCC-DFTB on monosaccharide puckering can be made, it has to be mentioned that the experimental *N/S* ratios obtained for monosaccharides **2.9** (entry 1) and **2.11**-**2.17** were obtained using the program PSEUROT[174] from NMR spectroscopy data. Thus, the available experimental data is indirect and is the result of some computations with the associated error. Henceforth the experimental data obtained with PSEUROT shall be referred to as pseudo-experimental data. This program requires starting *N* and *S* conformations (a two conformation system), which are then optimized; over multiple runs involving various starting *N/S* conformations the *N/S* ratio as well as the puckering parameters (P and ϕ_m) are determined and the set of conformers that best replicates experimental $^3J_{H,H}$ data is selected. However, it is important to note that more than one set of conformers can replicate the experimental coupling-constant data and thus a decision has to be made with regards to choosing one over others.[162] Moreover, the data obtained between each run may differ significantly[162] which might introduce an inherent error vis-à-vis the pseudo-experimental *N/S* ratios. Interestingly, in the case of monosaccharide **2.9** (Table 2.2, entries 1, 2

and 3), we found conflicting reports concerning the pseudo-experimentally determined *N/S* ratio, with one report[162] claiming that the *S* pucker was preferred while the other claiming the opposite.[164]

Overall, the data in Table 2.2 suggests that SCC-DFTB performs well when predicting the *N/S* ratios. Moreover, we found that, when compared to the crystal structures conformers, all our computed structures had a heavy atom position root-mean square deviation (RMSD) less than 1Å (Figure 2.6). As can be seen in Figure 2.6, the computed conformers for **2.9** and **2.11** are very similar to the ones obtained in the crystal structure (RMSD = 0.57 and 0.32Å respectively). For **2.12**, **2.15**, and **2.16** our predicted conformers differ slightly from the ones found in crystal structures (RMSD = 0.60, 0.69 and 0.80 Å respectively).

Chart 2.1. Compounds subjected to QM/MM umbrella sampling simulations (**2.1** and **2.8** are shown in Figures 2.1 and 2.2).

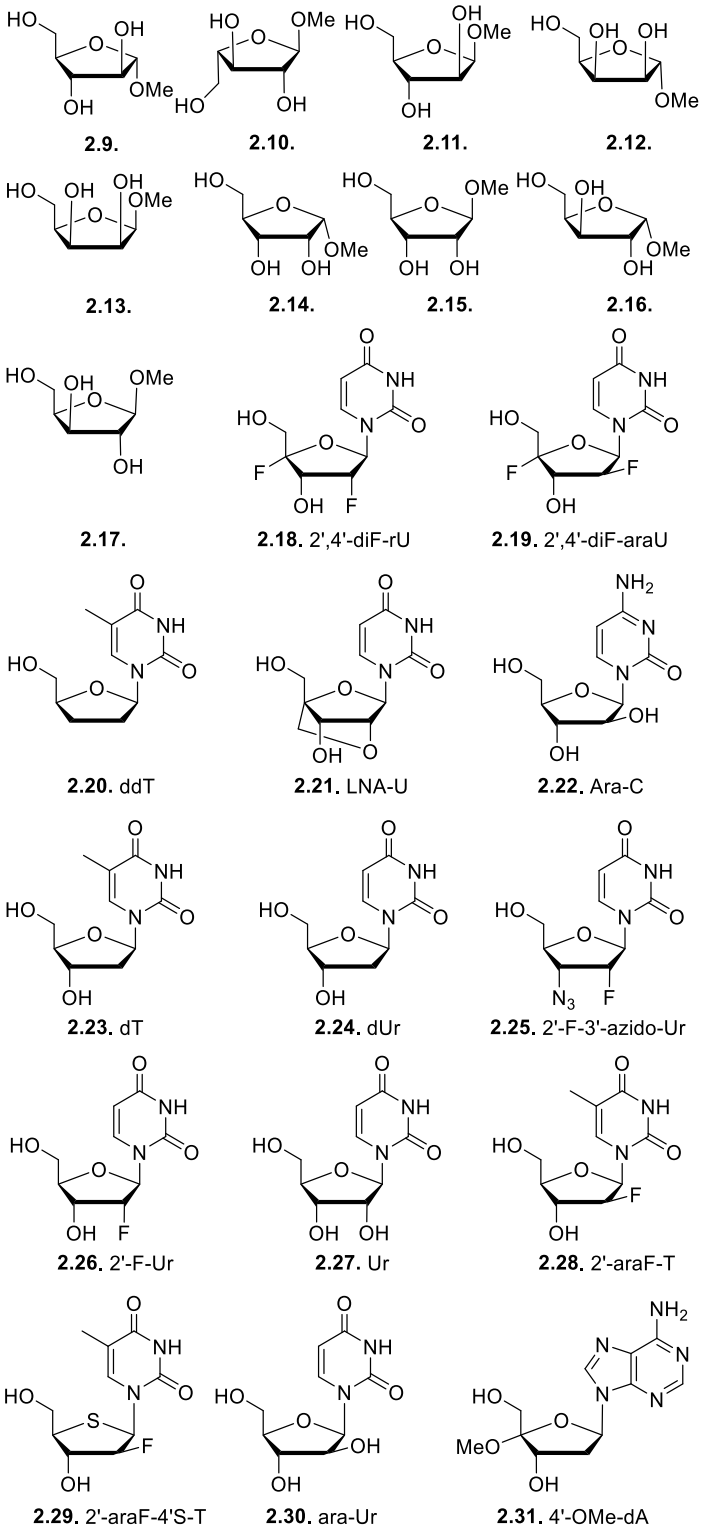

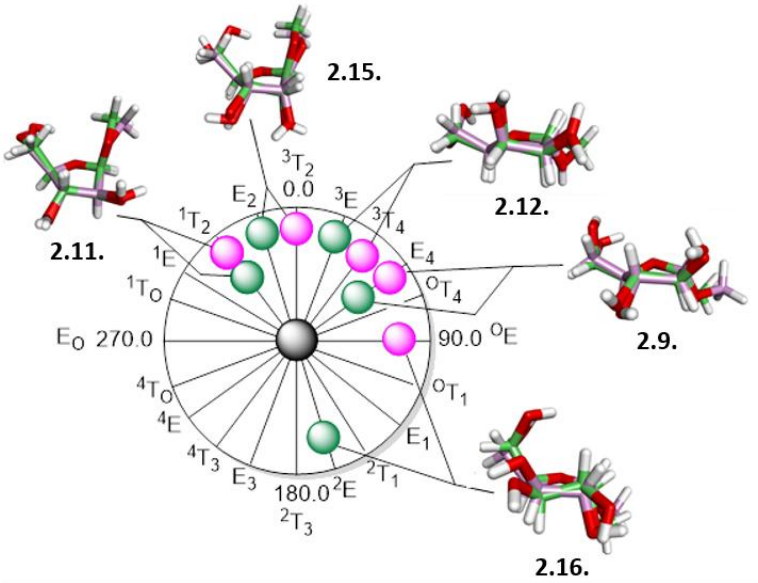

Figure 2.6. Superposition of the crystal structures and lowest-in-energy predicted conformers of **2.9**, **2.11**, **2.12**, **2.15** and **2.16** (pink – computed structure, green – crystal structure).

The computed structures, with the exception of **2.15**, show no intramolecular hydrogen bonding, which is consistent with the crystal structure data.[171] Moreover, we posit that the differences between the computed and crystal structures arise from a strong intermolecular hydrogen bonding network present in the crystal structure but broken in solution.[152] Having analyzed the differences between the computed lowest-energy conformers and available crystal structures we turned our attention to the *N/S* ratios predicted with SCC-DFTB.

Table 2.2. Comparison between the *N/S* ratios obtained for monosaccharides.

Entry	Monosacch.	Pseudo-Experimental *N/S* ratio[162-164]	Crystal Structure[171-173] Conformer	Method	Predicted *N/S* ratio[a]	Predicted Conformer N-S
1	**2.9**	39:61	E_4	DFT[c,162]	nd[d]	E_4 - E_1
2		83:17[b]		GLYCAM[164]	79:21	nd
3		83:17[b]		SCC-DFTB[164]	91:9	nd
4				our method	53:47	E_4 - ^2E
5	**2.10**	83:17[b]	nd	GLYCAM[164]	84:16	nd
6				our method	49:51	$^3T_2$ - ^4T_O
7	**2.11**	87:13	$^1T_2$	DFT[162]	nd	E_2 - ^4E
8				our method	64:36	$^1T_2$ - E_3
9	**2.12**	65:35	^3E	DFT[162]	nd	^OE - E_3
10				our method	56:44	$^3T_4$ - ^2E
11	**2.13**	77:23	nd	DFT[162]	nd	E_2 - ^4E
12				our method	70:30	$^3T_2$ - $^4T_3$
13	**2.14**	0:100	nd	DFT[162]	nd	E_4 - ^2E
14				our method	39:61	$^3T_4$ - E_1
15	**2.15**	86:14	E_2	DFT[162]	nd	^1E - ^4E
16				our method	61:39	$^3T_2$ - ^2E
17	**2.16**	0:100	^2E	DFT	nd	^3E - E_1
18				our method	48:52	$^3T_4$ - ^OE
19	**2.17**	78:22	nd	DFT[162]	nd	E_2 - ^4E
20				our method	58:42	$^3T_4$ - $^4T_3$

[a] For our method - at 303K based on the Boltzmann population distribution. [b] Not determined with PSEUROT. [c] The DFT predicted *N/S* conformers are determined in solution using a solvent model. [d] nd: not determined.

As mentioned earlier, the analysis of the computed *N/S* ratio for **2.9** (Table 2.2) proved to be difficult, since the pseudo-experimental data is conflicting. Nonetheless, the fact that our computed lowest energy conformer (Appendix A) matched that obtained in the crystal structure gave us confidence that our ratios were accurate. Furthermore, this assertion was supported by the data in Table 2.2 which showed good agreement between the pseudo-experimental and computed data with a few exceptions (monosaccharides **2.10, 2.14,** and **2.16**). The computed ring pucker distribution for **2.10** (Appendix A) showed a concentrated ring population in the *SE/S* region, on both sides of the *W* pucker (*SW* and *NW*), as well as in the *N* region. This behaviour was also described by Evdokimov *et al.*[172] in their furanoside crystal structure analysis where they showed that furanosides preferentially adopt conformations where the ring substituents have nominal eclipsing, namely in the *SE/SW* (P=160°-200°) and *NW/N* (P=340° - P=20°) areas and avoid regions of maximum eclipsing (P=90° and P=270°). In the case of **2.14** and **2.16**, the puckering distributions (Appendix A) revealed a three-state system, with important ring populations in the *NE*, *E* and *SE* conformations. Taking all this into account, we believe that our computations are dependable and supported by crystal structure studies.

2.3.2. Application to Nucleosides Investigations.

After validating our method on monosaccharides, we turned our attention to the nucleosides in Chart 2.1. The computed *N/S* ratios are shown in Table 2.3; this data indicates that our method predicts the conformational preferences of nucleosides, with a few exceptions (nucleosides **2.28**-**2.31**, entries 13-16), with ratios close to those derived from experimental NMR spectroscopy data. For every nucleoside in Table 2.3, we recorded the puckering parameters (pseudorotational angle P and the puckering amplitude ϕ_m – Appendix A) as well as the values of all the relevant angles for each *North* and *South* structure (Appendix A). Moreover, since we

wanted to understand why our method worked on some but not on all nucleosides, we decided to run a natural bond orbital (NBO) analysis on all the nucleosides in Table 2.3. Such an analysis allows the quantification of the anomeric and gauche effects and the accurate computation of the energetic contribution of these effects towards the overall puckering. Furthermore, the NBO analysis allows the computation of the molecular orbitals of every nucleoside, effectively offering important insight into potential intramolecular hydrogen bonding.

Table 2.3. The predicted *N/S* ratios obtained for the nucleosides in Chart 2.1.

Entry	Nucleoside	Experimental N/S ratio	Predicted N/S ratio[a]	Predicted N/S ratio[b]
1	**2.1**	50:50[175]	55:45	58:42
2	**2.8**	87:13[152]	84:16	86:14
3	**2.18**	100:0 [175]	80:20	91:9
4	**2.19**	80:20[176]	81:19	86:14
5	**2.20**	75:25[175]	60:40	58:42
6	**2.21**	100:0[177]	100:0	-[c]
7	**2.22**	54:46[178]	56:44	53:37
8	**2.23**	37:63[175]	41:59	44:56
9	**2.24**	39:61[175]	43:57	45:55
10	**2.25**	85:15[175]	66:34	76:24
11	**2.26**	87:13[175]	58:42	70:30
12	**2.27**	58:42[175]	48:52	56:44
13	**2.28**	37:63[179]	60:40	72:28
14	**2.29**	77:23[179]	1:99	0:100

15	**2.30**	46:54[175]	61:39	69:31
16	**2.31**	91:9[180](76:24)[d]	68:32	68:32

[a] At 303K; based on the Boltzmann population distribution; [b] At 303K, based on the differences in energy between the *North* and *South* minima; [c] For entry 6 only one minimum in the *North* conformation was observed; [d] according to our own calculations based on the data provided in the reference.

2.3.3. Nucleosides – Stereoelectronic Effects.

We started with compound **2.8** (entry 2) by performing NBO analysis on the lowest energy structures for the *North* and *South* conformations (Figure 2.7). The anomeric effect ($n_{O4'} \rightarrow \sigma^*_{C4'O}$) in the case of the *North* pucker is more pronounced than in the *South* pucker (with a computed difference in energy of 1.9 kcal/mol) due to the position of the anomeric oxygen (above the plane for the *N* conformation and within the ring plane for the *S* conformation). Nonetheless, the anomeric effect is not the sole contributor to the sugar puckering preference – several gauche effects also play an important role in this respect. For example, the $\sigma_{C3'H} \rightarrow \sigma^*_{C4'O}$ and $\sigma_{C3'H} \rightarrow \sigma^*_{C2'F}$ gauche effects are more prevalent in the *North* conformation (with a computed energy difference of 2.7 and 2.4 kcal/mol respectively), while the $\sigma_{C3'C4'} \rightarrow \sigma^*_{C2'F}$ and $\sigma_{C2'H} \rightarrow \sigma^*_{C3'O}$ gauche effects are more predominant in the *South* conformation (with a computed energy difference of 2.3 and 1.8 kcal/mol respectively). Moreover, we investigated the possibility of stabilizing intramolecular hydrogen bonding and found that three hydrogen bonds were observed for the *North* conformation and only one observed for the *South* conformation. It is also important to note that SCC-DFTB was shown to somewhat underestimate hydrogen-bond strengths,[181,182] and thus the effects of the intramolecular hydrogen-bonds might be far greater than presented here.

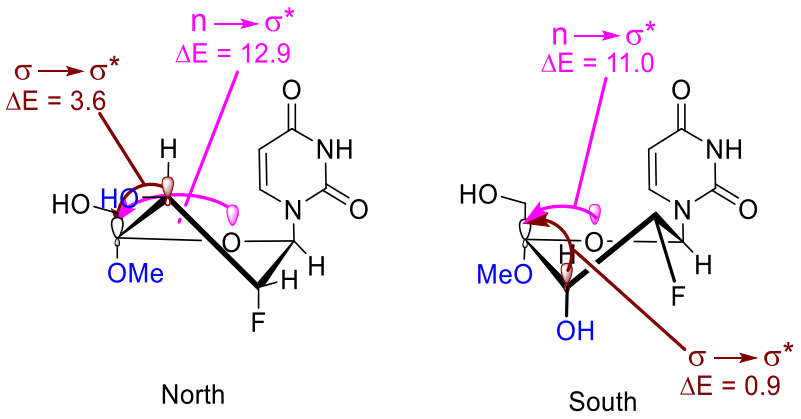

Figure 2.7. Anomeric and gauche effects observed after the NBO analysis for **2.8**. Relative energies are given in kcal/mol.

Following this analysis, we set out to understand why computations with compound **2.28** (entry 13) failed to yield a theoretical ratio close to the experimental one. For almost all our nucleosides (except entry 6), we expected a 2-state equilibrium (with 2 minima distinguishable in the *North* and *South* regions). However, a report by Watts and Damha[183] showed that 2′-fluoroarabinonucleosides can adopt a n-state (n=2, 3 and 4) equilibrium – with potential minima in the *N*, *NE*, *SE*, and *S* regions of the pseudorotational circle. While the conformational analysis of 2′-araF-T (nucleoside **2.28**) has only been described once (using the program PSEUROT, which can only describe 2-state equilibria), it is not unreasonable to assume that it may in fact adopt a 3- or 4-state equilibrium in solution.

To understand whether compound **2.28** could indeed adopt such an equilibrium, we plotted the PMF curve and puckering distributions (Figure 2.8). While Figure 2.8 does not show a significant minimum in the *E* region, the low energy barrier (~0.5 kcal/mol) for the *N*-*E* transition advances the possibility of a 3-state equilibrium. Moreover, a closer inspection of the inset of Figure 2.8 reveals that significant puckering populations are present in the *NE*, *SE* and *S* regions of the pseudorotational circle, thus making the 2-state equilibrium hypothesis unreliable.

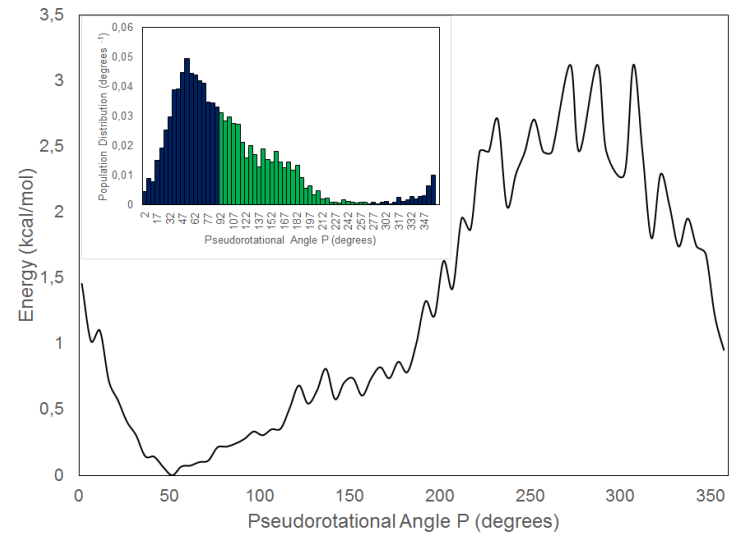

Figure 2.8. PMF curve for nucleoside **2.28**. Inset shows the sugar puckering distribution along the pseudorotational angle P.

The NBO analysis we performed on compound **2.28** revealed that the anomeric effect $n_{O4'} \rightarrow \sigma^*_{C4'O}$ was more pronounced in the *NE* conformation (ΔE= +0.3 kcal/mol). The gauche effects were overall prevalent in the *NE* conformation, although the energy differences were somewhat small. However, the $\sigma_{C3'C4'} \rightarrow \sigma^*_{C2'F}$ effect was significantly larger for the *NE* conformation (ΔE= +4.0 kcal/mol), most likely allowed by the better orbital overlap when compared to the *SE* conformation. Moreover, the molecular orbital analysis revealed no intramolecular hydrogen bonding that could affect the overall structure of compound **2.28**.

We then turned our attention to nucleoside **2.29**. Compared to all the other nucleosides in Table 2.3, compound **2.29** contains a sulfur atom, instead of the ring oxygen, which changes the stereoelectronic effects governing the sugar puckering. Moreover, the introduction of a sulfur atom at the 4′ position pushes the conformation of the nucleoside to the *North* region. However, our method predicts an overall 1:99 *N/S* ratio and suggests a primarily *South* conformation. This computed data is dissimilar to the experimental value and therefore it is important to understand

the reasons behind this failure. Interestingly, a report by Petraglia and Corminboeuf highlights the inherent flaw of sulfur atoms in the SCC-DFTB method.[184] According to their study, non-covalent interactions are poorly described by the current SCC-DFTB parametrization of sulfur, thus leading to qualitatively wrong results. As can be expected, along with stereolectronic effects, non-covalent interactions (especially polarization effects) play a significant role in sugar puckering. Thus, the failure of our method in this case could likely be attributed to the poor accuracy of SCC-DFTB method with sulfur-containing molecules.

In the case of nucleoside **2.30**, the apparent discrepancy between the experimental and theoretical values cannot be explained by an intrinsic flaw in the method. Although, as pointed earlier, experimental data is only indirect and may be inaccurate in some instances, we decided to further investigate this case to identify any potential limitations of our methods. When compared to nucleoside **2.22**, the two nucleosides only differ in the identity of the base. Nonetheless, the molecular orbital analysis of both **2.22** and **2.30** showed a pronounced intramolecular hydrogen bonding network (Figure 2.9). In **2.30**, the base when in the *North* conformation has one carbonyl oxygen oriented towards the sugar, which allows for the formation of hydrogen bonds with the 2'-OH and H3' atoms (Figure 2.9); these stabilizing interactions contribute to the overall puckering shift towards the *North* region. Moreover, the NBO analysis revealed that the anomeric effect is very slightly in favor of the *South* conformation (ΔE= -0.1 kcal/mol), while all the hyperconjugation effects are more dominant in the *North* conformation. The results are very similar to **2.22**, where the anomeric effect is also more dominant in the *South* conformation (ΔE= -0.6 kcal/mol) while the gauche effects are more predominant in the *North* conformation.

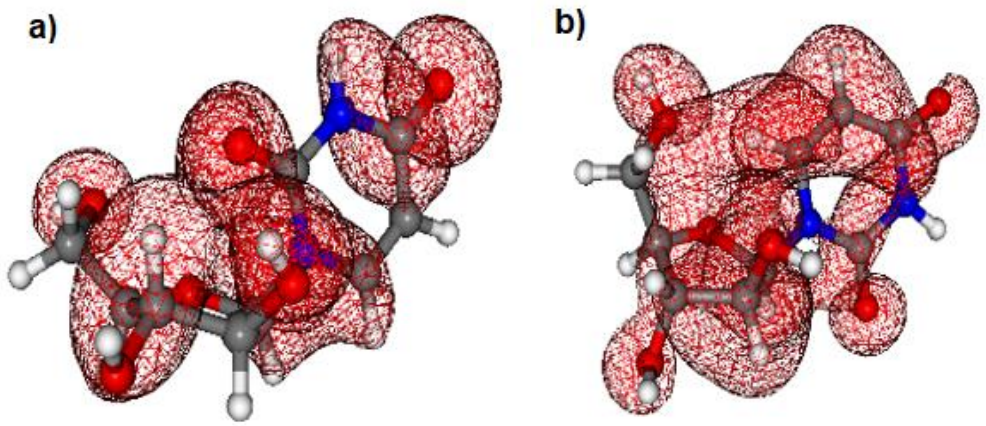

Figure 2.9. Intramolecular hydrogen bonds for the *North* pucker (a) and *South* pucker (b) for **2.30.** a) hydrogen bonding between C=O-H2′ and C=O-2′-OH. b) hydrogen bonding between O5-H(base).

The last nucleoside that presents a deviation from the experimental value was nucleoside **2.31** (entry 16). The introduction of an electron withdrawing substituent in the 4′ position is expected to shift the sugar puckering towards the *North* conformation, due to the more pronounced anomeric ($n_{O4'} \rightarrow \sigma^*_{C4'O}$) effect. Moreover, the experimental data available for this nucleoside suggests an almost fully *North* conformation (N/S-91:9), while our prediction, based on a distinct equation, is different (*N/S*-68:32). To understand where this discrepancy comes from, we decided to verify the experimental results associated with this nucleoside in the reported supplementary information. According to our calculations (based on the data provided in the SI of this original report[180]), the *N/S* ratios are closer to our predictions, namely 66:34. This is in line with our expectations, since the lack of a strong electron withdrawing substituent in the 2′ position affects the *N/S* ratios in favor of the *South* conformation (see nucleosides **2.18, 2.23** and **2.24**). This expectation is also met by the NBO analysis, which shows a significant hyperconjugation effect ($\sigma_{C2'H} \rightarrow \sigma^*_{C3'O}$) in favor of the *South* conformation (ΔE= -3.5 kcal/mol).

2.4. Conclusions.

Throughout these investigations, we have observed that neither pure DFT nor pure MM methods we tested could reproduce the conformational behavior of non-natural nucleosides in solution. While DFT accounts for hyperconjugation effects, solvent effects such as hydrogen bonds in water can only be reproduced by MM techniques (explicit solvent molecules). Thus, a hybrid QM/MM method (nucleoside treated by SCC-DFTB) and water (treated by MM) was the solution to investigate the conformational preferences of a variety of nucleosides and modified monosaccharides. The hybrid method yielded reliable structures that closely matched the crystal structures for the modified monosaccharides, as well as *N/S* ratios close to experimental ones for both the monosaccharides and nucleosides. Moreover, our method provided key insights into **a)** the role of the substituents on the sugar ring of nucleosides and **b)** the finely tuned control of sugar puckering by hyperconjugation effects and intramolecular hydrogen bonding. However, the method we described here also has some limitations, such as improper sulfur parametrization and underestimating the strengths of hydrogen bonds. Nonetheless, we believe that if the system of interest is a non-natural nucleoside, one can obtain reliable structures and *N/S* ratios (if only for a qualitative description of one's system before attempting synthesis) by using a QM/MM approach involving SCC-DFTB. Moreover, if resources permit, one can attempt the analysis of a non-natural nucleoside with DFTB3[181], which appears to describe hydrogen bonds better.

2.5.Methods.

2.5.1. Initial DFT Study.

Initial DFT calculations on **2.8** were performed in water (COSMO solvent model)[185] at the M06L/def2-TZVP[186,187] level of theory using ORCA v.3.0.3.[188] Eight idealized envelope conformations were built and subjected to restrained geometry optimizations (where one dihedral

angle would be constrained in order to maintain the envelope conformation) and frequency calculations to ensure the geometries were energy-minima. The pseudorotational phase angle P and puckering amplitudes were determined with the program PROSIT.[189]

2.5.2. QM/MM/MD Study.

All calculations were carried out in AMBER12[190], using SCC-DFTB[169] for the QM region (ligand) and the ff99SB force field[191] for the MM region (solvent). Compound **2.8** was initially optimized using GAMESS-US[42],[41] at the HF/6-31G* level of theory in order to generate the electrostatic potential, which was subsequently used to generate the restricted electrostatic potential (RESP) charges in AMBER12. The system was then constructed by solvating **2.8** in a pre-equilibrated rectangular box of TIP3P[192] water molecules (dimensions 10 x 10 x 10 Å). Following this step, the topology and coordinate files for the system were generated. Visual inspection of the final system was undertaken to ensure its integrity. With the solvated system in hand, 2000 steps of energy minimization were performed (500 steps of steepest descent energy minimization, followed by 1500 steps of conjugate gradient energy minimization). Then, an equilibration run of 200ps was performed (NPT, 303K) using a Langevin thermostat,[193] with a collision frequency $\gamma = 2.0\ ps^{-1}$ and a step of 2fs. The SHAKE[194] algorithm was used in order to fix all the hydrogen-containing bonds to equilibrium values; periodic boundary conditions were used, with a cut-off of 8Å for non-bonded interactions (including the QM method/TIP3P electrostatic interactions). The particle mesh Ewald (PME)[195,196] method was used to control the long-range electrostatic interactions. The equilibration run was followed by a production run of 500ns (NVT, 303K, 1atm) where the same conditions as above were applied. System integrity was ensured at the end of each step described above.

The structure of **2.8** obtained after the production run was used to generate starting conformations in which the dihedral angle O4′-C4′-C5′-O5′ had values of 60, 120, 180, 240, 300 and 360°. The structures for each angle were subjected to the same protocol described above. The angles were restrained by applying a harmonic biasing potential, with a force constant of 200 kcal/mol/rad^2. For each structure, the angle distribution was plotted to ensure that the dihedral angle was restrained at the correct value.

2.5.3. Umbrella Sampling Simulations.

The reaction coordinate for the umbrella sampling simulations was chosen to be the exocyclic torsion angle O4′-C4′-C5′-O5′.Using the above described structures 73 windows were built (window width of 5° each) to cover the 0-360° range for the O4′-C4′-C5′-O5′ dihedral angle– each window was subjected to a slightly modified protocol than the one describe above: the parameters were identical to the ones described above but the equilibration run was 100ps and the production run was 1ns, leading to a total of 73ns of production runs. Once the simulations were finished, the systems were visually inspected to ensure integrity was maintained. Data obtained from umbrella sampling simulations can be readily analyzed by using the weighted histogram analysis method (WHAM),[197] which provides the free energy of the reaction as a function of a chosen reaction coordinate (also known as potential of mean force or PMF) and average population distribution for the chosen reaction coordinate. Thus the PMF and average distributions for the pseudorotational phase angle P were obtained using the WHAM software.[198] For the pseudorotational angle P, a force constant of 0 was used to unbias the angle, since no biasing was applied in the first place. The lowest-energy structures were obtained by clustering the conformations during the 73ns simulation, and extracting the most representative conformation for both *North* and *South*.

2.5.4. Natural Bond Orbital (NBO) Analysis.

The 2 minima obtained following the QM/MM calculations for **2.8** were subjected to an NBO analysis using ORCA v.3.0.3[188] and the NBO6 program[199,200] at the M06L/def2 TZVP[186,187] level of theory. The threshold for the E_2 energies (hyperconjugation and anomeric effects) was 0.05 kcal/mol.

2.5.5. Molecular Orbital Analysis.

The molecular orbitals were built for the *North* and *South* conformations of **2.8** using the Molekel[201] software. The molecular orbitals used in building the maps were obtained following the natural bond orbital analysis described above.

Note: the same protocol was applied to all the other compounds studied in this report.

2.5.6. Crystal Structures.

Crystal structures were obtained from the CCSD with the following codes – monosaccharide **2.9** (CCSD112946), **2.12** (CCSD112951), **2.15** (CCSD112949) and **2.16** (CCSD112950). The crystal structure for monosaccharide **2.11** was taken from the SI of Evdokimov *et al.*[171]

Chapter 3 – Accurately Modeling the Conformational Preferences of Nucleosides – Applications

Preface.

As described in Chapter 2, QM/MM umbrella sampling simulations can be used to provide accurate *N/S* ratios of nucleosides in solution. However, these simulations are also useful in providing predicted lowest-energy structures that closely resemble crystal structures, which can help explain phenomena such as atypical fluorine-hydrogen bonds, as well as providing important insight into the effects of ring substituents on sugar puckering. In this chapter we will explore the applicability of the methodology developed in Chapter 2 to novel nucleosides that show interesting properties.

This chapter is based on the work published in the papers:

Malek-Adamian, E.,‡ **Burai Patrascu,M.;** Jana, S.; Montero-Martinez, S.; Moitessier, N.; and Damha M.J. *J. Org. Chem.*, **2018**, 83, 17, 9839-9849.

EMA designed and performed the wet lab experiments. MBP designed the computational experiments and performed all the calculations and data analysis. SJ obtained crystal structures. All authors contributed to writing the manuscript.

O'Reilly, D.;‡ Stein, R.; **Burai Patrascu, M.;** Jana, S.; Kurrian, J.; Moitessier, N.; and Damha M.J. *Chem. Eur. J.*, **2018**, 24, 61, 16432-16439.

DOR and RS designed the wet lab experiments. DOR performed the wet lab experiments. MBP designed the computational experiments and performed all the calculations and data analysis. SJ obtained crystal structures. All authors contributed to writing the manuscript.

‡ first author

Abstract.

In this chapter, we show that the protocol developed in Chapter 2 can be applied to a variety of nucleosides that exhibit valuable properties. In the first part of this chapter, we explore the conformational preferences of nucleosides containing various hyperconjugation acceptors at key positions on the sugar ring. We show that we can obtain accurate *N/S* ratios for these nucleosides, as well as compute structures that excellently resemble crystal structures, with heavy atom RMSDs < 0.8Å in all cases. In the second part of this chapter, we delve into the nature of elusive fluorine-hydrogen bonds, and we provide computational and experimental evidence of its existence in a non-natural nucleoside. Overall, this work highlights the application of computational, crystallographic, and solution-phase NMR experiments in the investigation of stereolectronic effects and their role in sugar puckering, as well as C−H···F hydrogen bond formation. The complementarity of these techniques offers invaluable insight into the nature of these effects, and interactions that are present and play a role in stabilizing nucleic acid structures. Our study opens the possibility of designing new nucleosides analogues that utilize these subtle but important interactions to favour diverse conformations and tune their biological activity.

3.1. Introduction.

Nucleoside analogues have been used predominantly as small-molecule therapeutic agents, as well as for oligonucleotide modification in gene silencing[146,202] and, more recently, gene editing applications.[203] In this context, the therapeutic and off-target effects are primarily determined by the conformation of the nucleotide components. This conformation is also a major factor in defining the binding affinity toward the target RNA or ssDNA. One of the nucleotide components that significantly contributes to the overall conformation of nucleosides in solution is the sugar ring.[147] Over the years, multiple modifications to the sugar ring have been proposed: electronegative substituents at C2′ in the ribo (α) configuration[204] such as methoxy (-OMe),[205] MOE,[206] and fluoro (-F)[207] promote the sugar pucker toward the C3′-endo (*N*) conformation, while electronegative C2′-β-substituents (e.g. 2′-F) drive the sugar toward the *S/E* conformation (see Chapter 2, Figure 2.2). It is important to understand that different sugar puckers lead to the usage of nucleosides in different ways. As described in Chapter 2 nucleosides that prefer the *N* conformation are widely used in RNA targeting applications (e.g. siRNAs and AONs)[208] while those that favor the *S/E* conformations have been shown to confer nuclease resistance and excellent tolerance by the cellular machinery needed for gene knockdown.[155-157]

Generally, to experimentally determine the ratio between *N* and *S* conformations in solution various nucleoside analogues bearing different EDGs or EWGs are synthesized and then subjected to NMR experiments to obtain $^{3}J_{H1'\text{-}H2'}$ coupling constants. These constants are highly sensitive to the H1′-C1′-C2′-H2′ dihedral angle and thus reflect the type of sugar pucker (Figure 3.1).[209]

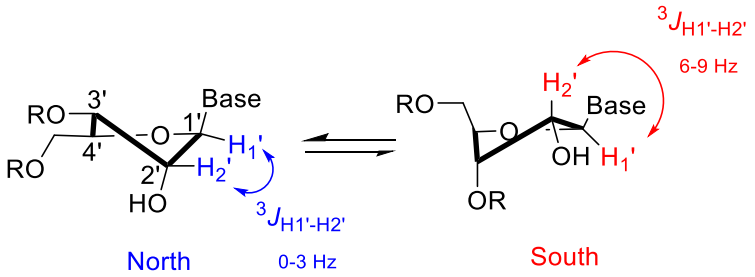

Figure 3.1. Definition of *J* coupling constants used in experimentally determining *N/S* equilibrium.

A $^{3}J_{H1'\text{-}H2'}$ value in the 0-3 Hz is consistent with a sugar pucker predominantly in the *N* conformation, while a $^{3}J_{H1'\text{-}H2'}$ value in the 6-9 Hz is representative of a sugar pucker in the *S* conformation.[209] These coupling constants are then used to obtain the *N/S* ratio (Eq. 3.1).[152,210]

$$\%\,\text{North} = 100 - 10 \times J_{(H1'\text{-}H2')} \qquad \text{Eq. (3.1)}$$

Equation 3.1. Experimental determination of %*N* populations.

This approach allows chemists to determine the overall sugar puckering preferences enabled by these substituents, but they do not allow any quantification of the amplitude or nature of their stereoelectronic effects. Moreover, several analogues bearing various combinations of these substituents must be synthesized and tested to obtain a nucleoside with the desired *N/S* ratio. To overcome this, in Chapter 2 we developed a highly robust computational protocol to determine the sugar puckering of non-natural nucleosides in solution. This methodology also proved effective in quantifying stereoelectronic effects induced by sugar ring substituents and allowed us to gain insights into their impact on the sugar puckering. Moreover, this computational protocol allows the screening and characterization of numerous nucleoside analogues prior to synthesis. This approach will contribute to reduced synthetic costs and waste production, since only nucleosides with desired characteristics would be synthesized.

In this chapter, we present our efforts to further our understanding of sugar puckering induced by various substituents and combinations thereof, and to uncover new evidence for possible

intramolecular interactions provided by these substituents that contribute to the overall sugar conformation.

3.2. Effect of Fluorine and Methoxy Substituents on Nucleoside Puckering.

In previous studies, we and others have shown that modification at the 4′-position (Figure 3.1) can have a strong effect on the sugar pucker preference.[152,158,176,210] More specifically we showed that 2′-F,4′-OMe-rU also adopts a more *N* conformation (~9:1 *N/S*) and that siRNAs containing several 2′-F,4′-OMe-rU units in the sense or antisense strands triggered RNAi-mediated gene silencing with efficiencies comparable to that of 2′-F-rU.[152] Furthermore, the C4′-α-OMe moiety conferred increased nuclease resistance due to the close proximity between the 4′-OMe substituent and the vicinal 5′- and 3′-phosphate groups. Guided by these results, we report herein the analysis of the conformations of several new 2′,4′-modified arabino- and ribonucleoside analogues (Chart 3.1) via computational methods. Moreover, we will draw comparisons to the conformational analyses of 2',4'-modified analogues that have been previously reported either by us or by others. Where appropriate, we will also refer to the NMR and X-ray crystallography analyses, although they do not represent the main focus of this chapter.

3.2.1. NMR Spectroscopy.

With our set of nucleosides in hand (Chart 3.1), we began to analyze their sugar conformations by NMR spectroscopy (experiments performed by our collaborators in the Damha group at McGill University). The percentage of *N* and *S* conformers of each ribonucleoside in solution was calculated by applying Eq. 3.1. (Tables 3.1). Table 3.1 summarizes the percentage of the *N* conformation for the nucleosides in Chart 3.1 in D_2O. Substitution of the 4′-H for electronegative substituents 4′-F and 4′-OMe resulted in a larger *N* bias in all 2′,4′-substituted nucleosides relative to their corresponding 2′-substituted nucleosides. This effect was more

pronounced in the case of 4′-fluoro substitution, in agreement with a fluorine being a better acceptor of hyperconjugation than a methoxy group,[211] thus providing stronger 4′ anomeric and gauche effects.

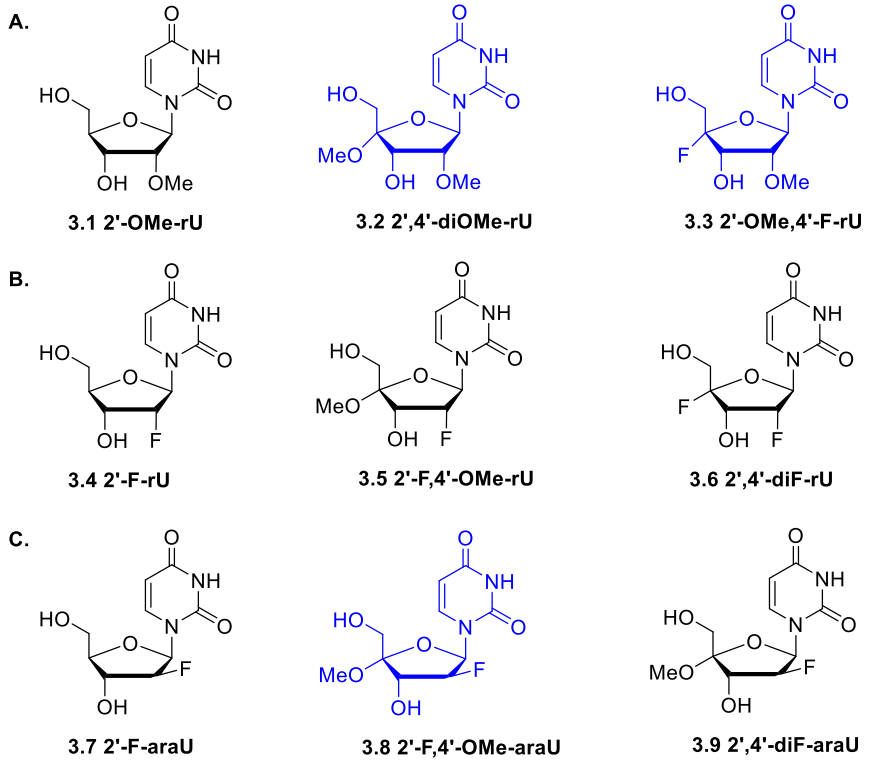

Chart 3.1. Structures of nucleoside analogues studied in this work: **(A)** 2′-OMe-modified ribonucleosides, **(B)** 2′-F-modified ribonucleosides, **(C)** 2′-F-modified arabinonucleosides. The structures colored in blue are analyzed here for the first time.

Table 3.1. $J_{H1'\text{-}H2'}$ coupling constants in D_2O obtained at 298K and %*N* populations.

Nucleoside	$J_{H1'\text{-}H2'}$	%*N*
3.1	4.0	60
3.2	2.8	72
3.3	1.3	87
3.4[a]	1.5	85
3.5[a]	1.3	87
3.6[b]	0.0	100
3.7	6.0	40
3.8	2.0	80
3.9[c]	2.0	80

[a] Data obtained from reference [152]. [b] Data obtained from reference [158]. [c] Data obtained from reference [176].

With the experimental *N/S* ratios in hand, we turned our attention to computational analysis to quantify the stereoelectronic effects governing the sugar puckering.

3.2.2. Predicted *N/S* Ratios and Lowest Energy Structures.

We applied the protocol developed in Chapter 2 to the nucleosides in Chart 3.1 to quantify the stereoelectronic effects and gain more insight into the origin of their conformational preferences. Predicted *N/S* ratios determined by either Boltzmann population distribution analysis or energy differences between the *N* and *S* conformations were in close agreement with the experimentally determined *N/S* ratios (Table 3.2). The overall mean unsigned error (MUE) for the %*N* populations determined through Boltzmann population distributions was 10.6%, while the MUE for the %*N* populations determined through energy difference between lowest energy *N* and *S* structures was 6.9%. This further confirmed the accuracy of the method, and the generated conformations could now be further analyzed.

Table 3.2. Computed *N/S* ratios[a] for the nucleosides in Chart 3.1.

Nucleoside	%*N* exp.	%*N*[b]	%*N*[c]
3.1	60	nd[d]	nd[d]
3.2	72	66	73
3.3	87	71	76
3.4	85	58[212]	70[212]
3.5	87	84[212]	86[212]
3.6	100	80[212]	91[212]
3.7	40	nd[d]	nd[d]
3.8	80	79	85
3.9	80	81[212]	86[212]

[a] In H_2O at 303K. [b] Based on Boltzmann population distributions. [c] Based on energy differences between the *N* and *S* minima. [d] not determined.

Since we were mostly interested in the novel nucleosides **3.2**, **3.3**, and **3.8**, our subsequent structural analysis was only performed for these three nucleosides. For each stable conformation

(i.e. lowest energy conformations in the *N* and *S* conformations – Figure 3.2), we determined the pseudorotational phase angle P and the puckering amplitude Φ_{max} (the maximum degree of pucker) (Table 3.3).

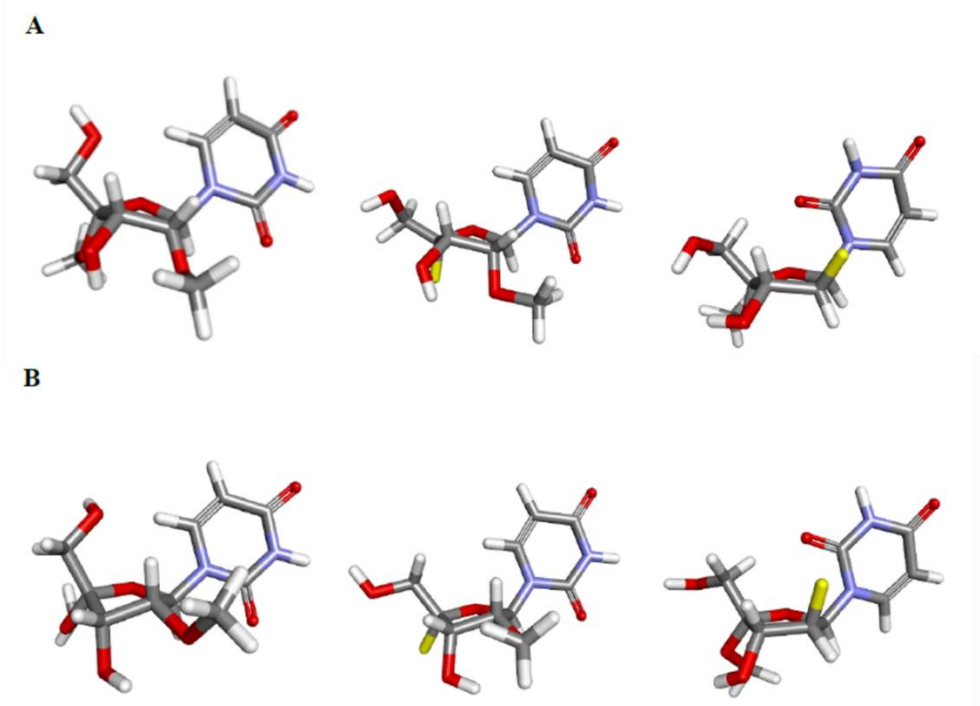

Figure 3.2. Computed lowest energy structures for **A.** *N* conformations: left – **3.2**; center – **3.3**; right – **3.8** and **B**. *S* conformations: left – **3.2**; center – **3.3**; right – **3.8.**

These parameters would be helpful in comparing the computed structures to X-ray crystallography data. Once these parameters were collected, we proceeded to analyze the hyperconjugation and anomeric effects that contribute to sugar puckering.

Table 3.3. Puckering parameters obtained for the lowest energy conformations in Figure 3.2.

Nucleoside	Conformation	P (°)	Φ_{max} (°)
3.2	*N*	60.54	29.98
	S	168.48	41.52
3.3	*N*	55.63	36.09
	S	158.60	28.16
3.8	*N*	47.24	22.06
	S	146.11	17.03

3.2.3. Quantifying Stereoelectronic Effects.

Anomeric and hyperconjugation effects through the means of NBO analysis were evaluated as described in Chapter 2. The anomeric effect $n_{O4'} \rightarrow \sigma^*_{C4'OMe/F}$ (Figure 3.3A) favors the *N* conformation except for **3.8**; the strength of the anomeric effect followed the order **3.3** (P = 55.6°) > **3.2** (P = 60.5°) > **3.8** (P = 47.2°) (values for the anomeric and hyperconjugation effects in kcal/mol given in Appendix B). Several factors seem to influence the strength of the anomeric effect: **(a)** the puckering amplitude of the sugar ring, with a weaker effect observed for lower amplitudes for both *N* and *S* conformations, **(b)** the hyperconjugation-accepting ability of the 4′-substituent, and **(c)** the P angle, with deviations from ideal envelope conformations associated with weaker anomeric effects.

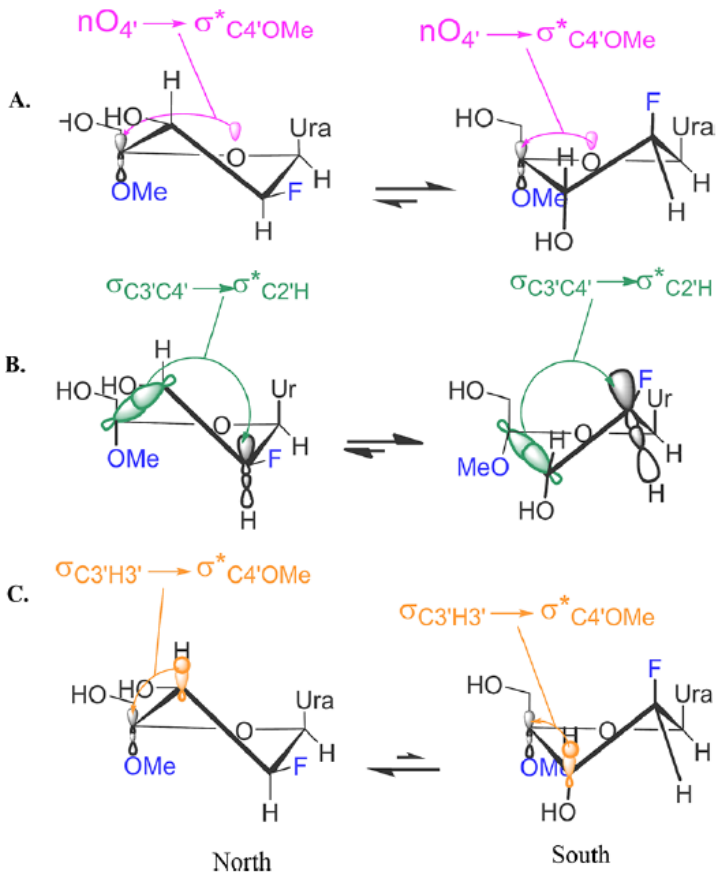

Figure 3.3. Stereoelectronic effects in **3.8**: **(A)** depiction of the $n_{O4'} \rightarrow \sigma^*_{C4'OMe}$ anomeric effect, **(B)** depiction of the $\sigma_{C3'C4'} \rightarrow \sigma^*_{C2'H}$ hyperconjugation effect, **(C)** depiction of the $\sigma_{C3'H3'} \rightarrow \sigma^*_{C4'OMe}$ hyperconjugation effect.

In the case of **3.8**, a plausible explanation for the *S* conformation exhibiting a slightly larger anomeric effect is that the *N* conformation (P = 47.2°, φ_{max} = 22.1°) deviates from an ideal envelope conformation (P = 54°, φ_{max} = 25−45°). This leads to a poor overlap between the lone pair on the anomeric oxygen and $\sigma^*_{C4'OMe}$ due to orbital misalignment. However, **3.8** was shown to be predominantly in the *N* conformation, and as such, another electronic effect apart from the anomeric effect should be the driving force behind the observed conformation. Indeed, the data in Appendix B suggest that the $\sigma_{C3'H3'} \rightarrow \sigma^*_{C4'OMe}$ hyperconjugation effect (Figure 3.3C) is the most

pronounced computed electronic effect (with an energy difference of ~1.9 kcal/mol in favor of the *N* conformation), similar in strength to that of **3.2** (~2.0 kcal/mol) and **3.3** (~3.1 kcal/mol). Interestingly, this effect is exhibited in conjunction with a $\sigma_{C3'C4'} \rightarrow \sigma^*_{C2'H}$ hyperconjugation effect (Figure 3.3B) (~0.8 kcal/mol in favor of the *S* conformer) that is significantly lower than that observed for **3.3** (~3.5 kcal/mol) and **3.2** (~2.2 kcal/mol), most likely afforded by the orientation of the fluorine in the arabino configuration. As such, the loss of an important hyperconjugation effect favoring the *S* pucker ($\sigma_{C3'C4'} \rightarrow \sigma^*_{C2'H}$), coupled with a strong hyperconjugation effect favoring the *N* pucker ($\sigma_{C3'H3'} \rightarrow \sigma^*_{C4'OMe}$), contributes to the observed *N* conformation of **3.8**.

3.2.4. Comparing Computed and Crystal Structures.

The structures of **3.2** and **3.3**, first described in this study, were unambiguously confirmed by X-ray crystallography. Additionally, we obtained the crystal structures of previously reported **3.5** and **3.6.**[212] These were compared to their predicted conformations by computational analysis, and the superposition of these are shown in Figure 3.4. **3.3** was crystallized in its most stable conformation (P_1 = 22.4°, $\Phi_{1,\,max}$= 34.1°, P_2 = 21.2°, $\Phi_{2,\,max}$= 33.8°). In the case of **3.5** (4′-*exo*), two slightly different conformations appeared in the asymmetric unit crystal (P_1 = 62.3°, $\Phi_{1,\,max}$ = 36.6°, and P_2 = 60.5°, $\Phi_{2,\,max}$ = 37.1°). However, the orientations of the base and the 3′- and 5′-hydroxyls differ from the computational data. In contrast, **3.2** and **3.6** were crystallized in the *S* conformation (P = 163.2°, Φ_{max} = 39.5°) and the *E* conformation (P = 74.7°, Φ_{max} = 35.4° 28), respectively. It is important to note that the conformations in which these nucleosides were crystallized do not necessarily represent the conformations in solution. As discussed in Chapter 2, crystal packing and intermolecular hydrogen bonding interactions between molecules in different unit cells likely affect the conformation of the nucleoside in the crystal.[213] However, although the positions of hydrogen-bond accepting/donating substituents on the ring differs between solution and crystals

due to intermolecular hydrogen bonding with solvent/other molecules in the crystal unit, the core 5-membered ring has the same puckering.

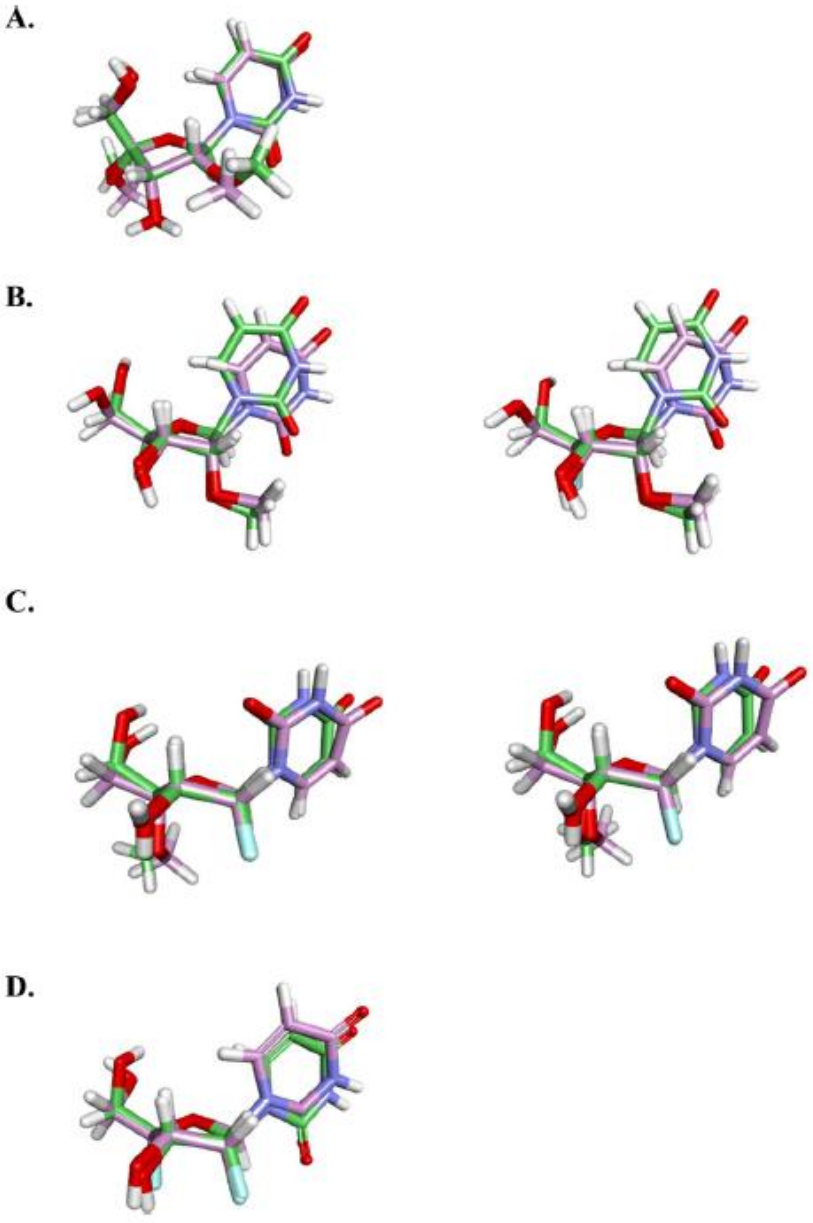

Figure 3.4. Superposition between the predicted conformation (green) and the crystal structure (pink): **(A) 3.2**, **(B) 3.3** (left) unit 1 and (right) unit 2, **(C) 3.5** (left) unit 1and (right) unit 2, **(D) 3.6**.

Overall, the computed structures are in excellent agreement with the crystal structures. One of the key features to account for when comparing the structures is the heavy atom RMSD. Importantly, the heavy atom RMSD for all four nucleosides is < 0.8Å (Table 3.5). Moreover, as can be seen in Figure 3.4, the sugar pucker in all four cases is nearly identical between the computed and the crystal structures. The major differences that arise between the structures are the orientations of the substituents, which can be explained through the intermolecular hydrogen bonding interactions existent in different crystal cells, which affect the orientation of the substituents containing hydrogen bond acceptors and donors. Nonetheless, in this section we have shown that the protocol described in Chapter 2 provides invaluable insight into hyperconjugation effects affecting sugar puckering and highly robust structures that excellently resemble crystal structures for non-natural nucleosides.

Table 3.4. Heavy atom RMSD between the computed and crystal structures described in Figure 3.4.

Nucleoside	Unit Cell	Heavy Atom RMSD (Å)
3.2	1	0.47
	2	-
3.3	1	0.82
	2	0.82
3.5	1	0.51
	2	0.59
3.6	1	0.59
	2	-

3.3. Atypical Fluorine-Hydrogen Bonds and Their Effects on Nucleoside Conformations.

One of the most important substituents used in controlling ring conformations is fluorine. Due to its electronegativity, fluorine is an excellent hyperconjugation acceptor (Figure 3.5) and can thus be used to modulate ring conformations.[214,215] Interestingly, fluorine can not only be used as a hyperconjugation acceptor to modulate conformations, but also as a hydrogen-bond acceptor. It has been debated for decades whether organic fluorine-hydrogen bonds exist, especially due to the fact that fluorine rarely accepts hydrogen bonds.[216] Moreover, different definitions of what constitutes a hydrogen bond contribute to this debate – these definitions range from a pure electrostatic nature of hydrogen bonds, to a combination of electrostatics and polarization effects as well as a significant covalent bond character.[217-219] Irrespective of these definitions, fluorine-hydrogen bonds can help modulate sugar conformations and thus represent an interesting component to designing new nucleoside-based drugs.

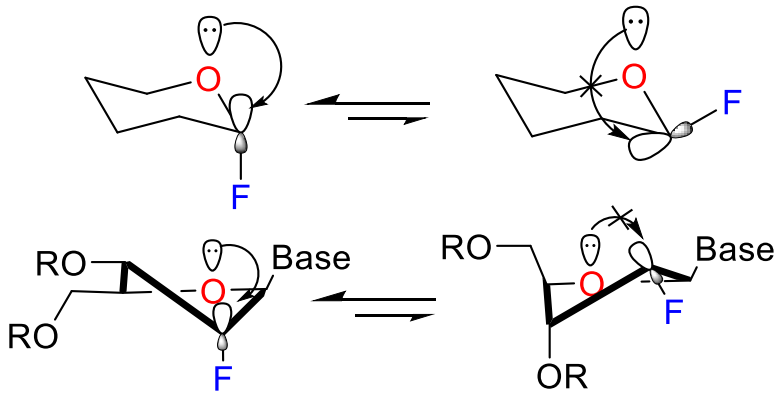

Figure 3.5. Top. Hyperconjugation in fluorinated pyranose rings. **Bottom.** Hyperconjugation in fluorinated furanose rings. The hyperconjugation acceptor (σ_{CF*}) is depicted in blue while the hyperconjugation donor (n_O) is depicted in red.

Due to the increasing usage of fluorine in medicinal chemistry applications, several key pieces of evidence have been found in favour of the existence of fluorine-hydrogen bonds in small molecules and nucleic acid-based systems.[220-222] These recent developments have led IUPAC to

establish guidelines for defining fluorine-hydrogen bonds (Figure 3.6), although different variations of these parameters have been proposed.[223]

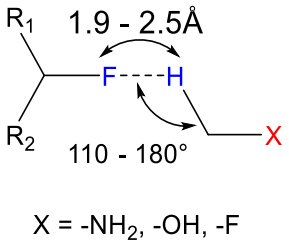

Figure 3.6. IUPAC guidelines for what constitutes a fluorine-hydrogen bond.

Experimentally, fluorine-hydrogen bonds in nucleosides can be observed by NMR through scalar J_{HF} coupling.[220] This however requires the synthesis of a nucleoside of interest. A cheaper, more attractive alternative is the computational modeling of nucleosides in which fluorine-hydrogen bonds are possible. As such, we posited that the protocol developed in Chapter 2 would be suitable for analyzing nucleosidic fluorine-hydrogen bonds in solution.

3.3.1. Nucleosides That Can Potentially Exhibit Fluorine-Hydrogen Bonds.

It is currently understood that C-F···H hydrogen bonds are present in oligonucleotides and can offer additional stability to the overall structure.[183] For example, the hybridization of 2′-F-ANA oligonucleotides with complementary RNA strands results in the formation of close C-F···H contacts.[224] Evidence for these bonds arises from C-F···H contacts observed through nuclear Overhauser effect (NOE) experiments, conformational analysis, and theoretical calculations of binding free energies.[225] On the other hand, 2′-F-araA (Chart 3.2, **3.10**) is also hypothesized to have a C2′-F···H_8-C interaction based on ^{1}H-NMR and deuterium exchange studies.[224] Several nucleosides,[226,227] and more recently, 6′-F-tricyclo-thymidine (6′F-tcT),[228] have been proposed to engage in a similar interaction (Chart 3.2, **3.15**). Methods for detecting these interactions in non-nucleic acid based systems are well developed.[220] However, it is less well understood why these

weak intramolecular interactions form and how they influence nucleoside and nucleic acid structure and stability.

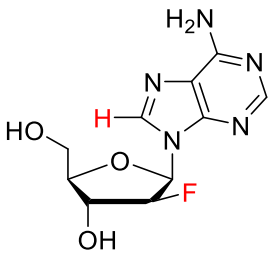

3.10 2'-F-araA

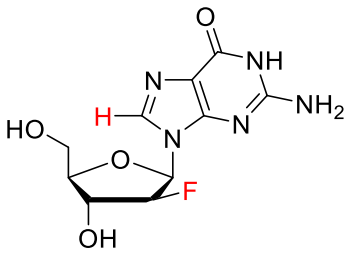

3.11 2'-F-araG

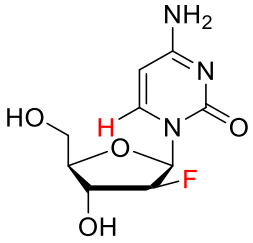

3.12 2'-F-araC

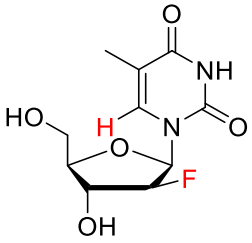

3.13 2'-F-araT

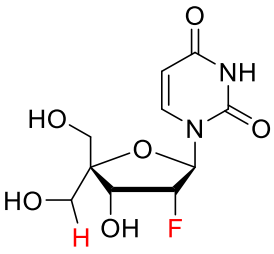

3.14 2'-F,4'-α-methylhydroxy-rU

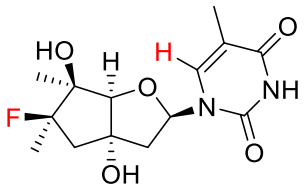

3.15 6'-F-tcT

Chart 3.2. Fluorinated nucleosides in which fluorine-hydrogen are hypothesized to occur. The fluorine and hydrogen atoms between which a hydrogen bond is possible are highlighted in red.

Herein, we examine nucleosides **3.10-3.14** via NMR, X-ray crystallography, and computational studies. Understanding whether C-F···H hydrogen bonds play a role in the conformation and stability adopted by these systems is important and could lead to the design of new modified nucleosides that incorporate these interactions.

3.3.2. Analysis of Nucleosides 3.10-3.13.

In D_2O, 2′-F-arabinonucleosides (**3.10-3.13**) exhibit similar sugar conformations, with a *N/S* pucker ratio of approximately 2:3 in all cases (Table 3.5). Moreover, since these nucleosides are in a *N/S* equilibrium, they pass from one conformation to another through the *E* conformation (Figure 2.2). Experimentally, the *E* conformation is most clearly established through $H_{1'}$-$H_{4'}$ NOE

contacts and can cause reduced $^{3}J_{H1'-H2'}$.[155] Evidence for the existence of the *E* conformation shows that; for example, **3.12** exhibits stronger $H_{1'}$-$H_{4'}$NOE contacts than **3.13**, and thus exhibits a stronger preference for the *E* conformation.[155] The calculations of these contacts, along with ^{1}H-^{19}F two-dimensional heteronuclear NOE (HOESY) NMR experiments, show that for nucleosides **3.10**-**3.13** the distance between the fluorine and hydrogen depicted in red in Chart 3.2 varies between 2.4 – 2.7Å (Table 3.5, Figure 3.7 – computed lowest energy structures and predicted distances for nucleosides **3.10** and **3.12**).

Table 3.5. Experimental and predicted *N/S* ratios along with experimental and predicted distances between the fluorine and hydrogen atoms.

Nucleoside	Exp. *N/S*	Pred. *N/S*[a]	HOESY Distance (Å)	Predicted Distance (Å)
3.10	41/59	47/53	2.5	2.7
3.11	41/59	48/52	2.4	2.7
3.12	38/62	45/55	2.7	2.9
3.13	40/60	60/40[212]	2.7	2.7
3.14	70/30	60/40	2.3	2.3

[a] based on Boltzmann population distributions.

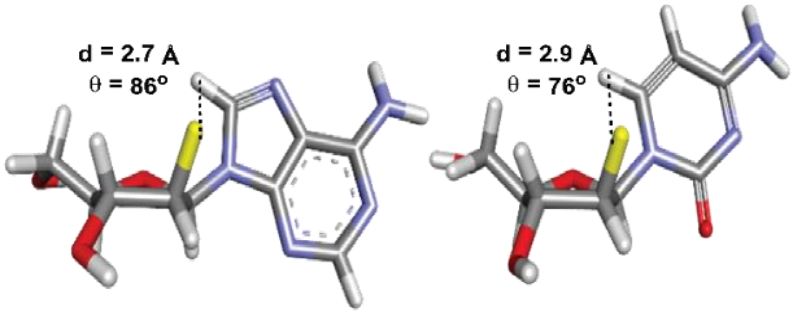

Figure 3.7. Lowest energy conformations for **3.10** and **3.12**. C-F···H-C distance shown with dashed line. θ is the value of the F···H-C angle.

As can be seen in Table 3.5, the *N/S* ratios are in very close agreement between experimental and predicted values. Moreover, the predicted distances between the fluorine and hydrogen atoms are within 0.1-0.3Å of the experimentally determined ones. To probe whether these distances were short enough to enable fluorine-hydrogen bonds for compounds **3.10**-**3.13**,

we examined the splitting of ^{13}C signals of the purine/pyrimidine bases by fluorine (Figure 3.8). The purine C8/C4 and the pyrimidine C6/C2 carbons are four bonds away from the 2′-F. If the interactions were purely long-range in nature, similar $^{4}J_{2'F\text{-}C}$ coupling values would be expected. However, in **3.10**, only the C8 shows significant splitting (4 Hz) from ^{19}F (Appendix B). All other ^{13}C signals showed a splitting of 0.5 Hz or less. The same was true for **3.11**. For **3.12** and **3.13**, we compared the C2 and C6 signals; splitting of only the latter was observed.

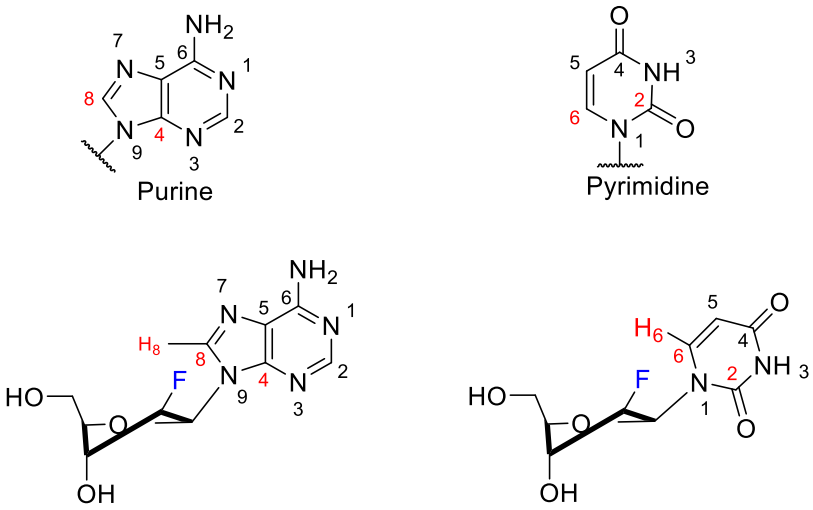

Figure 3.8. Interactions between fluorine and C8/C6 in purine bases, and between fluorine and C6/C2 in pyrimidine bases.

In addition to the ^{13}C NMR splitting, we explored the signals of H8 and H6 using ^{1}H NMR. For nucleosides **3.10**-**3.13**, a small splitting of 1.5 and 2.5 Hz was observed, which may suggest hydrogen bond-mediated coupling with fluorine as previously proposed for nucleosides, duplexes, and quadruplexes.[229,230] To verify whether the protocol we established in Chapter 2 was capable of identifying these potential hydrogen bonds in compounds **3.10**-**3.13**, we employed our NBO analysis protocol on the lowest energy structures obtained following our umbrella sampling simulations. The F···H-C angles for the four compounds were 86°, 54°, 75° and 76° respectively,

which fall outside the typical range of 110-180° necessary for fluorine-hydrogen bonding to occur (Figure 3.6). However, due to the nature of hydrogen bonding, we posited that electrostatic interactions might still be possible due to the short distance between the fluorine and hydrogen atoms. Our NBO analysis however revealed no attractive interaction between the two atoms.

3.3.3. Analysis of Nucleoside 3.14.

Next, we turned our attention to nucleoside **3.14**. This nucleoside is analogous to the previously reported branched nucleoside **3.16** (Figure 3.9),[231] which was predicted by DFT calculations and MD simulations to engage in a weak intramolecular C(sp^3)-H···F bond between the hydrogen atom of the 4′-C-CH_2 group and F2′.[231] Given their similarity and the greater electronegativity of O vs N, **3.14** was expected to exhibit the same interaction.

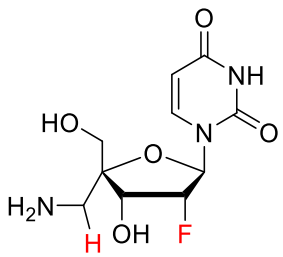

3.16 2'-F,4'-α-methylamino-rU

Figure 3.9. Analogue of **3.14** that is hypothesized to show a C(sp^3)-H···F bond.

After synthesizing **3.14**, we managed to obtain its crystal structure. This compound crystallized in its most stable *N* conformation (P=49.5º). The puckering angle was in very close agreement with the one obtained for the lowest energy predicted structure of **3.14** (P=52.1º). Overlay of the two structures revealed a heavy-atom RMSD of 0.78Å (Figure 3.10), while an analysis of the predicted *N/S* ratios shows very close agreement to experimentally obtained ones (Table 3.5).

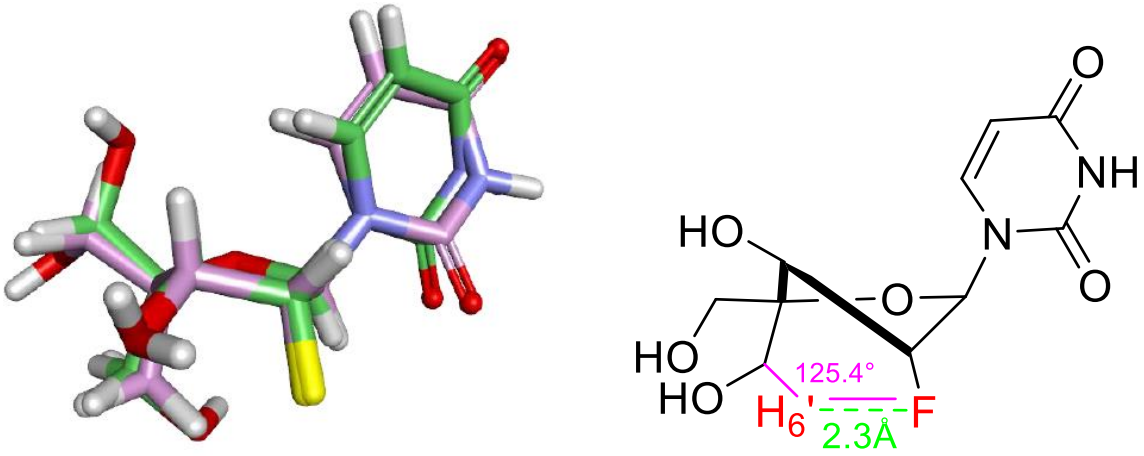

Figure 3.10. Left: Superposition of crystal structure of **3.14** (green) and predicted structure (pink). **Right:** 2D representation of the *N* conformation for **3.14**. Predicted distance (green) between 2′F-H_6′ is 2.3Å, while the C_6H_6′-2′F angle (purple) is 125.4°.

Importantly, several conclusions can be drawn after analyzing the experimental and predicted data. First, the predicted lowest energy structure is in excellent agreement with the crystal structure of **3.14**, which gives us confidence that the orientation of the substituents is correct in the predicted structure. Second, the parameters established in Figure 3.6 are fulfilled when considering the predicted structure, which shows a H_6′-2′F distance of 2.3Å, and a C_6H_6′-2′F angle of 125.4°. Combined, these conclusions allow us to posit that a C_6H_6′···2′F interaction is indeed possible. To verify this, we plotted the electron density and molecular orbitals for the *N* conformer (Figure 3.11).

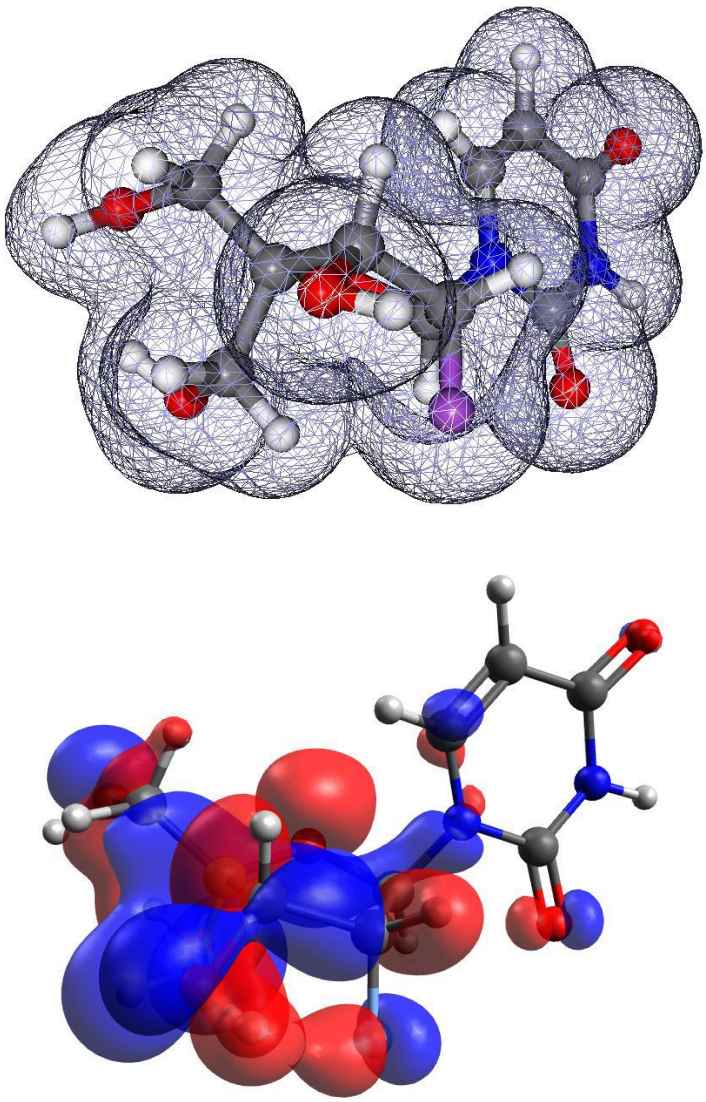

Figure 3.11. Top: 2′F-H_6′ electron density overlap observed in the *N* conformation of **3.14**. **Bottom:** Attractive orbital overlap between 2′F-H_6′ in the *N* conformation.

As can be seen in Figure 3.11, it is clearly visible that an attractive interaction between 2′F and H_6′ exists. As such we proceeded to quantify this interaction through NBO analysis, which yielded a strength of 0.74 kcal/mol for the C_6H_6′···2′F hydrogen bond. Given the relatively weak interaction quantified by NBO, we were interested in determining the nature of this bond. To achieve this, we employed quantum theory of atoms in molecules (QTAIM) analysis. Briefly, QTAIM explores the idea that chemical bonds can be expressed in terms of the topology of the

molecular electronic density. More specifically, the space occupied by a molecule is divided into "basins" (or atoms), which are connected through interatomic surfaces (IAS). If these basins interact through an attractive force, a bond critical point (BCP) in the electron density can be found and the two basins are said to be connected through a bond path (BP).[232] Moreover, at the BCP, the gradient of the electron density is 0. Importantly, QTAIM can be applied to any system in which both covalent and non-covalent interactions occur. In 1995, Popelier established that the existence of IAS, BCP, and BP between a hydrogen-bond donor and acceptor were sufficient to assert the existence of a hydrogen bond.[233] We analyzed the *N* conformation of **3.14** and we identified a BCP, BP, and IAS (Figure 3.12), confirming that between $C_6H_6'\cdots 2'F$ there was indeed a hydrogen bond that was most likely electrostatic in nature.[234]

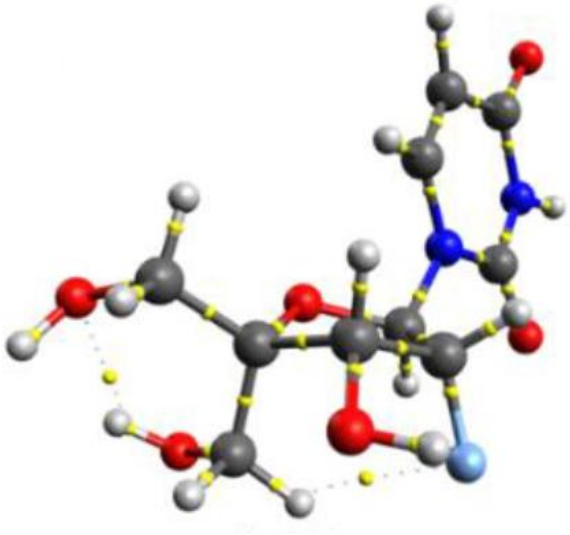

Figure 3.12. QTAIM BCP (yellow balls) and BP (dashed lines) showing the attractive interactions between atoms.

To verify whether the predicted $C_6H_6'\cdots 2'F$ hydrogen bond could be distinguished experimentally, we subjected nucleoside **3.14** to [^{19}F-^{1}H] heteronuclear multiple bond correlation (HMBC) NMR experiments. These experiments showed that the $J_{H6'\text{-}F}$ coupling was in the range of 1Hz, and that it primarily occurred through-bond rather than through dipole-dipole interactions.

3.4. Conclusions.

In the first part of this chapter we focused on three novel nucleosides containing electron-withdrawing substituents in key positions on the sugar ring: 2′,4′-diOMe-rU, 2′-OMe,4′-F-rU, and 2′-F,4′-OMe-araU. Conformational analyses of these nucleosides and comparison to other previously reported 2′,4′-disubstituted nucleoside analogues make it possible to evaluate the effect of fluorine and methoxy substitution on the sugar pucker, as assessed by NMR, X-ray diffraction, and computational methods. We found that in all cases the electronegative substituents promote the *N* conformation of the sugar puckers. Moreover, we were able to quantify the anomeric and hyperconjugation effects that arise from the excellent orbital overlaps afforded by the *N* conformation when using good hyperconjugation acceptors (-F, -OMe) at key positions (2' and 4') on the sugar ring.

In the second part of this chapter we directly probed the existence of fluorine-hydrogen bonds in nucleosides using NMR experiments and computational modeling studies in a series of C2′-fluorinated nucleosides. Specifically, QM/MM analysis and [^{19}F-^{1}H]-HMBC NMR experiments provided important support for a C-H···F hydrogen bond in a 2′-F,4′-C-α-alkylribonucleoside analogue. This interaction was also supported by QTAIM and NBO analyses which suggested that a C-H···F interaction (0.74 kcal/mol) indeed exists. In contrast, while conformational analysis and NMR experiments of 2′-deoxy-2′-fluoroarabinonucleosides indicated a close proximity between the 2′-F and the nucleobase's H6/8 protons, molecular simulations did not provide evidence for a C-H···F hydrogen bond.

3.5. Methods.

MD simulations were performed according to the protocol described in Chapter 2. Relevant angle values and bond distances were calculated in Avogadro v1.2.0. [235] as well as the plotting of

molecular orbitals. Visual QTAIM analysis was performed in Avogadro using wavefunction files obtained with Gaussian16[236] at the M06L/def2-TZVP level of theory. Quantitative QTAIM analysis was performed using the AIMALL[237] program on the same wavefunction files used for visual QTAIM analysis. NBO analysis was performed using the NBO6[200] program. Electron densities were plotted using Molekel,[201] while the lowest energy conformation figures were rendered with Discovery Studio 4.5.[238]

Chapter 4 – Predicting Cytochrome P450 Inhibition and Metabolism at the Drug Development Stage

Preface.

Drug design and discovery is a tedious and costly process. In some cases, after a drug has reached the market, it shows signs of idiosyncratic toxicity, which culminates with drug withdrawal from the market. This type of toxicity, along with adverse drug reactions, is a major hurdle in drug discovery and contributes significantly to the costs associated with bringing a drug to the market. These adverse drug reactions and toxicity primarily arise from phase 1 metabolism, where metabolic enzymes – Cytochrome P450 enzymes (CYPs) – are responsible for the metabolism of 75-90% of xenobiotics. Adverse drug reactions enabled by CYPs can result from two major routes: CYP inhibition and reactive metabolite formation after CYP oxidation.

Currently, expensive laboratory experiments are necessary to determine these types of toxicity. Importantly, these experiments can be undertaken only after a compound has been synthesized or purchased. To reduce the number of drugs that are withdrawn from the market and to allow the synthesis of drug-like molecules that lack CYP toxicity, we set out to use QM calculations, docking and ML models to build a tool capable of distinguishing between potential inhibitors and non-inhibitory molecules before synthesis is even attempted. Moreover, we aimed to improve our SoM prediction tool IMPACTS to better describe the oxidation products obtained following a drug's metabolism by CYPs.

Chapter 4

This chapter is partially based on the work presented in the following papers/manuscripts:

Burai Patrascu, M.;‡ Plescia, J.; Kalgutkar, A.; Mascitti, V.; and Moitessier, N. *Arkivoc*, **2019**, part IV, 280-298.

All authors contributed to writing the manuscript (invited review).

Burai Patrascu, M.;‡ and Moitessier, N. **2020**. Improvement of the IMPACTS Drug Metabolism Tool. – Manuscript in Preparation.

MBP and NM designed the computational experiments. MBP developed the SASA correction and implemented it in FORECASTER. MBP performed all calculations and analyzed all the data. MBP and NM contributed to writing the manuscript.

‡ first author

Abstract.

Adverse drug reactions (ADRs) and toxicity are major causes of the high attrition rates observed in drug discovery and development programs. These adverse reactions generally occur after phase I metabolism, where cytochrome P450 enzymes (CYPs) metabolize approximately 90% of xenobiotics. Often, these xenobiotics can either inhibit CYPs, or be metabolized into reactive metabolites that can further interact with DNA and proteins. Experimentally determining whether a xenobiotic metabolized by CYP enzymes can be toxic/an inhibitor is expensive and time-consuming. Most importantly, it requires that the xenobiotic be already synthesized. Computational prediction of CYP toxicity constitutes a viable and more time-efficient alternative. We have developed a computational tool that relies on QM calculations, docking and ML models to predict CYP inhibition at the drug development stage. Moreover, to better describe the binding of drugs to CYPs and identify whether a xenobiotic can be metabolized into a reactive metabolite, we made significant improvements to our SoM prediction tool IMPACTS.

4.1. Introduction.

Adverse drug reactions (ADRs) and toxicity are major causes of the high attrition rates observed in drug discovery and development programs. Severe and even fatal toxic effects have resulted in drug withdrawals, resulting in an enormous financial burden despite huge investments in toxicology and clinical trials. Although the primary causes of toxicity could be very different, the first pass bioactivation by metabolic enzymes such as CYPs is often the initiating step. The produced reactive metabolite further reacts with biomolecules such as proteins, DNA, or glutathione, leading to hepatotoxicity or DNA mutations causing cancer. Similarly, the co-administration of drugs with one inhibiting the CYP(s) involved in the metabolism of the other(s) may lead to the accumulation of the unmetabolised drug(s) resulting in severe toxicity. This process is known as drug-drug interactions (DDI). Medicinal chemists have relied on "structural alerts": functional groups known to possess high toxicity potentials, to flag potentially toxic drug candidates. Computational prediction of reactive metabolites and DDIs constitutes a viable and more time-efficient alternative.

4.2. Drug Metabolism, Bioactivation and Toxicity.

Most of the administered drugs are metabolised in the liver to be more efficiently excreted from the organism. In phase 1 metabolism, the molecules are modified by a set of enzymes, primarily oxidases and hydrolases. Numerous drugs currently on the market are metabolized by one of the 57 human CYPs. Out of this set of oxidases, six (CYP1A2, 2C9, 2C19, 2D6, 1E2, and 3A4), expressed mainly in the liver and in the gut, are responsible for more than 90% of this oxidative metabolism and represent the main focus of medicinal chemists and pharmacologists.[67,239,240] The oxidative metabolism of drugs by CYPs occurs by the means of heme-mediated oxidation (Chapter 1, Scheme 1.9).

In phase 2 metabolism, the drug (or the metabolite from phase 1) is conjugated to water soluble moieties (e.g., glucuronic acid), which facilitates its detoxification from the body. The metabolites produced in this process have their intrinsic pharmacologic effect and toxicity that may differ from the parent drug. More specifically, they can have longer periods of persistence in the CYP as inhibitors due to significant intrinsic chemical reactivity, which may result in cell damage. They can also exhibit high reactivity leading to hepatotoxicity and/or cancer and are referred to as reactive metabolites. The impact of reactive metabolites and ADR on drug toxicity and drug withdrawal has been extensively discussed in the literature.[241,242] About 75% of the drugs withdrawn due to ADRs were in fact activated into reactive metabolites.[27]

While there are several medium throughput techniques available, access to higher throughput techniques would enable medicinal chemists to make more informed decisions at early stages of the drug design and development process.[243] For instance, predicting the site of metabolism (SoM), binding mode of small molecules in the CYPs and inhibitory activity of drugs and their metabolites could be useful to **(1)** flag potential *in vitro* hits, **(2)** help prioritize experiments, **(3)** provide key insights enabling the design of compounds with modulated half-life, **(4)** predict potentially toxic metabolites, **(5)** predict potential CYP inhibitors or even **(6)** predict the effect of CYP polymorphism (i.e., inter-individual variability).[244] A number of computational approaches have been developed to tackle the challenges associated with drug metabolism and these include both LBDD and SBDD methods.[245-247] Among these approaches is IMPACTS (In-silico Metabolism Prediction by Activated Cytochromes and Transition States), a fully automated program developed by the Moitessier group at McGill University, which combines molecular docking, ligand reactivity estimation, and transition state (TS) structure prediction to predict the SoMs of drugs metabolized by CYPs. IMPACTS has been shown to accurately predict the SoMs of

over 600 drugs spanning 4 major CYP isoforms.[248] Moreover, its implementation in the drug discovery platform FORECASTER (also developed by the Moitessier group) makes it highly appealing to medicinal chemists. However, at this current stage, IMPACTS is unable to predict whether a drug or its metabolites can inhibit CYPs or not.

4.3. CYP Inhibition - Background.

The co-administration of drugs may result in DDIs, due to the ability of a drug to inhibit a CYP isoform involved in the metabolism of another drug. This leads to the accumulation of the unmetabolised drug(s) in the human body, causing potentially fatal side effects. CYP inhibition can either be reversible, quasi-irreversible and irreversible, with the most prevalent form being reversible inhibition.[249] Usually, reversible inhibition occurs when the so-called Type II ligands (typically molecules containing basic nitrogen atom(s))[250] coordinate to the heme iron (Figure 4.1). An important example of such a ligand is ketoconazole, an antifungal compound that inhibits CYP3A4 (Figure 4.2). In the case of quasi-irreversible and irreversible inhibition, at least one catalytic cycle is required for the formation of reactive metabolites that will then interact with the heme moiety.[249]

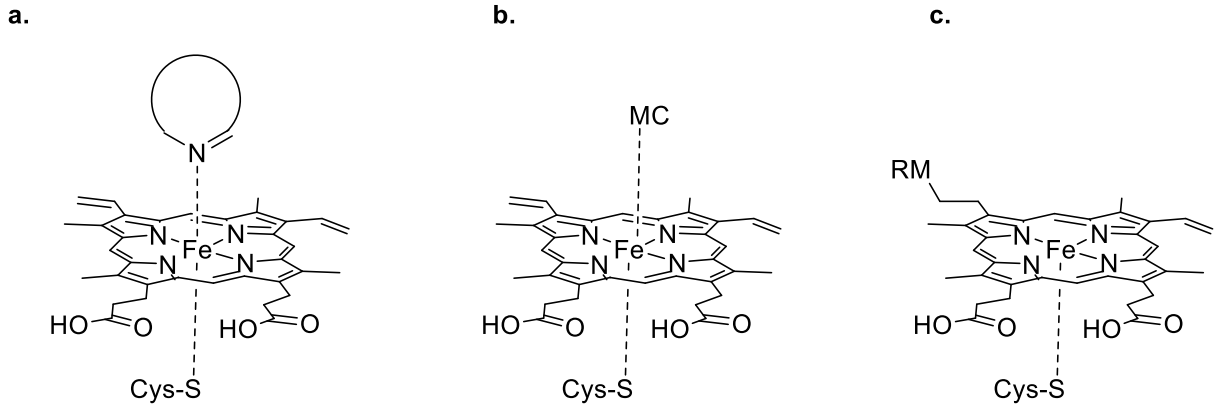

Figure 4.1. a. Reversible CYP inhibition. **b.** Quasi-irreversible CYP inhibition (MC = metabolic intermediate complex). **c.** Irreversible CYP inhibition (RM = reactive metabolite).

Quasi-irreversible CYP inhibition requires the formation of a metabolic intermediate complex (MC), which can be displaced by *in vivo* incubation with compounds that have high affinity for CYP enzymes. Examples of drugs that inhibit CYPs quasi-irreversibly are erythromycin and lapatinib.[251,252] For irreversible inhibition, a reactive metabolite (RM) can either alkylate the heme (for example by adding to the double bonds – see Figure 4.1c) or interact with key residues in the CYP active site i.e. acylation of a critical lysine residue by chloramphenicol is well documented.[253] Both these mechanisms inactivate the protein, which is then incapable of performing its biological function. To restore enzyme function, biosynthesis of new enzymes is required.

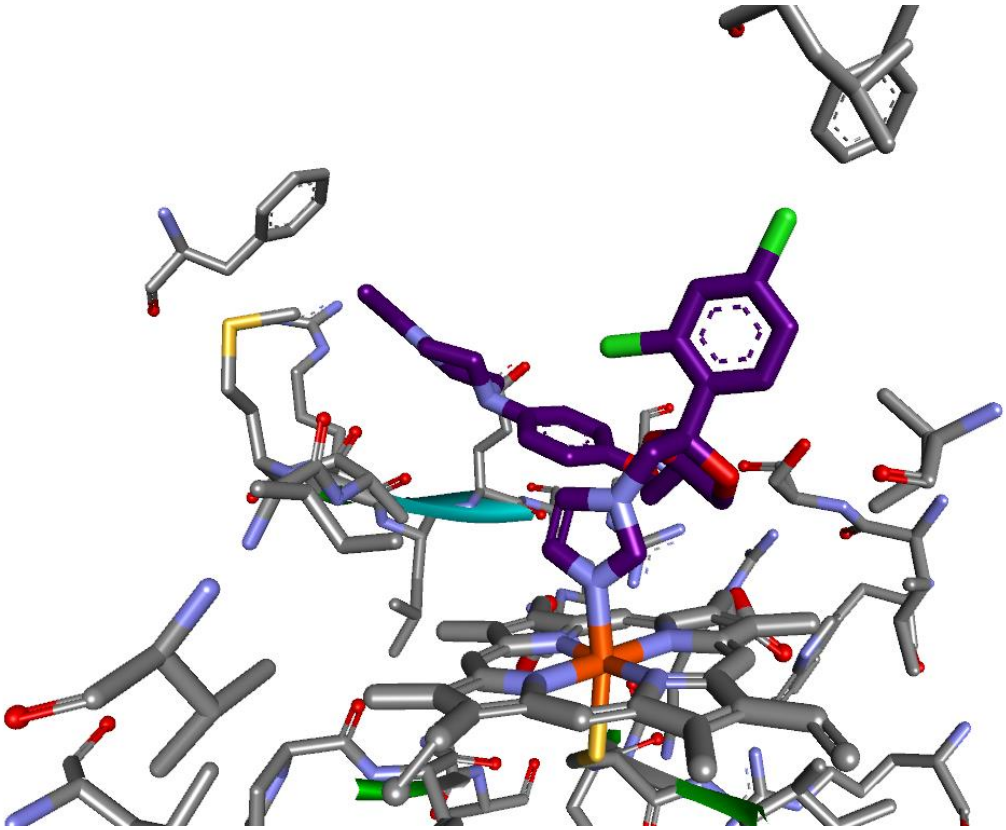

Figure 4.2. Reversible CYP inhibition of CYP3A4 by ketoconazole. Protein Data Bank (PDB) code: 2V0M. Active site snapshot. Ligand carbons are shown in purple; heme iron is shown in orange.

CYP inhibition is a major topic in drug discovery and has been the focus of several inhibition prediction studies. While quasi-irreversible and irreversible inhibition can be predicted through SoM methods (by identifying the formation of potential RMs), reversible CYP inhibition must be treated separately. To understand the importance of reversible CYP inhibition, one can refer to the study by Vitaku *et al.*[254] that showed that 84% of FDA approved drugs contain at least one nitrogen atom, with 59% containing at least one nitrogen-containing heterocycle. Thus, there is a possibility that some of these drugs are Type II ligands that can inhibit CYPs.

Although there are several approaches reported in the literature for predicting reversible CYP inhibition, particularly based on ML algorithms,[255,256] these do not offer insight on the heme-ligand binding profiles and are not generally transferable (i.e. their quality depends on the chemical space explored for the training set). In addition to ML methods, docking has also been used to investigate reversible CYP inhibition. The main advantage of docking methods over ML methods in this particular case is the ability to visualize the interactions between the ligand and the heme, which would allow medicinal chemists to undertake any changes necessary to a potential drug to modulate its binding to CYPs. Moreover, docking allows an isoform-specific description and visualization of CYP inhibition. For example, it is known that CYP1A2, which accounts for approximately 15% of the total CYPs, preferentially oxidizes aromatic hydrocarbons and heterocyclic and aromatic amines due to its narrow active site.[243] Such information is highly useful when developing an inhibition model, since it captures essential enzymatic properties.

The key to determine heme-drug binding energy in docking is to appropriately evaluate the iron-ligand binding process (coordination). Most commonly used docking programs do not model the heme-nitrogen coordination explicitly and are thus unsuitable for predicting CYP inhibition for Type II ligands. To the best of our knowledge, EADock is the only program which has been

trained to predict heme coordination, although the accuracy of 62% (31/50 heme structures that exhibited iron-nitrogen coordination) remains low.[257] Therefore, a framework to predict iron coordination and displacement of water when localized within a heme is required (in the CYP resting state there is a water molecule that acts as a distal heme ligand). Herein we set out to develop a novel predictor of reversible CYP inhibition and implement it in the drug discovery platform FORECASTER. This tool combines accurate high-level QM calculations on model systems with the predictive power of the docking program FITTED. Moreover, to complement these tools, we sought to build an artificial neural network (ANN) capable of analyzing thousands of data points and to provide accurate predictions on whether a drug or its metabolites can be a reversible CYP inhibitor. To understand the power of this approach, a drug design and design project such as the one presented in Figure 4.3 can be undertaken completely within FORECASTER, without the need for costly HTS.

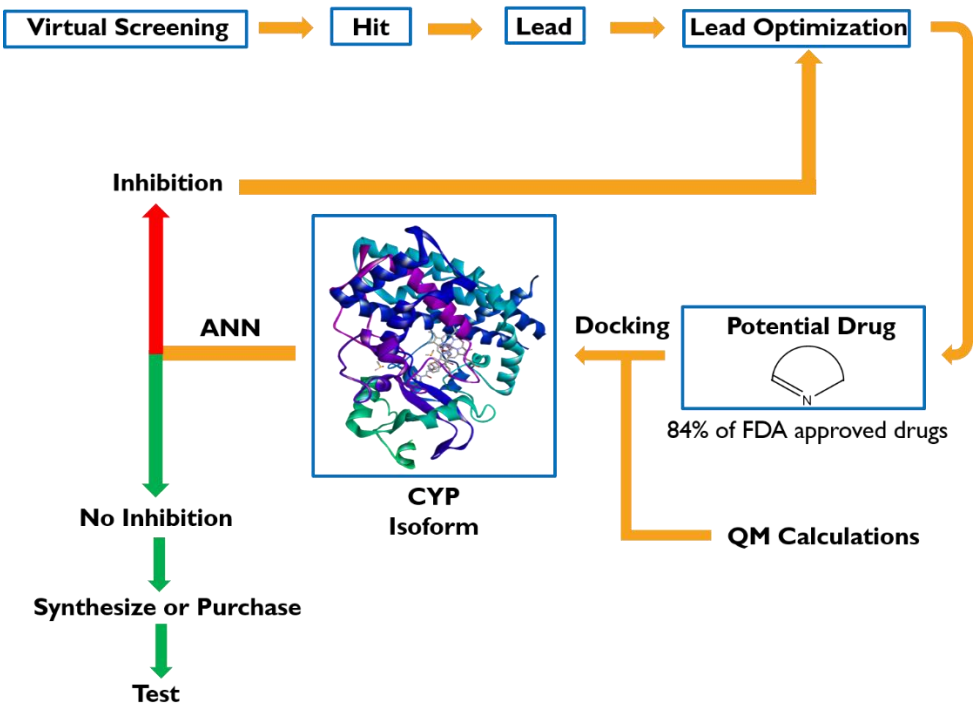

Figure 4.3. A typical drug design and development project that can be undertaken in FORECASTER.

It is important to note that the time-consuming QM calculations need only be performed once for the development of the model, which will be described in detail below. The entire *in silico* part of the workflow presented in Figure 4.3 can be resolved in a matter of weeks starting from a library of > 500,000 molecules, which could tremendously speed up the development process of a novel drug.

4.4. CYP Inhibition – Model Development – Preview.

Since the model we proposed has three distinct phases – QM calculations, docking and ANN development – we outlined the protocol required for each phase (Figure 4.4).

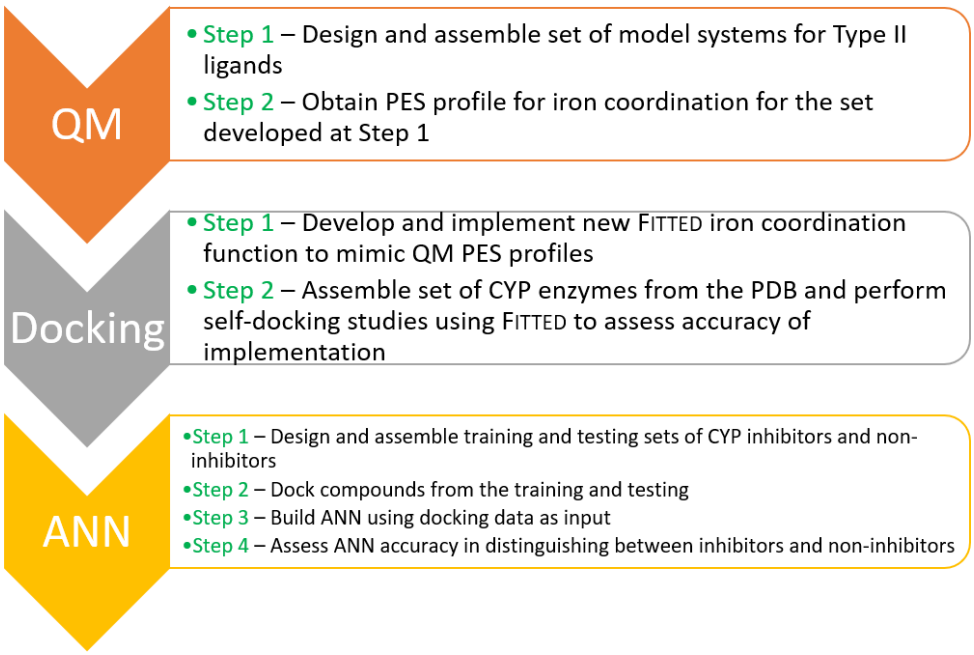

Figure 4.4. Protocol for developing a reversible CYP inhibition model to be implemented in FORECASTER.

As can be seen in Figure 4.4., each of these phases is comprised of multiple steps which must be tackled sequentially to ensure a robust model is built.

4.4.1. CYP Inhibition – Model Development – QM – Step 1.

A significant percentage of FDA approved drugs contain nitrogen heterocycles which could be capable of coordinating to the iron atom of the heme moiety. We proposed to compile a list of nitrogen heterocycles bearing various substituents and nitrogen hybridizations that cover as much of the chemical space as possible (Chart 4.1). This chart was also built based on the data we acquired from the PDB (Table 4.1) for CYP isoforms with resolution better than 2.5Å. These heterocycles represent our model systems for Type II ligands.

Chart 4.1. Set of nitrogen-containing heterocycles used as model systems for Type II ligands. The binding nitrogen atom is depicted in red.

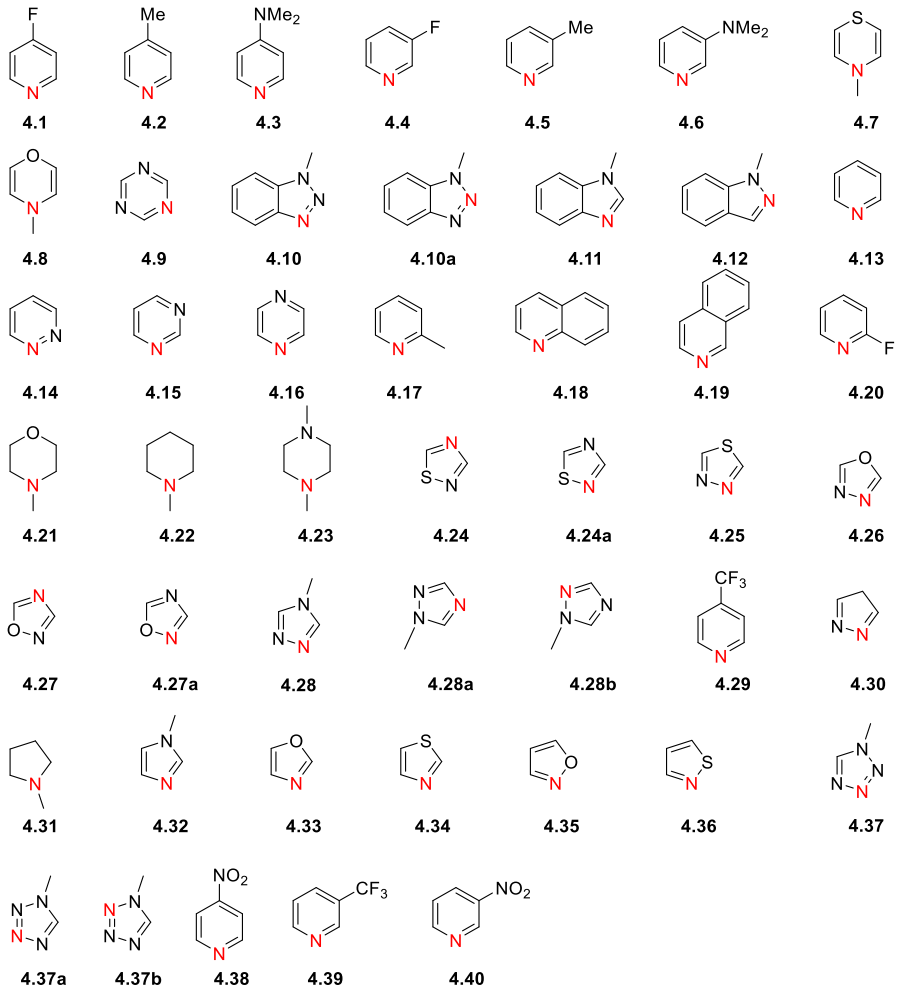

Table 4.1. Data acquired from the PDB for CYP isoforms with resolution better than 2.5Å that contain iron-coordinating nitrogen ligands.

Entry	PDB Code	Resolution	Isoform	Fe-Coordination	Nitrogen Hybridization
1	1e9x	2.10	CYP51	yes	sp^2
2	1ea1	2.21	CYP51	yes	sp^2
3	1pha	1.63	CAM	yes	sp^2
4	2fdw	2.05	2A6	yes	sp^3
5	3e6i	2.20	2E1	yes	sp^2
6	3ibd	2.00	2B6	yes	sp^2
7	3mdr	2.00	46A1	yes	sp^3
8	3mdt	2.30	46A1	yes	sp^2
9	3mdv	2.40	46A1	yes	sp^2
10	3nxu	2.00	3A4	yes	sp^2
11	3qoa	2.10	2B6	yes	sp^2
12	3r9c	2.14	164A2	yes	sp^2
13	3swz	2.40	17A1	yes	sp^2
14	3t3q	2.10	2A6	yes	sp^2
15	3t3r	2.40	2A6	yes	sp^2
16	3t3z	2.35	20	yes	sp^2
17	3tbg	2.10	2D6	yes	sp^2
18	3tjs	2.25	3A4	yes	sp^3
19	4d75	2.25	3A4	yes	sp^2
20	4eji	2.10	2A13	yes	sp^2
21	4fia	2.10	46A1	yes	sp
22	4k9w	2.40	3A4	yes	sp^2
23	4uhi	2.05	CYP51	yes	sp^2
24	4xrz	2.40	2D6	yes	sp^2
25	5ese	2.20	CYP51	yes	sp^2
26	5esf	2.25	CYP51	yes	sp^2
27	5esh	2.15	CYP51	yes	sp^2
28	5hs1	2.10	CYP51	yes	sp^2
29	5irq	2.20	17A1	yes	sp^2
30	5k7k	2.30	2C9	yes	sp^2
31	5tz1	2.00	CYP51	yes	sp^2
32	5uys	2.39	17A1	yes	sp^2
33	5vce	2.20	3A4	yes	sp^2
34	6bcz	2.23	3A4	yes	sp^2
35	6bd7	2.42	3A4	yes	sp^2
36	6bd8	2.38	3A4	yes	sp^2
37	6bdh	2.25	3A4	yes	sp^2

As can be seen in Chart 4.1, the set is comprised of a combination of five and six membered rings, both aromatic and aliphatic. In the case of six membered aromatic rings, we were interested in studying how different substituents affect the binding nitrogen reactivity, and, as such, we ensured that these rings contained both EWG and EDG in the *ortho*, *para,* and *meta* positions. In contrast, in the case of five membered aromatic rings, we wanted to study whether different heteroatoms in the heterocycle would enhance or decrease nitrogen binding to iron and so we looked into various combinations of heterocycles containing two, three or four heteroatoms.

4.4.2. CYP Inhibition – Model Development – QM – Step 2.

Because the iron-nitrogen coordination process is highly dynamic and requires consideration from both steric and electronic effects, we decided to capture the energetics of this process using QM calculations. Several aspects were considered before the start of the PES calculations for the ligands in Chart 4.1 and are outlined further. **a)** Since docking is a static process and the mobility of the heme moiety cannot be modeled with FITTED, we decided to undertake all our QM calculations with a pre-optimized truncated heme moiety that would not be further optimized during the iron-nitrogen coordination process of the ligands in Chart 4.1. The carboxylic acid, methyl, and terminal ethylene chains were removed to reduce computational cost. This approach eliminates heme mobility as a variable from developing a new MM potential for the iron-nitrogen coordination process. **b)** To obtain an optimized heme structure that was suitable for the coordination process of all ligands in Chart 4.1, we used the most sterically hindered ligand (**4.18**, Chart 4.1) in the optimization process. This ensures that the heme structure used during the iron-nitrogen coordination process of the ligands in Chart 4.1 sterically allows all ligands to bind. The optimized heme structure used in all PES calculations is shown in Figure 4.5. **c)** To determine what level of theory was suited for the PES calculations, we used compound **4.14** as a benchmark

ligand. For this purpose, we tested several methods (see section 4.6 for full description of methodology) and we observed that a PBE0(D3BJ)/def2-SVP/ LANLDZ(Fe) level of theory offered the most accurate and cost-efficient approach.[258] **d)** Once steps **a-c)** were completed, we investigated the computational conditions necessary for obtaining relevant PESs for the iron-nitrogen binding process. Since we were interested in the formation of the iron-nitrogen bond, we decided to perform unidimensional PES scans where the coordinate used in the scan was the iron-nitrogen bond distance. The distance was varied from 10Å – where there is no interaction (or very little) between the ligand and heme – to 1.6Å – where there is a repulsion between the iron and nitrogen – in increments of 0.2Å, thus obtaining 43 unique structures across the PES. At every point on the PES, the ligand was optimized while the heme was kept frozen at the pre-optimized geometry.

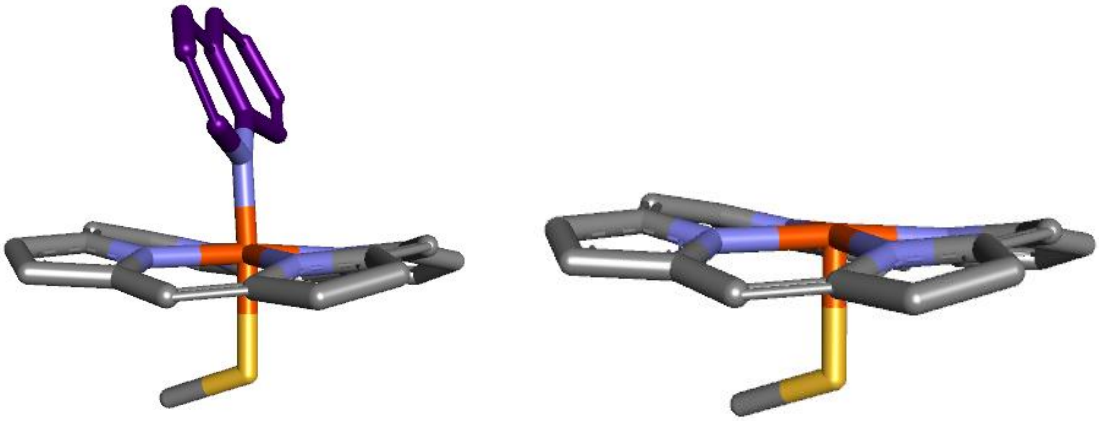

Figure 4.5. Left) Optimized heme-**4.18** complex**.** Ligand carbons shown in purple. **Right)** Optimized truncated heme moiety used in obtaining the PES scans. Hydrogens omitted for clarity. Cysteine residue is represented by -S-Me. Iron atom is shown in orange.

For each of the ligands presented in Chart 4.1 the protocol described at point **d)** was carried out. As an example, the full PES scan of ligand **4.1** is presented in Figure 4.6 along with snapshots of the binding process at 10.0 (no interaction), 2.0 (minimum) and 1.6Å (repulsion) (purple dots). The PES scans of the other ligands in Chart 4.1 are given in Appendix C.

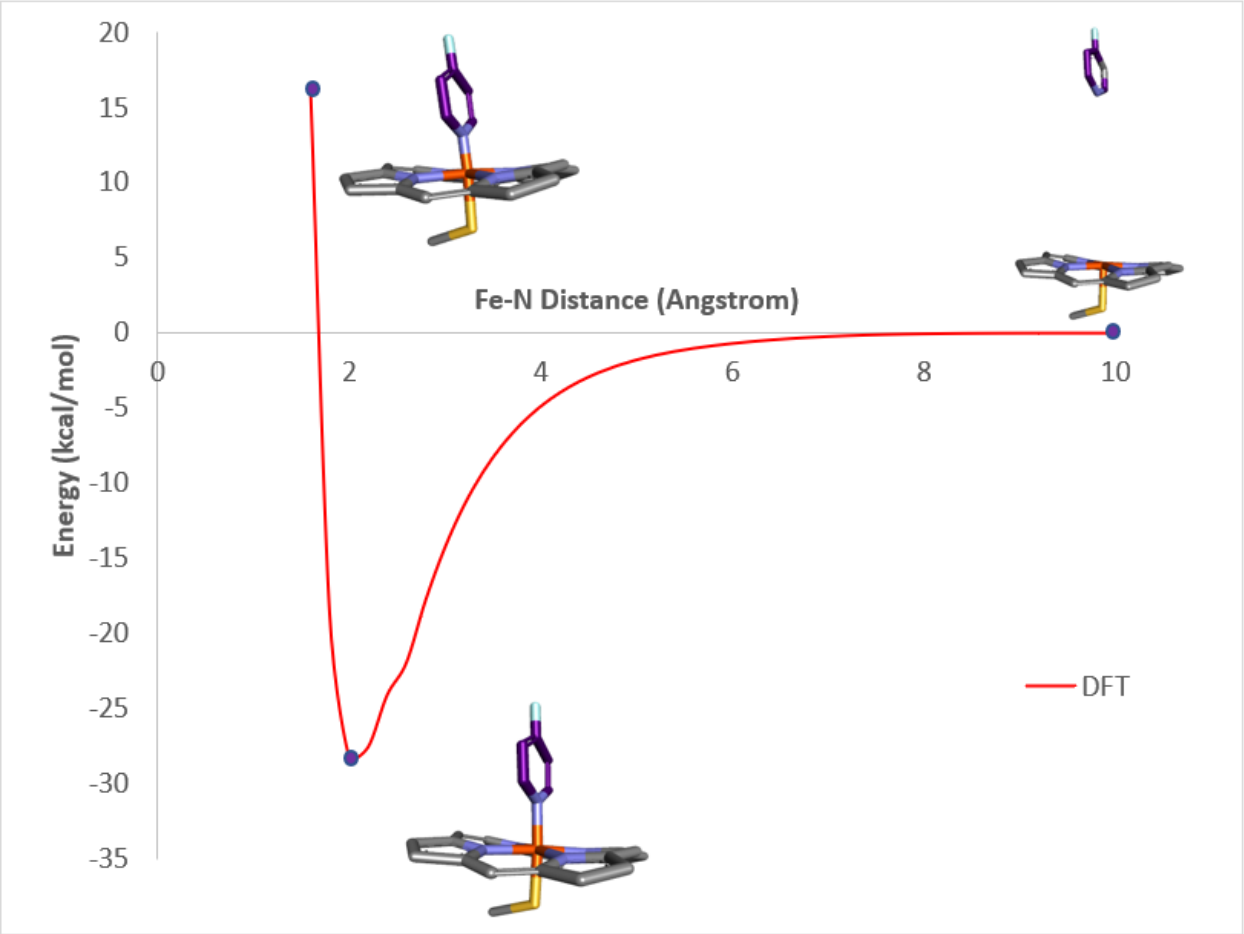

Figure 4.6. PES scan showing the binding process of ligand **4.1** to heme. Snapshots are given at an iron-nitrogen distance of 10.0, 2.0 and 1.6Å. Ligand carbons are colored in purple. Hydrogens omitted for clarity.

Importantly, the PES scans revealed that for compounds **4.7**, **4.8** and **4.30** the binding process is unfavorable. In all three cases, the binding process led to highly distorted ligand structures, which

contributed to the instability of the final complex. These compounds were not considered in the development of the new MM potential.

4.4.3. CYP Inhibition – Model Development – Docking – Step 1.

With the QM data in hand, we thought to develop a new MM potential to be implemented in FITTED. Since van der Waals (vdW) interactions are described in FITTED using a Lennard-Jones 12-6 (LJ(12-6)) potential (see Equation 1.8), the first step was to obtain the FITTED energy profile for the same 43 unique structures used in section 4.4.2. An overlay of the energy profiles obtained with QM and FITTED for compound **4.1** is given in Figure 4.7 (orange curve).

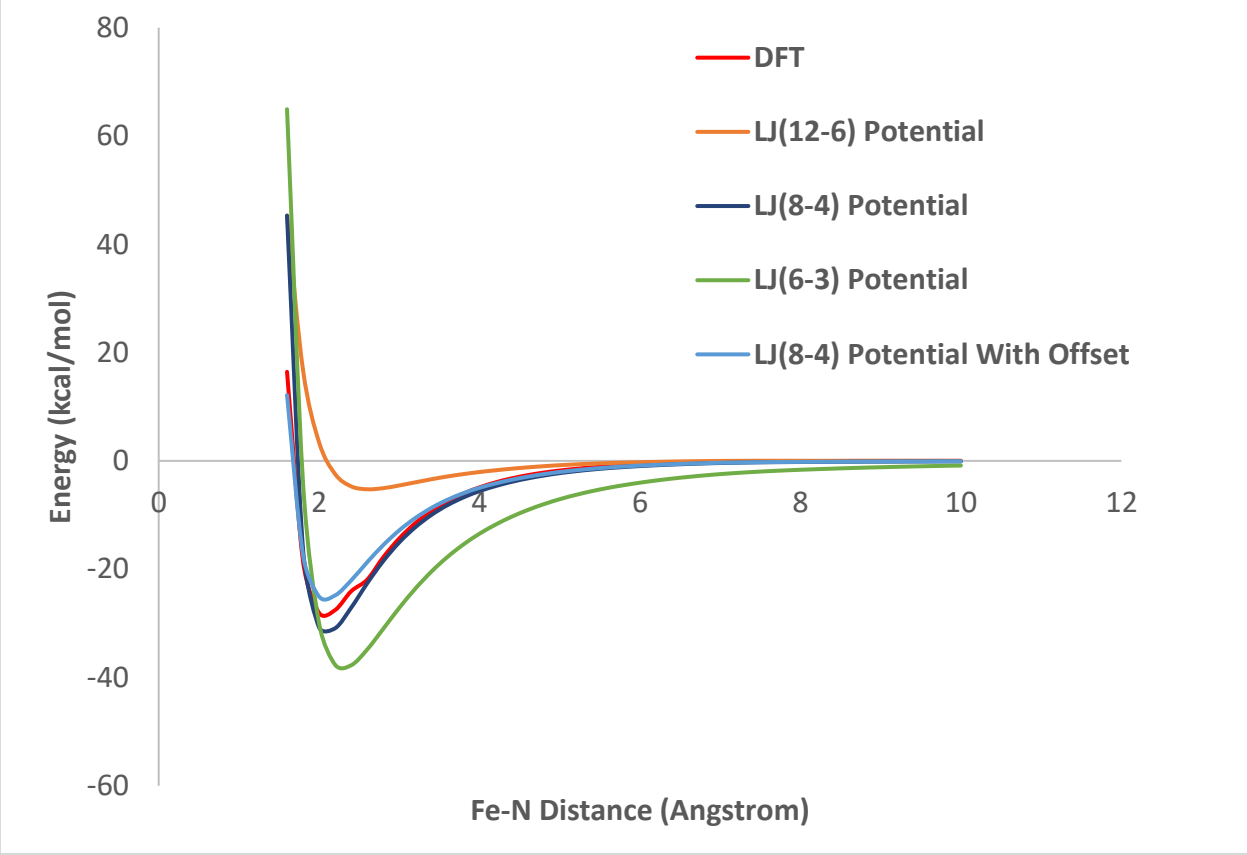

Figure 4.7. Overlay of QM and FITTED energy profiles obtained for compound **4.1**.

As can be seen in Figure 4.7, the LJ(12-6) potential is unable to describe the iron-nitrogen coordination process. As such, the development of a new LJ potential, similar to the one we had

previously developed for zinc coordination, was necessary. In this context we decided to verify whether two of the most commonly used LJ potentials (8-4 and 6-3, Equations 4.1 and 4.2) could be able to describe this process better than the LJ(12-6) potential. As can be seen in Figure 4.7, the LJ(6-3) potential (green curve) describes an energy minimum (~ 37 kcal/mol) that is too low in energy compared to the QM minimum (~ 28 kcal/mol). Moreover, the iron-nitrogen distance at which this minimum occurs is offset by 0.4Å when compared to the QM minimum (2.4Å vs 2Å).

$$E_{vdW(8-4)} = \sum_{pairs\ i,j} \varepsilon_{ij} \left[\left(\frac{R_{min,ij}}{r_{ij}} \right)^8 - \left(\frac{R_{min,ij}}{r_{ij}} \right)^4 \right] \qquad \text{Eq. (4.1)}$$

$$E_{vdW(6-3)} = \sum_{pairs\ i,j} \varepsilon_{ij} \left[\left(\frac{R_{min,ij}}{r_{ij}} \right)^6 - \left(\frac{R_{min,ij}}{r_{ij}} \right)^3 \right] \qquad \text{Eq. (4.2)}$$

Equations 4.1-4.2. LJ(8-4) and LJ(6-3) potentials for computing vdW interactions.

In contrast, the energy minimum (~ 31 kcal/mol) described by the LJ(8-4) potential is very close in energy to the QM one. However, the minimum described by the LJ(8-4) potential was also offset by 0.2Å when compared to the QM minimum (2.2Å vs 2Å). To verify whether incorporating the offset in the computation of the LJ(8-4) potential would improve the energy profile described by FITTED, we plotted the potential containing the offset in Figure 4.7. Interestingly, this led to an excellent overlap between the QM and FITTED energy profiles, with an overall MAE of 0.63 kcal/mol between the two curves. The necessity of using an offset was not a singular occurrence; in all cases, we observed that the LJ(8-4) potential required the inclusion of this offset to properly described the binding process. This led to the implementation of the modified potential shown in Equation 4.3 into FITTED for describing the iron-nitrogen binding process. Importantly, the overall

MAE across all compounds used in the development of the new potential is 0.66 kcal/mol, which suggests that FITTED would now be capable to describe the iron-nitrogen binding process with QM precision at an MM cost.

$$E_{vdW(8-4)-FITTED} = \frac{4\varepsilon\sigma^8}{(r-0.2)^8} - \frac{4\varepsilon\sigma^4}{(r-0.2)^4} \qquad \text{Eq. (4.3)}$$

Equation 4.3. Modified LJ(8-4) potential implemented in FITTED. ε – energy minimum obtained after subtracting the original FITTED profile from the QM profile. σ – distance (in Å) at which there is repulsion between the iron and nitrogen (in all cases σ = 1.6Å).

4.4.4. CYP Inhibition – Model Development – Docking – Step 2.

In FITTED, users can select two different docking modes depending on the nature of the protein (normal protein or metalloprotein).[259] Depending on the mode of choice, FITTED uses different conditions for preparing and processing the crystal structures for docking, as well as for performing docking (different scaling terms for non-covalent interactions, including different LJ potentials for vdW interactions). Thus, the new LJ(8-4) potential was implemented only in the metalloprotein mode of FITTED. Afterwards, we assembled a representative set of CYP-ligand complexes from the PDB in order to perform a self-docking study for both protein and metalloprotein docking modes. This set is comprised of 85 diverse crystal structures (see Appendix C for full list), with and without iron-coordinating nitrogen ligands. Briefly, self-docking assesses the ability of a docking program to dock a ligand extracted from a crystal structure to that same crystal structure and compare the RMSD between the docked pose and original crystal structure. Generally, an RMSD less than 2.0Å between the predicted and crystal structure is considered to be adequate.

The results of the self-docking study in both docking modes are given in Figure 4.8. Interestingly, when using the 2.0Å threshold for success of self-docking, there is a minimal difference between the docking modes (63.5 vs. 61.2% accuracy). This seems surprising, considering that the original LJ (12-6) did not properly describe the iron-nitrogen coordination process. However, before any conclusions can be made about the difference in accuracy between the two docking modes, we must take a closer look at the failures and differences in results and best binding poses between the two.

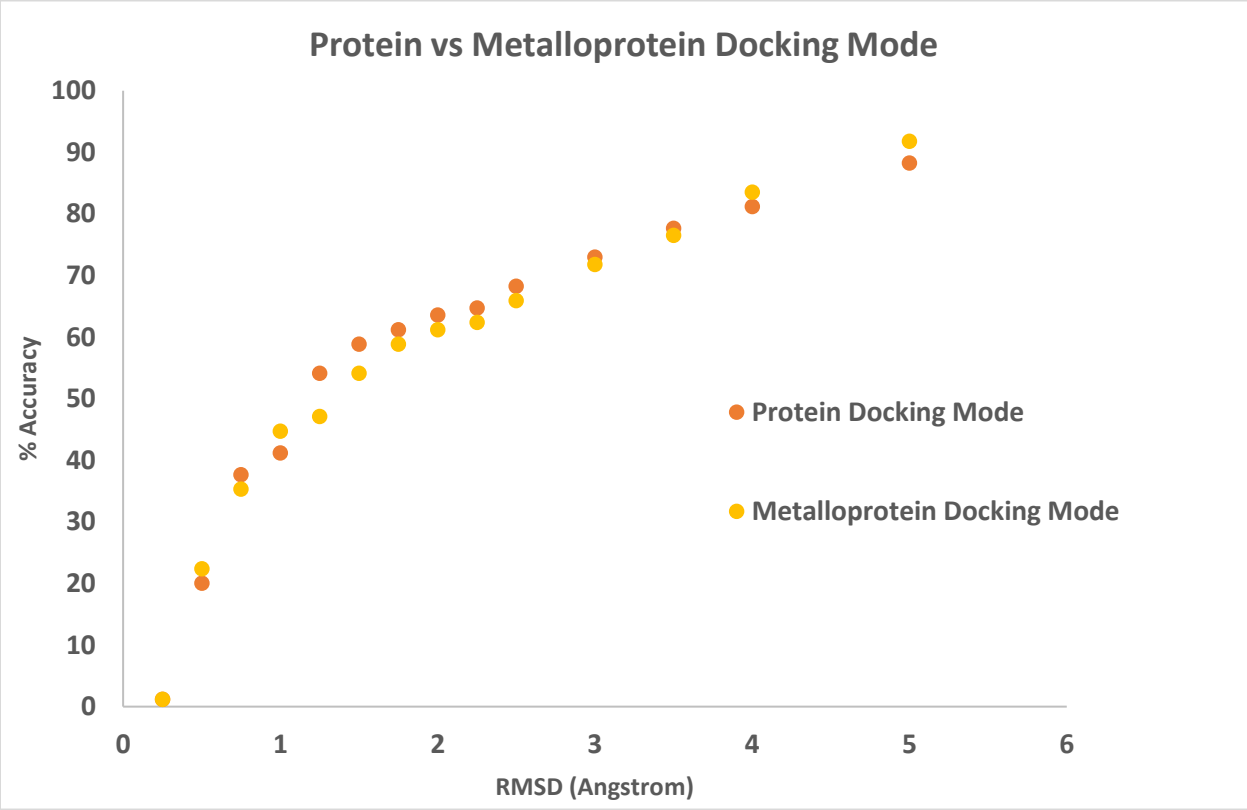

Figure 4.8. % accuracy of protein vs. metalloprotein mode in the self-docking of heme proteins.

One of the most striking differences in results is for the crystal structure with PDB id 3CZH (CYP2R1 in complex with Vitamin D2, non-iron coordinating ligand). In the case of the protein mode, the RMSD was 0.54Å, while for the metalloprotein mode it was 9.45Å (Figure 4.9). As can be seen in Figure 4.9, vitamin D2 is a large ligand that spans a significant portion of CYP2R1's active site. However, although large, vitamin D2 is rigid, containing only 5 rotatable bonds. This in turn should allow docking to perform well, as evident from the protein mode RMSD. One possible explanation for the inability of the metalloprotein mode to obtain a better RMSD lies in the stochastic nature of the docking process. FITTED relies on a genetic algorithm where, at the beginning of the docking process, an initial population of 100 conformations is generated randomly. If the ligand is large and/or flexible, then the number of initial conformations should be increased to explore the conformational space thoroughly. If the number of initial conformations is too small, then it is likely that a suitable conformation is not found. However, in the interest of speed vs. accuracy, as well as to be consistent with our previous self-docking studies, we decided to use 100 initial conformations for all the crystal structures assembled for this self-docking study, irrespective of the ligand size.

Another example in which the protein (RMSD = 6.30Å) and metalloprotein (RMSD = 0.69Å) modes differ significantly is in the case of the crystal structure with the PDB id 4EJI (CYP2A13 in complex with an iron-coordinating nitrogen ligand – Figure 4.10). While in the protein mode the best docked pose suggests the nitroso group to be close to the iron, in the metalloprotein mode the pyridine nitrogen is correctly bound to the iron. Importantly, the N-Fe bond length in the crystal ligand is 2.05Å, while the bond length in the best docked pose in metalloprotein mode is 2.07Å, suggesting that the new LJ(8-4) potential can properly describe iron-nitrogen coordination.

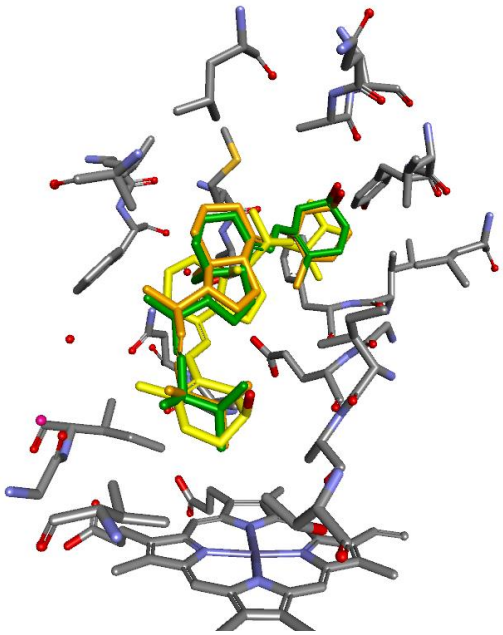

Figure 4.9. Self-docking results for 3CZH – active site snapshot. Green – crystal ligand; Orange – protein mode; Yellow – metalloprotein mode. Oxygen atom in ligands are colored red.

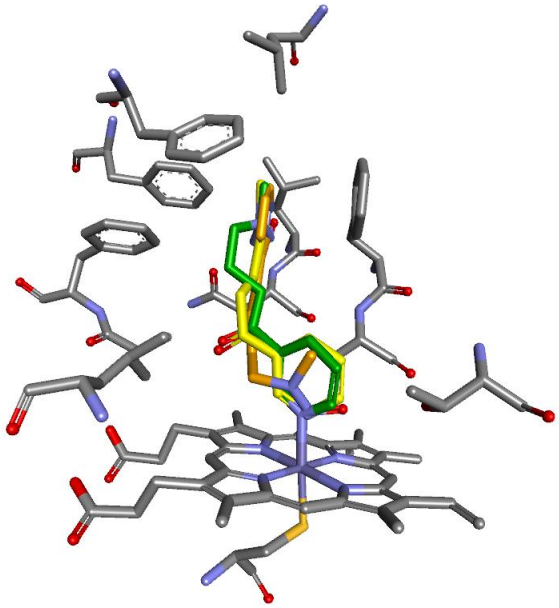

Figure 4.10. Self-docking results for 4EJI – active site snapshot. Green – crystal ligand; Orange – protein mode; Yellow – metalloprotein mode. In the ligands, nitrogen atoms are colored in blue, while oxygen atoms are colored in red.

Overall, as can be seen in Table 4.2, there are 37 instances (43.5%) in which the protein mode shows a lower RMSD than metalloprotein mode, while there are 48 instances (56.5%) in which the metalloprotein mode shows a lower RMSD than the protein mode. Moreover, in 91.8% of the cases the metalloprotein mode provides an RMSD < 5.0Å, while the protein mode can provide an RMSD < 5.0Å in 88.2% of the cases. When considering only the cases in which ligands are coordinating to the iron (50/85), the protein mode shows a lower RMSD than metalloprotein mode in 21 instances (42%), while metalloprotein produces a lower RMSD in 29 instances (58%). Out of the 29 instances when metalloprotein mode has a lower RMSD than protein mode, 20 (69%) have an RMSD < 2.0Å, while 15/21 (71.4%) are below 2.0Å in the cases protein mode provides a lower RMSD than metalloprotein mode. The detailed RMSD data from this study is provided in Appendix C.

Table 4.2. Statistics from self-docking study.

Condition	% Accuracy (Total) n=85	% Accuracy (sp^2) n=50
RMSD (Protein) < 5.0Å	88.2	86.0
RMSD (Metallo) < 5.0Å	91.8	92.0
RMSD (Protein) < 2.0Å	63.5	68.0
RMSD (Metallo) < 2.0Å	61.2	68.0
RMSD (Protein) < RMSD (Metallo)	43.5	42.0
RMSD (Metallo) < RMSD (Protein)	56.5	58.0
RMSD (Protein) < RMSD (Metallo) and RMSD (Protein) < 2.0Å	67.6	71.4
RMSD (Metallo) < RMSD (Protein) and RMSD (Metallo) < 2.0Å	63.8	69.0

The data in Table 4.2 suggests that the novel LJ(8-4) implementation provides an improvement for the metalloprotein docking mode compared to the protein docking mode. However, further optimization is necessary to improve the overall self-docking accuracy and a larger, more diverse set is needed to draw statistically relevant conclusions. Some avenues that

could be pursued include the development of optimized heme force field parameters, along with optimized scaling factors for non-covalent interactions specifically designed for heme proteins.

4.4.5. CYP Inhibition – Model Development – ANN – Steps 1 and 2.

As discussed in Chapter 1 and in one of our recently published reviews,[27] an ANN is only as good as the data used to train it. For CYP inhibition, this is especially true. It is important to mention that there are several types of assays used to determine CYP inhibition, including luciferase-based assays[260] or LC/MS/MS-based assays[261] to determine whether a compound inhibits a specific CYP. One important characteristic of these assays is that they indiscriminately detect inhibition, whether it is reversible or irreversible. These assays also measure different parameters such as AC_{50} (half maximal activity) or IC_{50} (half maximal inhibitory concentration) and have different thresholds for inhibition. Thus, it is paramount to account for different assays when assembling a training and testing set for determining the accuracy of an ANN. If possible, the set should contain thousands of data points (both inhibitors and non-inhibitors) and be built using data obtained with the same type of assay. Ideally, this data should be obtained from one source, since this would ensure that the data was gathered in the same manner and the systematic errors would be consistent throughout the assay.

To this end, we built a relevant set of CYP inhibitors that could be used as training and testing sets for our ANN. Following our literature search, we selected the AID-1851 CYP450 panel bioassay published on PubChem by the National Center for Advancing Translational Sciences as the source of our set.[262] This is a luciferase-based assay that determines the AC_{50} of ~17000 compounds in five major CYP isoforms: CYP1A2, 2C9, 2C19, 2D6, and 3A4. Briefly, the assay measures the dealkylation of various pro-luciferin substrates to luciferin, which is then measured using luminescence after a luciferase detecting agent has been added. Inhibitors limit the

production of luciferin and decrease the measured luminescence. According to the assay, compounds with AC_{50} equal or less than 10 μM are considered active.

As it is the case with most publicly available datasets, we had to curate it to obtain a usable set of drug-like compounds. Briefly, we initially filtered the 17000 compounds for atoms commonly found in drugs (C, N, H, O, F, Br, Cl, I, Si, S, P) and then subjected the set to filtering based on Lipinski's rule of 5 (molecular weight < 500 Da, hydrogen bond acceptors < 10, hydrogen bond donors < 5 and a logP < 5). Then, we split the full set into two subsets for each isoform comprising active and inactive compounds. The final number of compounds per set per isoform is given in Table 4.3.

Table 4.3. Breakdown of sets per isoform.

Isoform	Activity	Number of Compounds	Number of compounds containing a nitrogen atom capable of coordinating to the heme iron
1A2	active	4453	3330
	inactive	6132	2835
2C9	active	2708	1764
	inactive	7823	4333
2C19	active	4111	2526
	inactive	6580	3535
2D6	active	1905	934
	inactive	9953	5862
3A4	active	3118	2182
	inactive	6932	3657

For all isoforms, the active and inactive sets were then converted from 2D to 3D using our program CONVERT and prepared for docking using SMART. SMART is also capable of assigning atomic and molecular descriptors to compounds, including molecular weight, number of hydrogen bond donor and acceptors, number of rings and stereocenters, logP (a measure of hydrophobicity), logS (a measure of solubility in water), topological polar surface area, and number of heteroatoms (N, O and S). We believed that these descriptors could be as important as the docking data since

they provide essential information about the compounds. As such, after the docking process was complete, for each active and inactive a detailed breakdown of various energy terms from the best docking run (vdW, electrostatic, hydrogen bond energy etc.) and a breakdown of descriptors was output to be further used in the development of the ANN.

4.4.6. CYP Inhibition – Model Development – ANN – Step 3.

There are many flavors of ANNs available in the literature. Amongst these, one of the most common ones is the supervised ANN using a "back-propagation" algorithm.[263] Developed in 1986 by Rumelhart, Hinton, and Williams,[264] back-propagation quickly became the algorithm of choice for ANNs developed in chemistry.

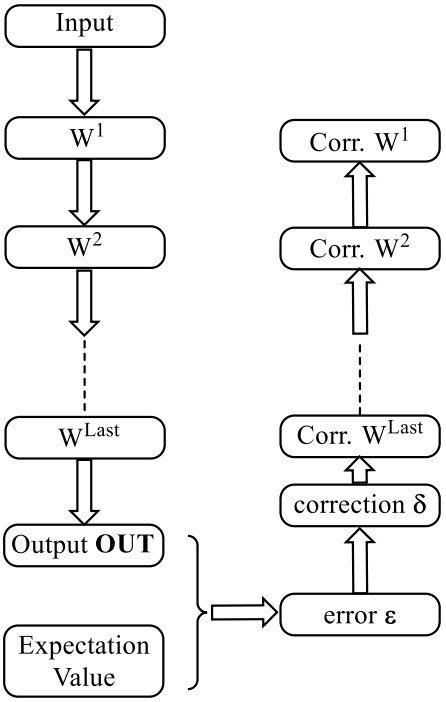

Figure 4.11. A schematic depiction of the back-propagation algorithm. Reproduced from reference 263.

Briefly, as depicted in Figure 4.11, the input data is delivered through the layers of neurons. If an ANN has multiple layers, the output data from layer **n** becomes the input data for layer **n+1**.

The main goal of such an ANN is for predictive output data to be delivered by the final layer. However, in the case of back-propagation, this is not the case in the beginning. The final layer will predict output data, which will then be compared to an expected value, which is known beforehand (experimental data coming with the dataset). The next step involves computing the error between the expected and output values by the final layer, which is then used to correct the data from the final layer using a conjugate gradient method. Subsequently, the weights from the penultimate layer are corrected with respect to the final layer. This process occurs layer by layer until the input layer is reached. Thus, the error is propagated backwards from bottom to top and is used to correct the weights in each layer. The main goal of this algorithm is to minimize the error in the output layer.

We believed that an ANN using a back-propagation algorithm was robust for our needs, and thus we implemented it in our drug discovery platform FORECASTER and connected it to our docking program FITTED. To remove the need for manual intervention in building the training and testing sets, we decided to automate this aspect as well (although the user can still select the training:testing set ratio). Afterwards, we opted for a single hidden layer, which would take as input both the docking and ligand data obtained in section 4.4.6. After building the ANN, we set out to identify the most appropriate descriptors for evaluating CYP inhibition and we found that out of 25 distinct descriptors a combination of docking-based energy values (vdW, electrostatic, hydrogen bond energy, metal coordination, Score and MatchScore) and ligand-based descriptors (number of rotatable bonds, net charge, number of hydrogen bond donors and acceptors) was optimal. The Score output by FITTED after docking describes how favorable the electronic interactions a ligand makes with the amino acids in the active site are, while MatchScore describes

how well a ligand fits inside the active site of an enzyme.[265,266] Once these tasks were completed, we proceeded to assess the accuracy of our ANN in distinguishing inhibitors vs non-inhibitors.

4.4.7. CYP Inhibition – Model Development – ANN – Step 4.

Several aspects must be accounted for when training a ANN. First, the accuracies of both the training and testing sets must be compared to ensure overfitting did not occur. Second, important insight into the behaviour of the ANN can be obtained if one computes the specificity and sensitivity, along with the positive and negative predicted values (PPV and NPV). The specificity of an ANN in the context of CYP inhibition describes the proportion of molecules predicted to be inactive among those that are experimentally inactive, while the sensitivity describes the proportion of molecules predicted to be active among those that are experimentally active. The PPV describes the probability that a predicted active is experimentally active while the NPV describes the probability that a predicted inactive is experimentally inactive. In our case, we computed all these parameters for each specific isoform (Table 4.4).

Table 4.4. ANN results.

CYP	Accuracy	Sensitivity	Specificity	PPV	NPV
1A2	94.6	91.1	97.2	95.9	93.8
	80.6	75.1	84.7	78.2	82.3
2D6	89.3	36.0	99.5	93.7	89.0
	85.1	27.4	96.2	57.8	87.4
2C9	93.5	76.9	99.3	97.3	92.6
	79.9	49.4	90.5	64.3	83.8
2C19	89.3	79.8	95.2	91.2	88.3
	78.3	65.9	86.0	74.8	80.1
3A4	91.6	76.7	97.1	90.8	91.9
	80.2	54.4	89.8	66.3	84.2

As can be seen in Table 4.4, the accuracy of the ANN for the training set is excellent. However, the accuracy of the testing set is lower in all cases, indicating that overtraining has

occurred. Moreover, in the case of CYP 2D6, our ANN performs poorly in terms of sensitivity in both the training and testing set cases. The same holds true for 2C9 and 3A4 in the case of the testing sets. It is clear from these results that more work is needed to improve the ANN and to avoid overfitting. To put the results in Table 4.5 in context, we have assembled data from three different publications that use the same bioassay to develop machine learning methods that discriminate between inhibitors and non-inhibitors. These results are given in Table 4.6 and show that throughout the literature the problem of overfitting seems apparent. Nonetheless, the foundation of our unique docking-ligand-ML approach to discriminate between inhibitors vs. non-inhibitors is laid, and further improvements are expected in the future.

Table 4.5. Comparison of our ANN with literature. Accuracies are given for testing and (training) sets.

Reference	1A2	2C9	2C19	2D6	3A4
Sun *et al.*[267]	0.79 (0.93)	0.77 (0.89)	0.86 (0.89)	0.90 (0.85)	0.73 (0.87)
Cheng *et al.*[268]	0.73	0.87	0.81	0.88	0.76
Li *et al.*[269]	0.97 (0.89)	0.86 (0.86)	0.81 (0.84)	0.89 (0.88)	0.89 (0.85)
Our ANN	0.81 (0.95)	0.80 (0.94)	0.78 (0.89)	0.85 (0.89)	0.80 (0.92)

4.5. SoM Prediction – IMPACTS 2.0 – Background.

For many years, we have been developing accurate software for drug discovery and development. For instance, in 2012, we developed IMPACTS, a tool outperforming experts in the prediction of SoM of xenobiotics by CYPs.[248] IMPACTS was developed based on the understanding of the CYP-mediated drug metabolism mechanism. Briefly, IMPACTS, is a hybrid method based on both ligand docking and ligand activation energies. Prior to docking of a drug-like molecule, the atoms that could potentially constitute SoMs are assigned pre-computed activation energies, obtained following the reaction of a set of representative fragments with the active CYP450 species

responsible for oxidation. Then, IMPACTS docks the molecule using routines derived from our in-house docking program FITTED, creates the likely transition states, and uses the collected information to decide which SoM will be preferred (Figure 4.13). The original version of IMPACTS showed an accuracy of 77% across 4 isoforms (CYP1A2, 2C9, 2D6 and 3A4).

With the implementation of our CYP inhibition prediction tool into FORECASTER and expansion of our drug metabolism-related predictive software, we sought to revisit IMPACTS through a fresh look at CYP-mediated drug metabolism mechanism in hopes of improving its accuracy.

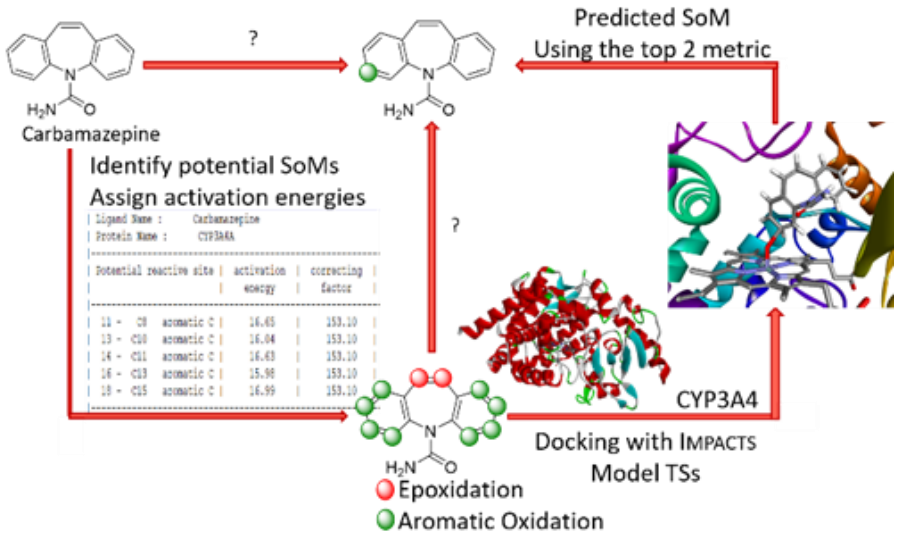

Figure 4.12. Automated IMPACTS protocol.

4.5.1. SoM Prediction – Improving IMPACTS – Approach.

As with many enzymatic reactions, the rate of CYP oxidation is driven by **1)** stabilization of the transition state by the enzyme, **2)** proper positioning of the reacting partners, **3)** substrate reactivity, and **4)** modified kinetics (e.g. first order in enzyme, second order in solution) of the chemical process. To tackle this problem, the original version of IMPACTS was modeling the transition state **(#1)** of the substrate enzyme complex using routines from our docking program

FITTED **(#1** and **#2)** considering the reactivity of each potential reactive SoMs of the substrate from DFT calculations of fragments **(#3)** and assuming similar effect of the kinetics on every substrate **(#4)**. While all these factors were considered, we believed that there was space for improvement. Over the years, we have found that water molecules and protein flexibility could be critical for optimal binding mode prediction. We are also aware of the impact of the basis set and functionals in DFT calculation on the accuracy of the resulting predictions. At this stage, our research focused on the following factors: **1)** an improved docking program (FITTED's accuracy has improved throughout the years) including a more accurate consideration of protein flexibility, **2)** higher-level calculations of fragment energy of activation, and **3)** additional consideration of steric effects.

The first step of our study consisted in assessing the accuracy of the current version of IMPACTS on the training set used in 2012. The accuracy values presented throughout this chapter are average values obtained over five different runs to ensure reproducibility (including standard deviations). The detailed data obtained from these runs can be accessed in Appendix C. As can be seen in Figure 4.13, the overall accuracy of IMPACTS has not changed significantly (within 2% overall). This small variation in accuracy can be attributed to significant changes made to the way molecules are prepared for docking (correctly treating aromaticity in molecules, proper resonance structure attribution and improved charging scheme) as well as to the docking process itself (improved convergence parameters and the nature of the stochastic process of docking). Moreover, we checked whether reducing the number of available SoM's prior to docking would improve the accuracy of IMPACTS. As such, we allowed only the top 5 activation energies to be considered in the docking process. However, this adjustment did not change the accuracy dramatically (Figure 4.13).

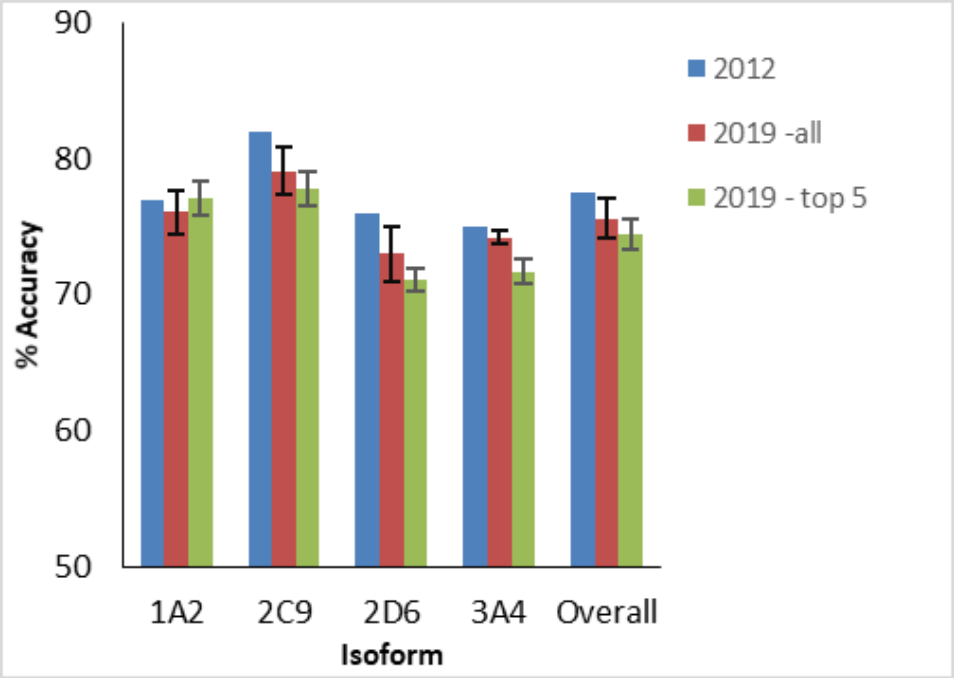

Figure 4.13. Accuracy using the current version of IMPACTS compared to the one determined in 2012.

With these results in hand, we investigated the different aspects presented in our approach to see whether IMPACTS could be improved.

4.5.2. SoM Prediction – Improving IMPACTS – Ligand Reactivity.

In the past few decades, several developments have been made in the field of chemical reactivity. Amongst these are chemical reactivity descriptors – computed values that can be used to determine whether a molecule or an atom in a molecule is reactive.[270] Molecular reactivity descriptors offer information across an entire molecule (i.e. chemical softness, hardness etc.) but provide no usable information about local sites of reactivity. For example, the HSAB theory developed by Pearson states that a hard molecule will preferentially react with a hard molecule as opposed to a soft one.[117] In contrast, LARIs have been developed to account for reactivity of individual atoms. Amongst these are the Fukui coefficients developed in the context of frontier molecular orbital (FMO) theory. These coefficients offer information about nucleophilic,

electrophilic, and radical attacks and have been discussed in Chapter 1 and thoroughly throughout the literature. To help with our efforts in the field of drug discovery, we implemented FCs as well as other LARIs and molecular properties (global hardness, softness, nucleophilicity, electrophilicity etc.) in the context of both HF and DFT in our QM program QUEMIST (for a detailed description of the development and implementation of QUEMIST see Chapter 5).

Since the CYP oxidation mechanism proceeds through radical attack on the SoM, we investigated whether FCs could be used in conjunction with or as a substitution to our activation energies to provide a more accurate description of the radical attack on potential SoMs. Preliminary results showed that computationally demanding atom-condensed FCs from Hirshfeld atomic charges can increase the accuracy of IMPACTS by no more than 2% overall.[271] In addition, a major drawback of this approach is that it requires three separate QM single point energy calculations for the neutral, anionic, and cationic molecules to obtain the FCs. Moreover, these coefficients showed a high dependence on the type of atomic charges used (i.e. Mulliken, Hirshfeld etc.). To offset these drawbacks and to reduce the computational cost associated with computing FCs, we turned our attention to a method that allows the quantification of atom-condensed FCs directly from only one QM energy calculation performed on the neutral molecule.[272,273] The QM information (molecular orbitals, orbital energies and overlap matrix) is easily obtained using QUEMIST. The FC's are then normalized in the 0-100 range and used automatically within IMPACTS itself. A comparison between the accuracies obtained in 2012 and 2019 (with and without FCs) is given in Figure 4.14.

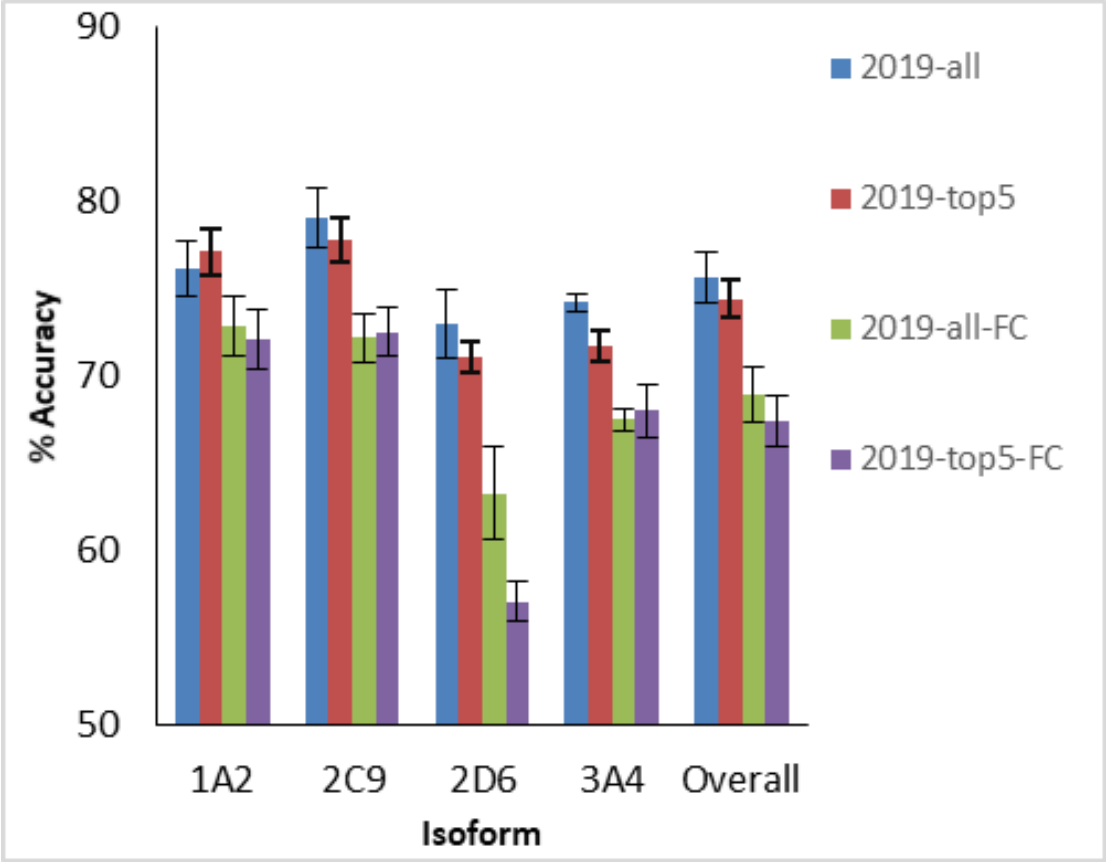

Figure 4.14. Accuracy using the current version of IMPACTS with and without FCs.

As can be seen in Figure 4.14, the usage of FCs (computed at the HF/def2-SVP level of theory) did not provide the expected accuracy improvement for IMPACTS. A detailed analysis of the results shows that across all sets the FCs have the highest values on aromatic carbons, which is consistent with aromatic rings being electron rich. However, this disfavors potential SoMs represented by sp^3 carbons, which generally have a low FC. This fact is particularly evident for the 2D6 set, which exhibits a high decrease in accuracy due to 72% of SoMs being comprised of sp^3 carbons.

4.5.3. SoM Prediction – Improving IMPACTS – New Activation Energies.

After assessing the usage of FCs in the prediction of SoMs, we posited that the approach developed in 2012 to assign activation energies could be improved. As such, we embarked on a

journey similar to that expanded in SMARTCyp 3.0[274] and decided to improve the assignment of activation energies through the following protocol:

1. Survey the literature and collect fragments of interest found in drug molecules (i.e. styrene, thiophene etc.)

2. Design and implement a fragment-matching algorithm that could efficiently identify fragments of interest in any given drug molecule.

3. For the fragments of interest – obtain TSs at the ωB97X-D3//def2-SVP (geometrical counterpoise correction - gCP)/def2-SVP (zero-point energy - ZPE) for the reactive atoms using a methoxy radical model.

4. Assign activation energies during IMPACTS based on the fragment-search protocol. If the fragment is not found, the activation energy is assigned based on the old protocol. Our approach led to a set of 156 fragments and over 450 TSs (e.g. *o,m,p*-substituted aryl fragments were counted as separate TSs). For the QM calculations, our choice of ωB97X-D3//def2-SVP(gCP)/def2-SVP(ZPE) level of theory was based on functional quality, speed, and accuracy,[275] while the choice of methoxy radical was based on our previous work and that of others.[248,276] While we expected comparable accuracies to the original activation energies, we were surprised to see a major drop in accuracy (almost 13% overall), especially for 2D6 (Table 4.6). We attributed this to the relatively small basis set we used to compute the energies, as well as to the fact that due to the vastness of the chemical space we probably did not cover enough fragments to assign them properly.

Table 4.6. Accuracy of IMPACTS when using the new activation energies.

Isoform	Run 1	Run 2	Run 3	Run 4	Run 5	Overall Accuracy	Std. Dev.
1A2	66.4	68.6	69.3	68.6	65.0	67.6	1.6
2C9	70.5	69.0	67.3	67.4	69.8	68.8	1.3
2D6	47.1	48.4	49.7	45.9	51.0	48.4	1.8
3A4	67.2	67.2	65.9	66.9	66.2	66.7	0.5

Moreover, the choice of a methoxy model, while the fastest in terms of speed, precludes the description of the possible radical spin transfer to the heme iron during the oxidation process.

4.5.4. SoM Prediction – Improving IMPACTS – Steric Effects and Ligand Accessibility.

In our quest to improve the accuracy of IMPACTS we were set on improving the activation energies obtained in 2012. However, from the investigations described above, the activation energies were reliable and multiple efforts to further improve them proved to be unfruitful. As such, we turned our attention to the other aspect of the CYP metabolism, namely sterics. While the docking routines are considering some of these effects, precluding some unrealistic binding modes, the intrinsic accessibility of the SoMs was not being addressed. To expand on this, we decided to "pre-filter" the potential SoMs using a very simple sterics descriptor – solvent accessible surface area (SASA). We implemented the Shrake-Rupley[277] algorithm for computing SASA in FORECASTER and developed an equation (Eq.4.4) to integrate the sterics descriptor within the activation energies:

$$\text{Corrected } E_{act} = E_{act} - \Delta \times SASA_{atomic} \qquad \text{Eq. (4.4)}$$

Equation 4.4. Corrected activation energies for IMPACTS. Δ is a correction factor that has an optimized default value of 0.1.

This approach would ensure that both intrinsic reactivity and accessibility would be accounted for at the moment of docking with IMPACTS. The results of this approach are presented in Figure 4.15.

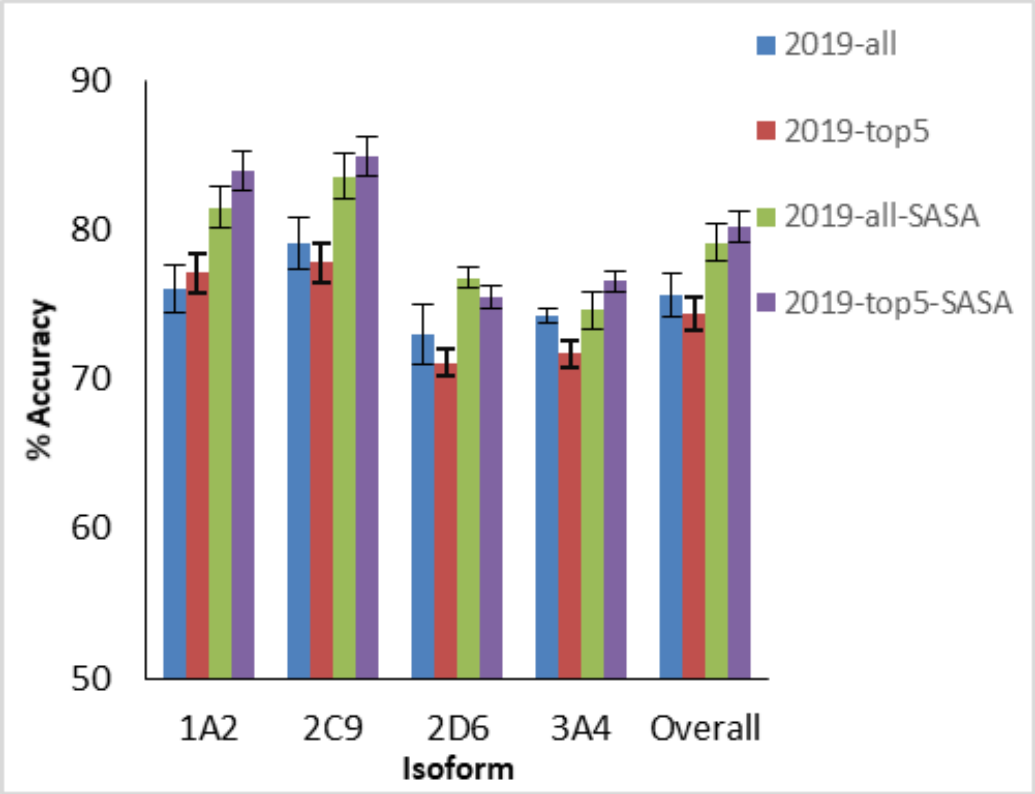

Figure 4.15. Accuracy using the current version of IMPACTS with and without SASA.

Figure 4.15 shows that the accuracy for each isoform increases significantly when adding the SASA correction. Overall, the accuracy of IMPACTS increases by almost 5% to when compared to the data in Figure 4.13 (80% overall). The decision to limit the number of SoM's for docking to 5 proved to be an inspired one in this case, since this condition shows the highest accuracy overall (Figure 4.15).

4.5.5. SoM Prediction – Improving IMPACTS – IMPACTS 2.0.

To test whether the data in Figure 4.15 was consistent across different sets, as well as across different isoforms that were not involved in the initial testing procedure, we assembled new sets for CYP1A2, 2C9, 2C19, 2E1, and 2D6 totaling 1125 drug molecules. The results in Figure 4.16 show that our SASA correction approach improves the accuracy of the overall set by 3%. Importantly, the use of SASA correction brings all isoforms over 70% accuracy.

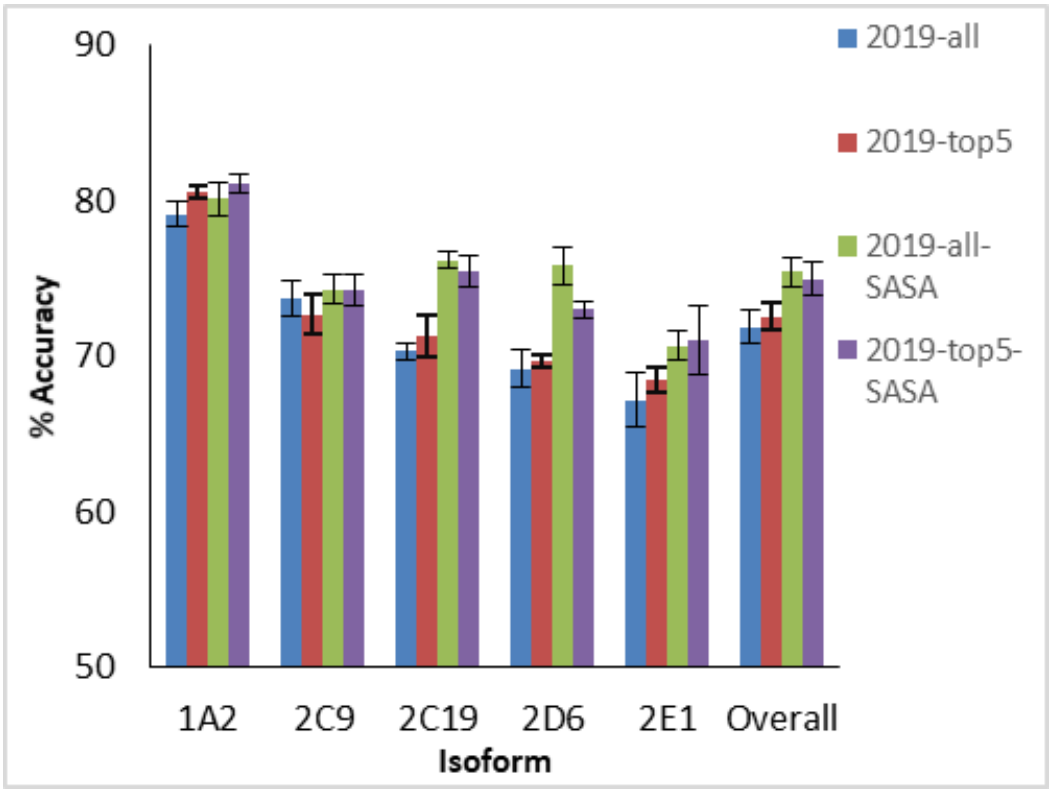

Figure 4.16. Accuracy using the current version of IMPACTS on external sets.

In the case of the external sets, limiting IMPACTS to 5 SoMs did not have the same effect as for our internal sets i.e. the accuracy with 5 SoMs is roughly the same as the one using all SoMs.

4.5.6. SoM Prediction – Improving IMPACTS – IMPACTS 2.0 – Protein Flexibility.

To verify whether protein flexibility played a major role in the results we had obtained so far, we decided to run IMPACTS on both the development and external sets in the flexible protein docking mode. For this purpose, we chose the best conditions we had determined during our study i.e. running IMPACTS on 5 SoMs using the SASA correction. To ensure that flexible docking is possible, we assembled a set of crystal structures from the PDB for each isoform except 1A2 and 2C19 (only one crystal structure available). This mode does not significantly affect the accuracy for most CYP isoforms. However, the accuracy in the case of 2C9 drops with both sets indicating that the selected protein structure in rigid mode is likely the one preferred by most substrates. As

observed with our previous version, adding flexibility to the protein is only adding noise to the calculations (Figures 4.17 and 4.18).

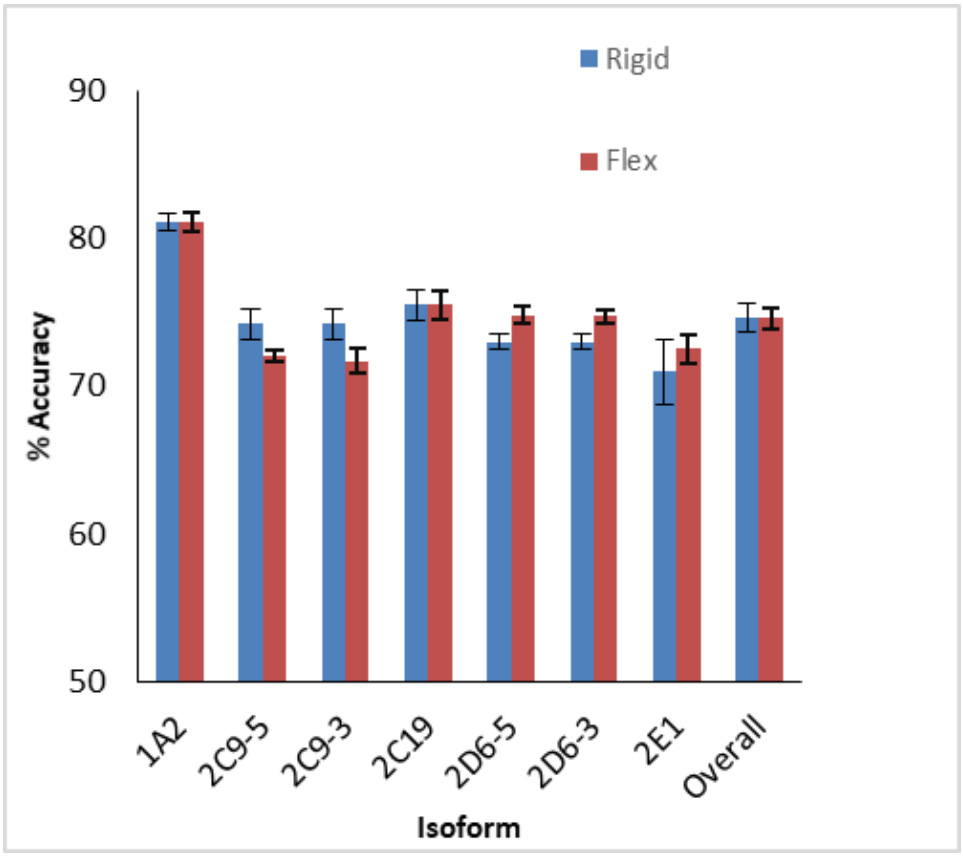

Figure 4.17. Accuracy using IMPACTS 2.0 on external sets with SASA correction in both rigid and flexible protein docking mode. 2C9-5 refers to all five selected isoforms used in docking; 2C9-3 refers to three representative isoforms used in docking. Same holds true for 2D6-5 and 2D6-3.

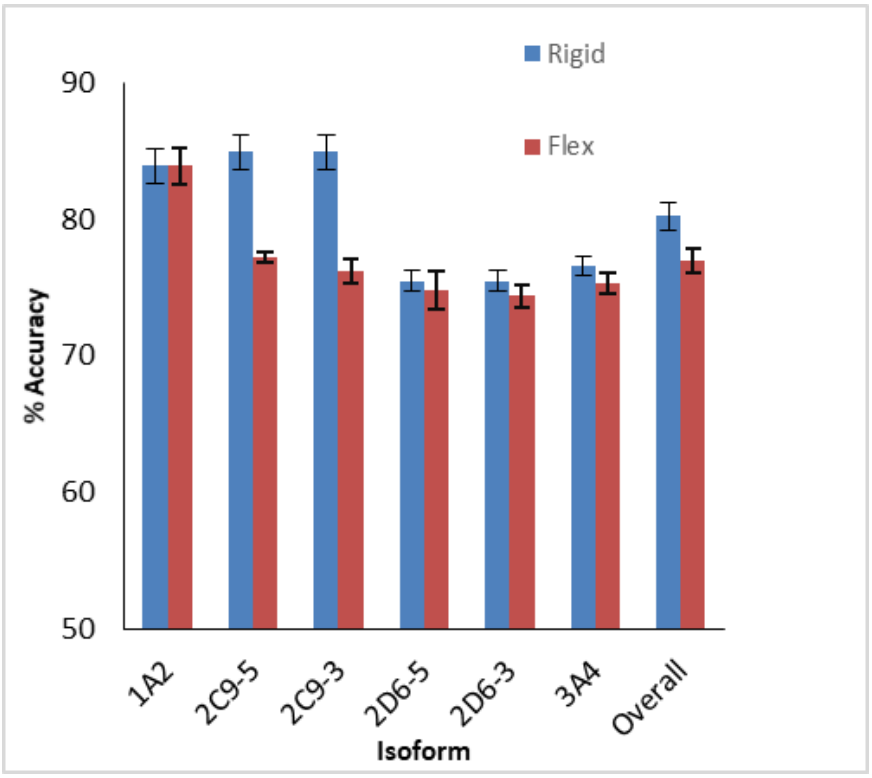

Figure 4.18. Accuracy using IMPACTS 2.0 on development sets with SASA correction in both rigid and flexible protein docking mode. 2C9-5 refers to all five selected isoforms used in docking; 2C9-3 refers to three representative isoforms used in docking. Same holds true for 2D6-5 and 2D6-3.

Overall, we thoroughly studied different avenues in which we could improve IMPACTS and managed to obtain a significant gain in overall accuracy for a very small computational cost.

4.6. Conclusions.

In this chapter we explored the expansion of our predictive drug metabolism software available in our drug discovery platform FORECASTER. First, we employed a unique QM-docking-ML approach to discriminate between CYP inhibitors vs. non-inhibitors. To this end we developed a novel LJ(8-4) potential to describe nitrogen-iron coordination and we implemented it into our docking program FITTED. We tested the accuracy of this novel implementation on a set of 85 CYP proteins assembled from the PDB by performing a self-docking study using both the protein and

metalloprotein docking modes available in FITTED. Overall, we observed that the metalloprotein docking mode with the novel LJ(8-4) performs slightly better at describing nitrogen-iron coordination than the protein mode. Afterwards, we assembled a set of experimentally determined inhibitors and non-inhibitors using a publicly available bioassay for five major CYP isoforms (1A2, 2C9, 2C19, 2D6, and 3A4), followed by subsequent docking to each specific isoform and the development of a back-propagation ANN. This ANN contains a single hidden layer and takes as input both docking energy terms and ligand properties. After training and testing our ANN, we observed that overfitting had occurred and that more work was needed to improve its accuracy across all five tested isoforms. Compared to existing ML methods trained on the same bioassay data, our ANN performs similarly. It is worth noting that overfitting had occurred in the other reported methods as well. Further studies are ongoing in our research group to further improve the current ANN methodology, including the usage of specific interactions with key residues for each of the isoforms, reducing sensitivity to poorly balanced sets (i.e. 2D6), evaluating the use of multiple hidden layers and optimizing the fitting parameters.

4.7. Methods.

All QM calculations for obtaining the PES profiles for the nitrogen heterocycles were performed with ORCA v.3.0.3.[188] As exemplified in the main text, we considered different computational methods to obtain the PES profiles (option c) was eventually chosen based on the results and cost vs. accuracy comparison):

a) B3LYP + def2-SVP + D3BJ + LANLDZ(Fe)
b) B3LYP + def2-TZVP + D3BJ + LANLDZ(Fe)
c) PBE0 + def2-SVP + D3BJ + LANLDZ(Fe)
d) PBE0 + def2-TZVP + D3BJ + LANLDZ(Fe)
e) SCS-MP2 + def2-SVP + LANLDZ(Fe)
f) SCS-MP2 + def2-TZVP + LANLDZ(Fe)

The ANN was written from scratch in C++ and implemented into our drug discovery platform FORECASTER. The SASA correction algorithm was written from scratch in C++ and implemented into our drug discovery platform FORECASTER. Self-docking study was performed with FORECASTER subversion 5815. IMPACTS study was performed with FORECASTER subversion 5764. The internal and development sets for testing IMPACTS will be available for download at http://moitessier-group.mcgill.ca/software.html.

Chapter 5 – From Desktop to Benchtop – A Paradigm Shift in Asymmetric Synthesis

Preface.

In Chapter 1, we introduced some aspects of asymmetric catalysts, including different ways to obtain chiral molecules and presenting several drawbacks related to transition-metal catalysis and biocatalysis. Recently, it was established that small organic molecules, such as proline (a naturally occurring amino acid), could catalyze reactions and induce enantioselectivity. This sparked the beginning of organocatalysis, which soon started gaining momentum. The benefits of organocatalysts are appealing: they are cheaper, have lower toxicity, greater availability when compared to metals, a higher substrate scope, and better stability when compared to enzymes. Many of these catalysts could be synthesized from enantiopure starting materials, usually natural products which are available in enantiopure form. Although several efficient asymmetric organocatalysts have been synthesized and reported for different chemical transformations in the past 20 years, progress in the field has been slow. This is mainly due to the difficulty in predicting how active and selective a catalyst would be before designing and synthesizing it.

When developing a new organocatalyst, a popular method for testing catalytic activity and selectivity relies on high throughput library screening (HTS). This method entails the synthesis or purchase of a vast amount of potential catalysts, which make up the library, and screening of their performance as enantioselective catalysts of a given reaction. This approach is not only costly, but also tedious and is, in general, a relatively low success rate process. The same basic HTS process has been applied in drug discovery. However, recent advances in computational chemistry tools have enabled the use of software which could predict the binding ability of a molecule to a known

target, thus reducing the number of molecules that need to be synthesized experimentally. Yet, very little work has been successfully done for enantioselectivity prediction of organocatalysts by computational tools. These tools are mostly used nowadays to help rationalize observations such as selectivity *post facto* rather than for design. The complexity of developing such tools requires the use of time and resource-intensive computations and a deep understanding of computational chemistry.

To streamline the process of catalyst design and to improve the overall molecular discovery rate by allowing chemists to synthesize only active, selective catalysts, we have focused our efforts to develop the VIRTUAL CHEMIST platform. This platform allows organic chemists to simulate an entire asymmetric synthesis project from start to finish, without the need for computational chemistry expertise.

This chapter is based on the work published in the paper below with a more detailed description of the program QUEMIST:

Burai Patrascu, M.;‡ Pottel, J.; Pinus, S.; Bezanson, M.; Norrby, P.O.; and Moitessier, N. *Nat. Catal.*, accepted, **2020**.

NM developed ACE and the UI for the VIRTUAL CHEMIST platform. JP and NM developed the CONSTRUCTS software. MBP developed QUEMIST and implemented it in the VIRTUAL CHEMIST platform. MBP and SP performed the VS studies. PON developed Q2MM. All authors contributed to writing the manuscript.

‡ first author

Chapter 5

Abstract.

The organic chemist's toolbox is vast with technologies to accelerate the synthesis of novel chemical matter. The field of asymmetric catalysis is one approach to access new areas of chemical space and computational power is today sufficient to assist in this exploration. Unfortunately, existing techniques generally require computational expertise and are therefore under-utilized in synthetic chemistry. We present in this chapter our platform VIRTUAL CHEMIST that allows bench chemists to predict outcomes of asymmetric chemical reactions ahead of testing in the lab, in just a few clicks. Modular workflows facilitate the simulation of various sets of experiments, including the four realistic scenarios discussed: one-by-one design, library screening, hit optimization, and substrate scope evaluation. Catalyst candidates are screened within hours and the enantioselectivity predictions provide substantial enrichments compared to random testing. The achieved accuracies within ~1 kcal/mol provide new opportunities for computational chemistry in asymmetric catalysis.

Chapter 5

5.1. Introduction.

Organic chemistry research is vital to the discovery, optimization, and ton-scale production of numerous small molecules, such as novel drugs that treat life-threatening diseases. It contributes to the design of innovative materials comprising modern electronics and low power consumption organic light-emitting diodes (OLEDs), and to the development of novel agricultural practices, cosmetics, textiles, inks, and paints, to name a few. Unfortunately, a major hurdle in the production of these complex small molecules is the challenging syntheses they often require. Although several research groups are focused on the development and optimization of new methodologies, they are often reaction-specific and universalizing them for mainstream wet lab chemistry requires substantial work.

For the design of novel organic synthetic methodologies to access novel compounds, chemists often make use of the vast organic chemistry toolbox at their disposal; chemists routinely incorporate NMR, mass spectrometry (MS), and chromatography. These complex scientific technologies are largely accessible without expert knowledge of their inner workings. For example, synthetic chemists run standard ^{1}H, ^{13}C, and various 2D NMR experiments without necessarily understanding and/or manipulating the magnetic pulse sequences. In contrast, computational chemistry remains largely inaccessible to the experimental chemistry community; complex theoretical calculations are neglected since coding/programming knowledge – sometimes advanced experience – is often a prerequisite. The omission of computational techniques from the larger toolbox is regrettable since interpreting unexpected observations[278] and proposing new reaction mechanisms,[279,280] have been attributed, in part, to computations.

With the rise of QM – HF and DFT – and MM methods – docking, MD simulations – organic chemists have caught a glimpse of the power and utility of such computations.

Computational experts frequently collaborate with experimentalists to rationalize the observations of the organic chemists. However, rather than only offering *post facto* theories, computational chemistry could prospectively hypothesize and screen organic chemistry transformations. We remain sanguine at such a possibility upon consideration of a similar successful implementation of computer simulations in drug discovery.[88,281] After the pioneering development of DOCK—a structure-based drug discovery tool—in 1982, an entire field of research emerged. In fact, many computational techniques including ML, MD simulations,[282] molecular docking,[283] and pharmacophore modelling[284] are now commonplace, addressing research challenges in drug discovery. Theoretically, analogous computational techniques could tackle synthetic chemistry challenges; already, robotics[285] and synthetic planning computational tools[286,287] have been reported and will likely be incorporated into many chemistry laboratories soon.

5.2. Asymmetric Synthesis and Stereoselectivity Prediction.

Among synthetic methodologies are asymmetric transformations. While biocatalysis and the use of the chiral pool are common approaches for the synthesis of chiral molecules (e.g., chiral drugs and chiral materials), their application is limited (substrate specificity and stability of biocatalysts, limited available chiral molecules). Asymmetric synthesis is an attractive alternative to generating chiral molecules in high quantity and purity. In practical terms, cheap, selective, synthetically accessible, and green asymmetric catalysts are highly desired to shorten synthetic routes to complex small molecules. The vastness of the chemical space suggests that many organocatalysts or transition metal catalysts exist, but their discovery is challenging, tedious, and physically intractable using solely traditional experimental techniques.[288] The exploration of the chemical space can, however, be more efficient when performed computationally. Furthermore,

virtually applying identified and selected catalysts to predict stereoselectivity for a specific reaction is within reach.[289]

Several groups have focused on the prediction of stereoselectivity of asymmetric transformations.[125,290,291] Among the proposed approaches are statistical models,[292,293] ANNs,[294,295] DFT, [125,290,296-303] QM/MM,[128] and MM-based methods (Q2MM[124,131] and ACE [123,304]), with DFT being the most widely used. However, despite the demonstration of their feasibility, it was not until 2009 that the first use of DFT for screening a small sized set of asymmetric catalysts and substrates was reported, [305] with little communicated thereafter. ANNs are newer on this scene but require a plethora of data and may not be appropriate to discover novel catalysts. Generally, most software in this domain has been plagued by poor usability and time inefficiency, although some research groups have been making progress in these aspects (i.e. CatVS described in Chapter 1). We posit that organic chemists should be able to truly screen potential asymmetric catalysts computationally. More broadly, we aim to continue to shift the organic chemistry paradigm to consider virtual asymmetric catalyst discovery and design as a complement to traditional and automated asymmetric catalysis. We present herein our efforts to develop a platform (VIRTUAL CHEMIST) that integrates all the tools, accessories, and automation required to be moved to organic chemistry labs for designing experiments rather than rationalizing data.

5.3. Challenges and Methodologies.

To deliver this technology to the hands of organic chemists, the accessibility aspect must be addressed without sacrificing accuracy. **Regarding accessibility**: this technology should not require large computational resources, should ideally be useable on a standard desktop computer (Windows, Linux, MacOS), and should be substantially faster than the experiments being simulated. We believe that this software should bring knowledge complementary to that of

chemists, taking advantage of complex calculations (machine) and years of expertise (human). For example, chemists should be able to interact with this technology instructing the software for specially desired properties (e.g. protecting groups, water solubility, and commercial availability of chemicals). **Regarding accuracy**: a difference of only 1 kcal/mol between diastereomeric transition states can distinguish highly from weakly stereoselective catalysts. To put this margin of error in context, in the drug discovery process, one often investigates molecules hitting a target with reasonable binding affinity. In this case, an accuracy of a few kcal/mol can differentiate between strong, weak, and non-binders (e.g., 4 kcal/mol would differentiate between a nanomolar and a micromolar enzyme inhibitor). As such, accuracy is a major challenge in asymmetric catalyst screening. The ultimate objective of this endeavour is to deliver software simulating an entire organic chemistry project from A to Z. Consider a general guide toward the development of a novel Diels-Alder organocatalyst to illustrate such a project (Figure 5.1).

In this scenario, we would need software to virtually **(1)** prepare libraries of potential catalysts and to understand chemistry concepts such as chirality, functional group compatibility (chemoselectivity) and similarity, **(2)** evaluate the catalytic activity of the potential catalysts, and **(3)** evaluate the enantioselectivity induced by these catalysts.

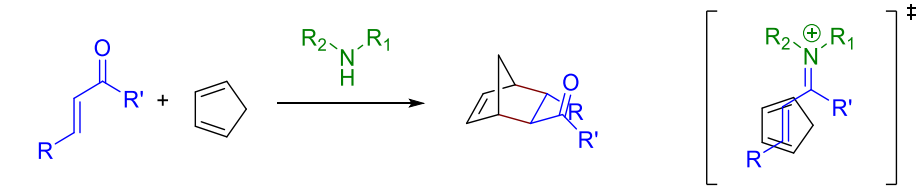

R groups cannot feature aldehyde, alkene, amine....

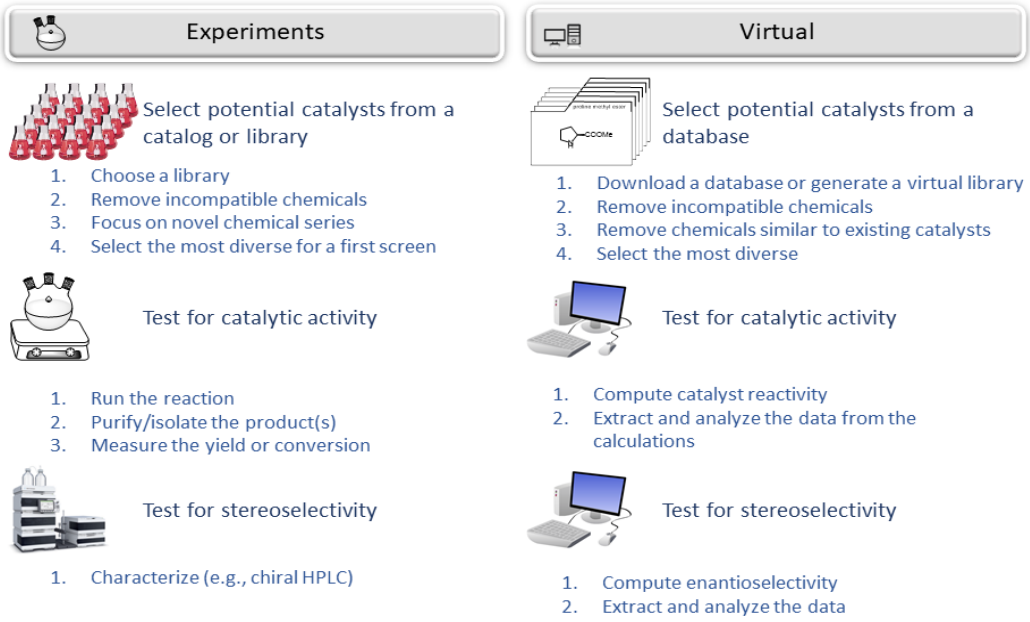

Figure 5.1. Top: Organocatalyzed Diels-Alder reaction. Bottom: Workflows undertaken by wet-lab chemists vs. those undertaken by computational chemists.

Ideally, a common platform would seamlessly execute all three actions without user intervention. Chemists should also be able to instruct the software through sketches using a program they are familiar with (e.g., ChemDraw). To run the gamut of simulations mentioned above, several transformations and computations must be automated and concealed from the user; herein lays an often forgotten, yet major challenge of this platform. We built on and expanded our drug discovery platform FORECASTER GUI to create a new platform, VIRTUAL CHEMIST. This new UI contains a 2D sketcher for drawing input catalysts and substrates and an easy-to-use 3D graphical interface for visualizing the calculated output TS structures (Figure 5.2). Additionally, resulting data is summarized in the UI (e.g., TS structures' potential energies, predicted enantioselectivities). Finally, we made strides toward universal application by enabling the creation of modular workflows.

5.3.1. Preparation of Libraries of Catalysts.

Previously reported programs SELECT (searches for analogues or dissimilar compounds, optimizes library diversity) and REDUCE (filters chemical library for presence of functional groups such as secondary amines for organocatalyzed Diels-Alder cycloaddition)[81] are accessible in modular workflows. A library of synthetic analogues can also be generated using previously developed and reported searching and combinatorial tools, FINDERS and REACT2D.[306] In contrast to other virtual combinatorial library tools,[307] these programs consider stereochemistry change during a reaction (e.g., in a Mitsunobu reaction), ensuring that the asymmetric catalysts virtually screened are truly synthetically accessible.

5.3.2. Predicting Enantioselectivities.

Generally, for each catalyst candidate, the software must compile a TS, parameterize that system, and then compute energies. First, where does a TS come from? As an example, consider the diethyl zinc addition to aldehydes previously investigated with Q2MM.[308] TSs were provided as supporting information using a common 'xyz' Cartesian coordinate format. These structures (text files) could be used as a starting point for screening asymmetric catalysts without any GUI or QM training. As shown in Figure 5.2, provided Cartesian coordinates yield TS templates that are subsequently used to assemble realistic TS structures for a series of catalysts and substrates.

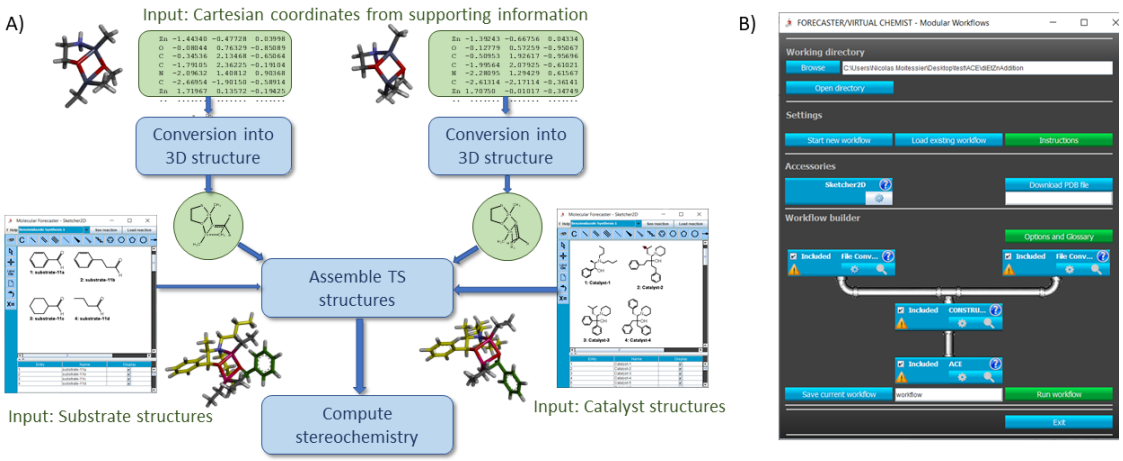

Figure 5.2. Screening catalysts for diethylzinc addition to aldehydes. A) From reported Cartesian coordinates and drawn catalysts and substrates to accurate TSs. B) Workflow corresponding to the tasks shown in A.

5.3.2.1. Preparing the TSs for Enantioselectivity Computations.

All the steps described above were successfully integrated into a single program (CONSTRUCTS - Converting and Orienting Native Structures on Templates of Rotatable and Unoptimized Chemical Transition States). Briefly, CONSTRUCTS uses simple text files (TS of simple models) and 2D sketches of substrates and catalysts (Figure 5.2A) to build reasonable 3D TS structures. The sketches of catalysts and substrates are converted into 3D structures using the program CONVERT[81] integrated into CONSTRUCTS and geometrically optimized using MM routines developed for this purpose. CONSTRUCTS then assembles the obtained 3D structures of catalysts and substrates into a TS structure by superimposing corresponding atoms onto a previously-stored template. This template is based on reported TS structures which are generalized and stored within the program for any given asymmetric reaction. Once the 3D structures are built, they are processed by SMART,[81] also integrated into CONSTRUCTS, which assigns atomic charges and atom

types, identifies rings and flexible bonds. The entire process of generating 3D TS structures for a given reaction is exemplified in Figure 5.3 using the proline-catalyzed aldol reaction.

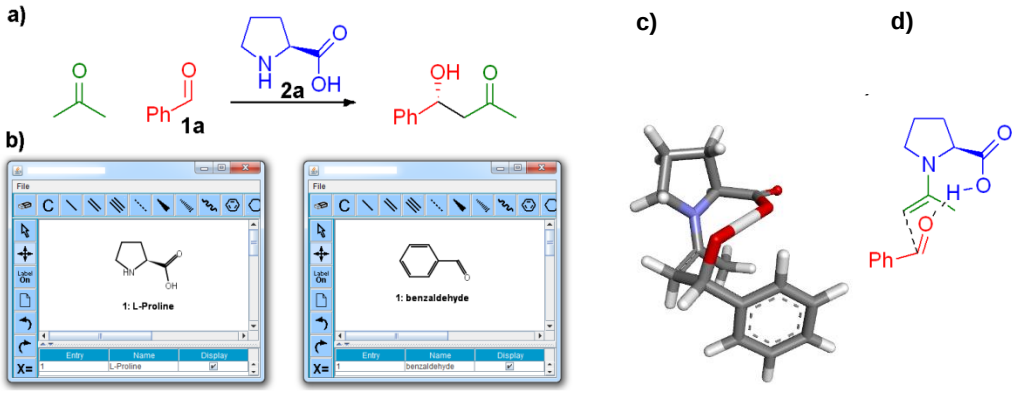

Figure 5.3. (a) Proline-catalyzed aldol reaction. (b) Sketches used as input. (c) Automatically generated 3D TS structure after SMART (4 different TSs are possible in this reaction but only one shown here as example). (d) The scheme of the TS is given in 2D for clarity.

5.3.2.2 ACE.

As described in section 1.4.3, ACE is the software which predicts stereoselectivity of reactions using the Hammond-Leffler and Curtin-Hammett principles. The underlying theory of ACE has been described in detail in section 1.4.3. In this section we will focus on the applications and limitations of the software. Being an MM-based method, ACE inherits all the limitations associated with MM, and more specifically with FFs. For example, the MM3 FF has no parameters for metals, and as such transition-metal catalyzed reactions (i.e. the Sharpless asymmetric dihydroxylation of alkenes – Scheme 1.7) cannot be modeled. This limitation is significant given the popularity of transition-metal catalysis and the importance of searching for cheaper transition metal catalysts or repurposing of existing ones. Another limitation refers to the necessity of knowing the mechanism of the reaction beforehand, in order to build proper TSs that can later be optimized. If the mechanism of the reaction is unknown ACE cannot be used in a predictive way.

To expand the usability of ACE, we decided to add the option to use Q2MM-derived TSFFs (described in Chapter 1). This decision has two-fold consequences: it improves the usability of Q2MM, which requires external MM packages and routines to perform conformational searches (now taken care of ACE) and it gives ACE the opportunity to use FFs developed for Q2MM for important reactions such as diethylzinc addition to aldehydes,[308] Sharpless asymmetric dihydroxylation of alkenes,[309] and rhodium-catalyzed hydrogenation of activated alkenes.[310]

5.3.2.3. QUEMIST.

One way of parametrizing metals in a FF is using on-the-fly QM calculations on model systems that can describe a reaction of interest. However, these calculations require computational chemistry expertise and the usage of external QM packages to obtain the parameters. To offset these drawbacks, we implemented our own QM package – QUEMIST (QUantum Energy of Molecules Inducing Structural Transformations) – in the VIRTUAL CHEMIST and FORECASTER platforms. QUEMIST is a cross-platform software written in C++ capable of performing HF, MP2 and DFT single point energy calculations as well as computation of HF gradients (analytically), geometry optimizations, and Hessian matrix calculations (numerically) necessary for generating parameters for ACE.

QUEMIST is capable of using a variety of basis sets (Cartesian for the Windows version and Cartesian and spherical for the Linux/MacOS versions) obtained from the Basis Set Exchange.[311] The linear algebra routines necessary to perform the highly demanding computations use the efficient Eigen3 library.[312] The Linux/MacOS versions of the program use the highly efficient LIBINT integral engine[313] as well as the LIBXC library for exchange-correlation functionals (in the case of DFT).[314] The pseudocode for the single point energy and geometry optimization/Hessian calculations routines available in QUEMIST is given in Appendix D.

To generate FF parameters for ACE we implemented the Seminario algorithm, which is used to compute parameters following a Hessian matrix calculation.[315] The Hessian matrix is a 3N x 3N matrix (where N is the number of atoms in the molecule) that contains the information about the change in energy with respect to changes in atomic coordinates (x,y,z). In short, this algorithm allows the computation of bond and bond-angle force constants from the eigendecomposition of the Hessian matrix in terms of atomic pair-wise interactions. For example, if one requires to compute the force constant of the C-C bond in ethanol (Figure 5.4a, blue bond), the Hessian submatrix corresponding to the interactions between the two carbons must be first extracted from the complete Hessian matrix (Figure 5.4b).

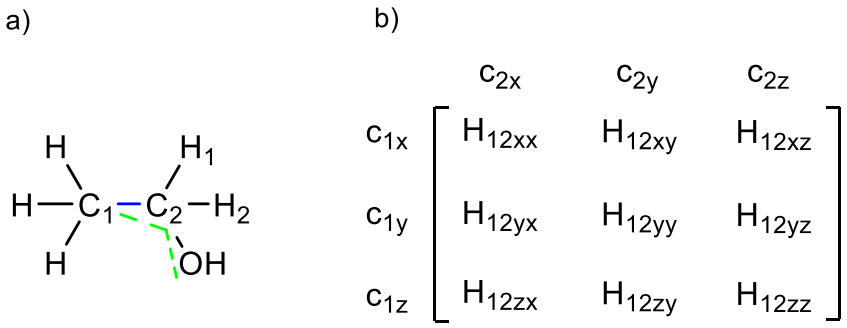

Figure 5.4. (a) Structure of ethanol. C1-C2 bond subjected to force constant computation is shown in blue. C1-C2-O2 angle subjected to force constant computation is shown in green. (b) Hessian submatrix extracted from the complete Hessian matrix depicting the interactions between the two carbon atoms in the x,y and z coordinates.

This submatrix is known as the interatomic force constant matrix and its analysis allows the determination of the nature of the interaction between atoms (in this case, the two carbon atoms). The three eigenvalues and eigenvectors associated with this submatrix can then be used to compute the force constant of the bonded interaction through the relationship described in Eq. 5.1.

$$k_{C1C2} = \sum_{i=1}^{3} \lambda^{i}{}_{C1C2} \left| \vec{u}_{C1C2} \cdot \vec{v}^{i}_{C1C2} \right| \qquad \text{Eq. (5.1)}$$

Equation 5.1. Description of the formula used to compute the bond force constant according to the Seminario algorithm.

A positive λ^{i} value corresponds to a reaction force on carbon C1 due to the displacement of carbon C2 that is in the same direction as the eigenvector $\vec{v}^{i}$. If the bond between carbons C1 and C2 is not in the direction of any of the eigenvectors $\vec{v}^{i}$, the force constant k_{C1C2} can have contributions from multiple eigenvalues. These contributions are proportional to the projection of the eigenvector $\vec{v}^{i}$ onto the unit vector $\vec{u}_{C1C2}$. If all three λ^{i} eigenvalues are positive, it follows that for any displacement occurring on carbon C2, there will always be a restoring force on carbon C1 that seeks to maintain the equilibrium bond length. According to the original Seminario algorithm, this necessarily means that atoms C1 and C2 are pairwise stable, equivalent to describing the atoms as being bonded.[315] Importantly, Eq. 5.1 allows the computation of force constants for atoms involved in bonds that are not covalent in nature (i.e. strongly polarized dative bonds found in transition-metal catalysis).

The Seminario algorithm also allows for the computation of bond angle force constants. For example, one might want to compute the force constant for the C1-C2-O angle in ethanol (Figure 5.4, green). The first step is identical to the one used in computing the force constants for bonds i.e. extracting the Hessian submatrices for the C1-C2 and O-C2 bonds and computing the eigenvectors $\vec{v}^{i}_{C1C2}$ and $\vec{v}^{i}_{OC2}$ and eigenvalues $\lambda^{i}{}_{C1C2}$ and $\lambda^{i}{}_{OC2}$. Once this is done, unit vectors $\vec{u}_{PO}$ and $\vec{u}_{PC1}$ perpendicular to the C1-C2 and O-C2 bonds are built. These unit vectors represent the displacements of atoms C1 and O when the angle opens or closes. The unit vectors, eigenvectors,

and eigenvalues, along with the bond lengths R_{C1C2} and R_{OC2}, can then be used to assemble Eq. 5.2, which gives the bond angle force constant.

$$\frac{1}{k_\theta} = \frac{1}{R_{C1C2}^2 \sum_{i=1}^{3} \lambda^i{}_{C1C2} \left| \vec{u}_{PC1} \cdot \vec{v}^i_{C1C2} \right|} + \frac{1}{R_{OC2}^2 \sum_{i=1}^{3} \lambda^i{}_{OC2} \left| \vec{u}_{PO} \cdot \vec{v}^i_{OC2} \right|} \qquad \text{Eq. (5.2)}$$

Equation 5.2. Description of the formula used to compute the bond angle force constant according to the Seminario algorithm.

Recently, Allen *et al*.[316] proposed a modified Seminario method for computing bond angle force constants to account for the geometry of the molecule and the number of angles the central atom in an angle is part of. For example, the bond force constant computation of angle C1-C2-O now changes to account for the presence of atom C2 in the angles C1-C2-H1 and C1-C2-H2. This is shown in Eq.5.3.

$$\frac{1}{k_\theta} = \frac{1 + \frac{\sum_{i=1}^{N} \left| \vec{u}_{PC1} \cdot \vec{u}^i_{PC1} \right|^2 - 1}{N-1}}{R_{C1C2}^2 \sum_{i=1}^{3} \lambda^i{}_{C1C2} \left| \vec{u}_{PC1} \cdot \vec{v}^i_{C1C2} \right|} + \frac{1 + \frac{\sum_{i=1}^{M} \left| \vec{u}_{PO} \cdot \vec{u}^i_{PO} \right|^2 - 1}{M-1}}{R_{OC2}^2 \sum_{i=1}^{3} \lambda^i{}_{OC2} \left| \vec{u}_{PO} \cdot \vec{v}^i_{OC2} \right|} \qquad \text{Eq. (5.3)}$$

Equation 5.3. Description of the updated formula by Allen et al.[316] used to compute the bond angle force constant.

The N and M variables in Eq. 5.3 are the total number of angles in which C2 is the central angle and that involves the movement of the C1-C2 (N) and O-C2 (M) bonds. The updated formula for computing the bond angle force constants was shown to reduce the error in the force constants by 6% on a set of 70 representative molecules.[316] We have thus decided to use the implementation of Eq.5.3 in our program. One drawback of the original Seminario algorithm is related to the computation of dihedral angle force constants. Because of the nature of the definition of the torsional angle term in the MM3 FF (see Eq.1.6), force constants for dihedral angles cannot be

determined because of the lack of V1, V2 and V3 terms in the original algorithm. As such, all dihedrals force constants are set to 0.

Of course, the theory and equations described above are somewhat tedious and may not be of interest to an organic chemist. Thus, we automated the generation of these parameters and concealed the underlying theory and equations to allow the development of parameters in a user-friendly manner. At the end of any Hessian calculation, QUEMIST will analyze the Hessian matrix for imaginary frequencies to ensure the optimized structure is a minimum on the PES and will write out a customized FF file containing the atoms, atomic charges, hybridization and atomic coordinates, along with the bond and bond angle force constants in the units used in the MM3 FF. If a negative or imaginary force constant is found, a warning message will be output in the FF file for the respective bond/bond angle. This file will then be automatically loaded into ACE during the enantioselectivity computations, thus making user intervention obsolete. An example of the customized FF parameters obtained for ethanol at the HF/6-31G* level of theory is given in Figure 5.5.

```
-----------------------------------------------------------------------------------------------------
# ATOM TYPES
-----------------------------------------------------------------------------------------------------
   1    C    3    2    3    4    5   00   00   -0.5020   -4.3299    0.6004    0.0777
   2    C    3    1    6    7    8   00   00    0.0090   -3.0850    1.4666   -0.0716
   3    H    0    1   00   00   00   00   00    0.1589   -5.0129    0.7596   -0.7539
   4    H    0    1   00   00   00   00   00    0.1494   -4.8651    0.8367    0.9964
   5    H    0    1   00   00   00   00   00    0.1770   -4.0604   -0.4513    0.1061
   6    H    0    2   00   00   00   00   00    0.1388   -3.3624    2.5197   -0.1295
   7    H    0    2   00   00   00   00   00    0.1699   -2.5669    1.2202   -0.9913
   8    O    3    2    9   00   00   00   00   -0.7344   -2.1534    1.2560    0.9597
   9    H    0    8   00   00   00   00   00    0.4334   -2.5275    1.5336    1.7859
10 **********************
-----------------------------------------------------------------------------------------------------
# K is given in mdyn/A
# If Rel = 0 K is completely reliable
# If Rel = 1 an imaginary eigenvalue > 0.1 was detected for the bond - K is moderately reliable
# If Rel = 2 a negative eigenvalue was detected for the bond - K is unreliable since there is no bond between the atoms
# Bond length (L0) is given in Angstrom
-----------------------------------------------------------------------------------------------------
# BOND-GENERAL
-----------------------------------------------------------------------------------------------------
#           I-J         REL.          K           L0        Bond moment    Bond Order     Comments
-----------------------------------------------------------------------------------------------------
BM-1       1   2         0          3.7267       1.5240        -0.0110        0.9700          None
BM-2       1   3         0          5.3107       1.0878        -0.1460        0.9530          None
BM-3       1   4         0          5.2545       1.0891        -0.1372        0.9601          None
BM-4       1   5         0          5.4215       1.0861        -0.1630        0.9542          None
BM-5       2   6         0          5.1847       1.0905        -0.1273        0.9560          None
BM-6       2   7         0          5.5199       1.0840        -0.1567        0.9575          None
BM-7       2   8         0          4.6379       1.4055         0.2141        0.8754          None
BM-8       8   9         0          9.2581       0.9485        -0.4570        0.7715          None
-----------------------------------------------------------------------------------------------------
# K is given in kcal / mol*deg ^ 2
# If Rel = 0 K is completely reliable
# If Rel = 1 an imaginary eigenvalue > 0.1 was detected for the bond - K is moderately reliable
# If Rel = 2 a negative eigenvalue was detected for the bond - K is unreliable since there is no bond between the atoms
# Angle value (A0) is given in Degrees
-----------------------------------------------------------------------------------------------------
# ANGLE-GENERAL
-----------------------------------------------------------------------------------------------------
#          I-J-K          REL.          K            A0            Comments
-----------------------------------------------------------------------------------------------------
AM-1     1  2  6          0          1.0178       110.2591          None
AM-2     1  2  7          0          3.7740       110.1376          None
AM-3     1  2  8          0          6.3041       112.6040          None
AM-4     2  1  3          0          0.8872       110.7838          None
AM-5     2  1  4          0          1.5474       111.1466          None
AM-6     2  1  5          0          2.5779       110.5042          None
AM-7     2  8  9          0          0.8392       109.5042          None
AM-8     3  1  4          0          2.3784       107.7300          None
AM-9     3  1  5          0          2.9074       108.5112          None
AM-10    4  1  5          0          0.9753       108.0552          None
AM-11    6  2  7          0          3.0296       107.2209          None
AM-12    6  2  8          0          5.0335       110.6270          None
```

Figure 5.5. Customized FF parameters obtained for ethanol at the HF/6-31G* level of theory.

In the case of a new reaction being implemented in ACE, FF parameters have to be derived for both reactants and products (i.e. geometry optimizations followed by Hessian matrix calculations have to be undertaken separately for both reactants and products, generating different customized FF parameters). However, it is essential to note that once the FF parameters have been determined for a model system of a reaction of interest, they are stored and re-used every time. As

such, every reaction of interest need be parametrized only once. For example, a workflow for implementing the Sharpless asymmetric dihydroxylation of alkenes is presented in Figure 5.6.

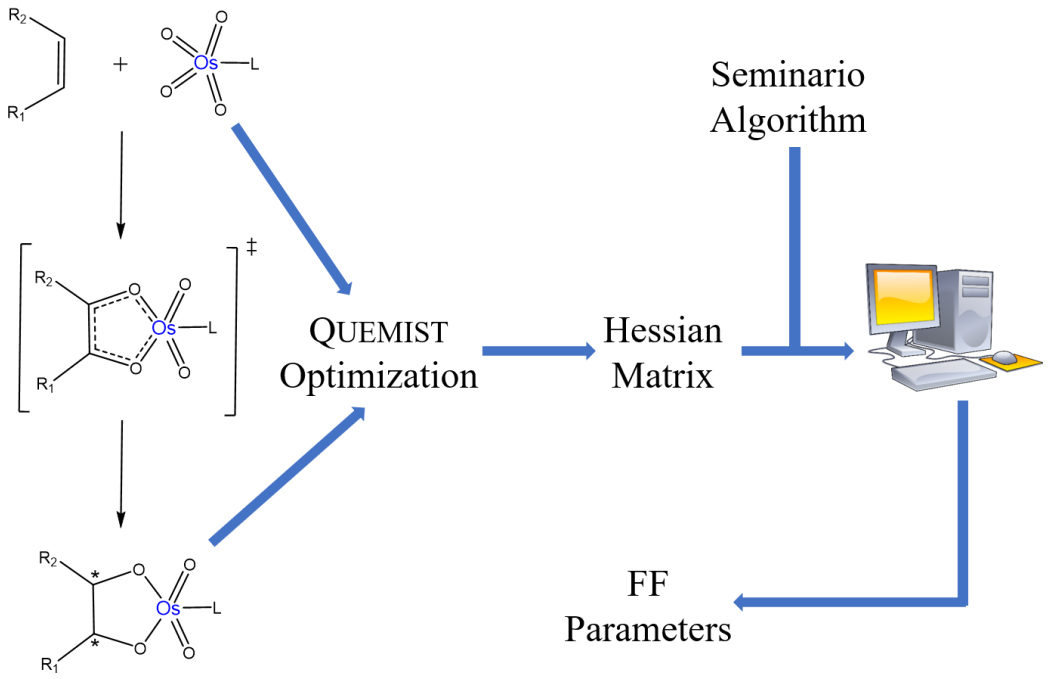

Figure 5.6. Workflow for implementing the Sharpless asymmetric dihydroxylation of alkenes in ACE. R_1=R_2=Me; L=NMe_3.

Importantly, the protocol shown in Figure 5.6 can be applied to any reaction of interest as long as the mechanism is known. Moreover, all the steps for obtaining the FF parameters are clearly outlined in the GUI and require little to no user input since the default parameters for the geometry optimizations and Hessian matrix calculations have been optimized over multiple reactions and substrates.

5.3.3. Evaluating Catalytic Activity.

While ACE can accurately compute the stereoselectivities of potential catalysts, it is unable to determine whether a catalyst is reactive or not (i.e. if it would catalyze a reaction or not). To

offset this limitation, we implemented several global and local reactivity parameters in QUEMIST (Figure 5.7) in the context of HF and cDFT frameworks.[270,272,273,317,318]

Molecule ... ethanol			
MOLECULAR PROPERTIES			
LUMO energy (eV)	=	6.52456	
Electron Affinity (EA) (eV)	=	-6.52456	
HOMO energy (eV)	=	-11.83182	
Ionization potential (IP) (eV)	=	11.83182	
Chemical hardness (nu) (eV)	=	9.17819	
Chemical hyperhardness (eV)	=	17.18488	
Chemical potential(miu)(eV)	=	-2.65363	
Mulliken electronegativity	=	2.65363	
Chemical softness (S) (eV)	=	0.10895	
Chemical hypersoftness (eV)	=	0.05819	
Global electrophilicity (w)(eV)	=	10.43866	
Global nucleophilicity index #1 : N = en(HOMO) - en(TCE)		-(eV) =	-11.83182
Global nucleophilicity index #2 : N = 0.5 * (miu^2 / nu^2) * nu		-(eV) =	0.38361
Electrodonating power : edp = I^2 / 2 * (I-A) -		-(eV) =	3.81317
Max. accepted charge	=	0.28912	

Atom # 6 O

Orbital	Orbital #	rho	Energy (eV)	Reactive	f(-)	f(+)	f(0)
LUMO + 2	15	0.3962	8.4898	NO	-	0.0006	0.0000
LUMO + 1	14	1.8385	7.8762	NO	-	0.0062	0.0000
LUMO	13	3.1961	6.5246	YES	-	0.0113	0.0000
HOMO	12	2.6912	-11.8318	YES	0.5972	-	0.3043
HOMO - 1	11	1.8330	-13.0033	NO	0.3028	-	0.0000
HOMO - 2	10	0.6968	-14.3185	NO	0.1661	-	0.0000
HOMO - 3	9	1.0016	-14.7440	NO	0.2419	-	0.0000

Figure 5.7. Top: Global reactivity parameters for ethanol at the HF/pc-1 level of theory. **Bottom:** Local reactivity parameters (Fukui functions) for the oxygen atom in ethanol at the HF/pc-1 level of theory.

We embedded QUEMIST into SMART to allow the computation of these parameters along with multiple other descriptors such as molecular properties and presence of functional groups. These descriptors are essential when screening a library of catalysts to ensure that only desirable catalysts are selected for CONSTRUCTS and ACE. For example, depending on the reaction of interest, one could filter possible catalysts by a global parameter such as electrophilicity (in the

case of Shi epoxidation) or by a local parameter such as the nucleophilic Fukui function on an sp^3 nitrogen atom (as is the case of the organocatalyzed Diels-Alder reaction).

5.4. Validation of the Platform.

To assess the applicability of the tools presented above, we envisioned four different realistic scenarios:

1. A chemist may draw catalysts one by one and test the potential stereoinduction.
2. A chemist may screen a large database of chiral molecules to identify novel chemical series.
3. A chemist may search for analogues as part of a lead optimization of a hit molecule (with analogy to drug discovery).
4. A chemist may assess the substrate scope of a specific catalyst.

5.4.1. Scenario #1 – One by One Design.

A chemist may want to test one catalyst at a time and virtually identify the most promising. In this scenario, each catalyst may be drawn using the provided sketcher; TS templates are either available directly or may be built from literature data, as described in the sections above. We tested this scenario on over 350 reactions from 7 reaction classes (Figure 5.8, complete set given in Appendix D) and compared the results from random predictions to assess the accuracy of the methodology (Figure 5.9).

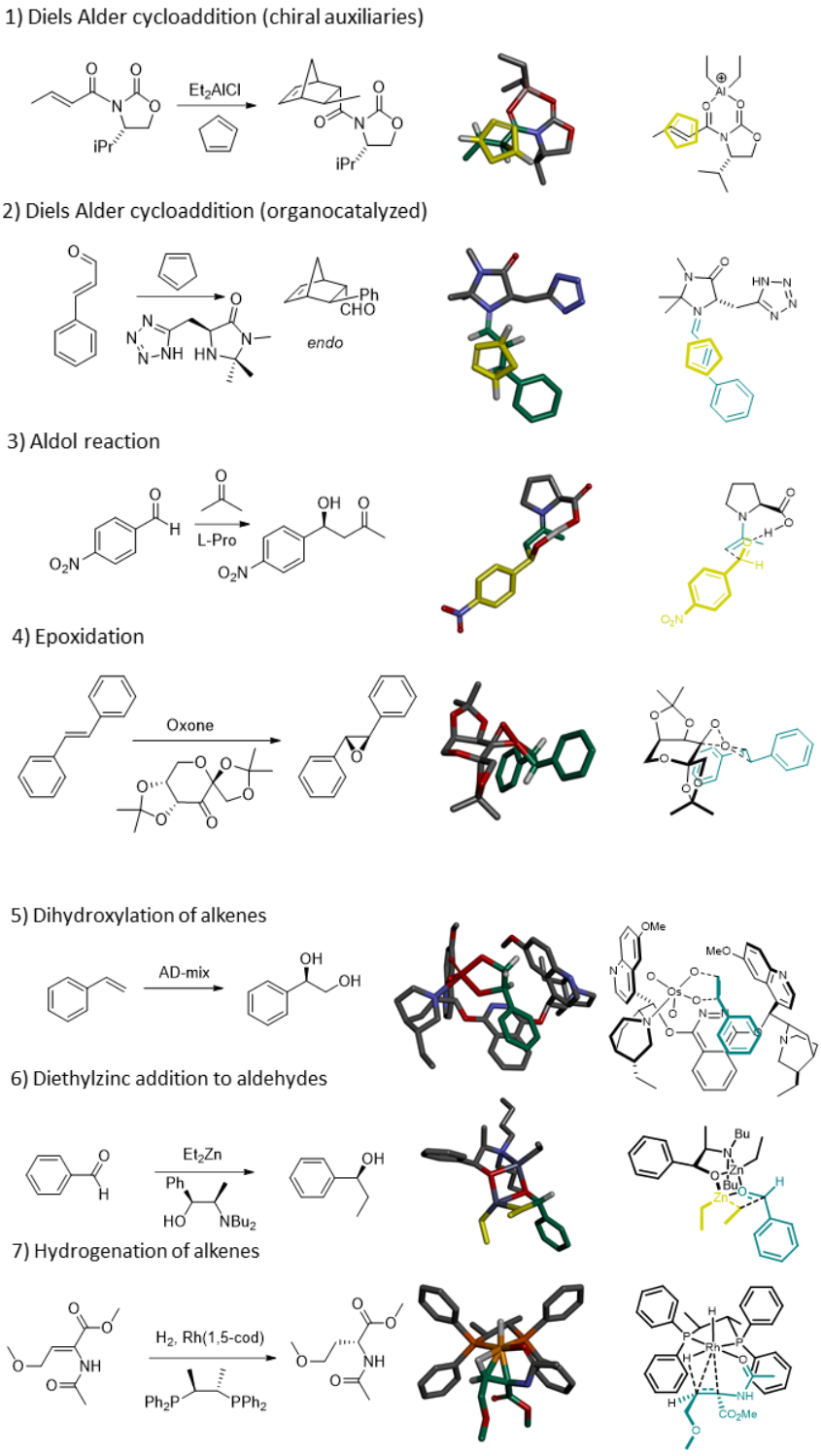

Figure 5.8. ACE-optimized TS structures for selected reactions. General reaction schemes are drawn, followed by 3D and 2D representations of transition state models.

To evaluate accuracy, we first visualized the TS structures (Figure 5.8). As previously observed,[123,304] ACE-generated TS structures resemble those previously proposed (see Appendix D for references). We then investigated whether the stereoselectivity predictions were accurate. The error of the prediction of $\Delta\Delta G^{\ddagger}$ between the major diastereomeric TS's was computed and compared to a random assignment (Figure 5.9). We note that none of the FFs used by ACE in these tests have been trained specifically on these reactions. Since Q2MM TSFFs have been derived to complement MM3* and ACE is using MM3, the accuracy presented herein may underestimate the accuracy of the TSFFs.

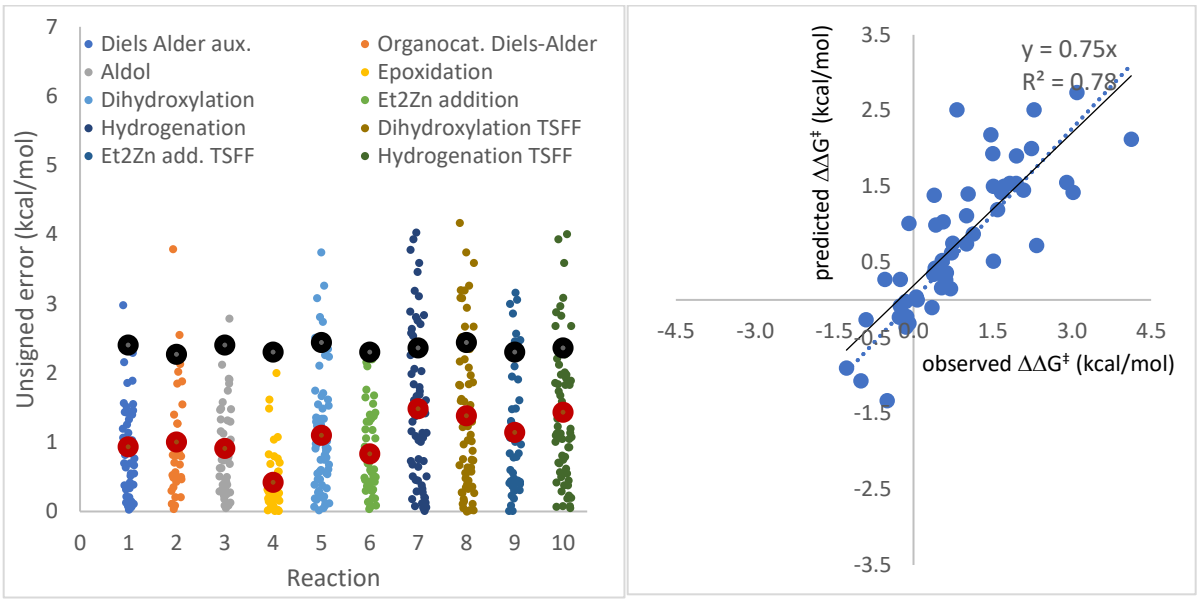

Figure 5.9. Left: Mean unsigned error for $\Delta\Delta G^{\ddagger}$ (kcal/mol) between the predicted and experimentally measured reactions for each catalyst/auxiliary-substrate pair; 1 to 7 refer to seven reaction types using ACE; 8-10 refers to three reactions using ACE and reported Q2MM-derived TSFFs. The black dots refer to the error should we select a random value from -4.12 to 4.12 kcal/mol (i.e., maximum stereoselectivity of 1000:1). In red is shown the average of the unsigned error over the set of catalysts/auxiliaries used for each reaction type. **Right:** Predicted vs. observed

$\Delta\Delta G^{\ddagger}$ for a set of 51 asymmetric catalyst/substrate pairs (epoxidation reaction). Positive $\Delta\Delta G^{\ddagger}$ represents one enantiomer, while negative $\Delta\Delta G^{\ddagger}$ represents the other enantiomer.

As can be seen in Figure 5.9, the overall average error ranges between 0.94-0.97 kcal/mol (over five runs). This ~1.0 kcal/mol value, often referred to as chemical accuracy, is the gold standard in quantum chemistry and catalysis.[319] With this accuracy, the platform can distinguish poor asymmetric catalysts (0% ee, $\Delta\Delta G^{\ddagger}$ ~0 kcal/mol) from good asymmetric catalysts (90% ee, $\Delta\Delta G^{\ddagger}$ ~1.4 kcal/mol) and good from excellent asymmetric catalysts (99% ee, $\Delta\Delta G^{\ddagger}$ ~2.8 kcal/mol). It is noteworthy that some of the catalysts used in this set have been reported producing various enantioselectivities depending on conditions (e.g., acid co-catalyst, solvent and temperature, see for example [320]). Although, ACE considers solvent (implicit model) and temperature (Boltzmann population), manipulating the two parameters did not improve accuracy. The nature of the acid co-catalyst in the Diels–Alder reaction was not considered.

ACE produces a similar average mean unsigned error (within 0.2 kcal/mol) whether using the original MM3 implementation or the Q2MM-generated TSFF. A closer look at the Shi epoxidation reaction (Figure 5.9 right), revealed that most weakly stereoselective catalysts (e.g., $\Delta\Delta G^{\ddagger}$ <1.0 kcal/mol) were predicted to be weak, while most strongly stereoselective (e.g., $\Delta\Delta G^{\ddagger}$ > 2.0 kcal/mol) were predicted to induce strong stereoselectivity. We then investigated the false-positives and false-negatives that, in large part, result from poor parameters in the MM3 force field rather than intrinsic problems in the methodologies. For example, sugar derivatives such as **6**, conjugated systems (aniline nitrogen and axial chirality) such as **3**, sulfonamides (**5**), silylethers (**4**), polycyclic compounds (**8**, **9**) and complex phosphine ligands (**10**) are not well parameterized in MM3 (Figure 5.10). In particular, phenyl sulfonamides have a very specific torsional energy

profile (although MM3 parameters for alkyl sulfonamides have been reported [321]), while phosphines can adopt different cone angles.[322]

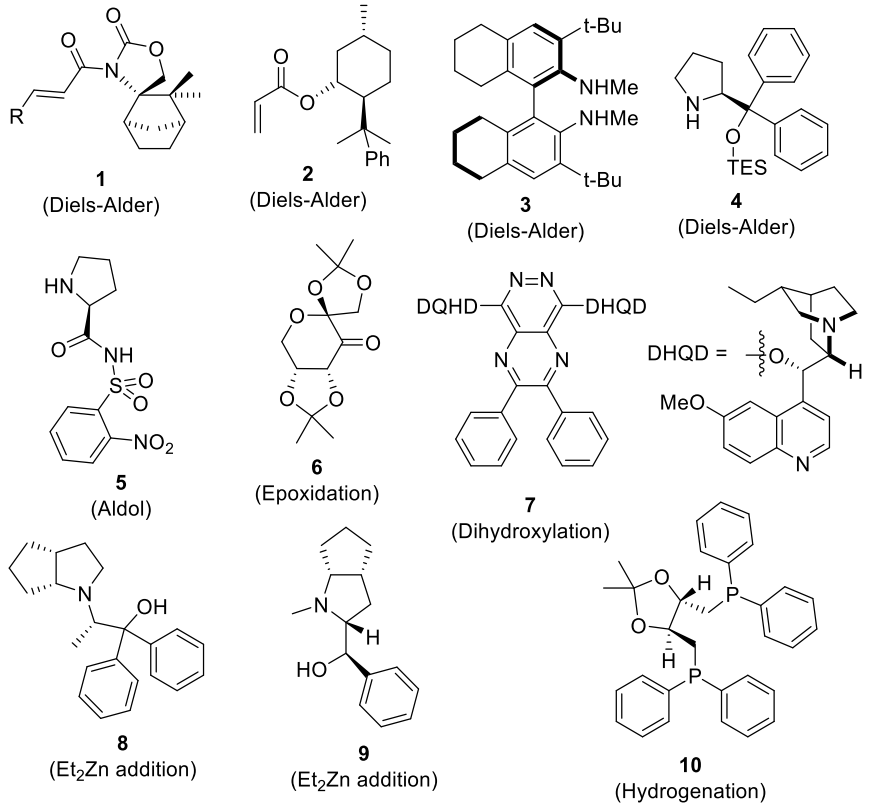

Figure 5.10. Example of substrates and catalysts which resulted in $\Delta\Delta G^{\ddagger}$ errors of 2 kcal/mol or more.

Overall, the data demonstrated that this platform can be used to retrospectively evaluate asymmetric catalysts through interaction with the chemists and prompted us to start a larger virtual screening study.

5.4.2. Scenario #2 – Novel Chemical Series.

A chemist may be looking for a new chemical series as catalysts for a known reaction. To exemplify this scenario, we chose the Shi epoxidation and organocatalyzed Diels-Alder reaction. The two well-characterized reactions are chosen here due to the existence of few known, highly

selective catalysts. As a result, we expect to generate decoys from library filtering and attempt to recover the known molecules embedded in this list.

A library of ca. 140,000 chiral amines was assembled from the ZINC database[323] for the Diels-Alder reaction and the workflow shown in Figure 6A was assembled. Molecular descriptors were computed for these molecules and used to extract only those of interest (MW<500, uncharged compounds, only secondary amines, aldehydes, and other reactive functional groups removed). Then any molecules too similar to known catalysts (e.g., proline methyl ester in organocatalyzed reactions) were removed since the objective was to discover "new chemical series". At this stage, nearly 10,000 potential catalysts were selected. SELECT was used to remove analogues and pick the most diverse molecules (for optimal computing time). To ensure that no duplicates were left, our program DIVERSE was applied. 1,307 candidate catalysts remained for screening.

The evaluation of the 1,307 chiral secondary amines was carried out in two steps. A second workflow (Figure 5.11B) filters molecules for their reactivity. It is well established that some amines are more reactive (basic and/or nucleophilic) than others.[324] In this workflow, various reactivity parameters were computed using QUEMIST. Subsequently, REDUCE filtered molecules predicted to be less reactive than proline methyl ester (a known catalyst for the Diels-Alder reaction) based on the nucleophilicity indices computed with QUEMIST. CONSTRUCTS processed the remaining 798 molecules to assemble the TS structures that are finally used by ACE to compute stereoselectivity. These calculations were completed in 10 days using a single core. Six known catalysts were added to the library to assess the accuracy of ACE to recover them (Figure 5.11C).

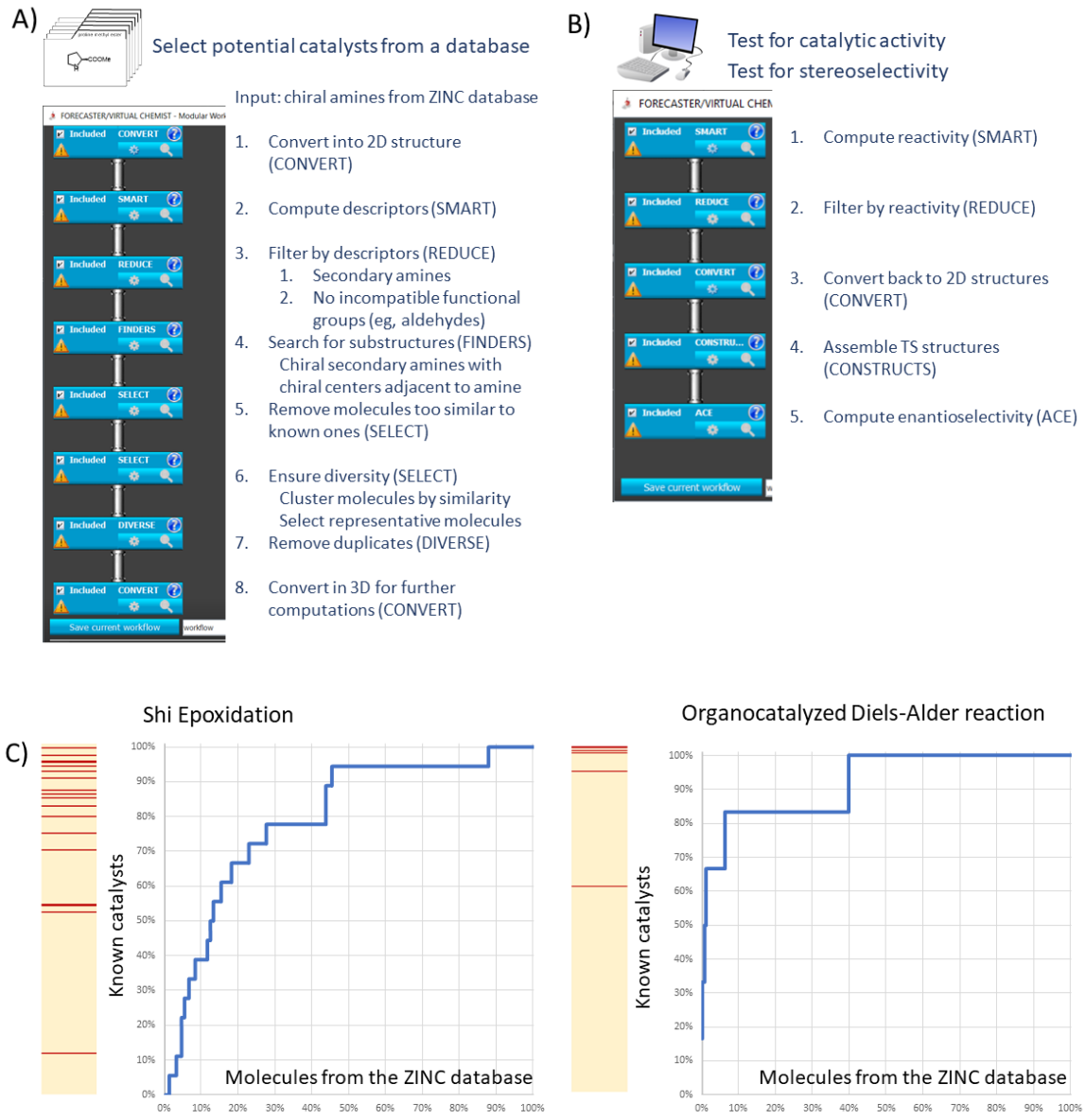

Figure 5.11. A) Workflow for selecting most diverse molecules for screening with description of the actions on the right. **B)** Workflow for screening molecules with description of the actions on the right. **C)** Ranking of predicted catalyst enantioselectivity by ACE in the Shi epoxidation and Diels-Alder reactions. The red lines in the bar indicates the ranks of known stereoselective catalysts. The graph indicates the portion of known catalysts vs. the portion of molecules from the ZINC database.

The same overall process was applied to the search for Shi epoxidation catalysts starting from chiral ketones (very few in available chiral chemical databases) complemented with chiral secondary alcohols converted into chiral ketones using our program REACT2D. 18 known stereoselective catalysts were added to the library (Figure 5.11C). Most of the known stereoselective catalysts are ranked high, shown in Figure 5.11C (Area Under Receiver Operating Curve (AUROC): 0.79 for Shi Epoxidation and 0.92 for Diels-Alder).

The evaluation of the program in this second scenario suggests that our platform can virtually screen numerous chemicals and discover novel chemical series of asymmetric catalysts. In addition, the options to use these programs in workflows enable chemists to guide the platform towards novel chemical series with specific features and to reduce chemical compatibility issues.

5.4.3. Scenario #3 – Virtual Analogue Search.

A chemist may have a hit molecule (e.g., from Scenario #2) and will look for analogues with improved selectivity. We used a detailed study by Gerosa *et al.*[325] to simulate this scenario. In this report, chiral pyrrolidine derivatives were synthesized and tested as organocatalysts for the Diels-Alder cycloaddition after the core scaffold was identified as a promising candidate. As shown in Figure 5.12, this research project can be simulated within a single workflow. Imines are synthesized and subsequently reacted with a chiral dipolarophile to make three potential diastereomers. These pyrrolidines are then assessed in both *endo*-Diels Alder and *exo*-Diels Alder cycloadditions. In practice, each reaction step requires extensive experimental work to isolate and characterize the stereoisomers.

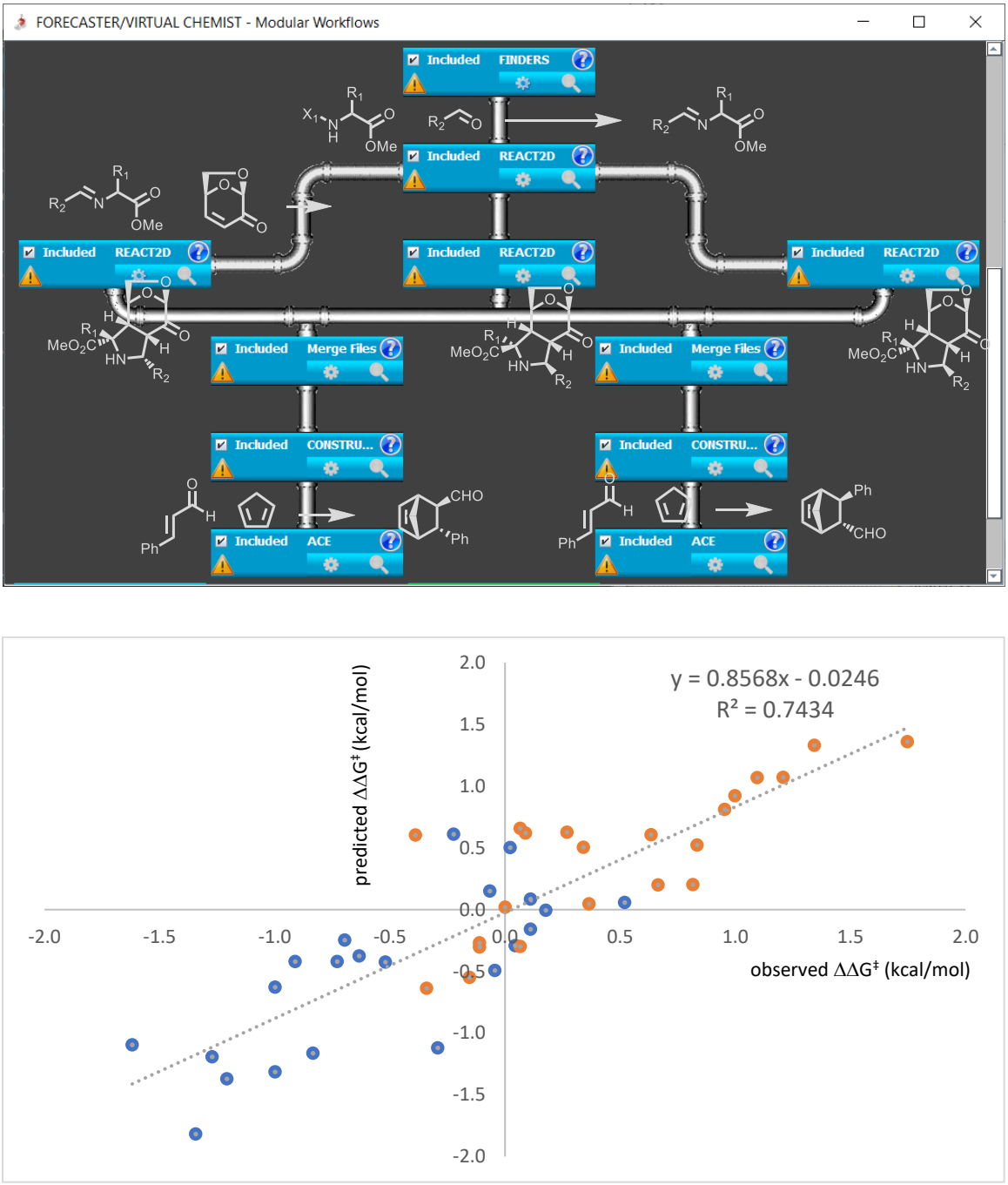

Figure 5.12. Optimization of asymmetric organocatalysts for Diels-Alder cycloaddition. **Top:** Workflow. **Bottom:** Predicted and experimentally observed enantioselectivity obtained with chiral pyrrolidine derivatives. Orange: *endo* adduct, blue: *exo* adduct. Insert: mean unsigned error (blue: each substrate, red: average, black: random). Positive $\Delta\Delta G^{\ddagger}$ represents one enantiomer, while negative $\Delta\Delta G^{\ddagger}$ represents the other enantiomer.

As seen in Figure 5.12, this virtual lead optimization had a mean unsigned error as low as 0.33 kcal/mol. The most stereoselective catalysts predicted by ACE were the best (*endo*) and second best (*exo*) experimentally. This study was completed in just a few days on a standard Windows PC and could be extended to hundreds of analogues.

5.4.4. Scenario #4 – Catalyst Substrate Scope.

A chemist may evaluate the potential substrate scope of a given catalyst. This last set of calculations was done using $(DHQD)_2PHAL$, a now commercially available catalyst for the Sharpless asymmetric dihydroxylation of alkenes. This catalyst has been virtually (and previously experimentally) applied to 25 substrates and compared to experimental data (Figure 5.13).

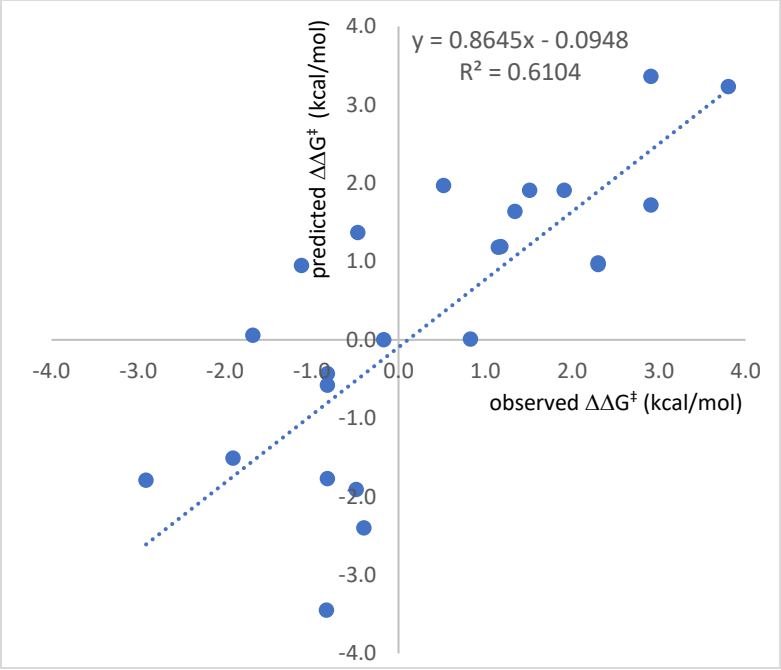

Figure 5.13. Substrate scope study with $(DHQD)_2PHAL$. Insert: mean unsigned error (blue: each substrate, red: average, black: random). Positive $\Delta\Delta G^{\ddagger}$ represents (*R*) and (*R*,*R*) isomers, while negative $\Delta\Delta G^{\ddagger}$ represents the other isomers.

Overall, this last simulation suggests that the catalyst would be highly enantioselective (≥97%ee) on ca. 25% of the substrates and on ca. 20% it would be poorly selective (≤40%ee), in excellent agreement with the experiments. However, we observed a poorer reproducibility for dihydroxylation (large standard deviation over multiple runs) than with the other reactions (Figure 5.10, Table 5.1). This can be explained by the significantly larger size and flexibility of the catalysts used in dihydroxylation (Figure 5.10) and suggests a limitation of the approach. More time and computational resources may be required to adequately search the conformational space of such systems. Three substrates are consistently poorly predicted (over 5 runs). One of these failures can be attributed to the poor parameterization of sulfur-containing groups (tosylate in this case). The other two are a *cis* olefin (the FF parameters were developed using a *trans* olefin) and a naphthalene derivative which contributes significant π-π interactions with the catalyst. Interestingly, the predicted average enantioselectivity varies from 67 to 76%ee over 5 runs while it is 73.6%ee experimentally with an overall good correlation with experiments.

5.5. Reproducibility.

Because ACE relies on a stochastic method (genetic algorithm with random generation of conformations to start from), we ran the same experiments 5 times with different seed numbers (affecting the random number generator) to evaluate the reproducibility of the method for scenarios #1, #3 and #4 (Table 5.1). As can be seen in Table 5.1, the accuracy on all the reaction sets is highly reproducible. However, when looking at individual results, dihydroxylation seems to be less reproducible likely due to the significantly large size and flexibility of the systems.

Table 5.1. Reproducibility of ACE on scenarios #1, #3 and #4.

Entry	Reaction	MUE $\Delta\Delta G^{\ddagger}$ (std dev.)	
		Whole set[a]	**Average individual [a]**
1	Diels-Alder with chiral aux.	0.93 (0.00)	0.93 (0.01)
2	Aldol reaction	0.94 (0.02)	0.94 (0.07)
3	Organocatalyzed Diels Alder	0.99 (0.03)	0.99 (0.10)
4	Epoxidation	0.44 (0.02)	0.44 (0.05)
5	Dihydroxylation	1.14 (0.03)	1.14 (1.30)
6	Dihydroxylation (TSFF)	1.39 (0.15)	1.39 (1.25)
7	Et_2Zn addition	0.83 (0.01)	0.83 (0.09)
8	Et_2Zn addition (TSFF)	1.07 (0.05)	1.07 (0.23)
9	Hydrogenation	1.42 (0.04)	1.42 (0.21)
10	Hydrogenation (TSFF)	1.44 (0.05)	1.44 (0.25)
11	Lead optimization study	0.32 (0.01)	0.32 (0.02)
12	Substrate scope study	0.96 (0.08)	0.96 (0.62)

[a] Whole set: MUE is average over the whole set of catalyst/substrate systems for each seed and average and standard deviation for these 5 overall accuracy values are measured. Average individual: the standard deviation is computed for each catalyst/substrate systems and averaged over the set.

5.6. Conclusions.

Our efforts to interface computational and organic chemistry have led to the creation of the VIRTUAL CHEMIST platform, which aims to shift the paradigm of pursuing asymmetric synthesis projects. This platform is user-friendly (designed for organic chemists) and highly customizable through the introduction of modular workflows. The power of these modular workflows and of the

individual programs making up the VIRTUAL CHEMIST software suite (free for academic use) has been demonstrated through the in-depth analysis of four realistic scenarios which could comprise various asymmetric synthesis projects. We believe that every computational approach carries its own caveats.

Here, we acknowledge that the methodology presented requires a mechanism-based transition state to study—much like docking potential drug molecules requires a target structure. Additionally, the MM-based computations suffer from current FF limitations, although efforts are ongoing to overcome this obstacle. Last, large catalytic systems provide a challenge for conformational searching in transition state optimization and can lead to simulations trapped in local energy minima. Notwithstanding these obstacles, we demonstrated the reliability and accuracy of our platform, which can distinguish weak from good, and good from great asymmetric catalysts with chemical accuracy in most cases. With this platform, chemists could now test ideas in a matter of hours, a fraction of the time needed to synthesize and test novel catalysts. We believe that our computational approach will lead to a more efficient catalyst discovery, as our simulated experiments allow a broader exploration of the chemical space than experiments allow, in a shorter amount of time. Moving forward, we hope that computational chemistry will have the same impact on organic chemistry as NMR, MS and chromatography had at the time of their incorporation into the chemists' toolbox or as structure-based design software had in medicinal chemistry.

Chapter 6 – Conclusions and Future Work

Looking back over the last 60 years of computational chemistry development, it is evident that the current state of the field has surpassed the expectations of its pioneers. With the advent of increased computational power for even a simple user, along with the development of highly efficient and user-friendly computational tools, the usage of these tools within the experimental community has become widespread. This, in turn, allows experimentalists to provide essential feedback to the computational chemistry community, which drives the computational development efforts forward. There is a plethora of applications of computational tools in experimental chemistry, but, in this thesis, we have focused on nucleoside modeling, cytochrome P450 inhibition prediction and the development of a virtual asymmetric catalysis platform.

To begin with, in Chapter 1 we gave a brief overview of computational tools and their applications in organic and medicinal chemistry. These tools range from fast and less accurate methods such as molecular mechanics (MM) to accurate, time-consuming, and computationally expensive quantum mechanics (QM) methods. One can also combine these two methodologies to run QM/MM simulations or can move away from these methods to focus on machine learning (ML) methods. We showed that MM is widely used in fields ranging from protein dynamics and folding to docking and catalyst design while QM methods are useful in explaining reaction mechanisms, describing chemical reactivity and predicting drug sites of metabolism (SoMs), as well as designing catalysts. To describes events such as bond breaking/forming in enzyme catalysis, MM and QM methods must be combined to yield accurate, cost, and time-effective calculations (QM/MM calculations). Due to their cumbersome setup which requires expertise in computational chemistry, QM/MM simulations are generally less accessible to medicinal chemists, but efforts are continuously made to make these simulations more user-friendly. The last

class of computational methods we discussed was ML, which has become widespread in computational chemistry, and has led to some very interesting applications, particularly in medicinal chemistry. For example, several ML tools have been proposed for predicting the SoMs of drug-like molecules. These tools are fast and easy to use when setup in user-friendly environments (i.e. standalone programs or webservers) but are highly dependent on the quality of the data they have been trained on.

Following the introduction to computational tools in Chapter 1, in Chapter 2 we focused our attention on nucleoside modeling. Generally, nucleosides preferentially adopt two different conformations that are in equilibrium in solution: *North* and *South*, determined through the computation of the pseudorotational phase angle P. The distinction between these conformations is important, since nucleosides with a sugar pucker in the *South* conformation are preferentially phosphorylated by kinases, while *North* type nucleosides are preferentially incorporated by polymerases. To establish the *North/South* equilibrium, each nucleoside must be synthesized and subjected to NMR experiments. This methodology involves significant synthetic cost, waste production, energy expenditure, and time. To expedite the process and reduce the cost associated with synthesizing nucleosides, we developed a medium-throughput computational protocol based on hybrid QM/MM umbrella sampling simulations that allows the accurate determination of *North/South* equilibrium *in silico*. This approach allows the design and *North/South* ratio determination of hundreds of nucleoside analogues with the only cost being CPU time. In our study, we observed that our approach yields accurate *North/South* ratios for a range of non-natural nucleosides and low-energy structures that are comparable to crystal structures in the case of a set of carbohydrates. However, this methodology is not without fault. For example, we discovered that sulfur-containing nucleosides are not properly described by our simulations due to the lack of

specific parameters for sulfur-containing rings in SCC-DFTB, the semiempirical model used for the QM part of the simulations. Future work would thus involve the development of more accurate parameters for heavy atoms such as sulfur. Moreover, it would be interesting to benchmark the duration of the simulations at which a *North/South* equilibrium convergence arises. For now, our simulations run for 73 ns, but this time could be shortened depending on the results of the benchmark (in real time 1 ns of simulation takes on average 12-14 hours on 12 CPUs; however, having supercomputers at our disposal allows us to run the simulations in parallel, which means that all 73 ns of simulation can be run at the same time). In addition, the current methodology is fairly involved and requires some computational expertise in setting up the simulations. Thus, it would be essential to explore the implementation of a user-friendly way to setup the simulations and analyze the results, which could make it highly attractive to organic and medicinal chemists.

Taking advantage of the methodology developed in Chapter 2, we decided to apply this tool to non-natural nucleosides that exhibited valuable properties as described in Chapter 3. In this chapter, we focused on two different situations. First, we determined the conformational preferences of nucleosides containing various electronegative substituents at key positions on the sugar ring. These substituents are excellent hyperconjugation acceptors and are known to modulate the sugar conformations. Using our methodology, we demonstrated that we could obtain both accurate *North/South* ratios for these nucleosides and computed low-energy structures that are close to crystallographic ones, with heavy atom RMSDs < 1Å. Second, we explored the nature of nucleosidic fluorine-hydrogen bonds, and we provided evidence (confirmed by experimental data) of their existence.

Further work. From this work, we gained invaluable insight into how non-natural nucleosides with different electronegative substituents behave in solution, which opens the possibility of

designing novel nucleosides that make use of subtle interactions. Further work in this area is underway. We have recently started a collaboration with Prof. Jack Szostak's laboratory at Harvard University in which we are using our methodology to establish the origin of RNA life. The RNA world hypothesis proposes an early stage in the evolution of life in which RNA was responsible for both catalysis and genetic inheritance. Before the evolution of protein enzymes, a replicase made of RNA (ribozyme) may have catalyzed RNA synthesis. A more challenging problem is how these ribozymes could have emerged from a non-enzymatic process of chemical RNA replication. Currently, the chemical copying of RNA is not able to produce RNA products of the length and complexity necessary to sustain ribozyme evolution. An essential component in this process is a primer, which is added by an enzyme to the RNA template to be copied. Thus, we aim to study the effect of the sugar conformation of the terminal residue of the primer on the rate of chemical RNA copying. Moreover, we are further working on establishing a protocol for describing RNA-RNA and DNA-RNA duplexes involving oligonucleotides comprised of non-natural nucleosides, which would give us important information into how oligonucleotides would behave in macromolecular complexes.

Another area of interest for organic and medicinal chemists is the xenobiotic metabolism by Cytochrome P450 enzymes, which was discussed in Chapter 4. As part of phase 1 metabolism, six CYP isoforms metabolize up to 90% of drugs currently on the market. Depending on the nature of the drug, CYPs can metabolize it either to harmless or toxic metabolites. Moreover, if a patient is concurrently taking multiple drugs metabolized by the same CYP isoform, the metabolism of these drugs is altered, giving rise to drug-drug interactions. These drug-drug interactions can also arise if one of the drugs metabolized by a CYP isoform is an inhibitor of that isoform. Most commonly, inhibition by these drugs is reversible and takes place if a drug contains a basic nitrogen

atom with an available lone pair that can coordinate to the heme iron (so-called Type II ligands). Currently, CYP inhibition and toxicity is assessed using expensive experimental assays. To offset this, we proposed a novel predictor comprised of QM, docking, and ML to enable the detection of potential CYP inhibitors *in silico*, without the need to synthesize compounds of interest. Using QM on a set of representative Type II ligands, we obtained QM energy profiles which we used to develop a novel LJ(8-4) vdW potential in FITTED that could describe nitrogen-iron coordination. Our self-docking study performed on 85 CYP crystal structures assembled from the PDB showed that the novel potential can describe the nitrogen-iron coordination. Then, we developed an ANN that could distinguish between inhibitors and non-inhibitors, and we determined its accuracy on a set of five major CYPs using curated sets of compounds obtained from experimental bioassays. While our ANN proved to be accurate for the training set, we observed that overtraining had occurred, which affected the accuracy on the testing sets. In addition, we worked on improving our SoM prediction tool IMPACTS, a hybrid method comprised of both QM-derived activation energies for possible SoMs and docking. Our work focused on different areas, such as reactivity indices for SoMs or new activation energies. In the end, it was a fast-to-compute SASA correction for SoM accessibility that provided the best overall increase in accuracy (~5%). The work presented in this chapter will be valuable and aid medicinal chemists in the drug design and development process.

Future work. Efforts are ongoing in our research group to improve the CYP inhibition tool: **1)** we are extracting key interactions between isoform-specific residues and the ligands and including them into the ANN input; **2)** we are trying to balance out the sets to improve sensitivity; **3)** we are evaluating the use of multiple hidden layers as opposed to only one currently in use; **4)** we are optimizing hyperparameters such as dropout rate and conjugate gradient parameters; **5)** we are

currently testing a variety of ML methods, including SVM, and Random Forest models, to see which one performs better in the task of predicting CYP inhibition.

In the last chapter (Chapter 5) we described a unique computational platform – VIRTUAL CHEMIST – designed for organic chemists to undertake an asymmetric synthesis project from A-Z, using only a few clicks. This platform was designed with the needs of experimentalists in mind, meaning that no computational chemistry expertise is needed to use it. Moreover, we implemented a user-friendly GUI that makes the entire process streamlined and easy to use, along with modular workflows, which allows users to create their own customized projects. We validated VIRTUAL CHEMIST on four different realistic scenarios. In the first scenario, we validated ACE on over 350 reactions from seven well-known reaction classes, obtaining an overall average mean unsigned error (MUE) of ~ 1kcal/mol. Due to the inclusion of metal-catalyzed reactions in this set, as well as the lack of parameters for metals in the MM3 FF used by ACE, we resorted to developing our own QM program QUEMIST, which can optimize model systems involving any type of atom and obtain customized FF parameters that can be used by ACE. In the second scenario, we determined the recovery rate of known catalysts for the Shi Epoxidation and organocatalyzed Diels-Alder cycloaddition reactions. Using VIRTUAL CHEMIST, we curated libraries for both reactions starting from several hundred thousand molecules, and we seeded the libraries with known catalysts. Then we computed the enantioselectivities with ACE and ranked the compounds in terms of their *%ee*, obtaining an AUROC of 0.79 for Shi Epoxidation and 0.92 for organocatalyzed Diels-Alder cycloaddition. In the third scenario we reproduced a study from the literature in which chiral pyrrolidine derivatives were synthesized after the identification of a promising core scaffold. Using VIRTUAL CHEMIST, we prepared the necessary customized workflow and assessed the derivatives in both *endo*-Diels Alder and *exo*-Diels Alder cycloadditions, managing to find the best (*endo*) and

second best (*exo*) analogues that had been determined experimentally. In the fourth scenario we determined the substrate scope of $(DHQD)_2PHAL$, a commercially available catalyst for the Sharpless asymmetric dihydroxylation. Our predicted average enantioselectivity varied from 67-76 *%ee* over 5 runs while it is 73.6 *%ee* experimentally, showing that our platform can be used reliably in such a scenario.

Future work in this area is currently underway. We are set to improve the performance of our predictive software, as well as to improve the GUI. Based on the invaluable feedback we have received from the organic chemistry community, we are working on implementing new features to improve the accuracy and usability of the platform and post-calculation data processing. For example, we are working on providing users the ability to potentially obtain improved *%ee*'s by running single point DFT energy calculations using QUEMIST on the lowest-energy transition states that ACE produces and using these energies in the stereoselectivity computations. This approach would have the added advantage of including electrons and more accurate dispersion corrections, which play a significant role in large catalytic systems. Moreover, we are committed to providing VIRTUAL CHEMIST users the ability to automate AUROC computations, as well as a streamlined processing of results in the case of thousands of screened molecules.

Overall, the work presented in this thesis aims to aid organic and medicinal chemists in their endeavours. We have made all efforts to provide detailed descriptions of the hypotheses, study designs, results and limitations for each chapter. Moreover, we are committed to keeping all the software we develop free for academic use, and are fully transparent in our validation studies, with all our results being available for download.

Appendix A

Table A1. Angle information on the lowest energy *North* conformations for the nucleosides used in this thesis.

Entry	Nucleoside	V_0 (°)	V_1 (°)	V_2 (°)	V_3 (°)	V_4 (°)	γ (°)	χ (°)
1	**2.1**	14.93	-8.05	27.84	-36.52	31.78	21.72	-136.57
2	**2.8**	-28.57	2.62	21.89	-40.15	42.31	112.01	69.20
3	**2.18**	-21.63	-0.53	21.33	-34.03	35.30	114.17	-122.12
4	**2.19**	-15.04	-5.96	23.31	-32.10	29.38	113.66	42.59
5	**2.20**	-0.25	-9.59	16.34	-17.56	10.83	46.03	-112.44
6	**2.21**	-2.25	-32.50	53.43	-56.79	35.76	-33.62	-168.66
7	**2.22**	-7.41	-3.18	11.63	-16.17	15.08	120.85	35.72
8	**2.23**	-16.89	1.80	13.51	-24.13	26.00	156.95	-123.16
9	**2.24**	-8.37	-2.43	12.86	-18.32	16.35	156.58	-165.26
10	**2.25**	-17.62	-3.26	21.71	-31.66	31.57	175.19	75.60
11	**2.26**	-27.42	5.82	16.72	-34.06	38.13	-132.54	70.57
12	**2.27**	-26.35	-0.02	24.83	-41.64	41.17	-88.80	63.29
13	**2.28**	-18.47	-3.23	22.08	-33.24	31.65	123.31	67.31
14	**2.29**	-24.91	5.61	23.12	-39.95	39.09	163.86	-2.37
15	**2.30**	-11.54	-5.40	19.07	-25.38	23.35	131.15	58.72
16	**2.31**	-4.83	-15.91	31.73	-34.48	24.76	109.19	55.99

Table A2. Angle information on the lowest energy *South* conformations for the nucleosides used in this thesis.

Entry	Nucleoside	V_0 (°)	V_1 (°)	V_2 (°)	V_3 (°)	V_4 (°)	γ (°)	χ (°)
1	**2.1**	-12.78	32.56	-38.88	31.75	-12.48	96.23	-127.14
2	**2.8**	-15.88	29.15	-30.58	21.60	-3.87	59.28	-142.56
3	**2.18**	-19.25	34.39	-35.61	22.89	-1.53	58.64	-114.31
4	**2.19**	-23.59	24.70	-18.47	5.04	11.85	-68.32	-133.62
5	**2.20**	-11.19	26.16	-31.23	24.93	-7.56	108.37	-120.33
6	**2.21**	-	-	-	-	-	-	-
7	**2.22**	-19.68	30.46	-31.51	19.82	-0.08	151.07	52.86
8	**2.23**	-12.20	17.96	-18.28	10.66	1.22	116.75	-143.97
9	**2.24**	-15.34	22.64	-23.07	14.72	0.30	125.43	-119.38
10	**2.25**	-7.78	21.93	-27.35	22.40	-9.60	-55.30	179.87
11	**2.26**	-25.75	41.19	-42.47	26.42	0.39	95.89	-125.28
12	**2.27**	-6.76	9.49	-8.89	4.81	1.41	-110.09	-123.60
13	**2.28**	-27.74	33.13	-25.94	8.30	12.47	-97.86	-144.34
14	**2.29**	-20.94	42.86	-50.19	33.67	-7.08	161.64	-31.60
15	**2.30**	-14.69	22.22	-22.52	13.73	1.07	133.92	-145.11

16	**2.31**	-9.89	26.79	-34.23	28.98	-11.62	153.75	56.80

Table A3. Puckering information obtained for the nucleosides following the umbrella sampling simulations

Entry	**Nucleoside**	**P_N* (°)**	**ϕ_m**(°)**	**P_S* (°)**	**ϕ_m**(°)**
1	**2.1**	41.3	37.0	179.5	38.9
2	**2.8**	58.5	43.0	168.5	31.2
3	**2.18**	54.0	36.3	165.1	36.9
4	**2.19**	44.5	32.7	135.5	25.7
5	**2.20**	20.7	17.5	177.1	31.3
6	**2.21**	20.8	57.1	0.0	0.0
7	**2.22**	44.8	16.4	162.7	33.0
8	**2.23**	58.9	26.1	159.8	19.5
9	**2.24**	45.7	18.4	161.7	24.3
10	**2.25**	49.3	33.3	181.6	27.4
11	**2.26**	64.0	38.1	162.6	44.5
12	**2.27**	55.0	43.3	154.8	9.8
13	**2.28**	49.7	34.1	140.8	33.5
14	**2.29**	57.0	42.5	171.5	50.8
15	**2.30**	43.1	26.1	160.7	23.9
16	**2.31**	26.3	35.4	182.1	34.3

*P = pseudorotational phase angle; **ϕ_m = puckering amplitude;

Table A4. Data obtained following the NBO analysis carried out at the M06L/def2-TZVP level of theory.

Entry	Nucleoside	$\Delta\sigma_{C3'H} - \sigma^*_{C4'R}$ (kcal/mol)	$\Delta\sigma_{C3'H} - \sigma^*_{C2'R}$ (kcal/mol)	$\Delta\sigma_{C2'H} - \sigma^*_{C3'R}$ (kcal/mol)	$\Delta\sigma_{C3'C4'} - \sigma^*_{C2'R}$ (kcal/mol)	$\Delta\sigma_{C1'2'} - \sigma^*_{C3'R}$ (kcal/mol)	$\Delta n_{O4'} - \sigma^*_{C4'R}$ (kcal/mol)
1	**2.1**	+1.8	+1.5	-4.7	-2.5	+1.8	+1.8
2	**2.8**	+2.7	+2.4	-1.8	-2.3	+0.2	+1.9
3	**2.18**	+5.2	+2.3	-3.4	-3.3	+2.2	+7.7
4	**2.19**	+2.8	-0.3	+0.3	+2.2	+1.3	+5.0
5	**2.20**	+2.1	+0.3	-1.6	+1.1	+1.2	+1.1
6	**2.21**	+2.8	+2.5	0.0	+0.1	+5.8	+7.5
7	**2.22**	+1.2	+0.8	+0.5	+1.2	+1.0	-0.6
8	**2.23**	+0.4	+0.3	-0.8	-0.3	+0.4	+3.6
9	**2.24**	+1.8	+0.7	-1.4	-0.6	+1.1	+2.2
10	**2.25**	+1.9	+2.2	-2.3	-2.1	+1.37	+1.1
11	**2.26**	+1.8	+3.1	-2.9	-2.3	+1.5	+1.5
12	**2.27**	+1.9	+2.0	-1.1	-1.0	+2.2	+1.2
13	**2.28**	+0.8	+0.0	+0.3	+4.0	+1.9	+0.3
14	**2.29**	+3.3	+1.4	+0.5	+1.8	+1.4	+2.2
15	**2.30**	+0.9	+0.2	+0.4	+1.7	+1.6	-0.1
16	**2.31**	+3.7	+0.0	-3.5	+1.3	+1.8	+0.8

The values in Table A4 are presented as energy differences of the stereoelectronic effects found in the *North* and *South* conformation (a + value denotes a stereoelectronic effect dominant in the *North* conformation, while a – value denotes a stereoelectronic effect dominant in the *South* conformation).

The molecular orbitals depicting intramolecular hydrogen bonding (wireframe) for the *North* and *South* conformations were determined using the molecular orbitals obtained following the natural bond orbital analysis. The structures were built in Molekel, using an isosurface value of 0.01.

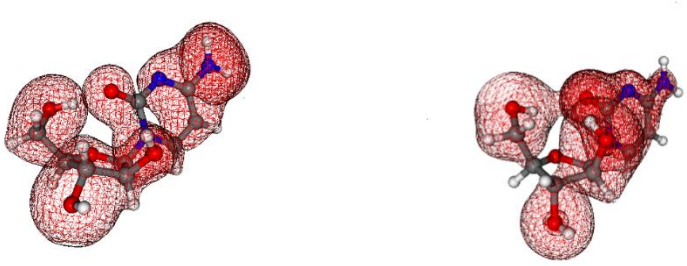

Figure A1. Intramolecular hydrogen bonds for the *North* and *South* puckers for **2.22.** Left – *North* conformation – hydrogen bond between C=O and C5'-OH. Right – *South* conformation – hydrogen bonds between C5'-OH-C=O and C=O-C2'-OH.

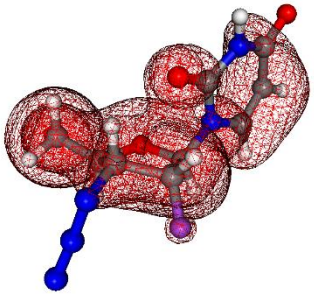

Figure A2. Intramolecular hydrogen bonds for the *North* pucker for **2.25.** Hydrogen bonds between C5'-OH-O4' and C=O-H2' and C=O-H3'.

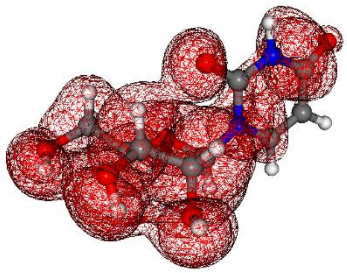

Figure A3. Intramolecular hydrogen bonds for the *North* pucker for **2.27.** Hydrogen bonds between C5'-OH-C3'-OH, C2'-OH-C3'-OH and C=O-C2'H.

Figure A4. Intramolecular hydrogen bonds for the *North* pucker (Left) and *South* pucker (right) for **2.31.** Left – hydrogen bonding between O5-H5-N(base). Right – hydrogen bonding between O5-H5-N(base).

The puckering distributions and PMFs were obtained using the weighted histogram analysis method. For an optimal resolution 73 bins were selected for constructing the graphs and curves.

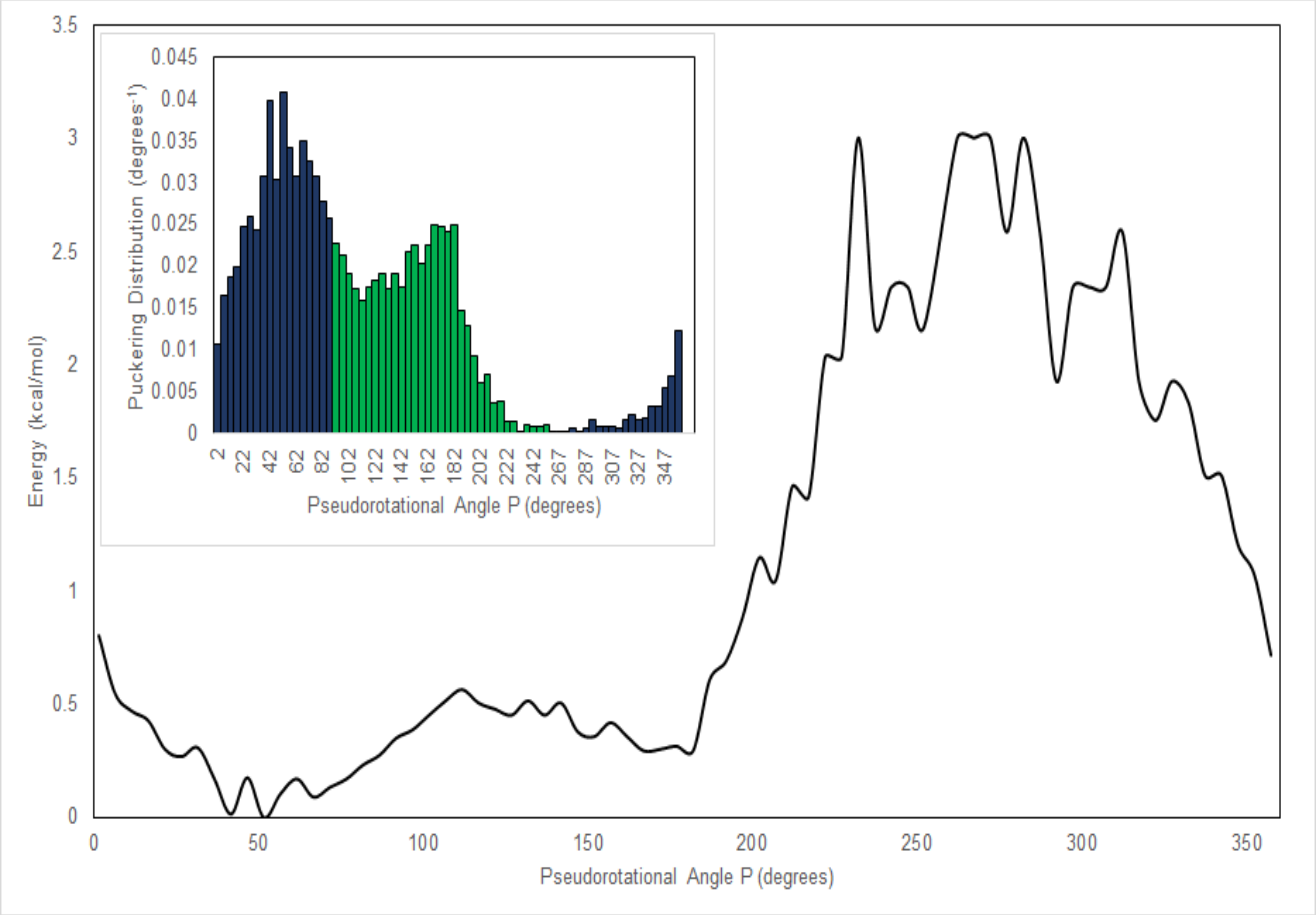

Figure A5. PMF curve for **2.1** along the pseudorotational angle P. Inset shows the puckering distribution around the same angle. Blue – *Northern* conformation, Green – *Southern* conformation.

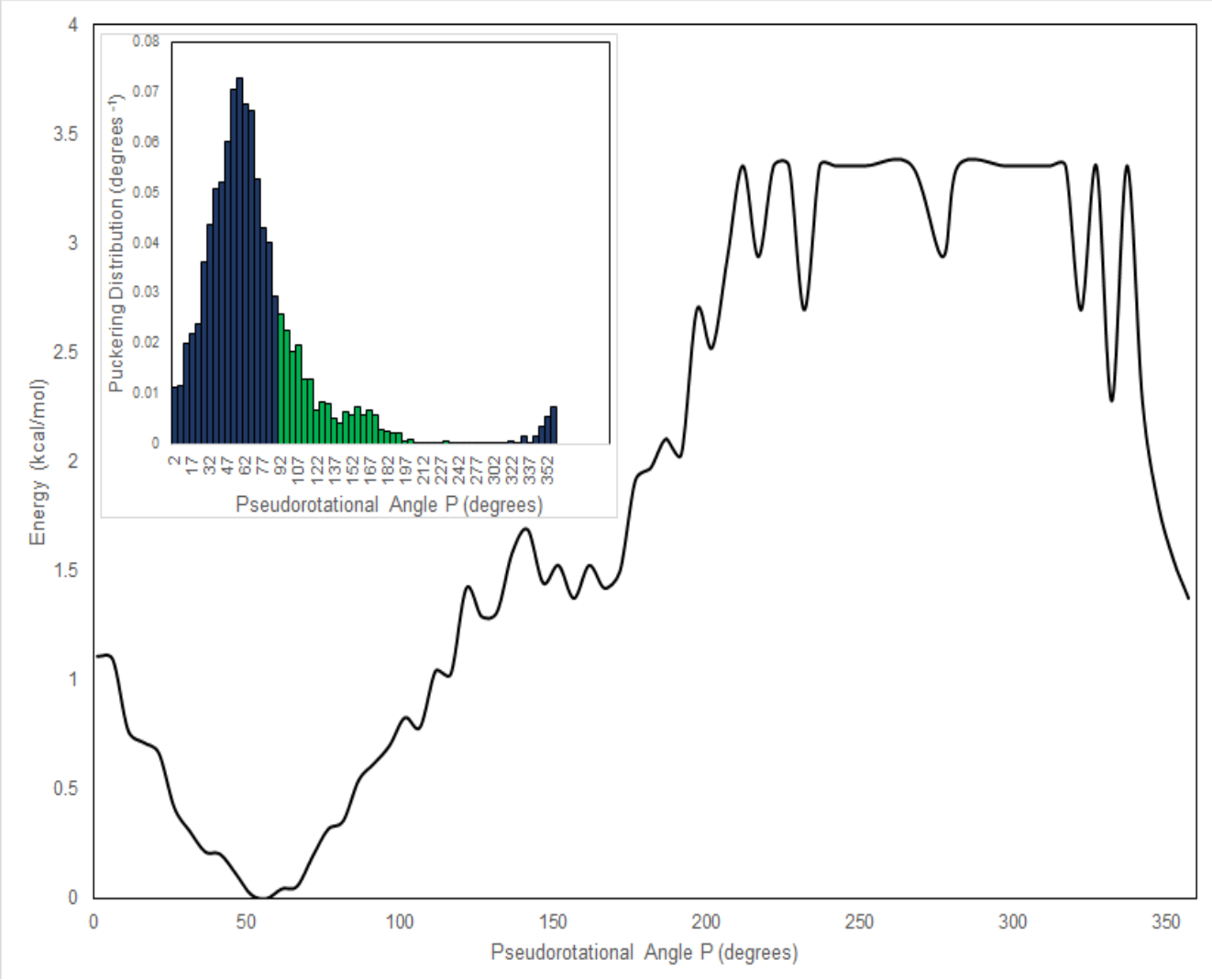

Figure A6. PMF curve for **2.18** along the pseudorotational angle P. Inset shows the puckering distribution around the same angle. Blue – *Northern* conformation, Green – *Southern* conformation.

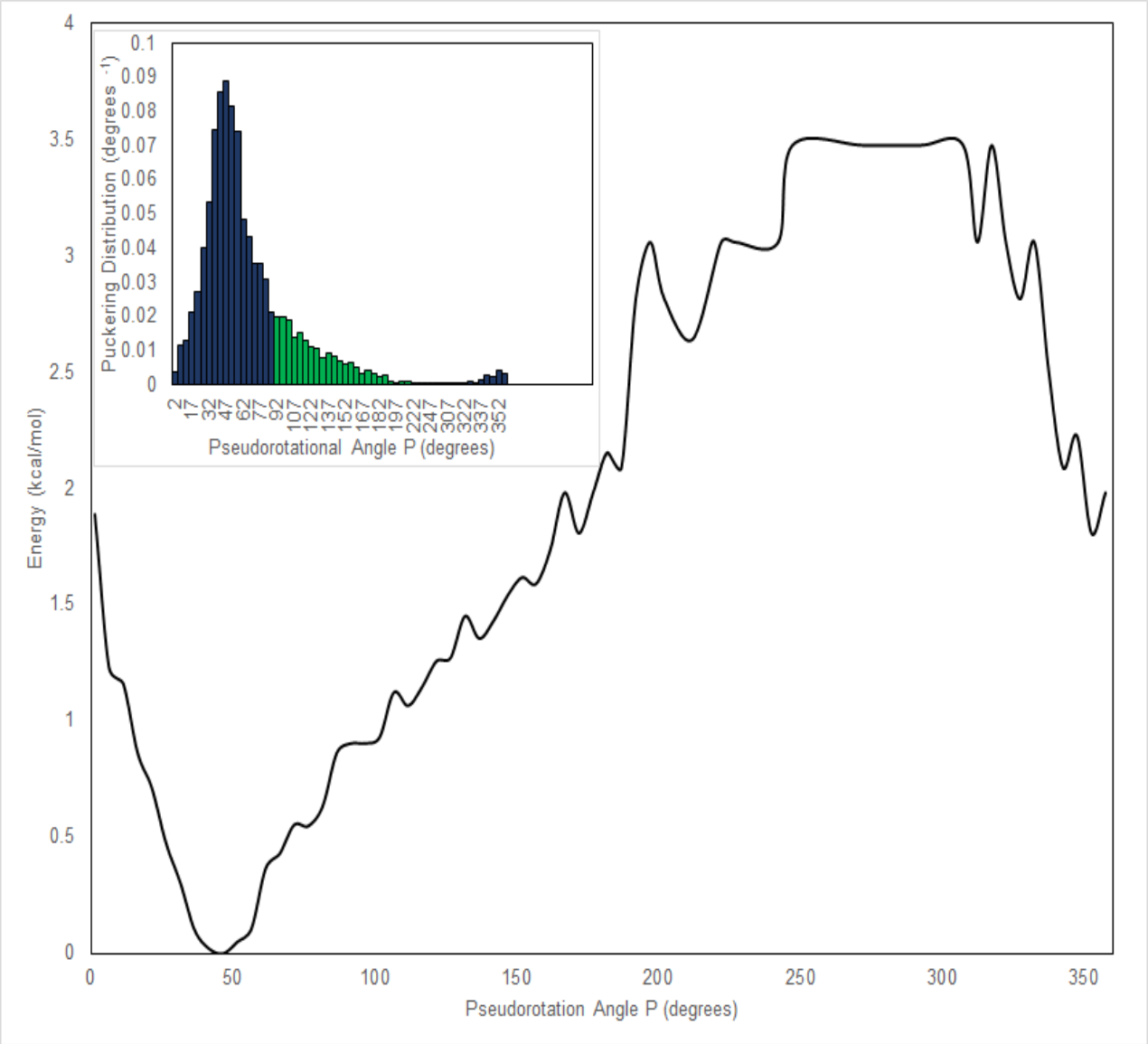

Figure A7. PMF curve for **2.19** along the pseudorotational angle P. Inset shows the puckering distribution around the same angle. Blue – *Northern* conformation, Green – *Southern* conformation.

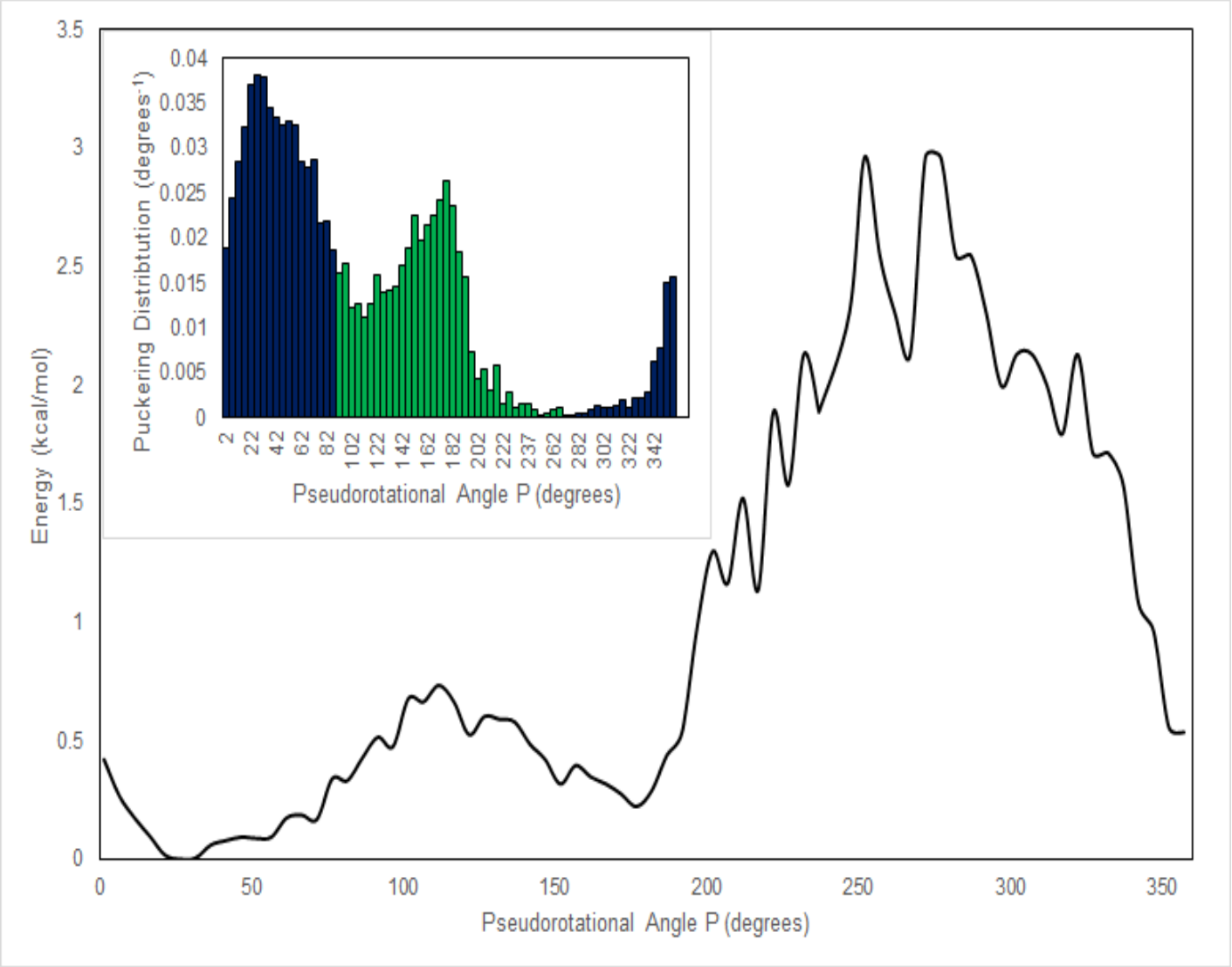

Figure A8. PMF curve for **2.20** along the pseudorotational angle P. Inset shows the puckering distribution around the same angle. Blue – *Northern* conformation, Green – *Southern* conformation.

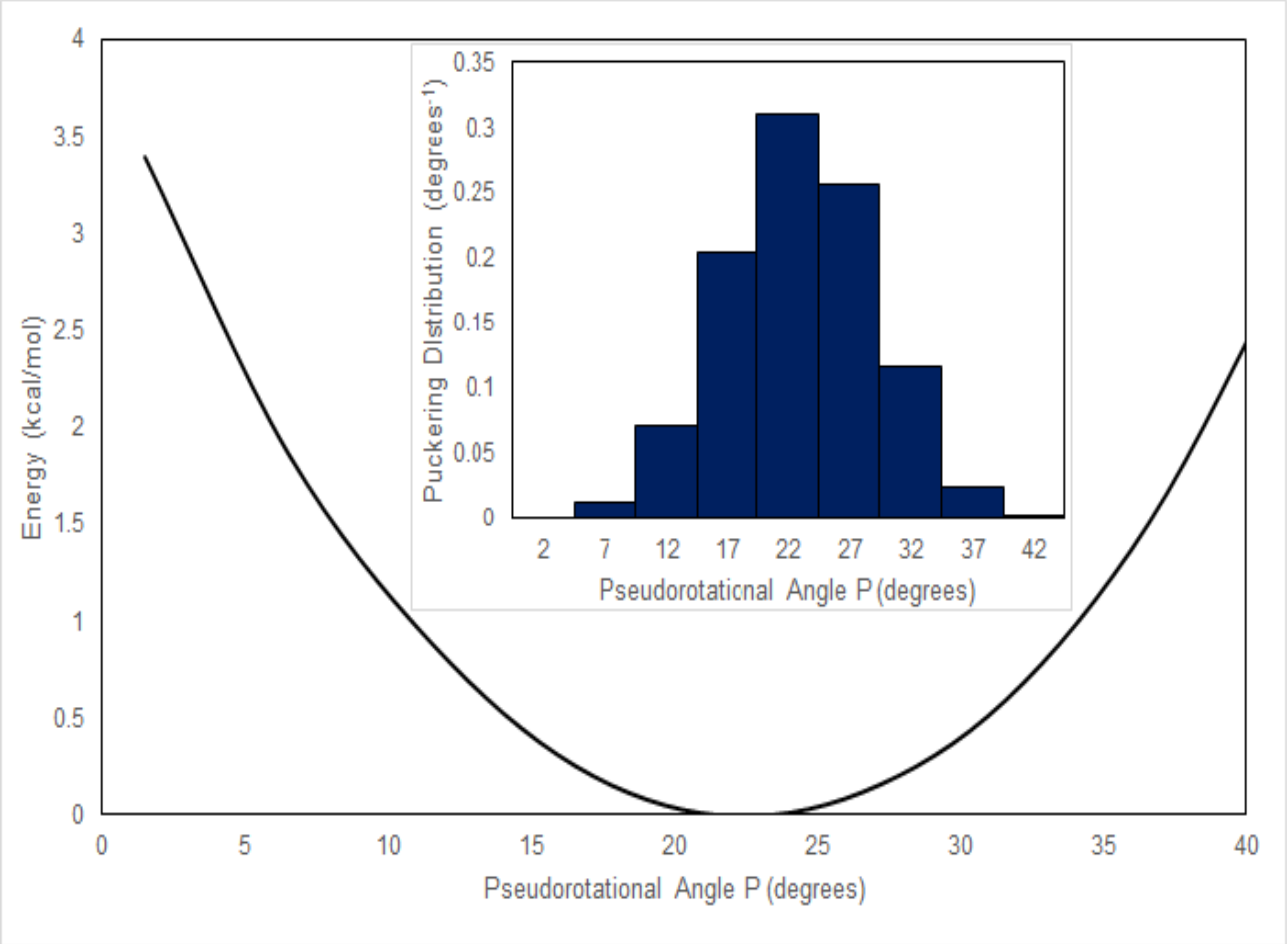

Figure A9. PMF curve for **2.21** along the pseudorotational angle P. Inset shows the puckering distribution around the same angle. Blue – *Northern* conformation.

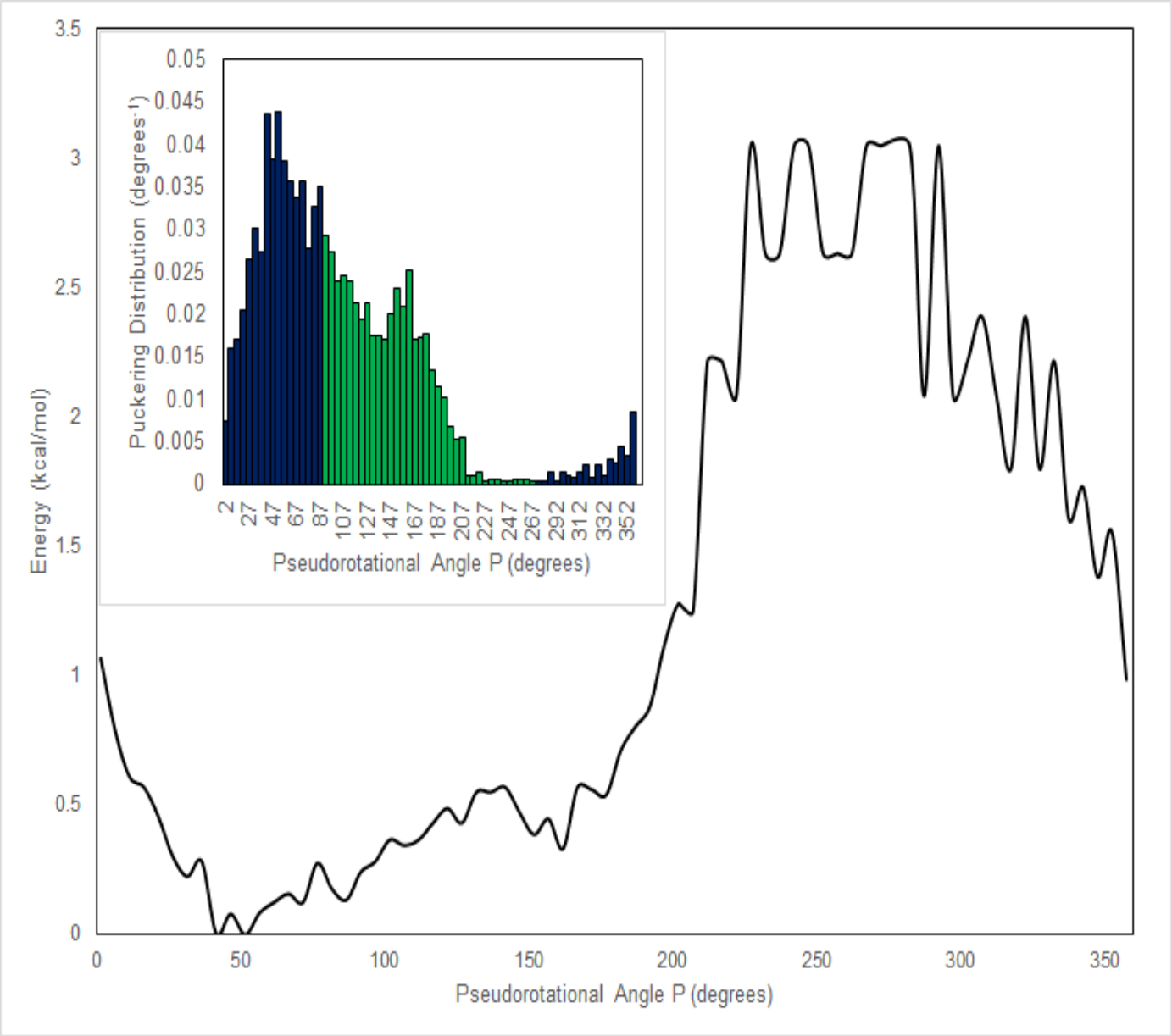

Figure A10. PMF curve for **2.22** along the pseudorotational angle P. Inset shows the puckering distribution around the same angle. Blue – *Northern* conformation, Green – *Southern* conformation.

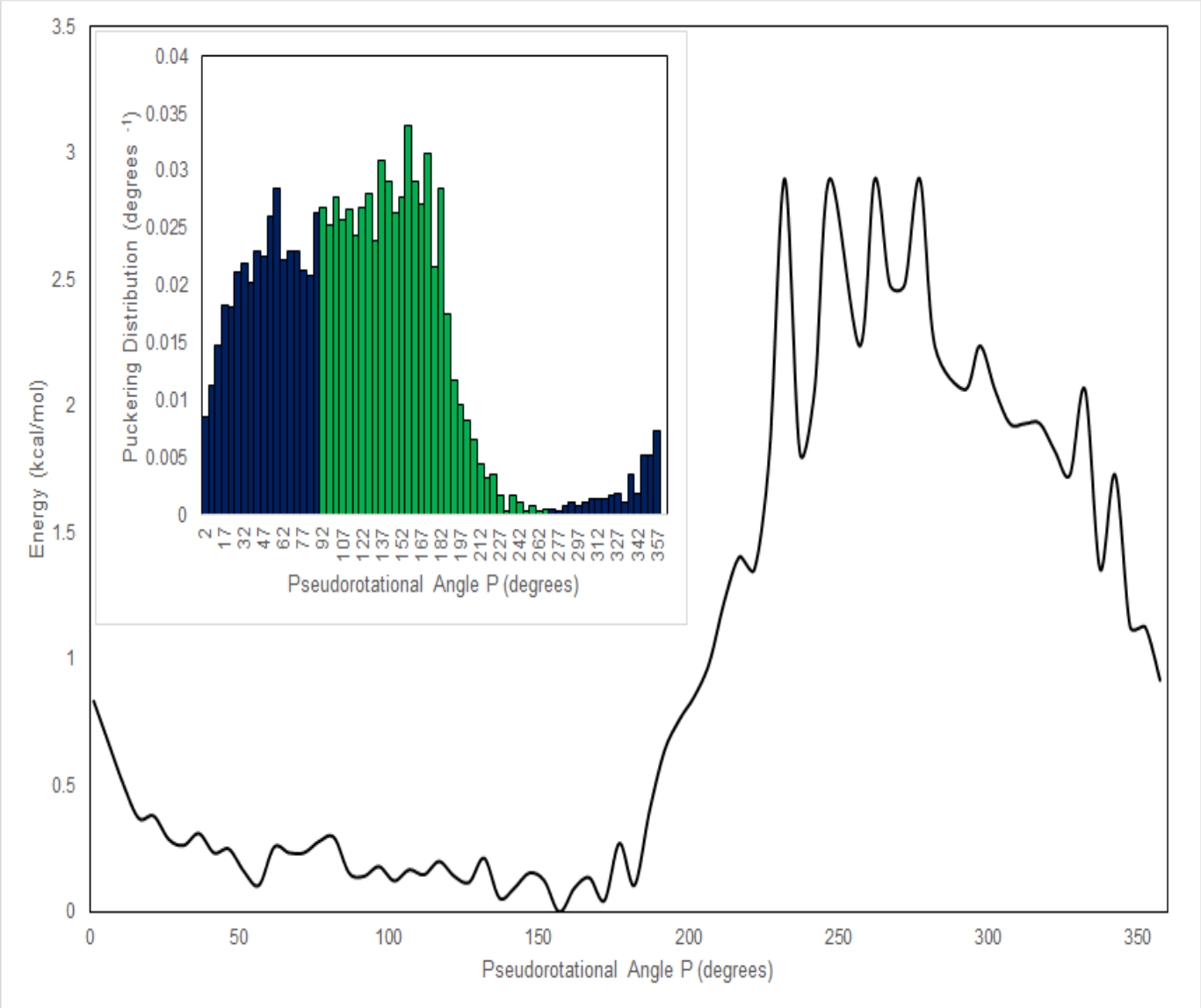

Figure A11. PMF curve for **2.23** along the pseudorotational angle P. Inset shows the puckering distribution around the same angle. Blue – *Northern* conformation, Green – *Southern* conformation.

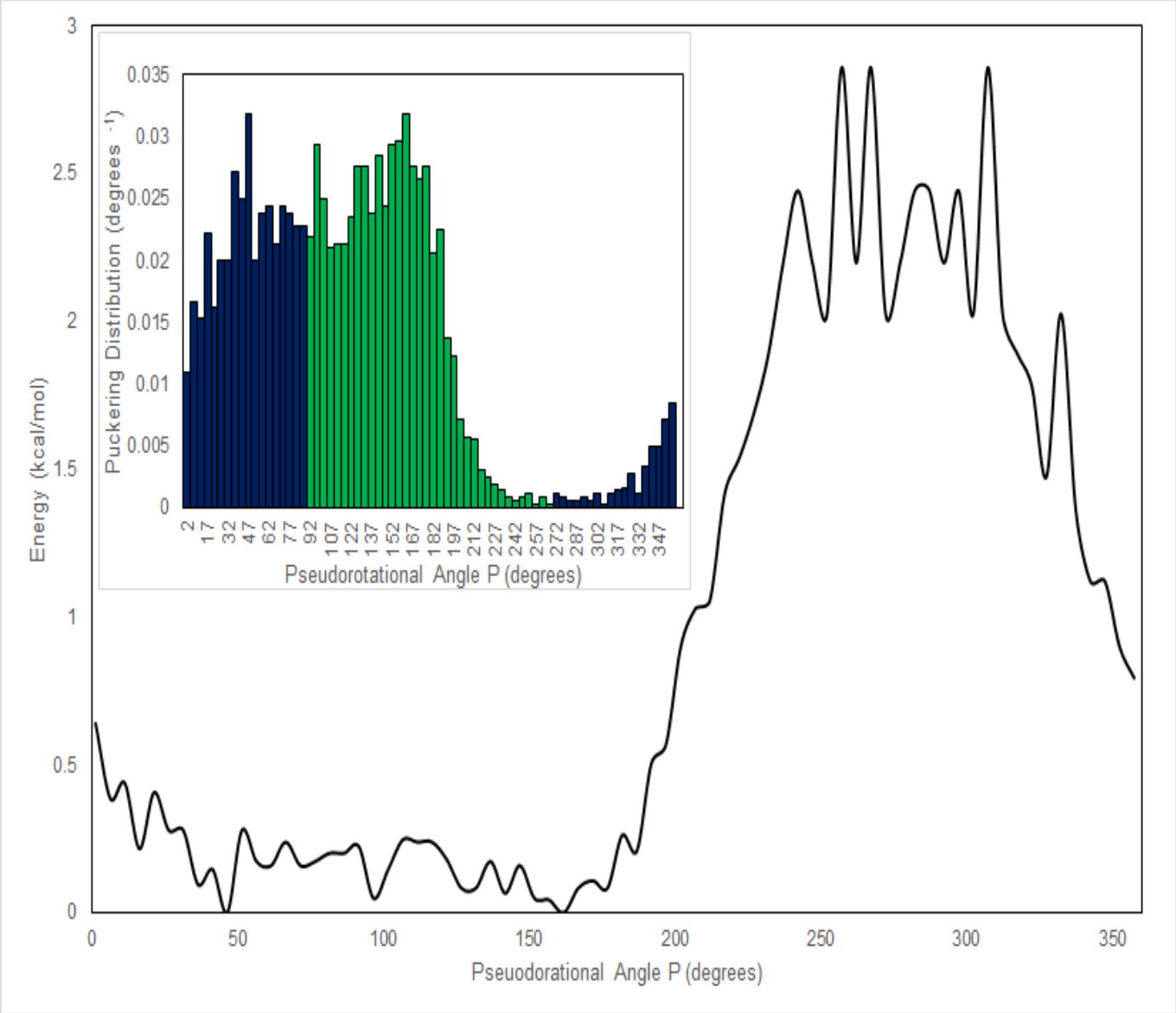

Figure A12. PMF curve for **2.24** along the pseudorotational angle P. Inset shows the puckering distribution around the same angle. Blue – *Northern* conformation, Green – *Southern* conformation.

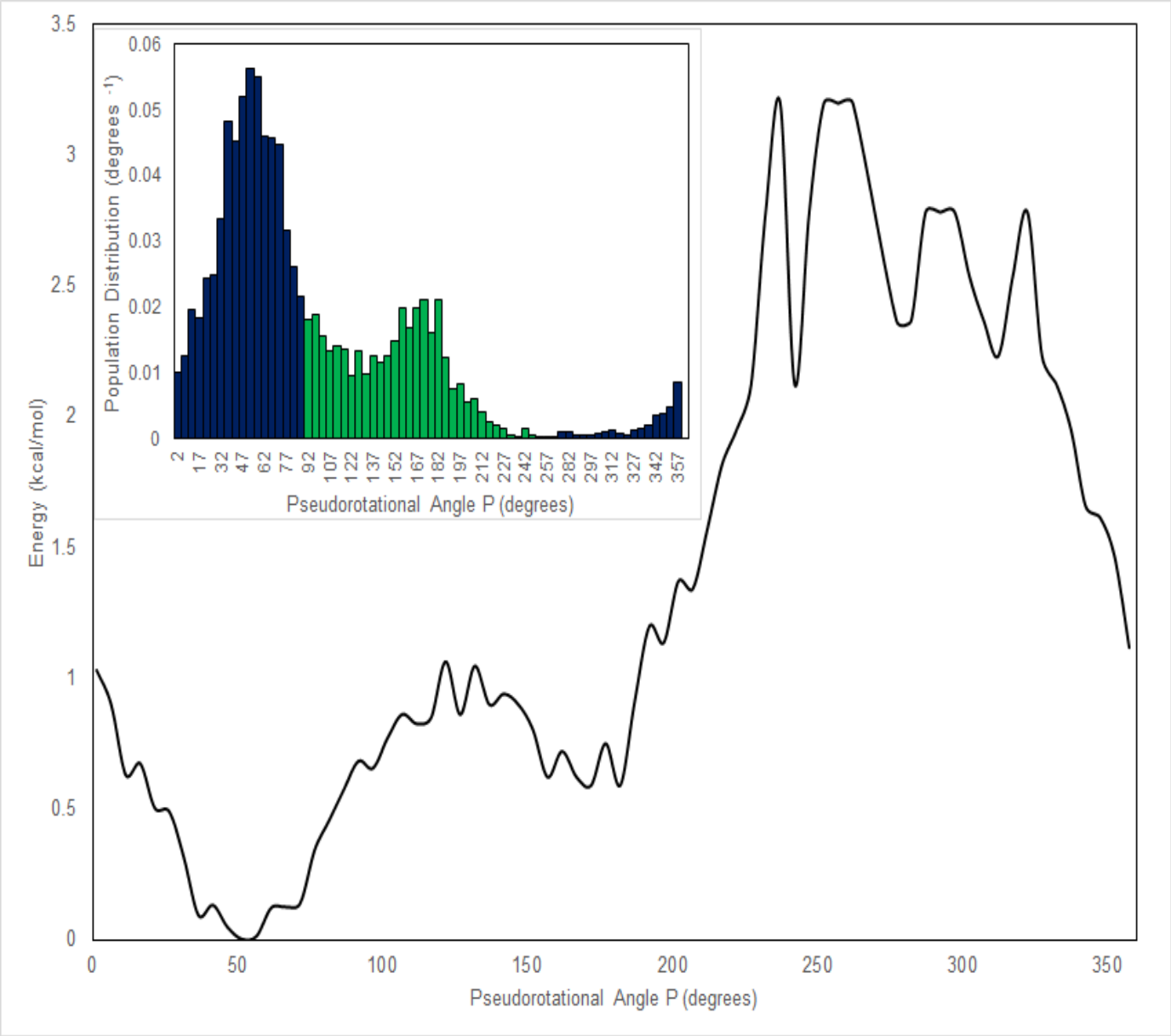

Figure A13. PMF curve for **2.25** along the pseudorotational angle P. Inset shows the puckering distribution around the same angle. Blue – *Northern* conformation, Green – *Southern* conformation.

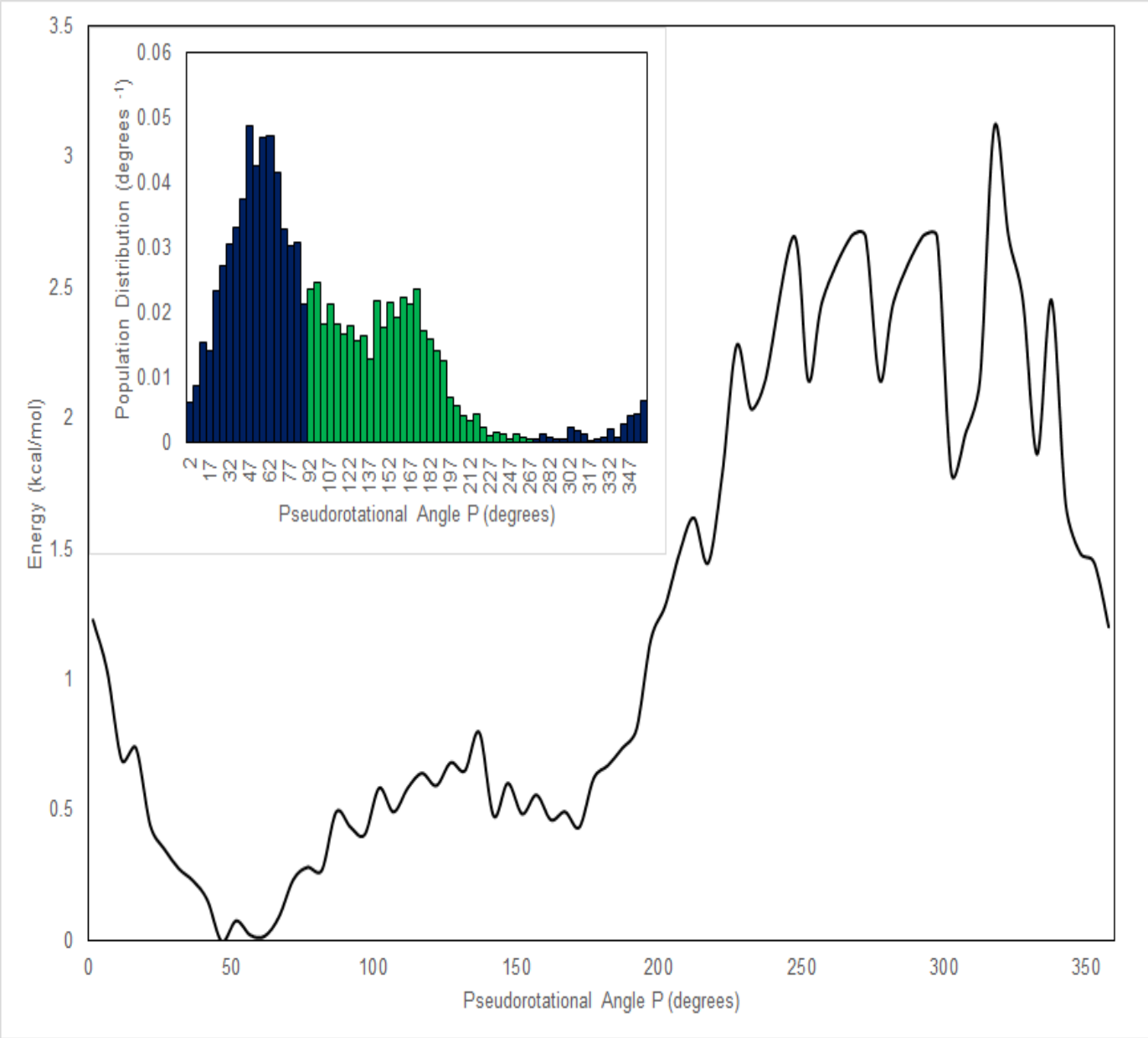

Figure A14. PMF curve for **2.26** along the pseudorotational angle P. Inset shows the puckering distribution around the same angle. Blue – *Northern* conformation, Green – *Southern* conformation.

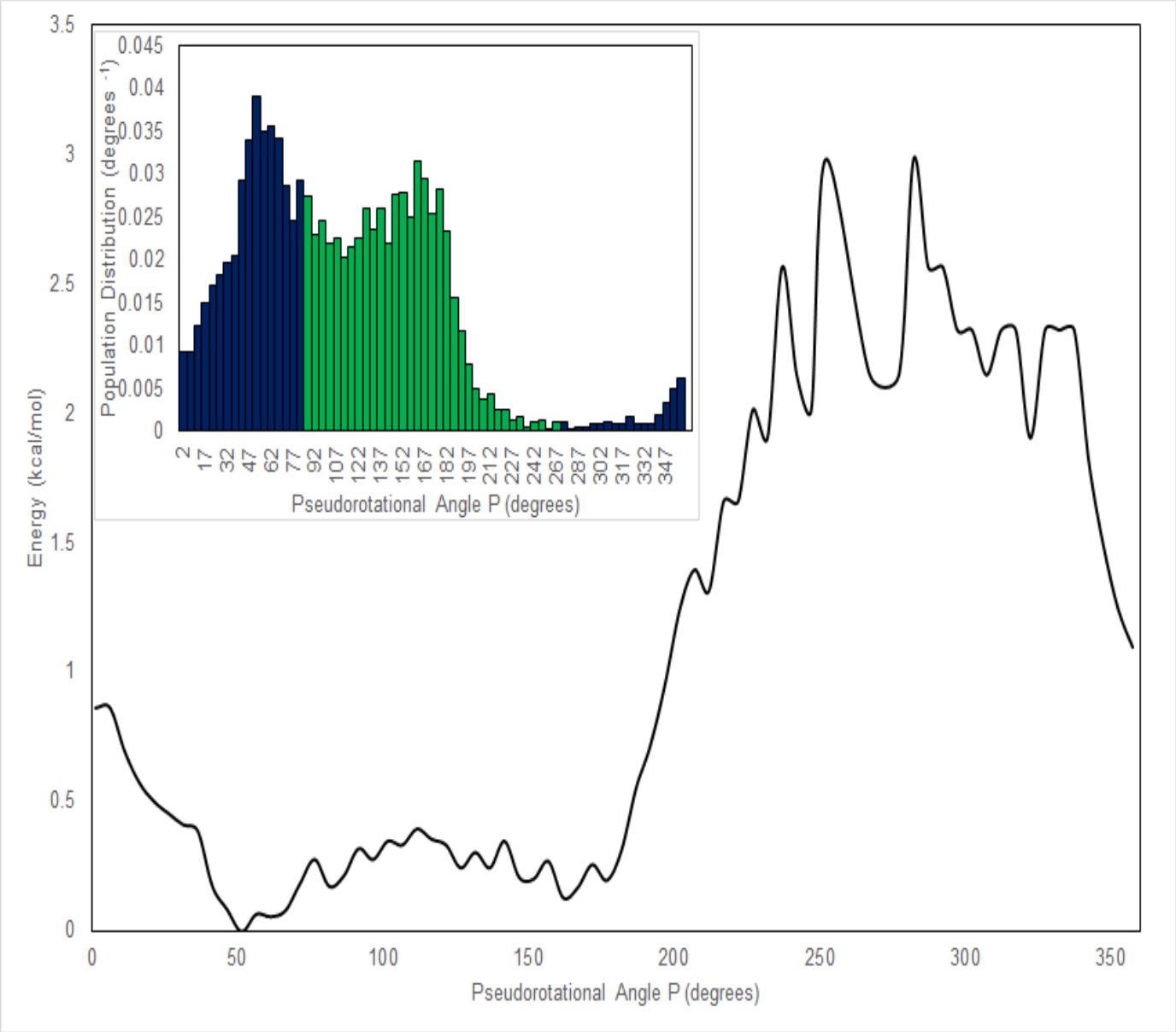

Figure A15. PMF curve for **2.27** along the pseudorotational angle P. Inset shows the puckering distribution around the same angle. Blue – *Northern* conformation, Green – *Southern* conformation.

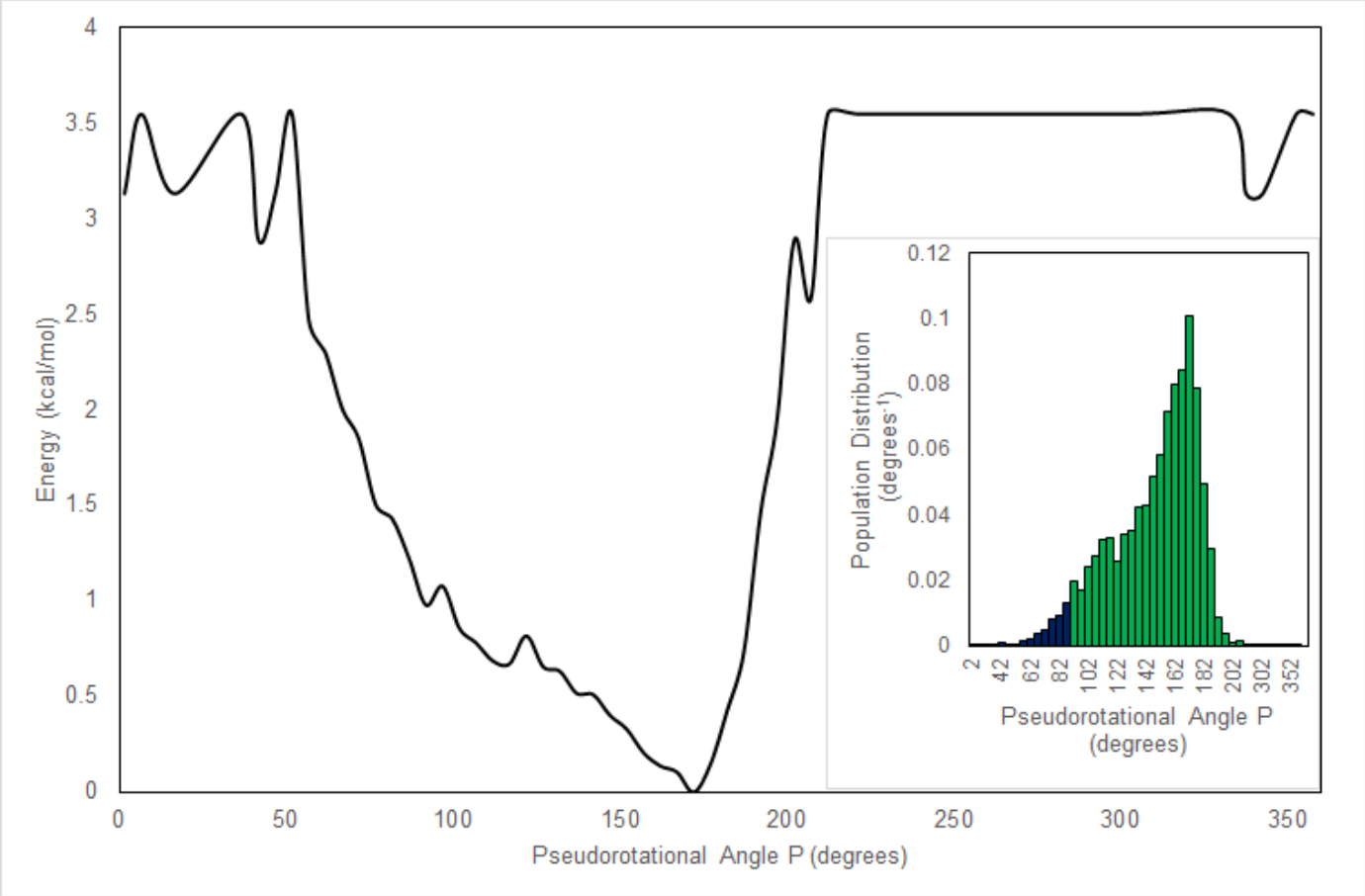

Figure A16. PMF curve for **2.29** along the pseudorotational angle P. Inset shows the puckering distribution around the same angle. Blue – *Northern* conformation, Green – *Southern* conformation.

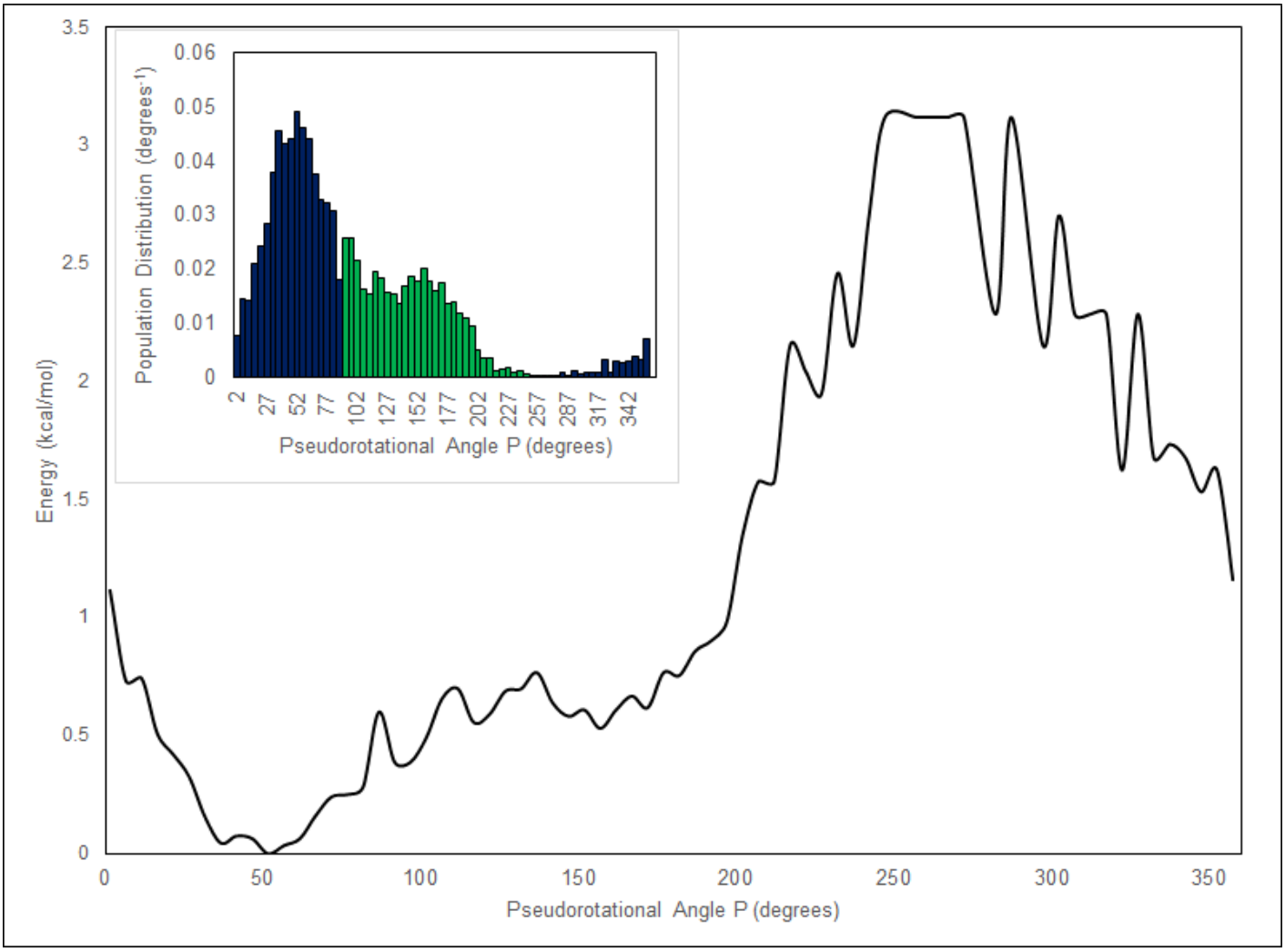

Figure A17. PMF curve for **2.30** along the pseudorotational angle P. Inset shows the puckering distribution around the same angle. Blue – *Northern* conformation, Green – *Southern* conformation.

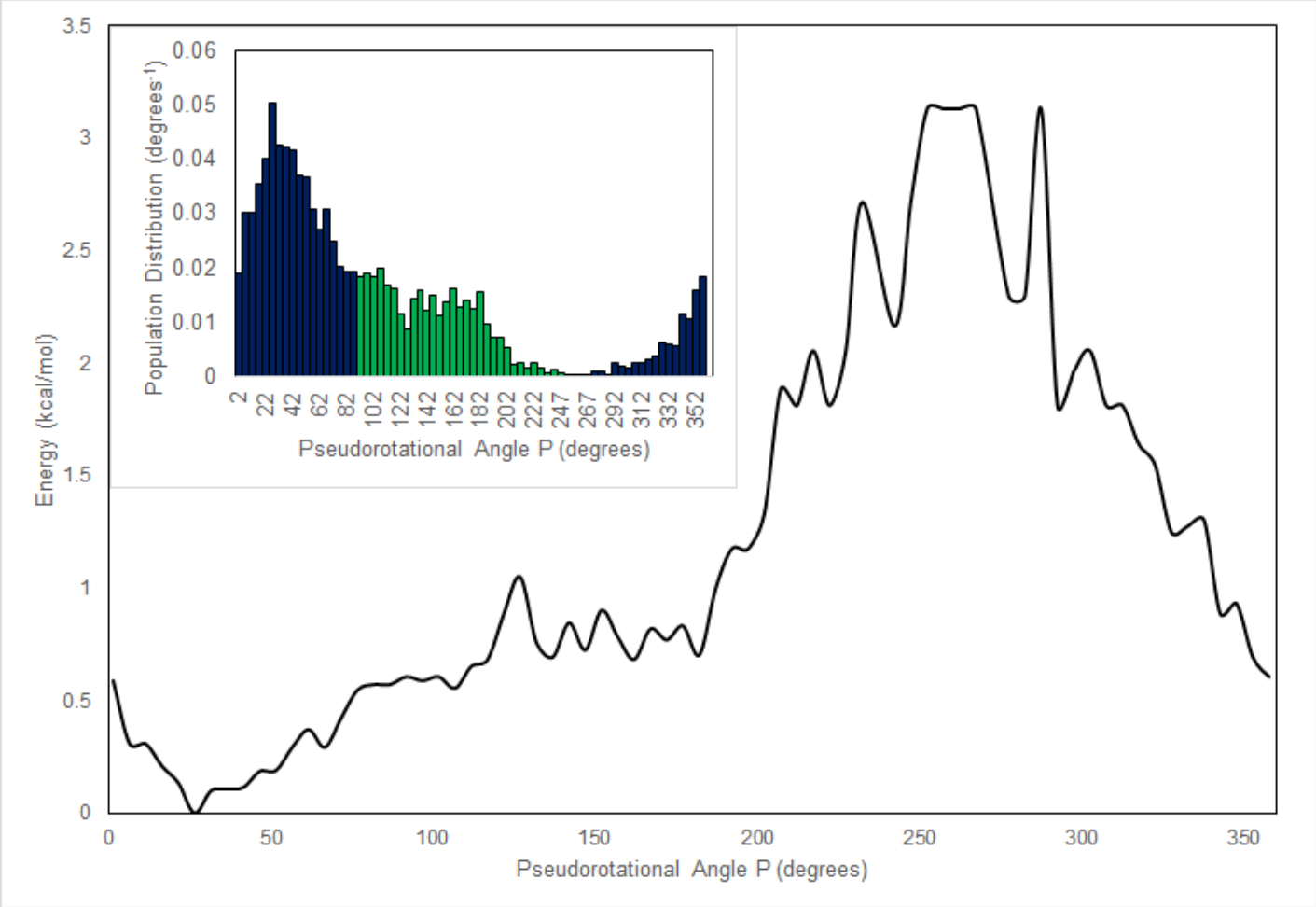

Figure A18. PMF curve for **2.31** along the pseudorotational angle P. Inset shows the puckering distribution around the same angle. Blue – *Northern* conformation, Green – *Southern* conformation.

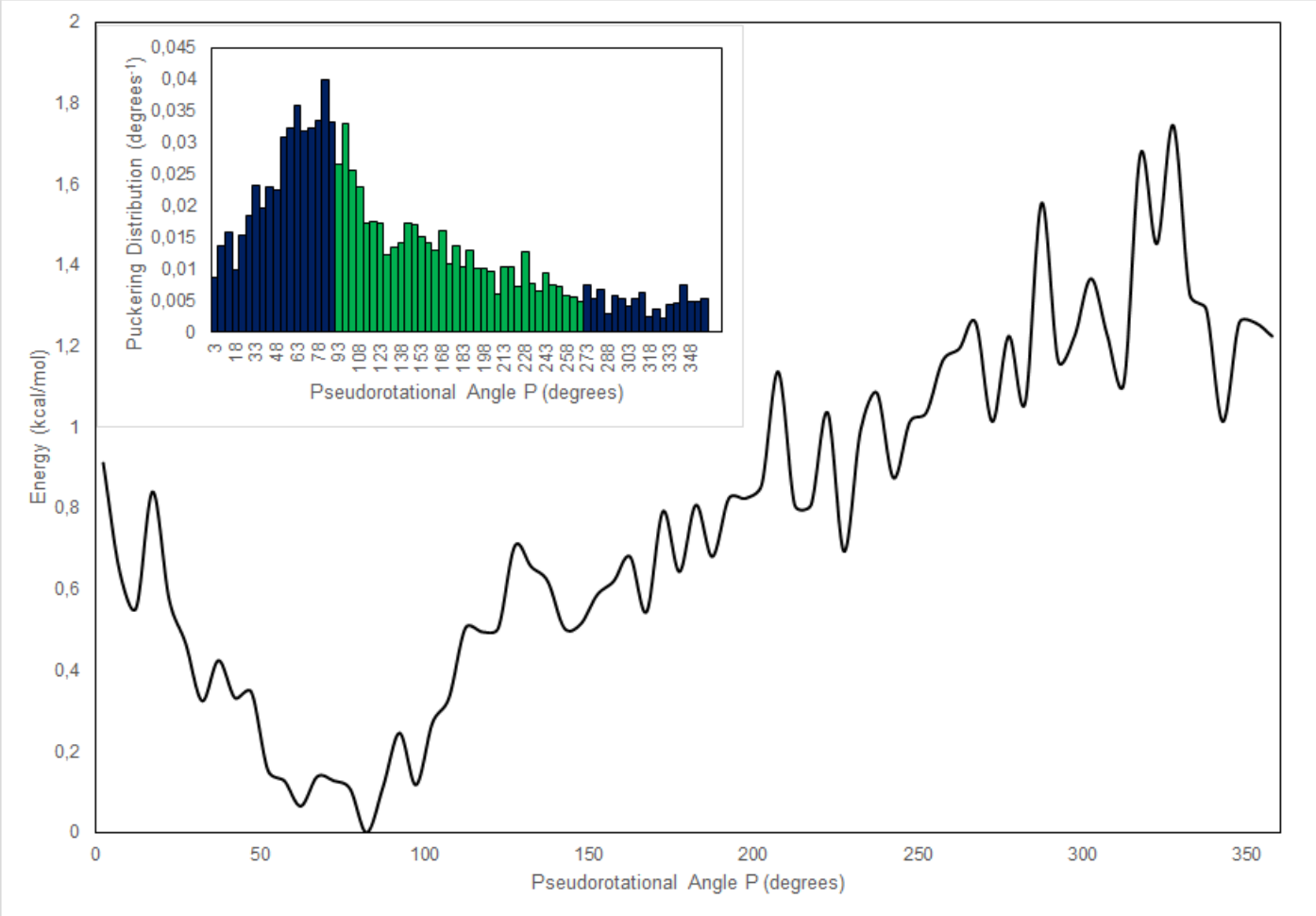

Figure A19. PMF curve for **2.9** along the pseudorotational angle P. Inset shows the puckering distribution around the same angle. Blue – *Northern* conformation, Green – *Southern* conformation.

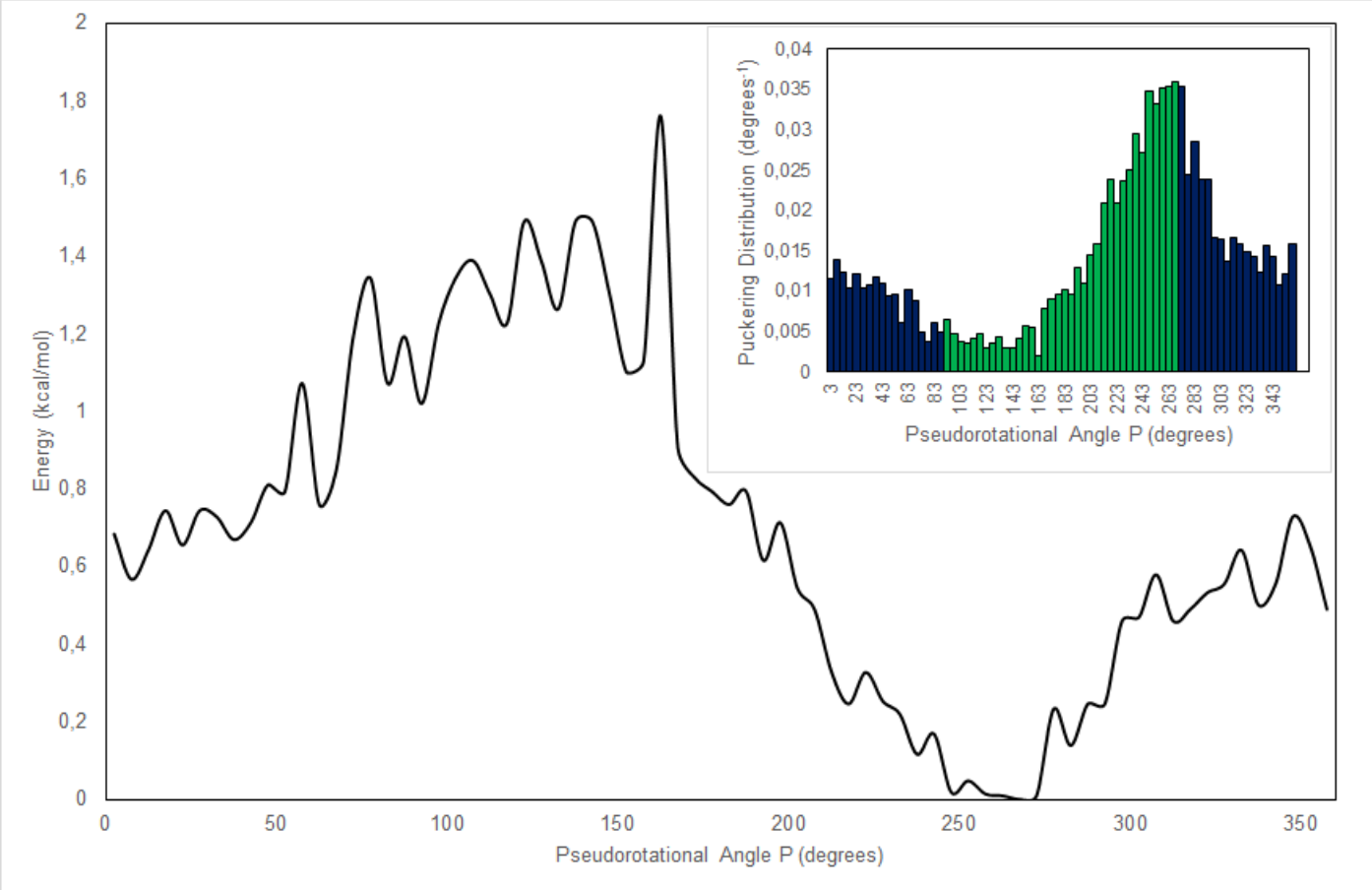

Figure A20. PMF curve for **2.10** along the pseudorotational angle P. Inset shows the puckering distribution around the same angle. Blue – *Northern* conformation, Green – *Southern* conformation.

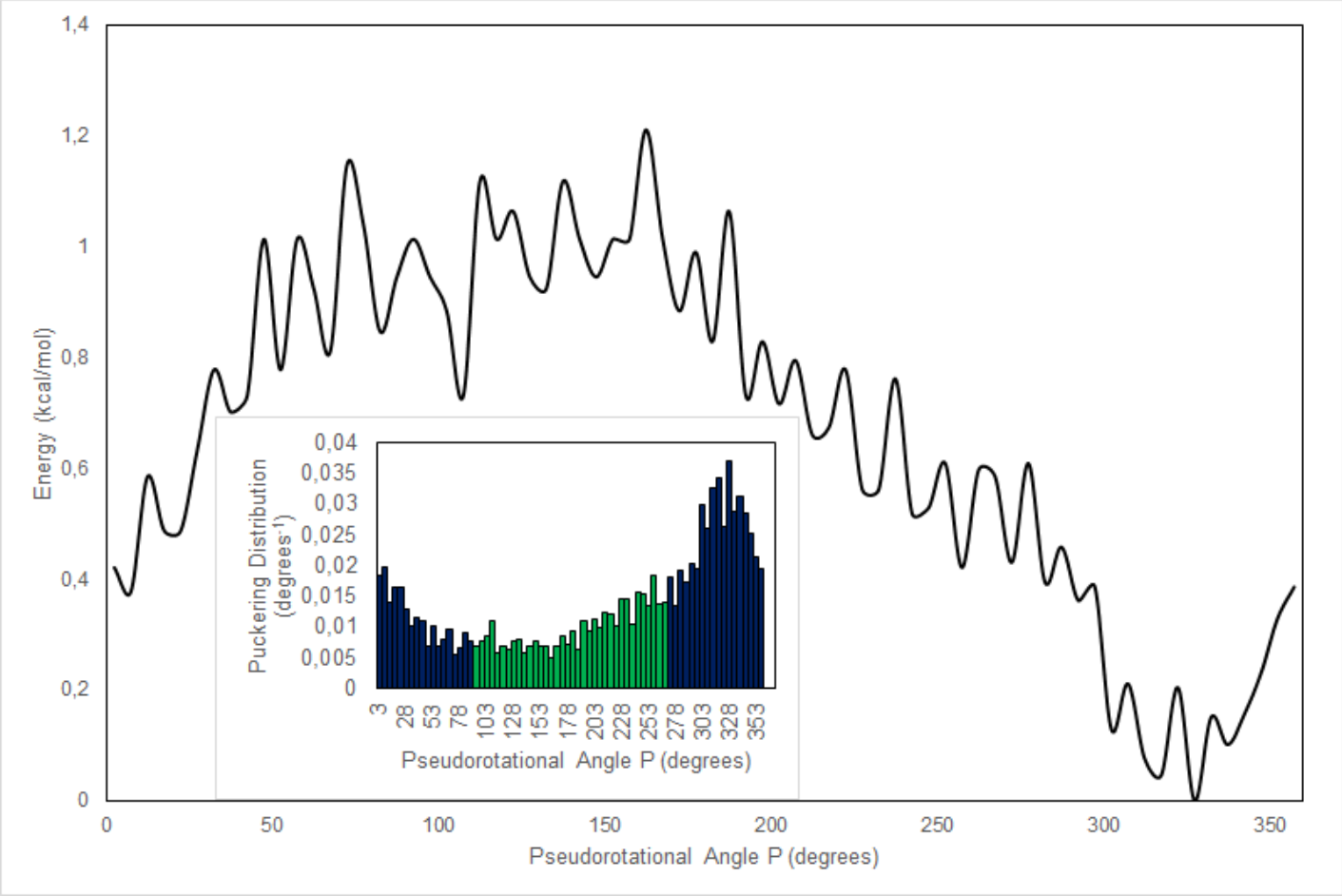

Figure A21. PMF curve for **2.11** along the pseudorotational angle P. Inset shows the puckering distribution around the same angle. Blue – *Northern* conformation, Green – *Southern* conformation.

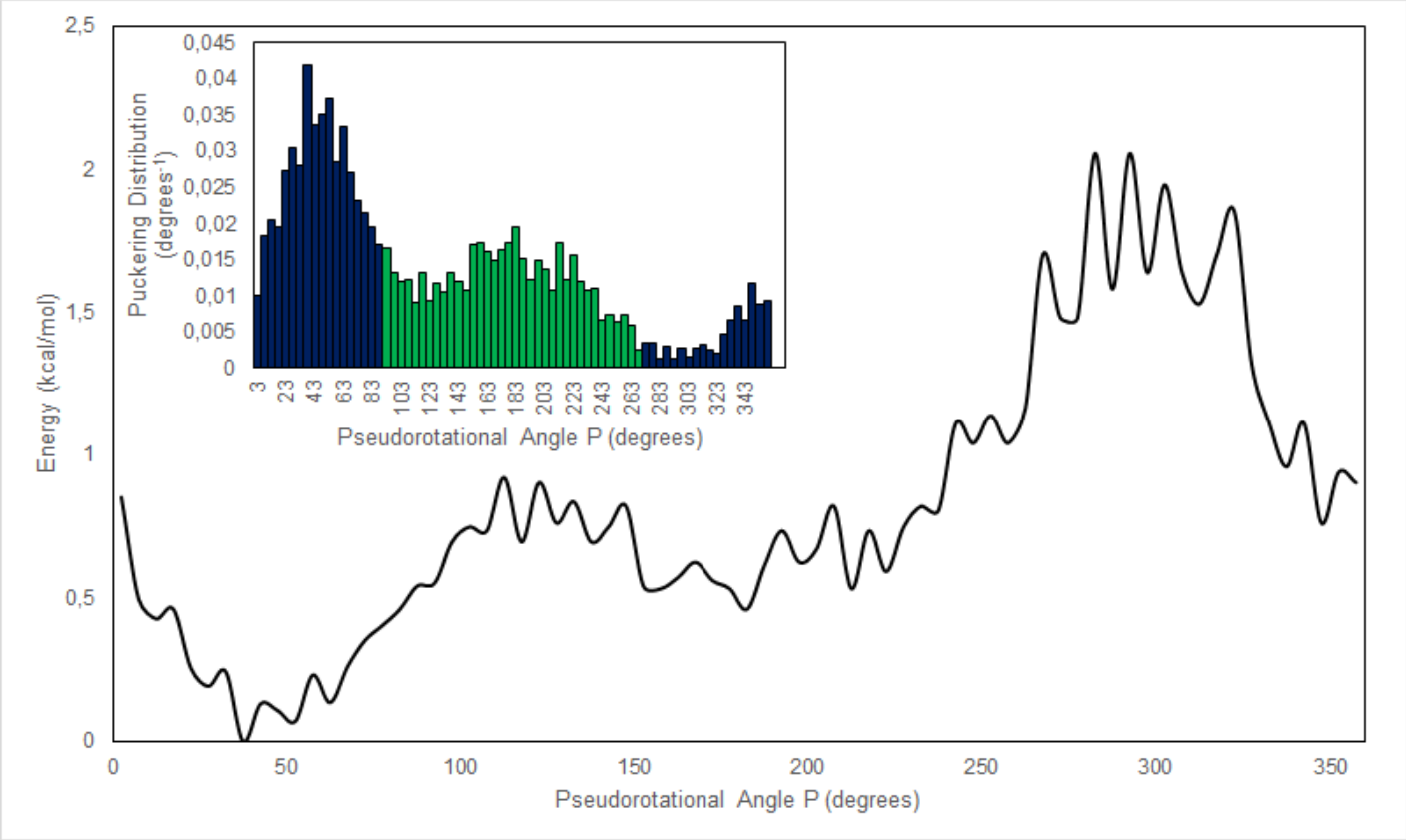

Figure A22. PMF curve for **2.12** along the pseudorotational angle P. Inset shows the puckering distribution around the same angle. Blue – *Northern* conformation, Green – *Southern* conformation.

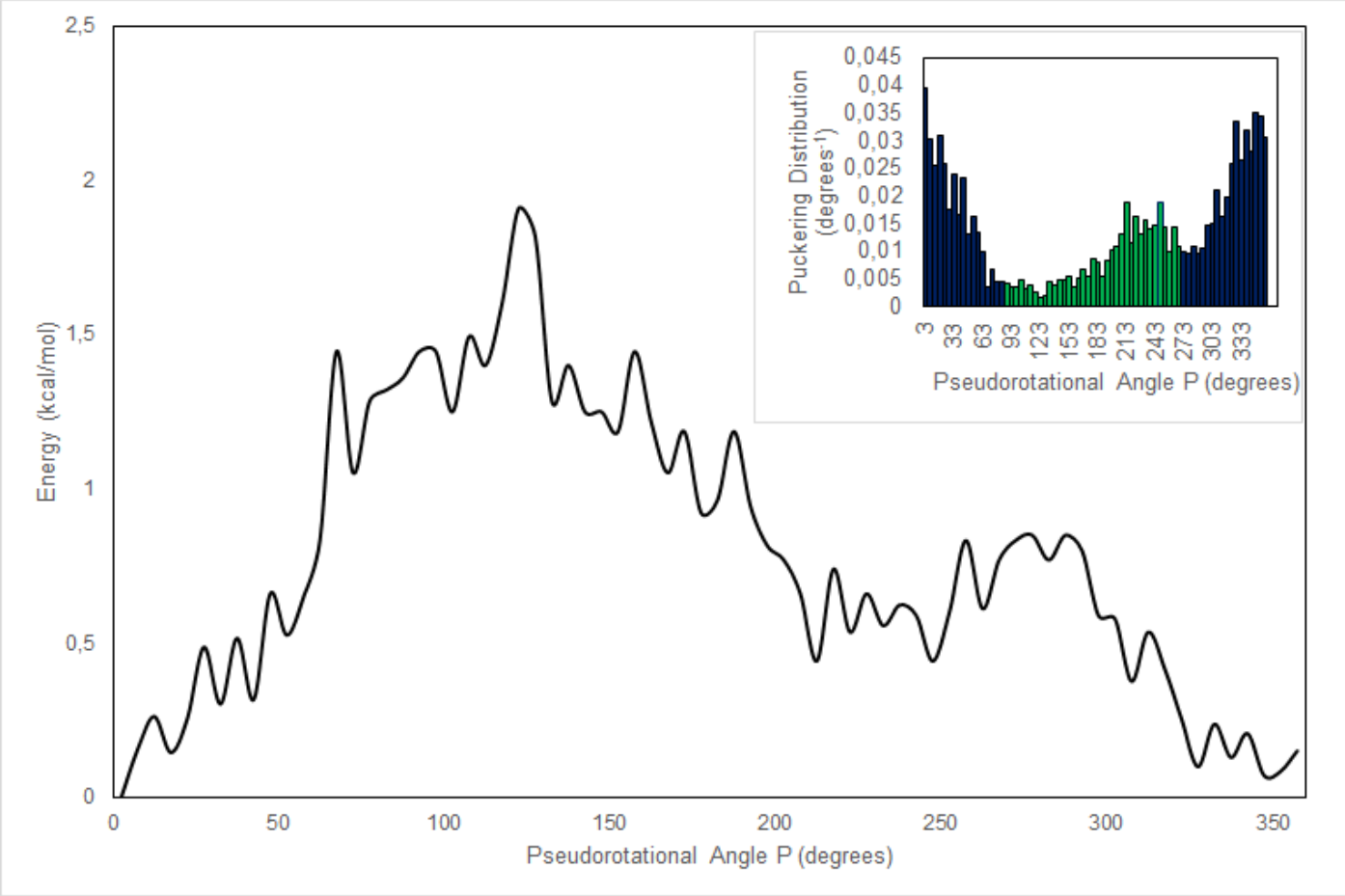

Figure A23. PMF curve for **2.13** along the pseudorotational angle P. Inset shows the puckering distribution around the same angle. Blue – *Northern* conformation, Green – *Southern* conformation.

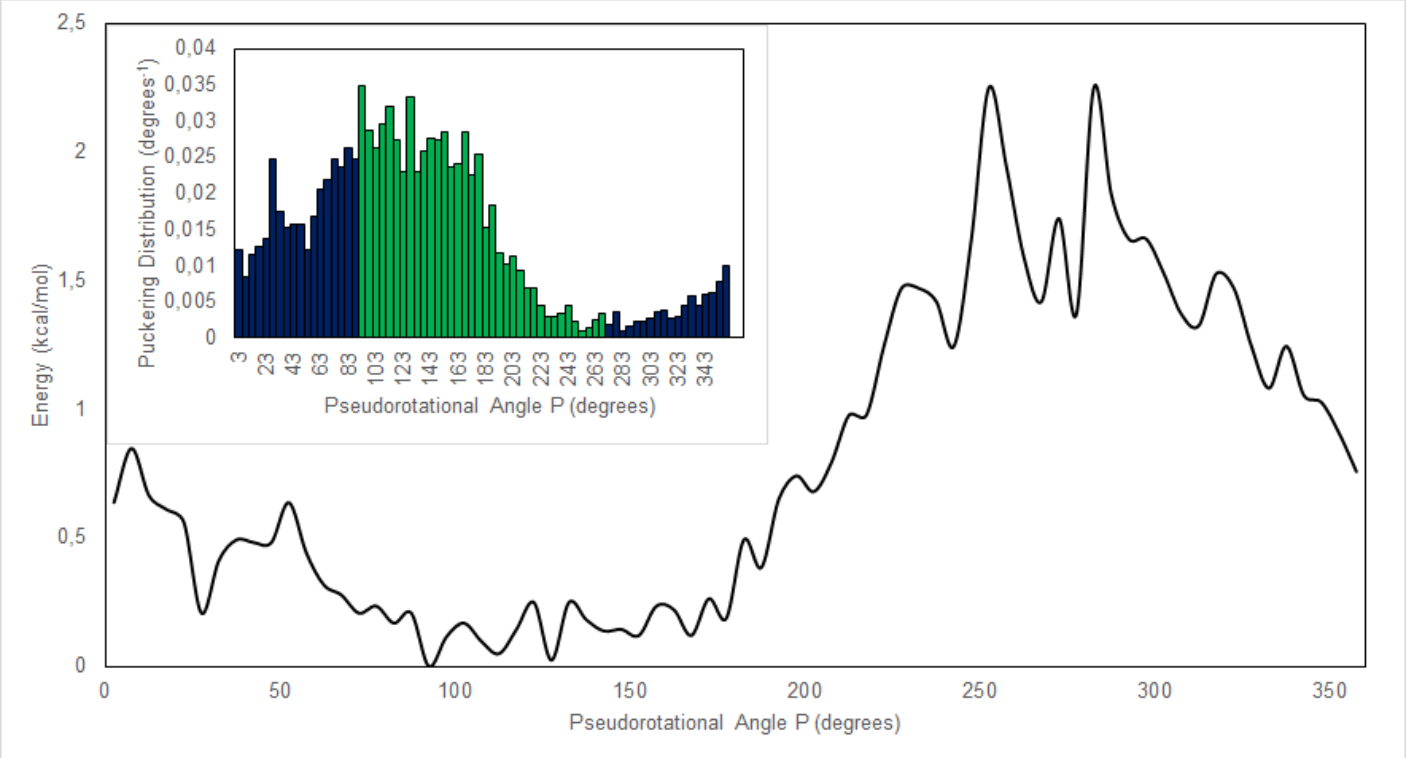

Figure A24. PMF curve for **2.14** along the pseudorotational angle P. Inset shows the puckering distribution around the same angle. Blue – *Northern* conformation, Green – *Southern* conformation.

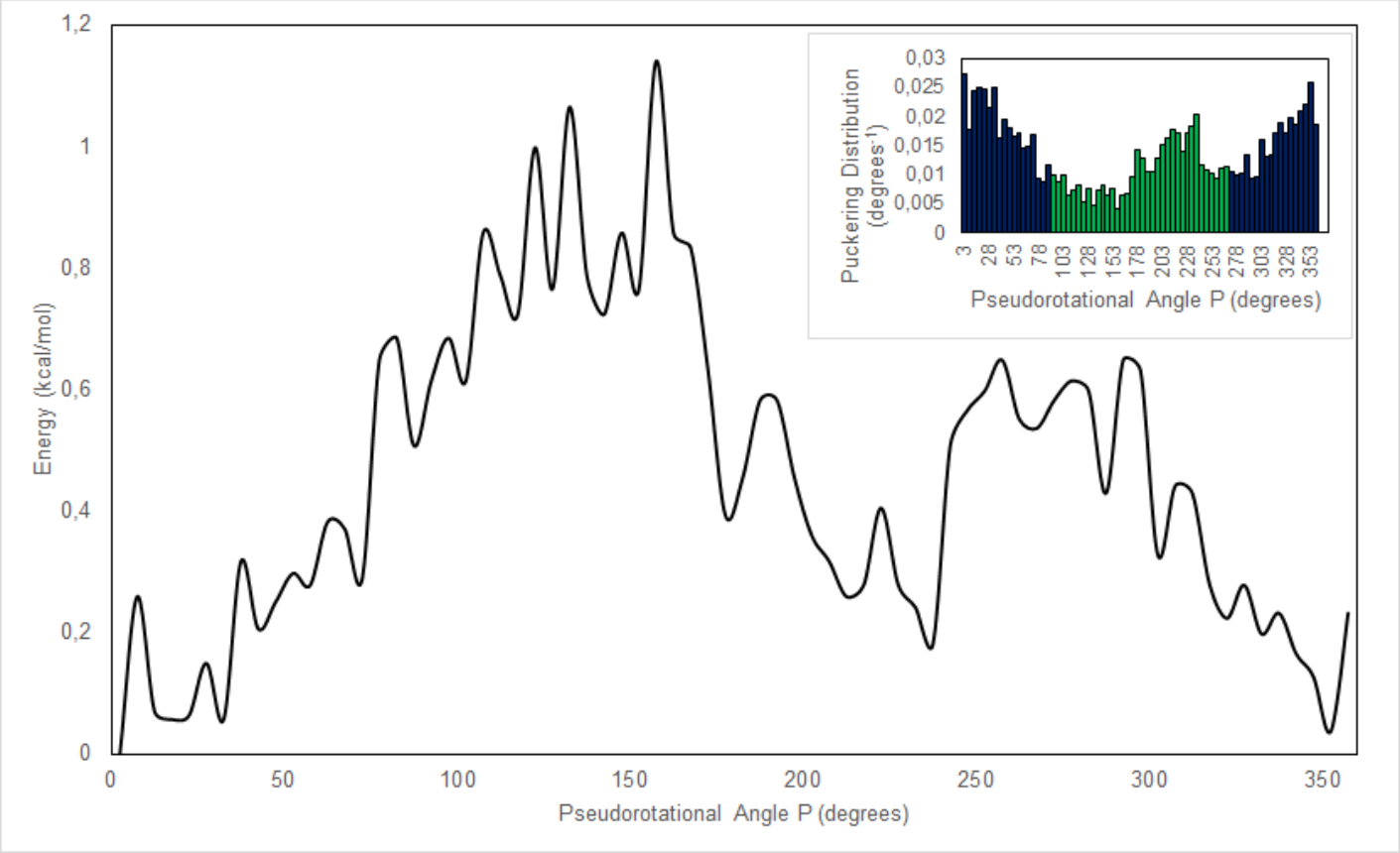

Figure A25. PMF curve for **2.15** along the pseudorotational angle P. Inset shows the puckering distribution around the same angle. Blue – *Northern* conformation, Green – *Southern* conformation.

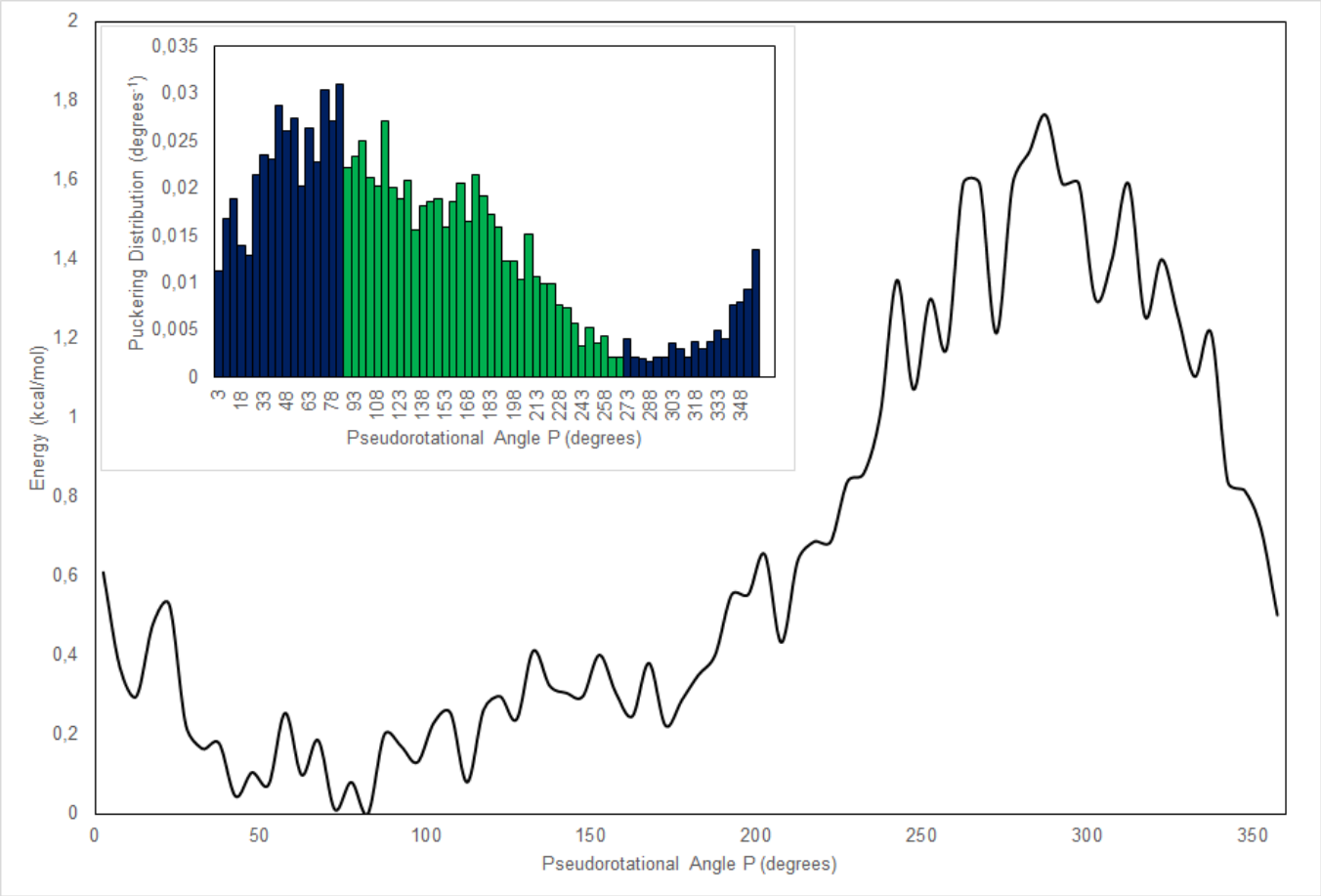

Figure A26. PMF curve for **2.16** along the pseudorotational angle P. Inset shows the puckering distribution around the same angle. Blue – *Northern* conformation, Green – *Southern* conformation.

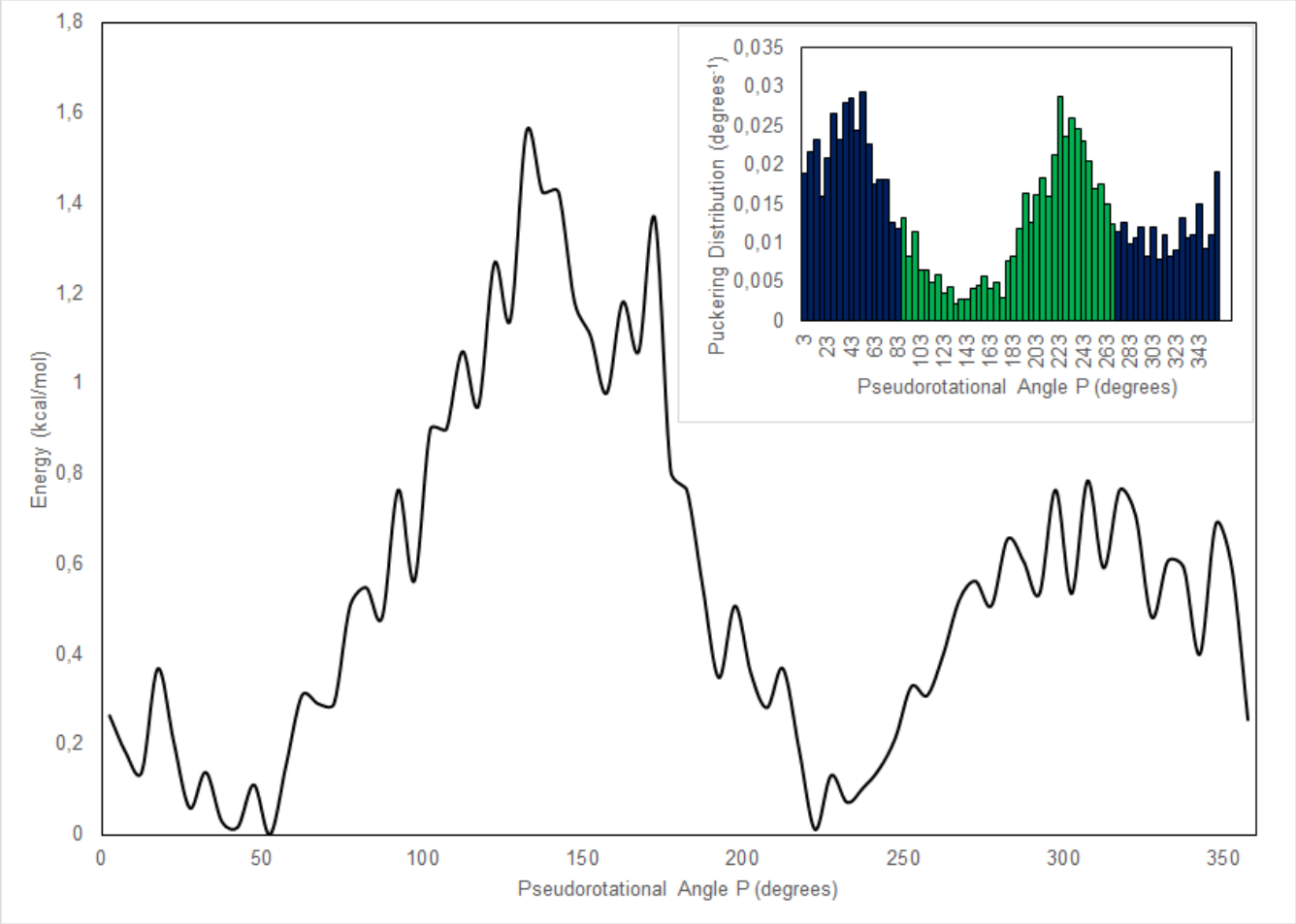

Figure A27. PMF curve for **2.17** along the pseudorotational angle P. Inset shows the puckering distribution around the same angle. Blue – *Northern* conformation, Green – *Southern* conformation.

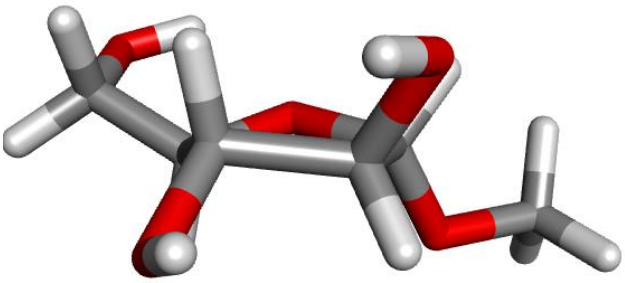

Figure A28. E_4 conformer – monosaccharide **2.9**.

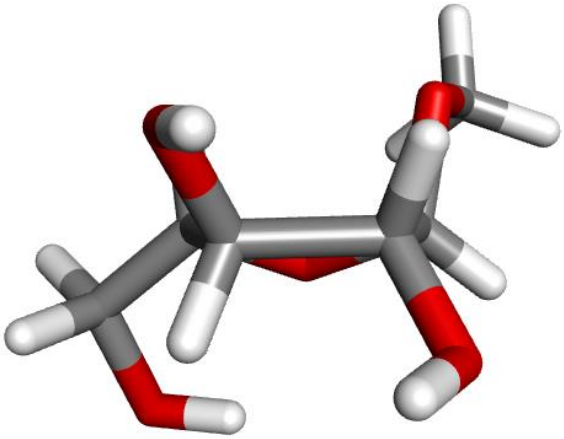

Figure A29. ^4T_O conformer – monosaccharide **2.10**.

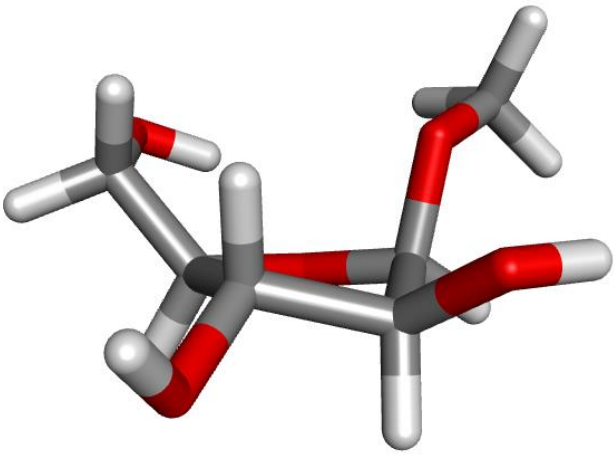

Figure A30. $^1T_2$ conformer – monosaccharide **2.11**.

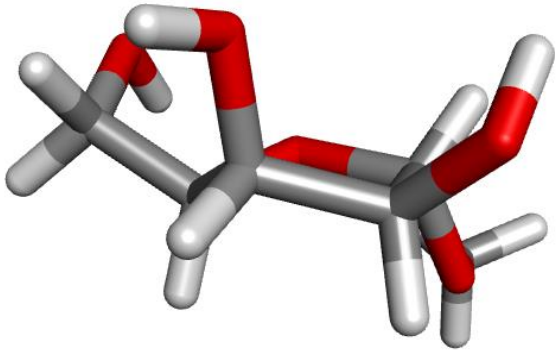

Figure A31. ^{3}E conformer – monosaccharide **2.12**.

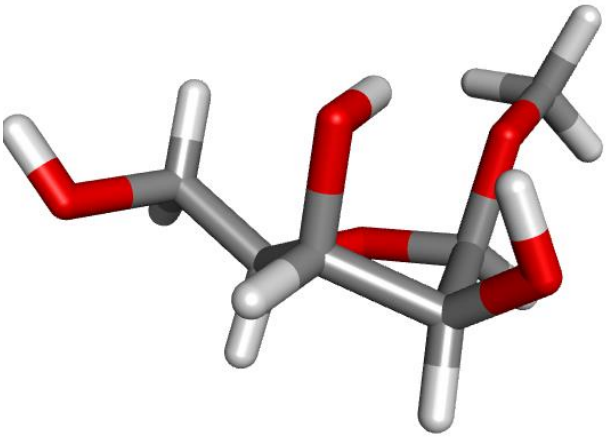

Figure A32. $^{3}T_{2}$ conformer – monosaccharide **2.13**.

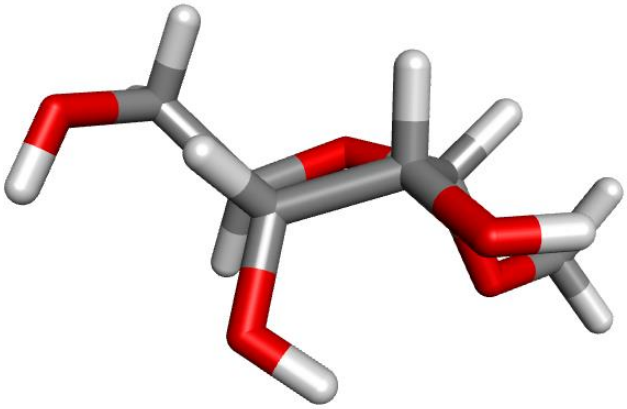

Figure A33. E_{1} conformer – monosaccharide **2.14**.

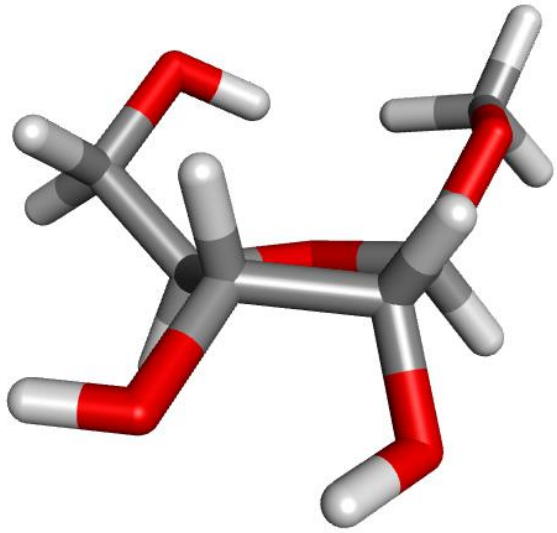

Figure A34. $^{3}T_{2}$ conformer – monosaccharide **2.15**.

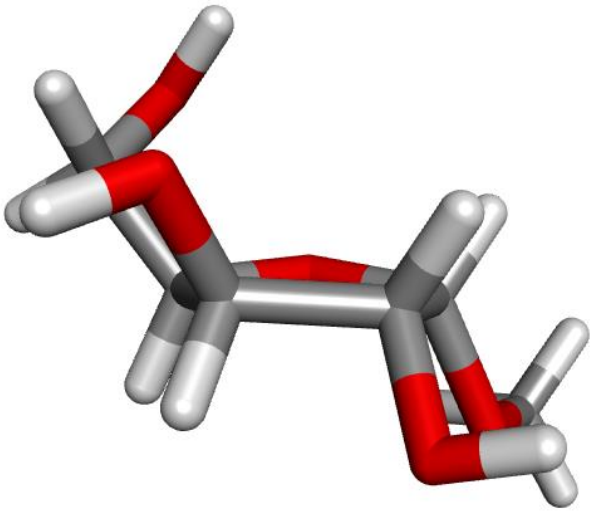

Figure A35. ^{O}E conformer – monosaccharide **2.16**.

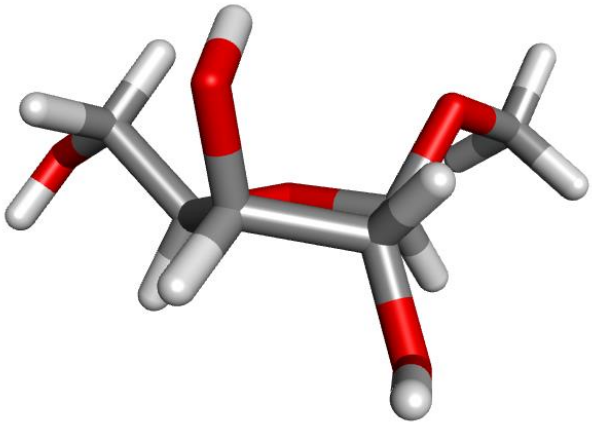

Figure A36. $^{3}T_{4}$ conformer – monosaccharide **2.17**.

Appendix B

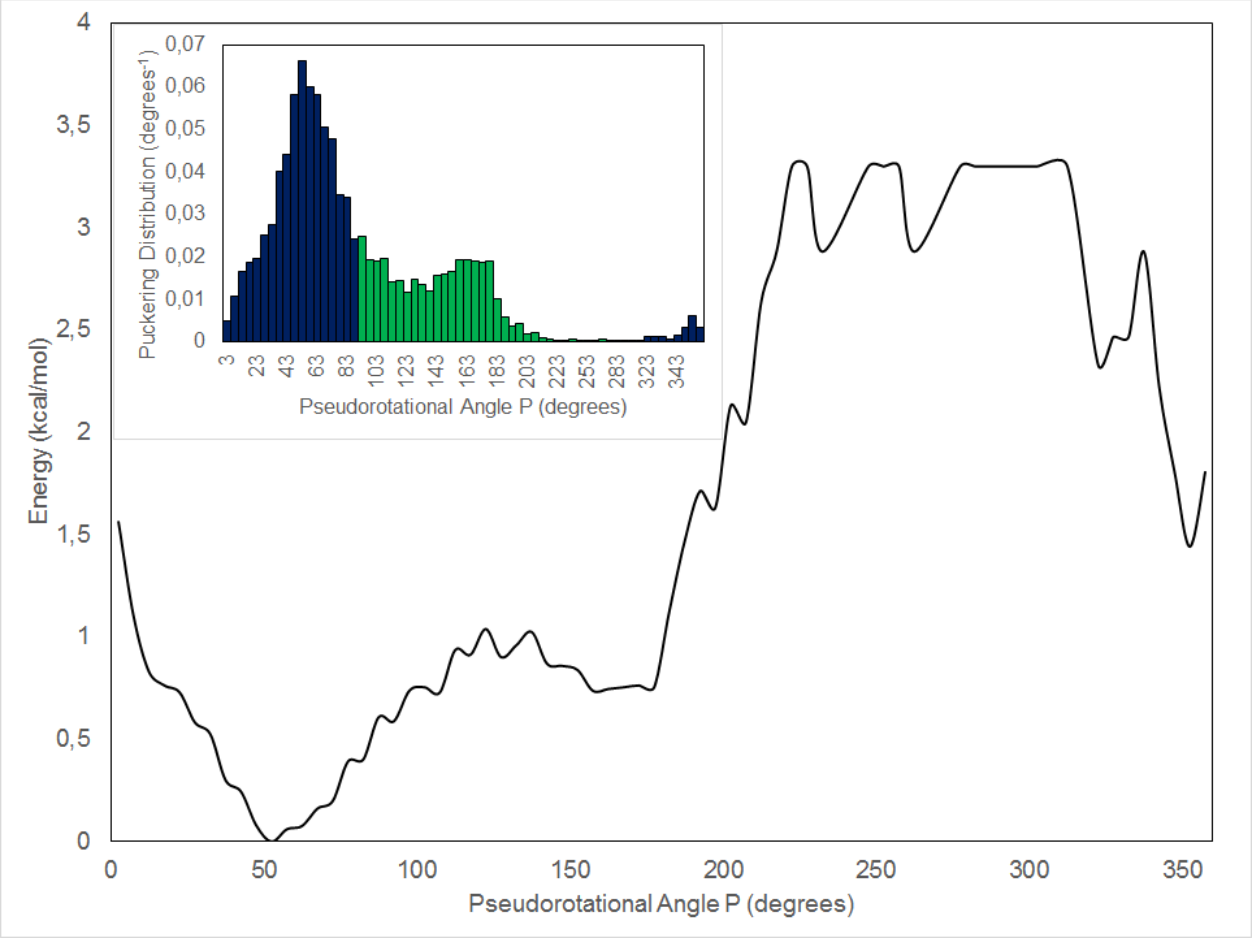

Figure B1. PMF and distribution for **3.2**. Experimentally determined *N/S* ratio is 72:28; predicted *N/S* ratio is 66:34 (based on Boltzmann population distribution). Ratio by energy difference: 73:27.

Table B1. Dihedral angle data obtained for the lowest energy structures of **3.2** in Figure 3.2. The dihedral angles are described in Chapter 2.

Conf.	V_0 (°)	V_1 (°)	V_2 (°)	V_3 (°)	V_4 (°)	χ (°)	γ (°)
North	-21.39	3.03	14.74	-26.68	29.22	-147.16	-55.87
South	-19.83	37.71	-40.68	27.58	-4.44	-136.14	102.10

Table B2. Hyperconjugation and anomeric effects obtained for the lowest energy structures of **3.2** in Figure 3.2. Energies given in kcal/mol.

Conf.	σC3'H3' – σ*C2'OMe	nO4' – σ*C4'OMe	nO4' – σ*C2'OMe	σ C2'H2' – σ*C3'OH	σ C3'H3' – σ*C4'OMe	σC3'C4' – σ*C2'OMe	σC1'C2' – σ*C3'OH	σ C3'H3'– σ* C2'H2'	σ C2'H2' – σ* C3'H3'
North	1.95	10.47	0.06	0.74	2.15	0.54	1.34	0.71	0.93
South	0.00	9.88	0.52	3.63	0.10	4.08	0.08	0.24	0.35
Δ	+1.95	+0.59	-0.46	-2.89	+2.05	-3.54	+1.26	+0.47	+0.58

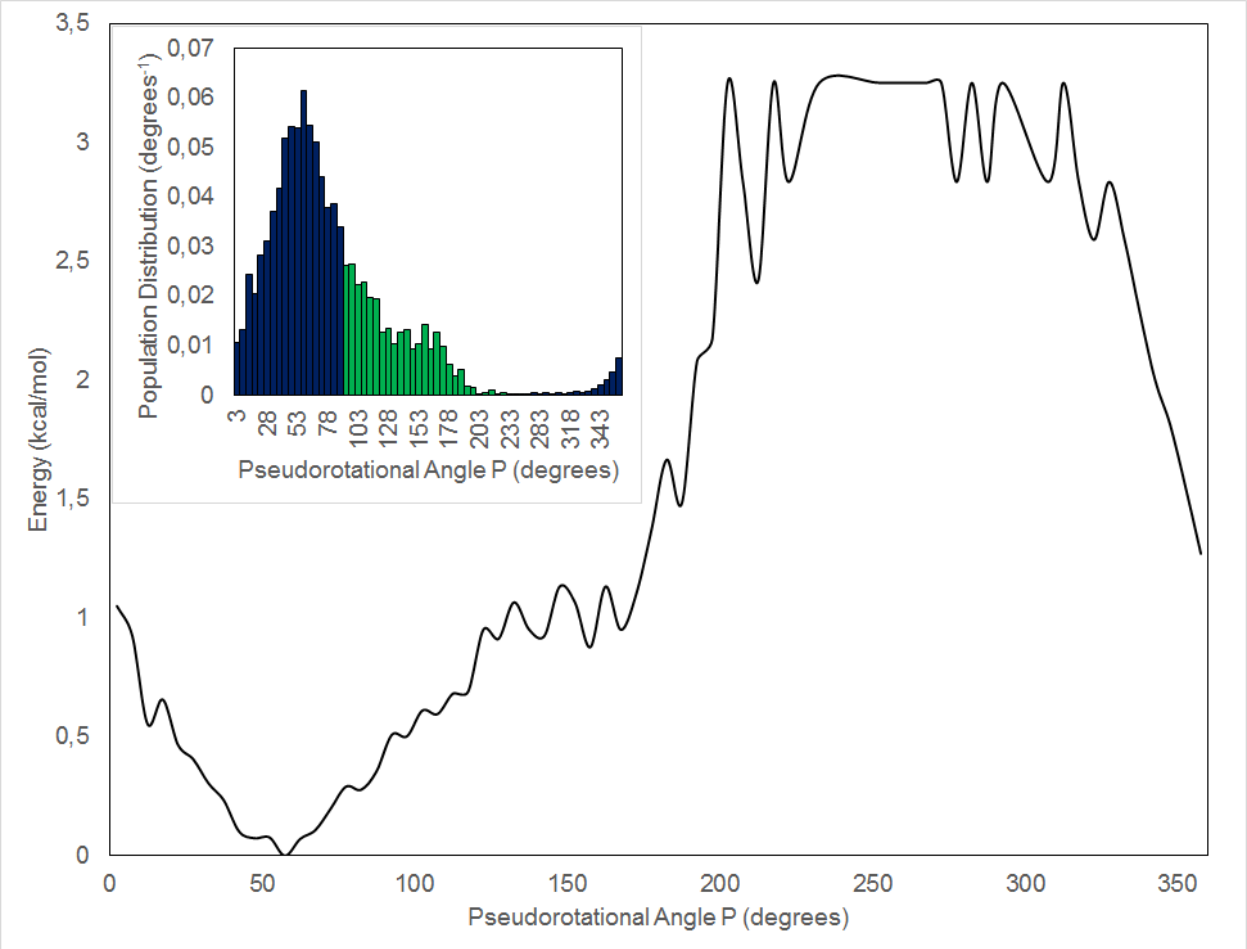

Figure B2. PMF and distribution for **3.3**. Experimentally determined *N/S* ratio is 87:13; predicted *N/S* ratio is 71:29 (based on Boltzmann population distribution). Ratio by energy difference: 76:24.

Table B3. Dihedral angle data obtained for the lowest energy structures of **3.3** in Figure 3.2. The dihedral angles are described in Chapter 2.

Conf.	V_0 (°)	V_1 (°)	V_2 (°)	V_3 (°)	V_4 (°)	χ (°)	γ (°)
North	-22.81	0.08	20.38	-33.73	35.07	-130.03	10.57
South	-17.84	27.09	-26.21	14.94	1.63	-129.18	-79.39

Table B4. Hyperconjugation and anomeric effects obtained for the lowest energy structures of **3.3** in Figure 3.2. Energies given in kcal/mol.

Conf.	σC3'H3' – σ*C2'OMe	nO4' – σ*C4'F	nO4' – σ*C2'OMe	σ C2'H2' – σ*C3'OH	σ C3'H3' – σ*C4'F	σC3'C4' – σ*C2'OMe	σC1'C2' – σ*C3'OH	σ C3'H3'– σ* C2'H2'	σ C2'H2' – σ* C3'H3'
North	2.00	14.12	0.00	0.09	3.63	0.00	1.48	0.47	0.35
South	0.00	11.13	0.29	2.97	0.49	2.23	0.00	0.29	0.44
Δ	+2.00	+2.99	-0.29	-2.88	+3.14	-2.23	+1.48	+0.18	-0.09

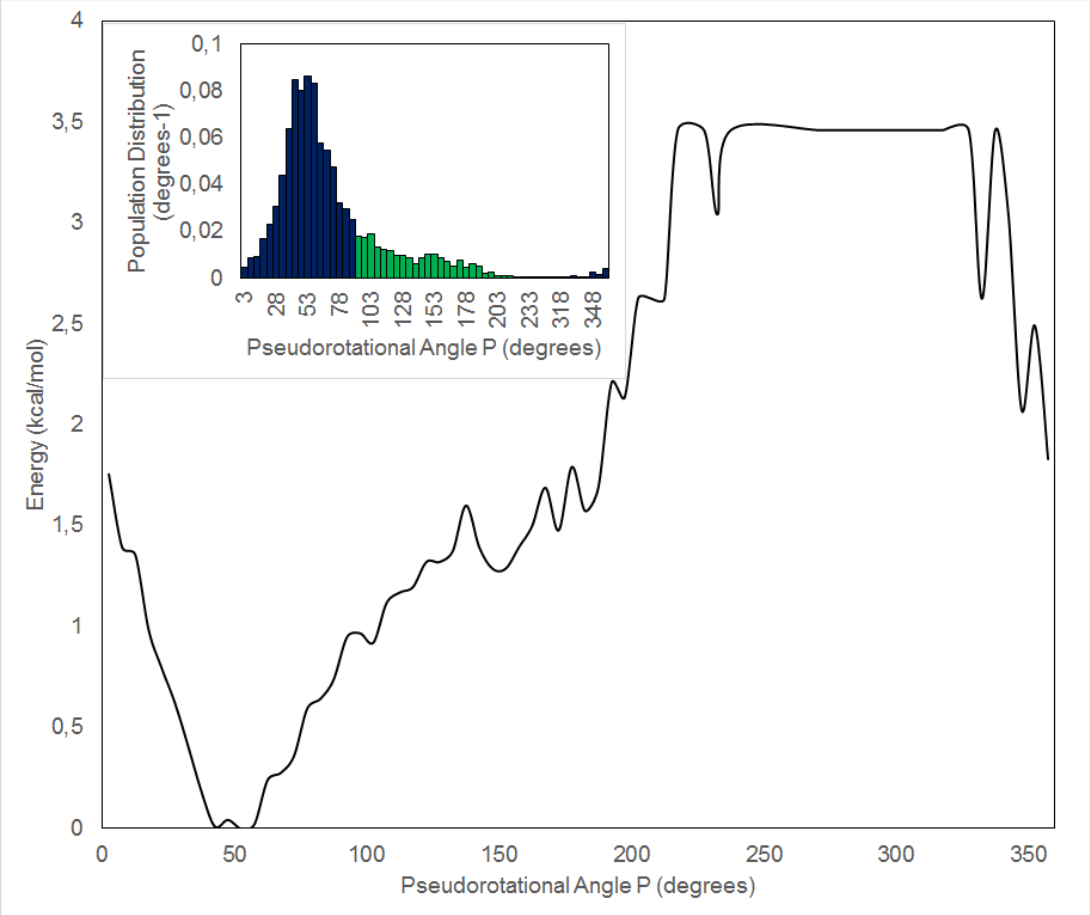

Figure B3. PMF and distribution for **3.8**. Experimentally determined N/S ratio is 80:20; predicted N/S ratio is 79:21 (based on Boltzmann population distribution). Ratio by energy difference: 85:15.

Table B5. Dihedral angle data obtained for the lowest energy structures of **3.8** in Figure 3.2. The dihedral angles are described in Chapter 2.

Conf.	V0 (°)	V1 (°)	V2 (°)	V3 (°)	V4 (°)	χ (°)	γ (°)
North	-11.40	-3.17	14.98	-20.98	20.64	54.97	-34.78
South	-13.92	16.47	-14.14	6.35	5.19	55.25	-139.92

Table B6. Hyperconjugation and anomeric effects obtained for the lowest energy structures of **3.8** in Figure 3.2. Energies given in kcal/mol.

Conf.	σC3'H3' – σ*C2'H2'	nO4' – σ*C4'OMe	nO4' – σ*C2'H2'	σ C3'H3' – σ*C4'OMe	σC3'C4' – σ*C2'H2'	σC1'C2' – σ*C3'OH	σ C2'F – σ* C3'H3'
North	1.10	12.60	0.00	3.23	0.22	1.40	0.11
South	0.50	12.74	0.11	1.36	0.99	0.73	0.21
Δ	+0.6	-0.14	-0.11	+1.87	-0.77	+0.67	-0.10

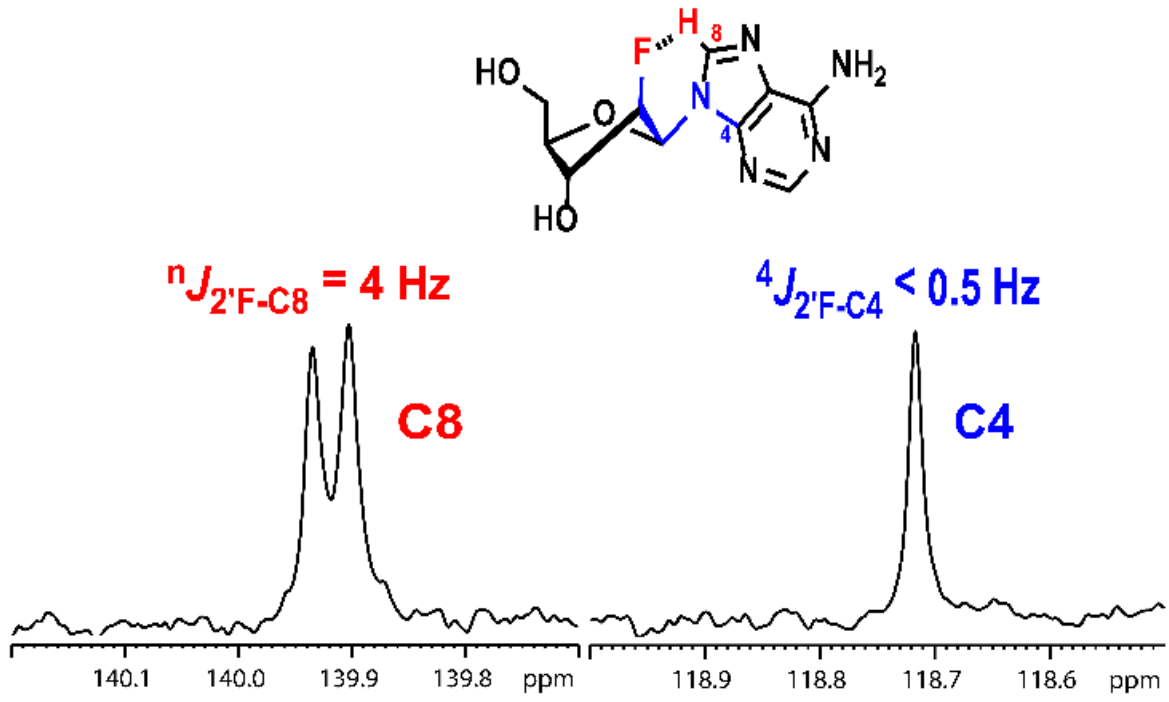

Figure B4. Portion of the ^{13}C spectrum of **3.10** in DMSO-d_6 showing the region where the C8 and C4 signals appear.

Appendix C

PES scans for the ligands in Chart 4.1.

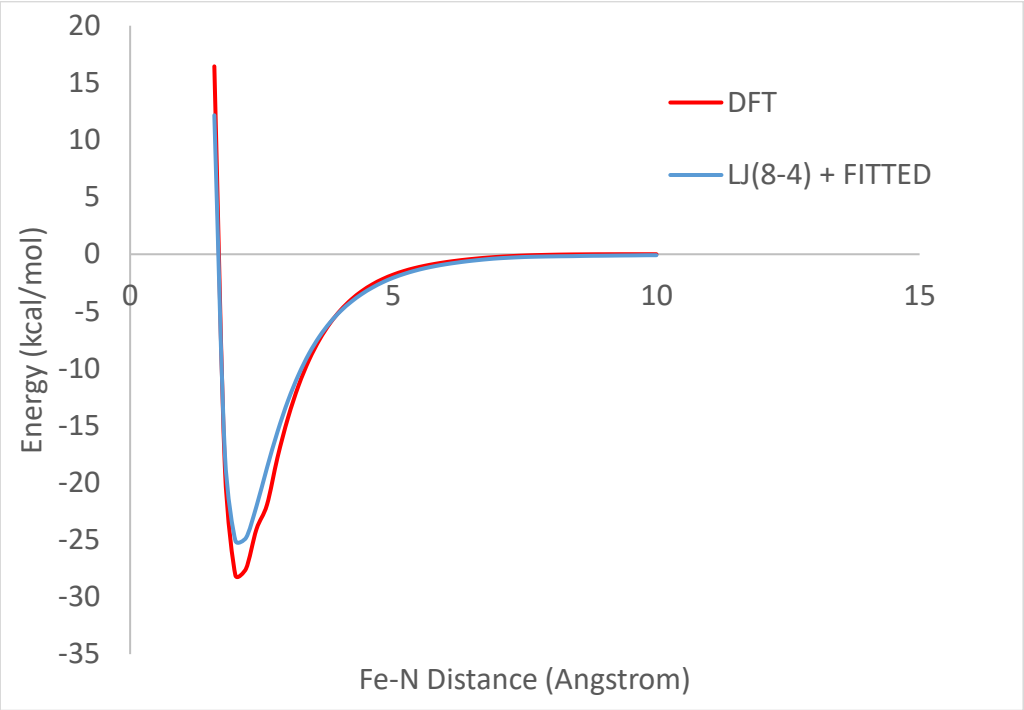

Figure C1. PES Scan for ligand 4.1. Red – QM. Blue – new potential developed in FITTED.

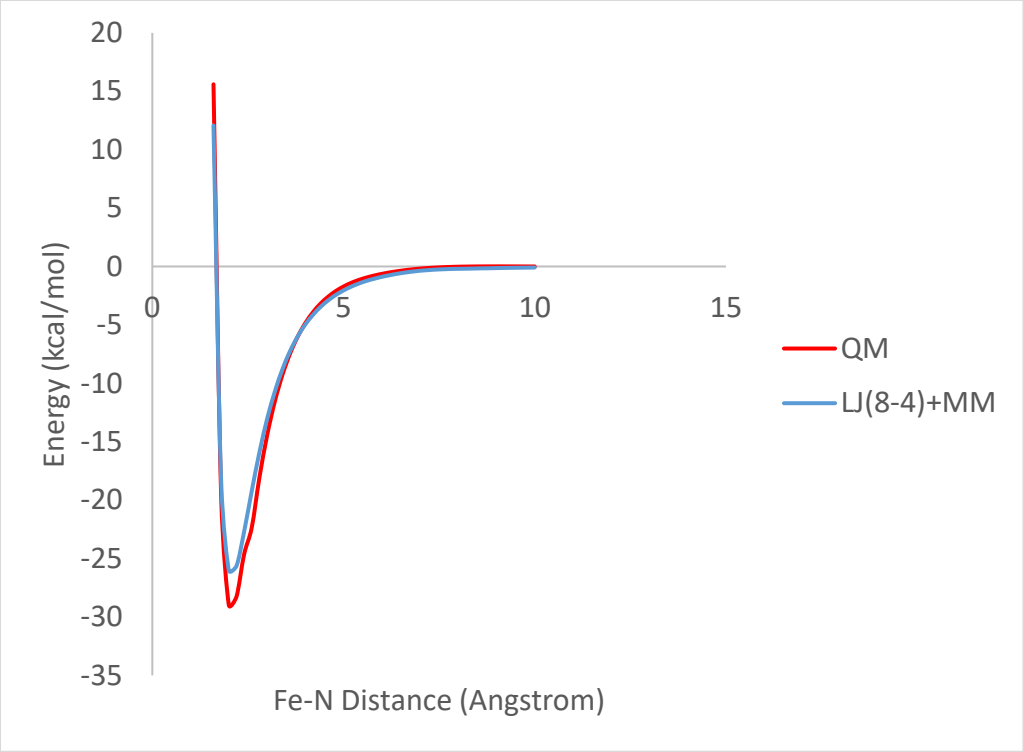

Figure C2. PES Scan for ligand 4.2. Red – QM. Blue – new potential developed in FITTED.

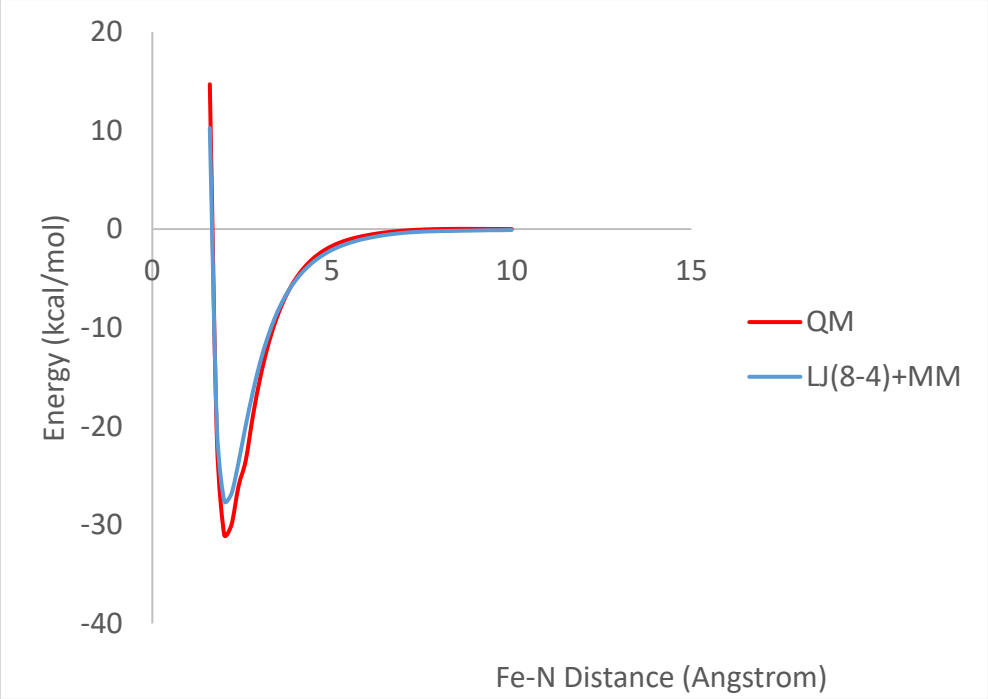

Figure C3. PES Scan for ligand 4.3. Red – QM. Blue – new potential developed in FITTED.

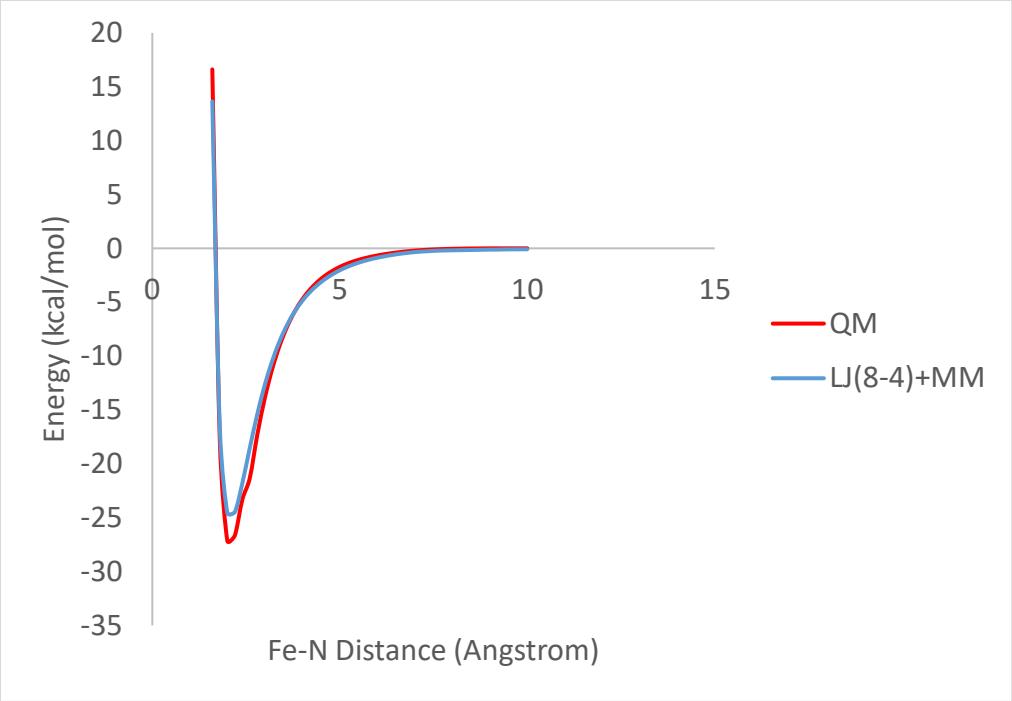

Figure C4. PES Scan for ligand 4.4. Red – QM. Blue – new potential developed in FITTED.

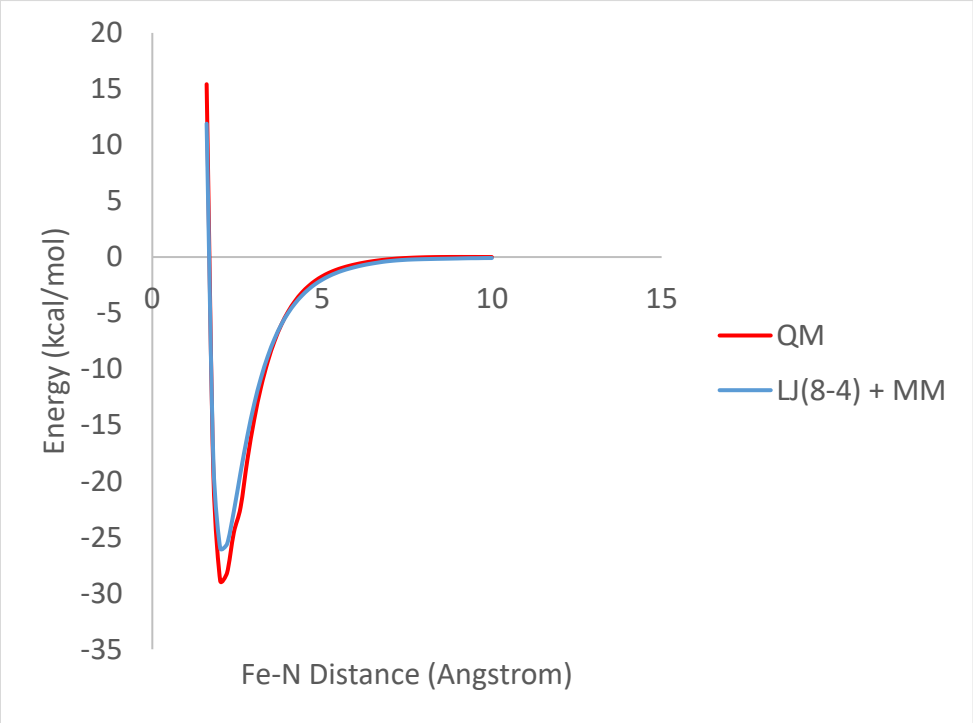

Figure C5. PES Scan for ligand 4.5. Red – QM. Blue – new potential developed in FITTED.

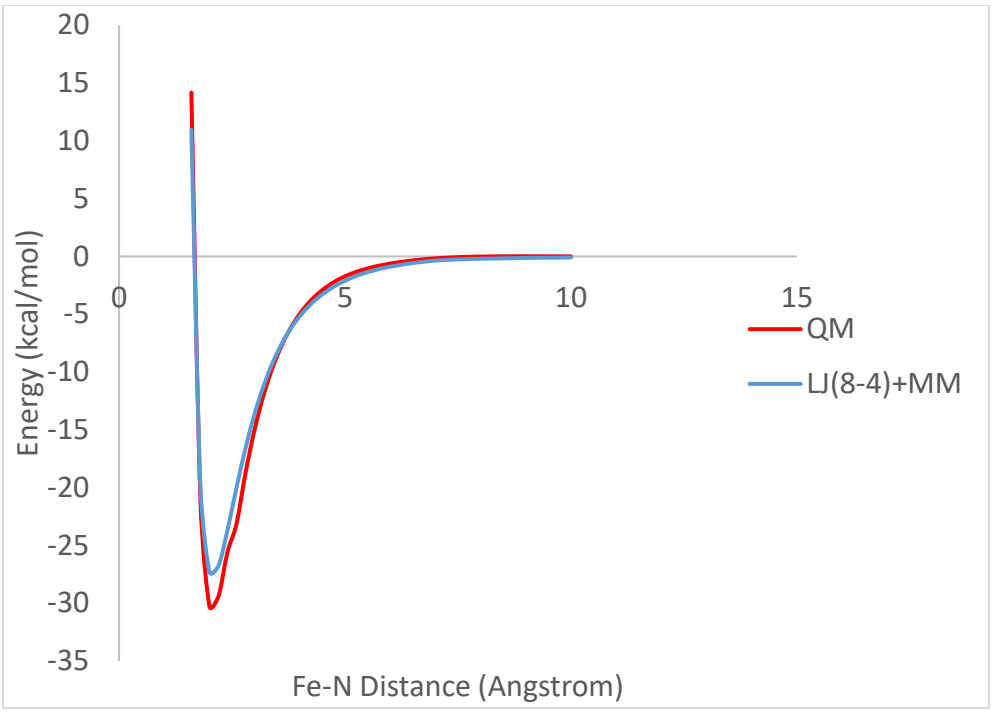

Figure C6. PES Scan for ligand 4.6. Red – QM. Blue – new potential developed in FITTED.

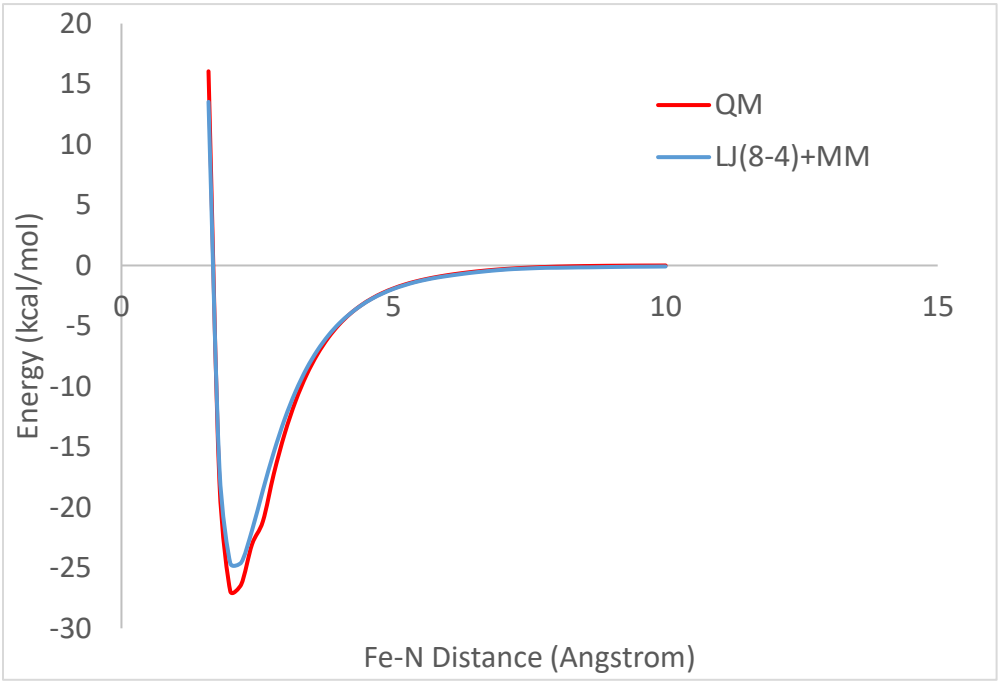

Figure C7. PES Scan for ligand 4.9. Red – QM. Blue – new potential developed in FITTED.

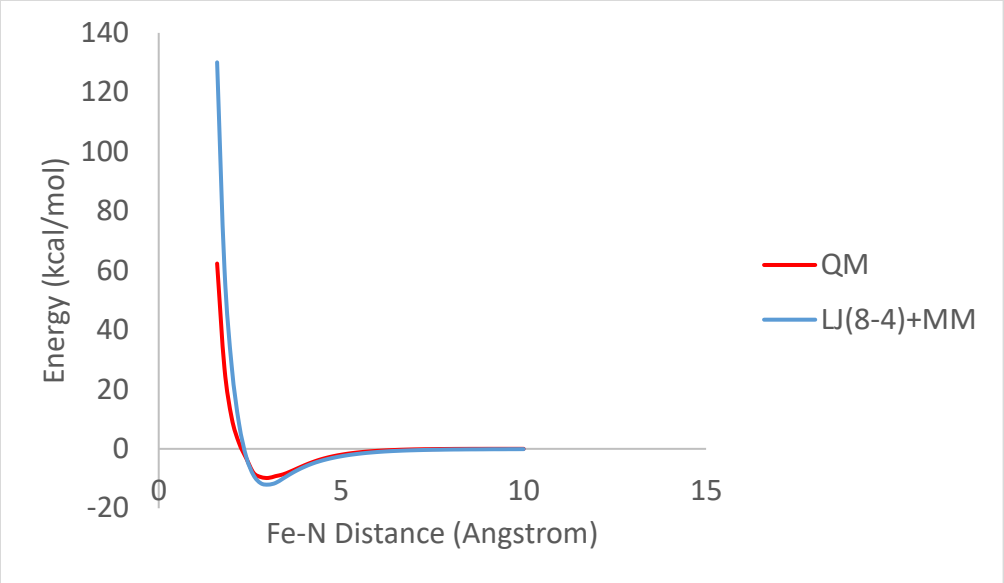

Figure C8. PES Scan for ligand 4.10. Red – QM. Blue – new potential developed in FITTED.

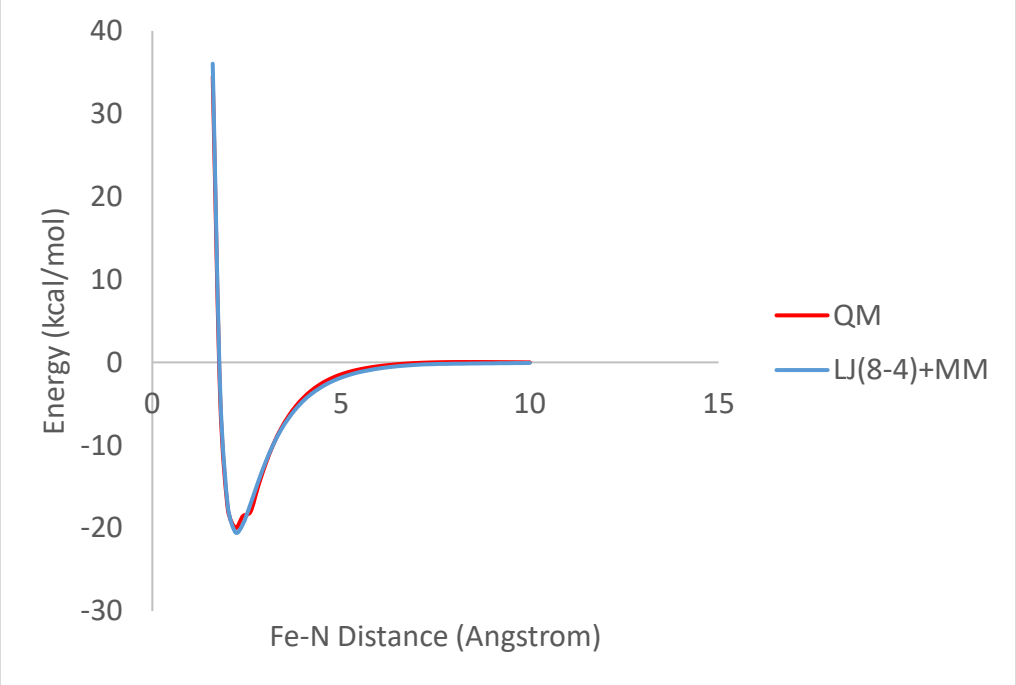

Figure C9. PES Scan for ligand 4.10a. Red – QM. Blue – new potential developed in FITTED.

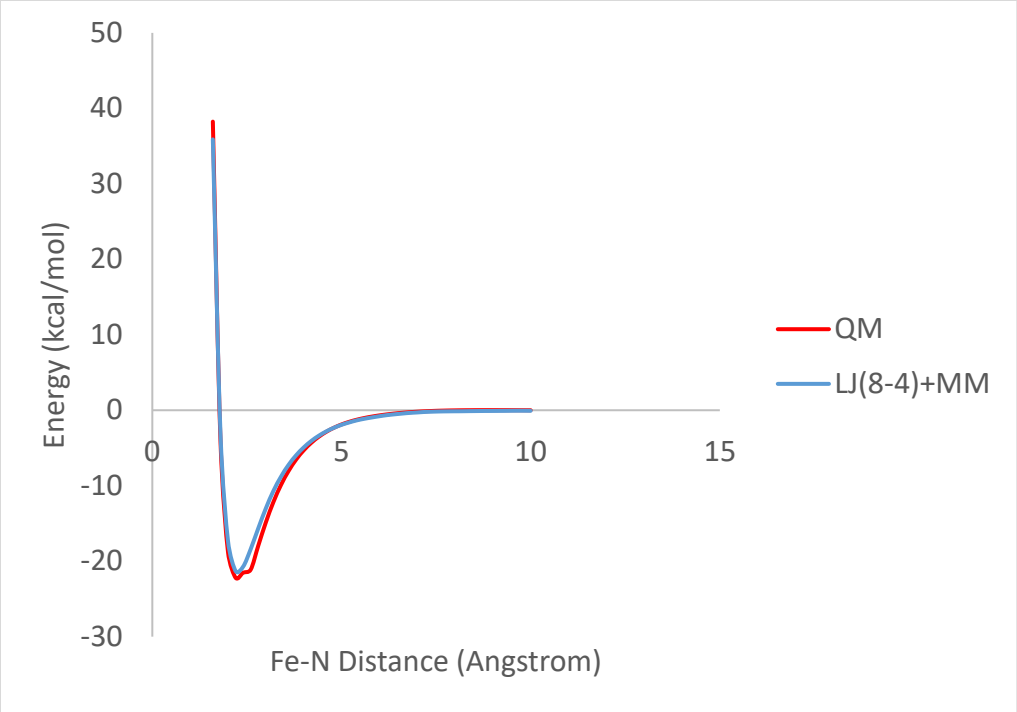

Figure C10. PES Scan for ligand 4.11. Red – QM. Blue – new potential developed in FITTED.

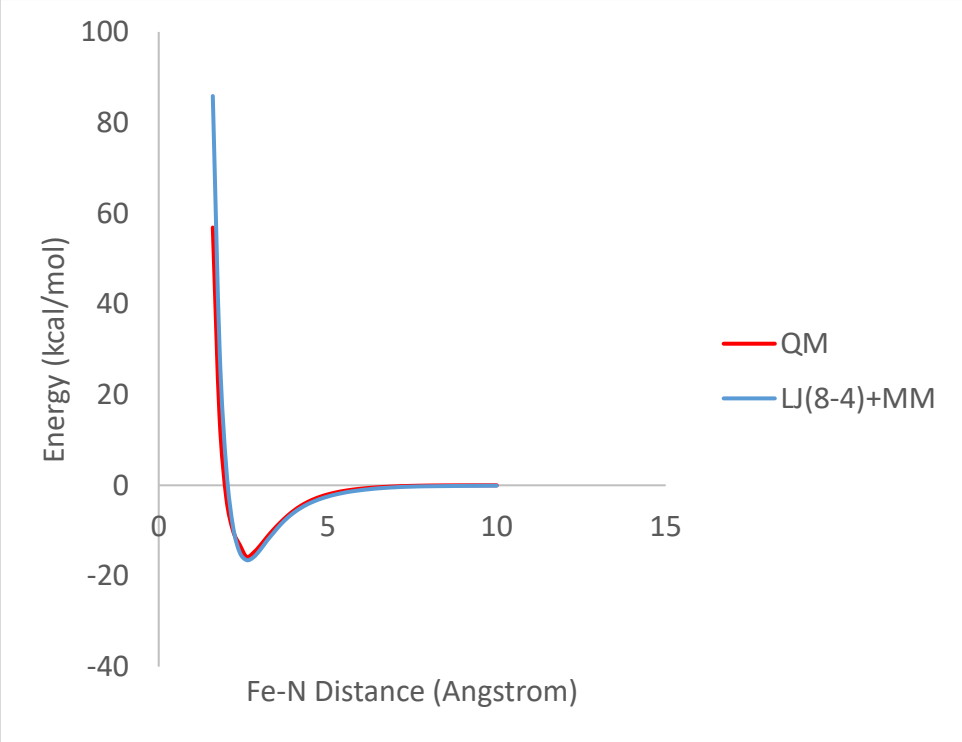

Figure C11. PES Scan for ligand 4.12. Red – QM. Blue – new potential developed in FITTED.

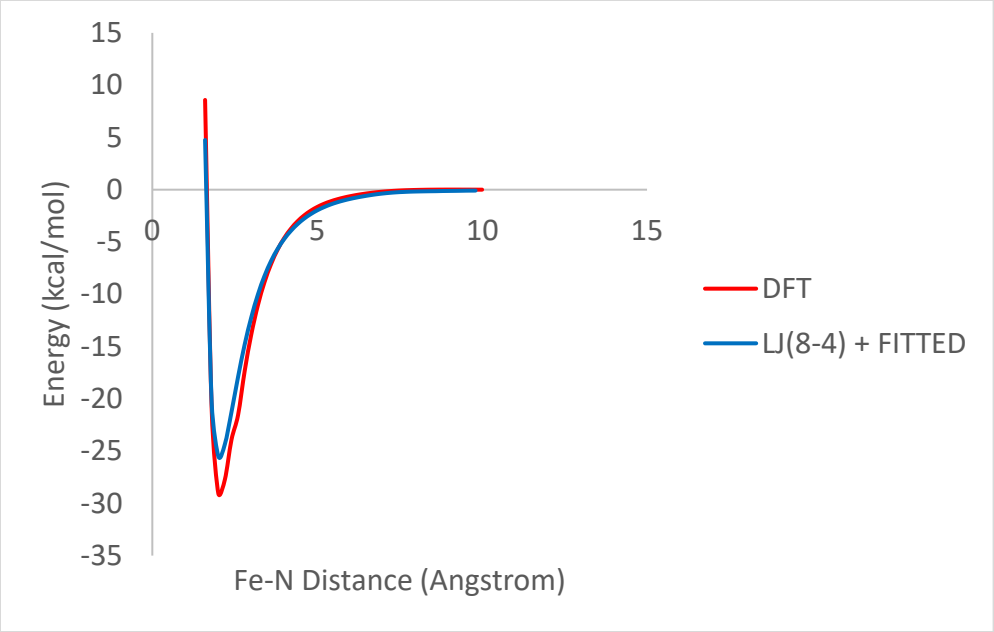

Figure C12. PES Scan for ligand 4.13. Red – QM. Blue – new potential developed in FITTED.

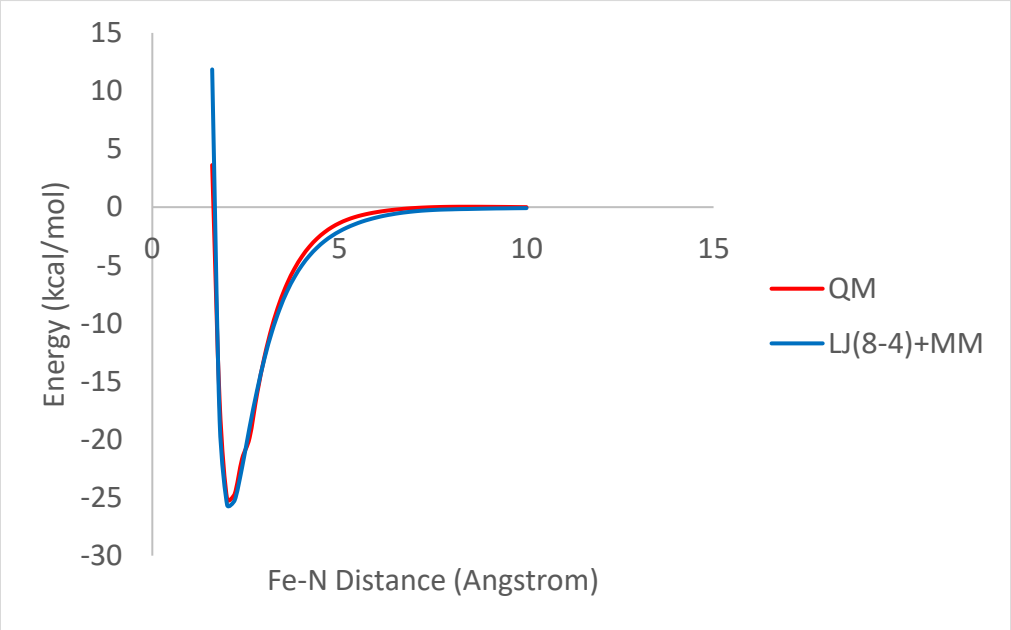

Figure C13. PES Scan for ligand 4.14. Red – QM. Blue – new potential developed in FITTED.

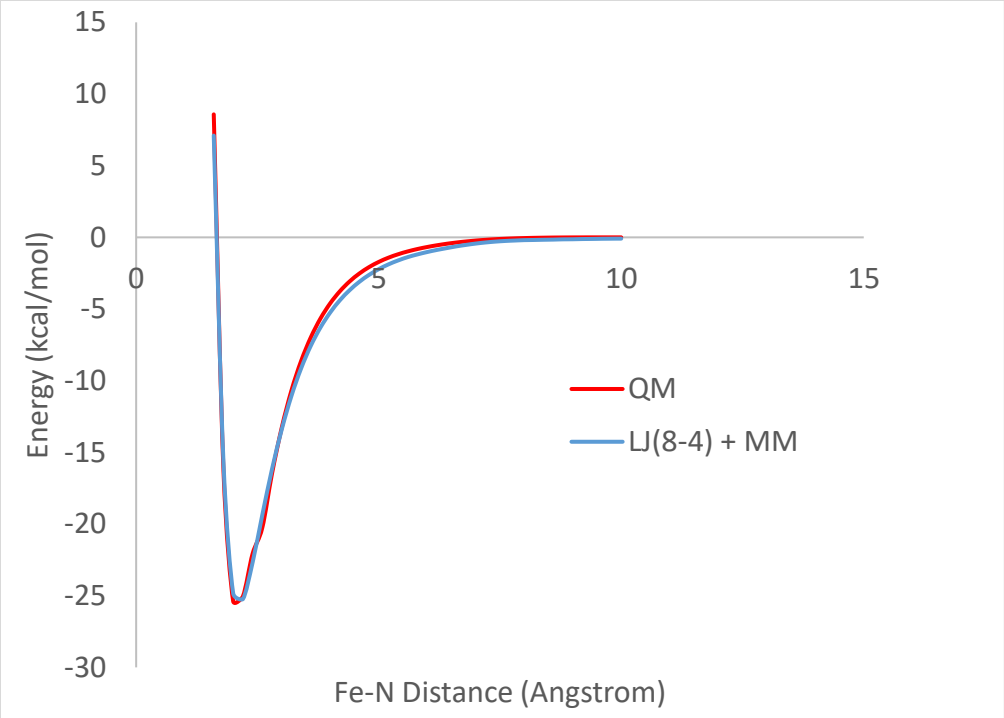

Figure C14. PES Scan for ligand 4.15. Red – QM. Blue – new potential developed in FITTED.

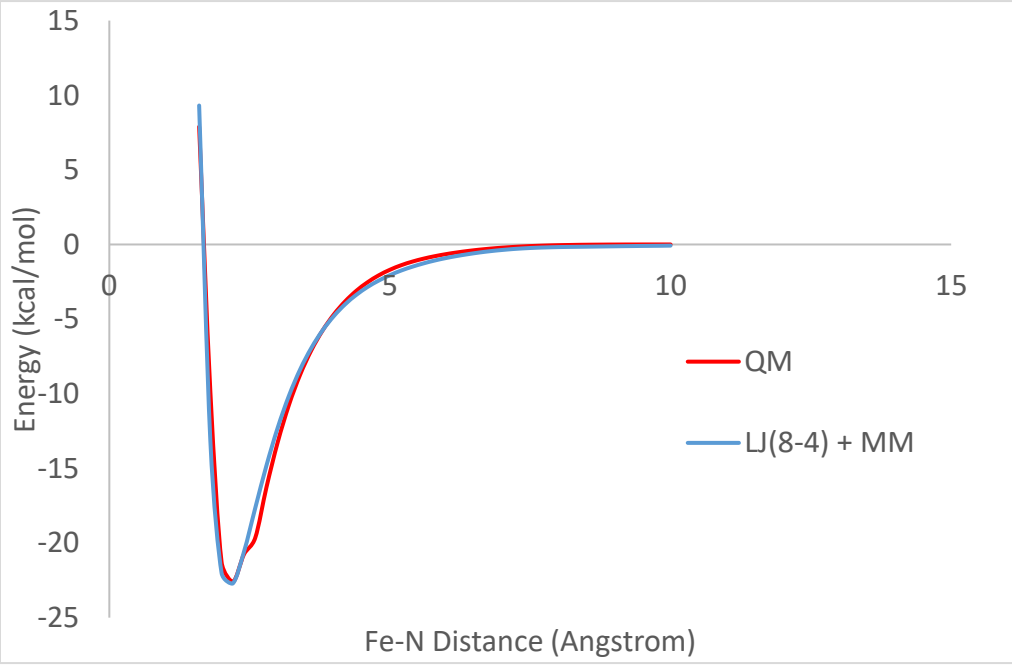

Figure C15. PES Scan for ligand 4.16. Red – QM. Blue – new potential developed in FITTED.

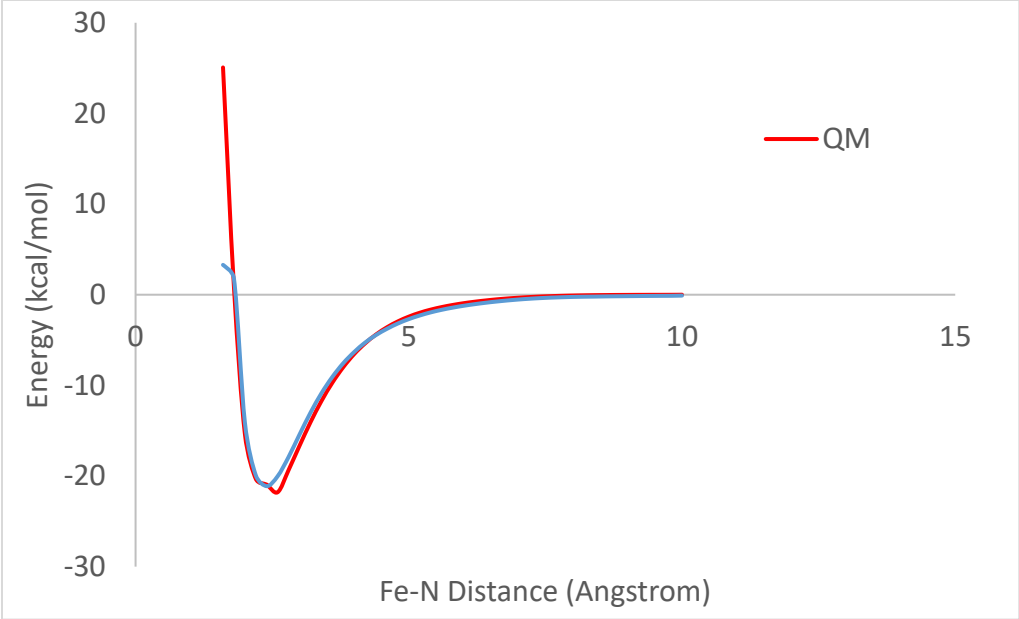

Figure C16. PES Scan for ligand 4.17. Red – QM. Blue – new potential developed in FITTED.

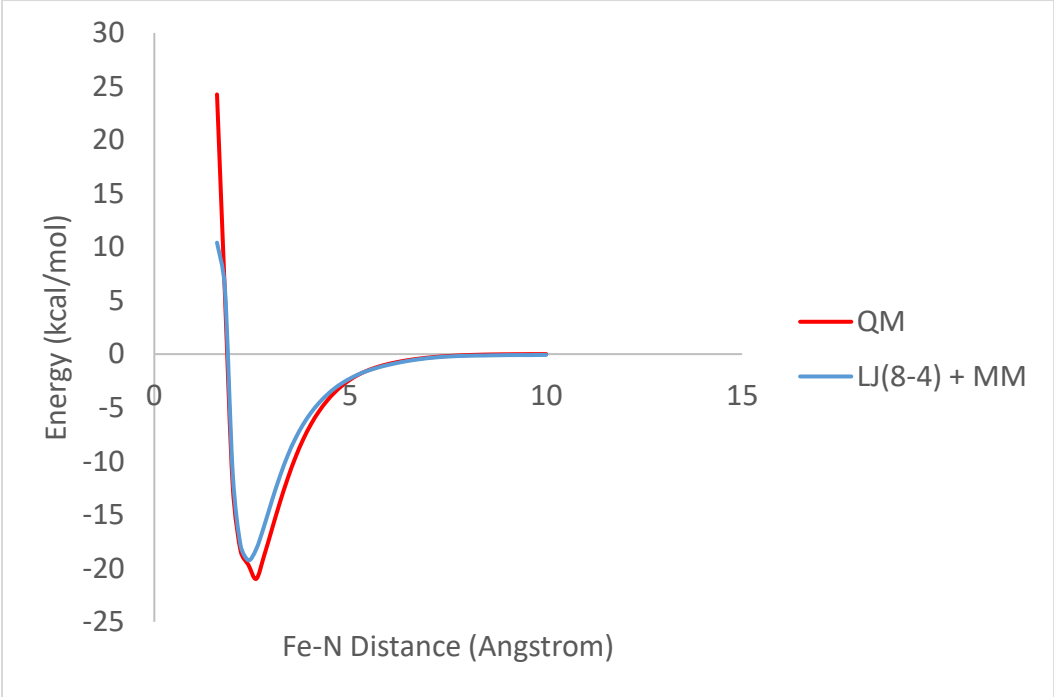

Figure C17. PES Scan for ligand 4.18. Red – QM. Blue – new potential developed in FITTED.

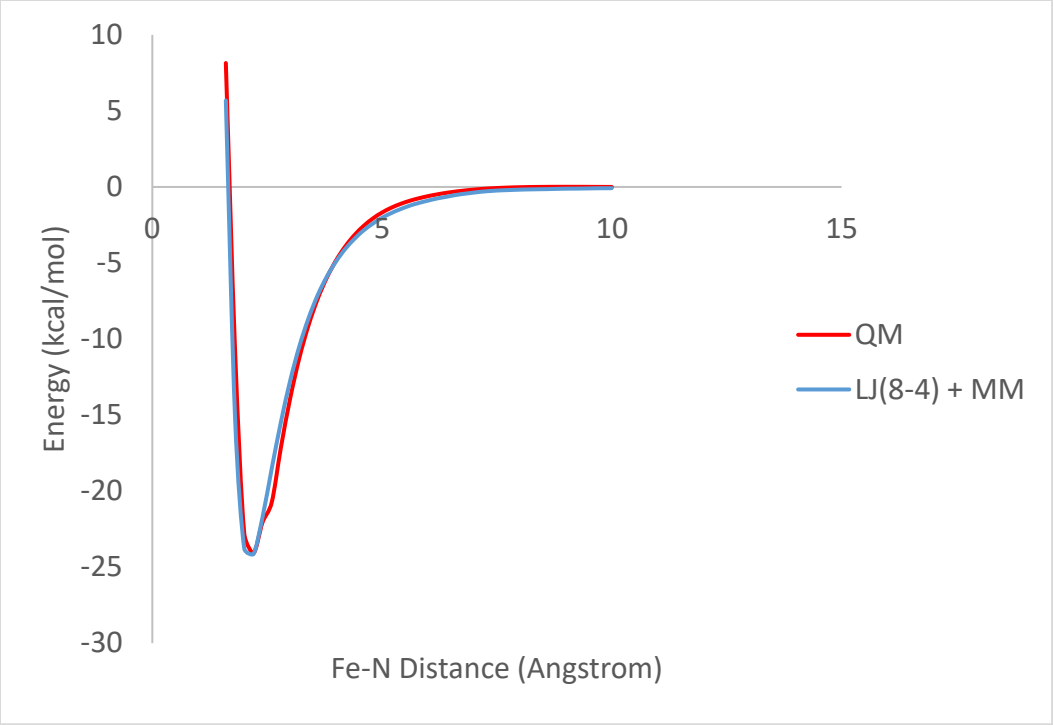

Figure C18. PES Scan for ligand 4.19. Red – QM. Blue – new potential developed in FITTED.

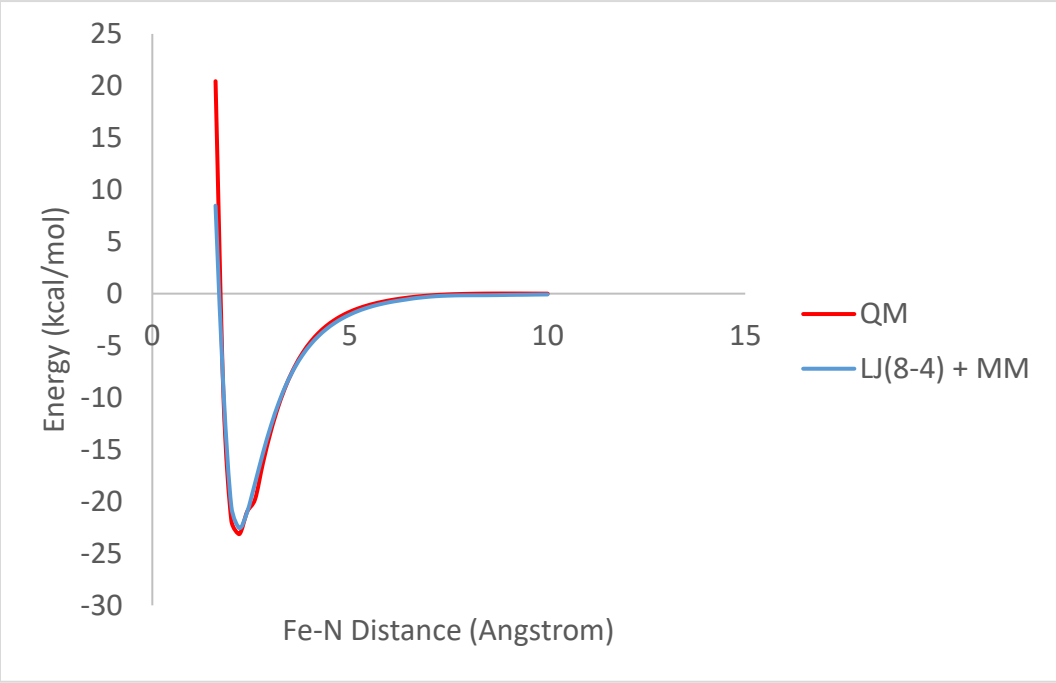

Figure C19. PES Scan for ligand 4.20. Red – QM. Blue – new potential developed in FITTED.

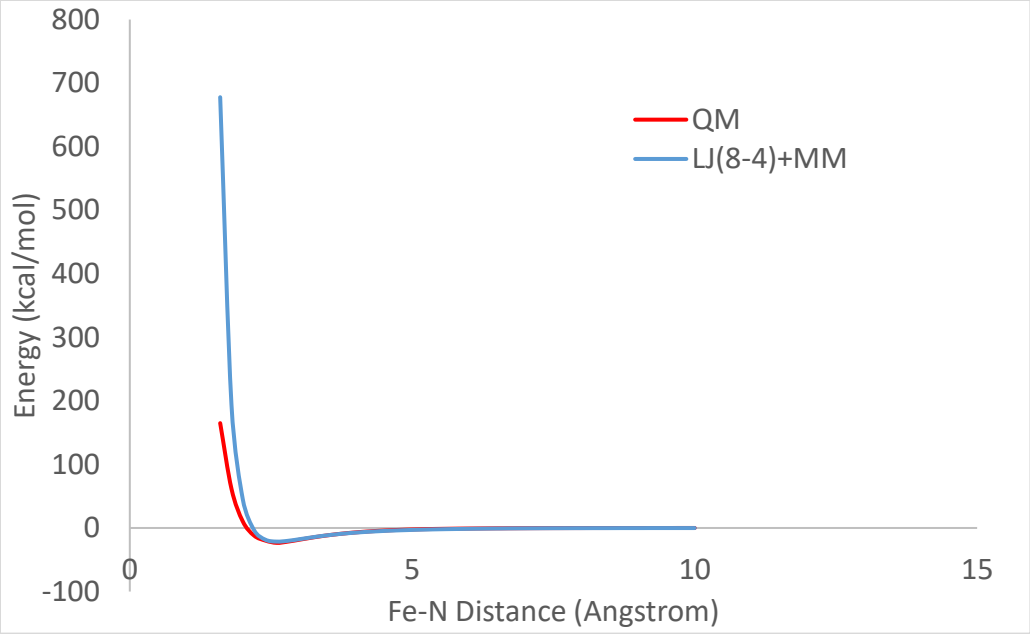

Figure C20. PES Scan for ligand 4.21 – axial conformation of N-Me. Red – QM. Blue – new potential developed in FITTED.

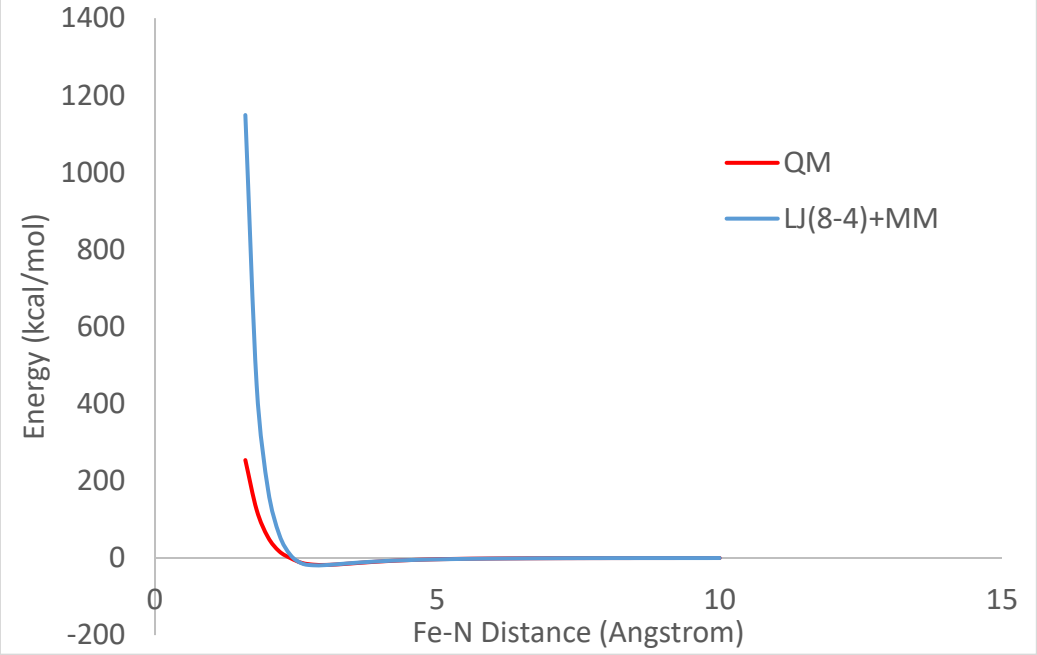

Figure C21. PES Scan for ligand 4.21 – equatorial conformation of N-Me. Red – QM. Blue – new potential developed in FITTED.

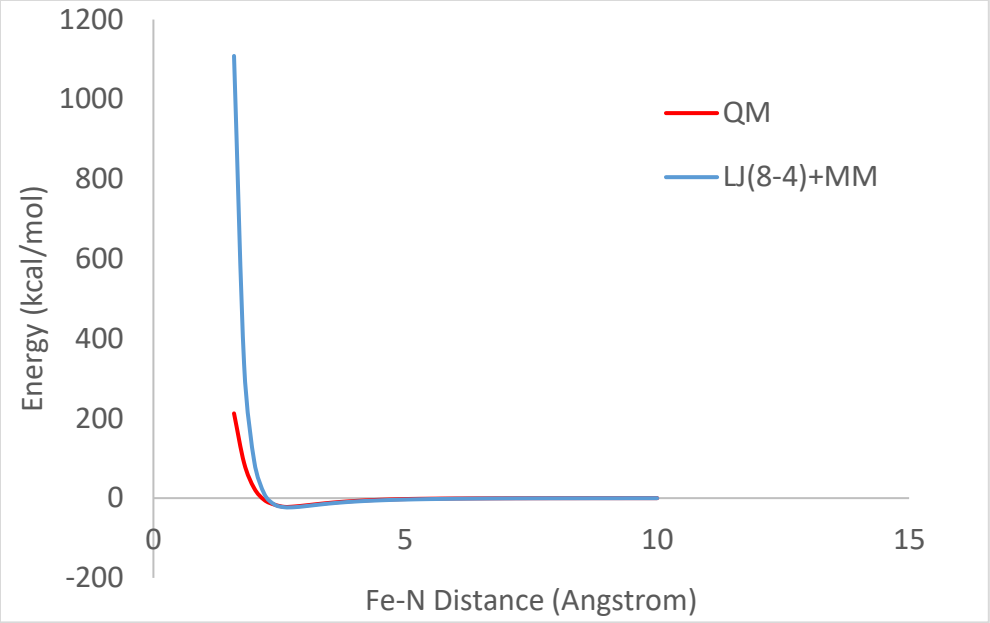

Figure C22. PES Scan for ligand 4.22 – axial conformation of N-Me. Red – QM. Blue – new potential developed in FITTED.

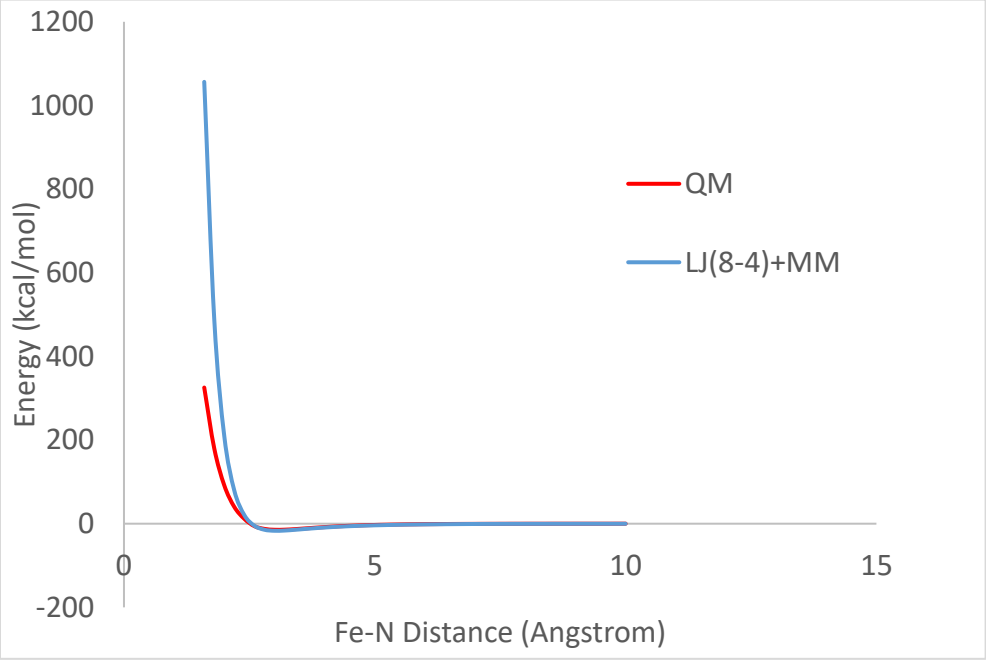

Figure C23. PES Scan for ligand 4.22 – equatorial conformation of N-Me. Red – QM. Blue – new potential developed in FITTED.

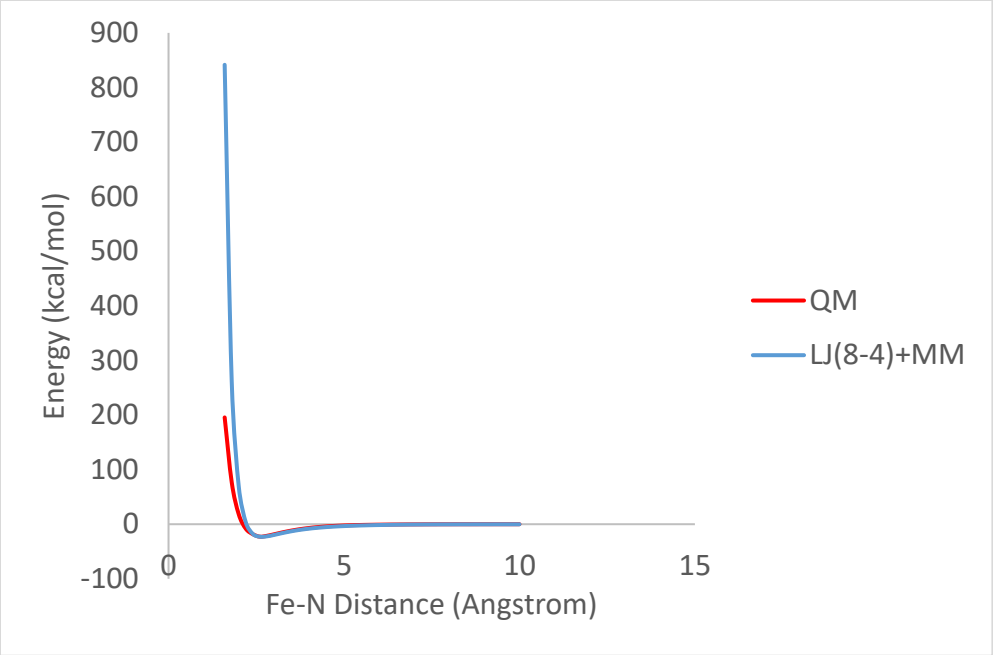

Figure C24. PES Scan for ligand 4.23 – axial conformation of N-Me. Red – QM. Blue – new potential developed in FITTED.

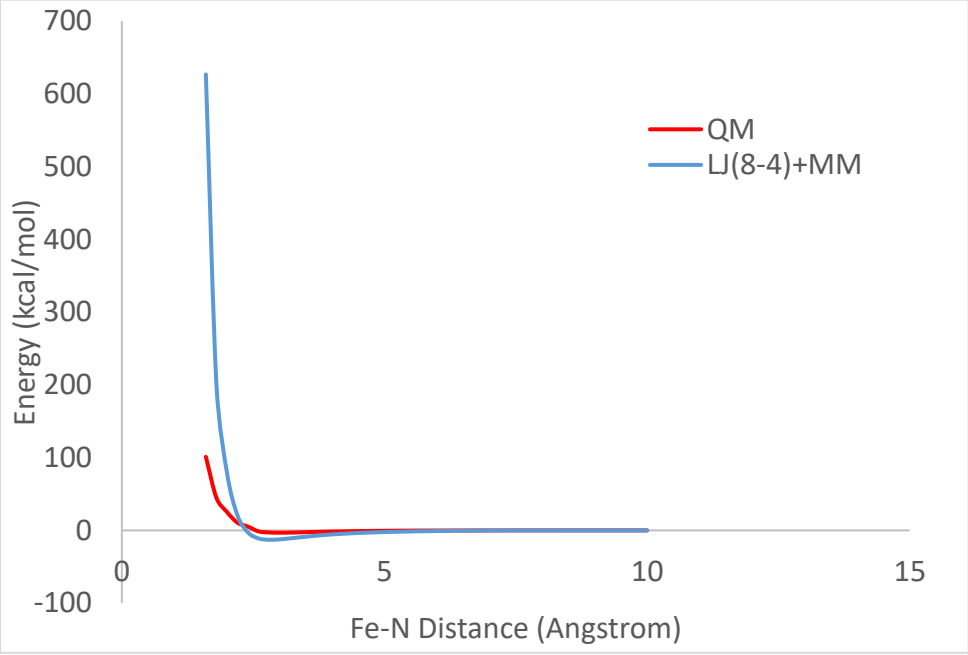

Figure C25. PES Scan for ligand 4.23 – equatorial conformation of N-Me. Red – QM. Blue – new potential developed in FITTED.

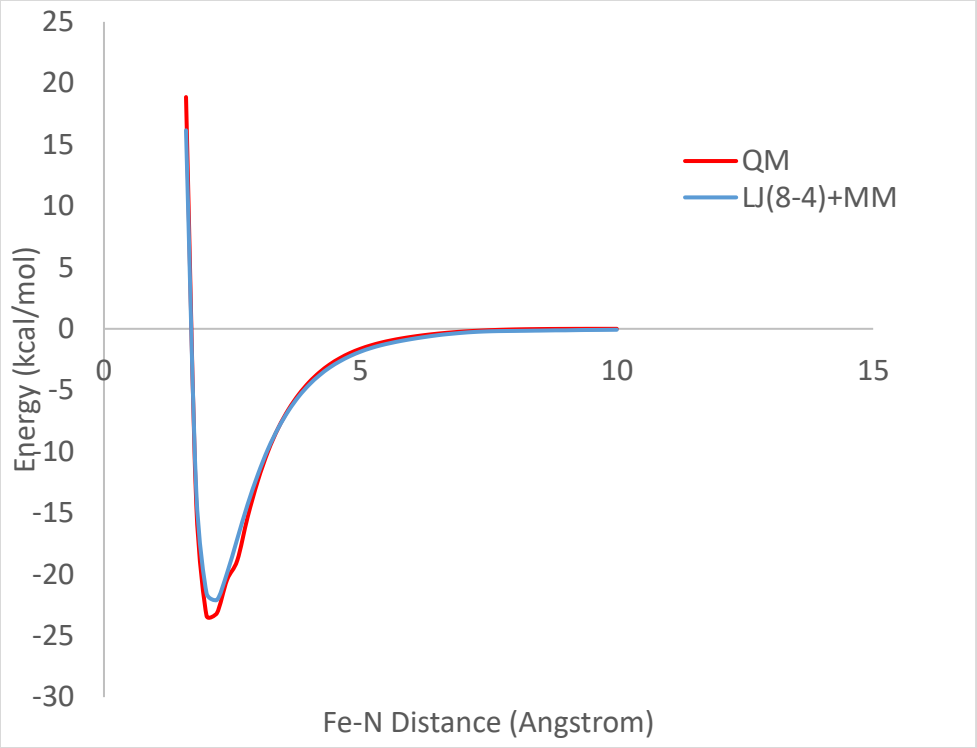

Figure C26. PES Scan for ligand 4.24. Red – QM. Blue – new potential developed in FITTED.

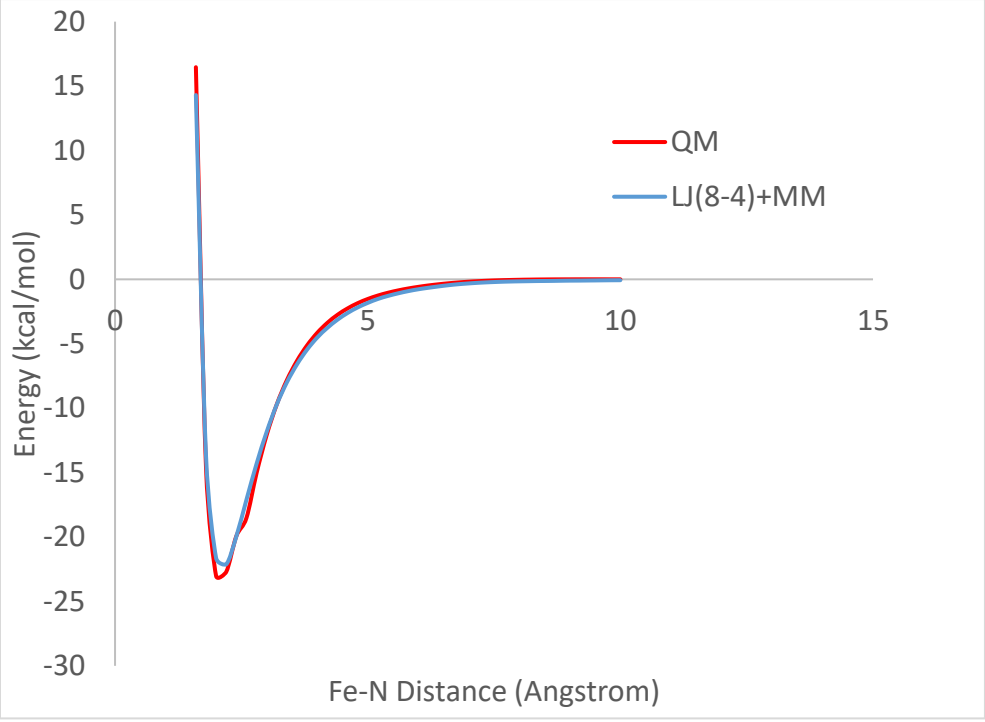

Figure C27. PES Scan for ligand 4.24a. Red – QM. Blue – new potential developed in FITTED.

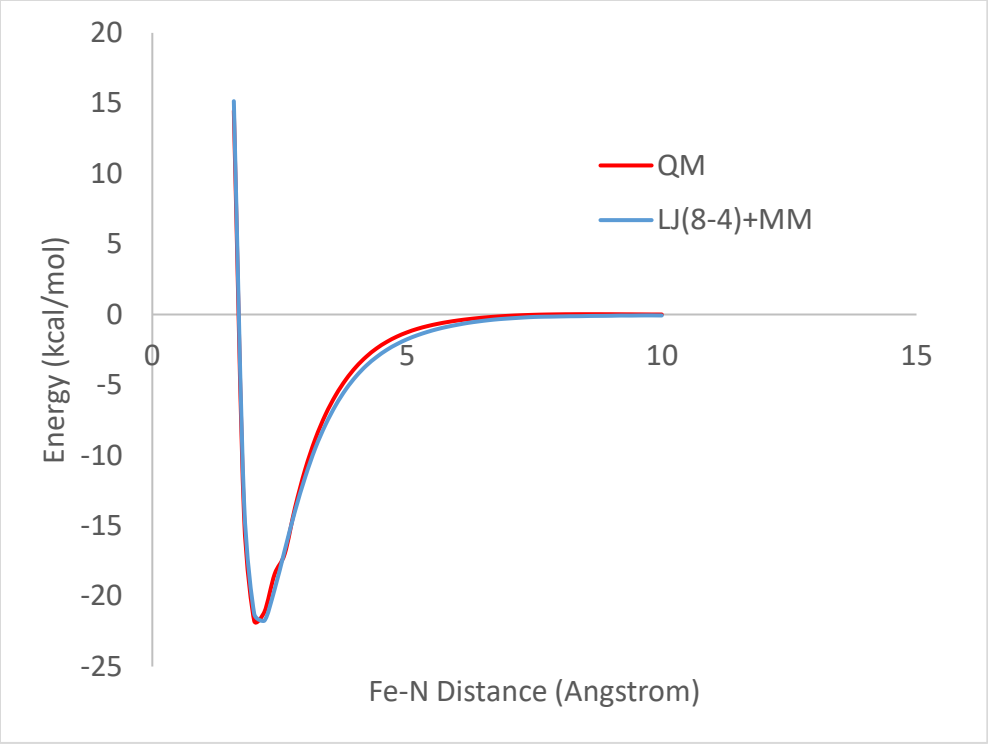

Figure C28. PES Scan for ligand 4.25. Red – QM. Blue – new potential developed in FITTED.

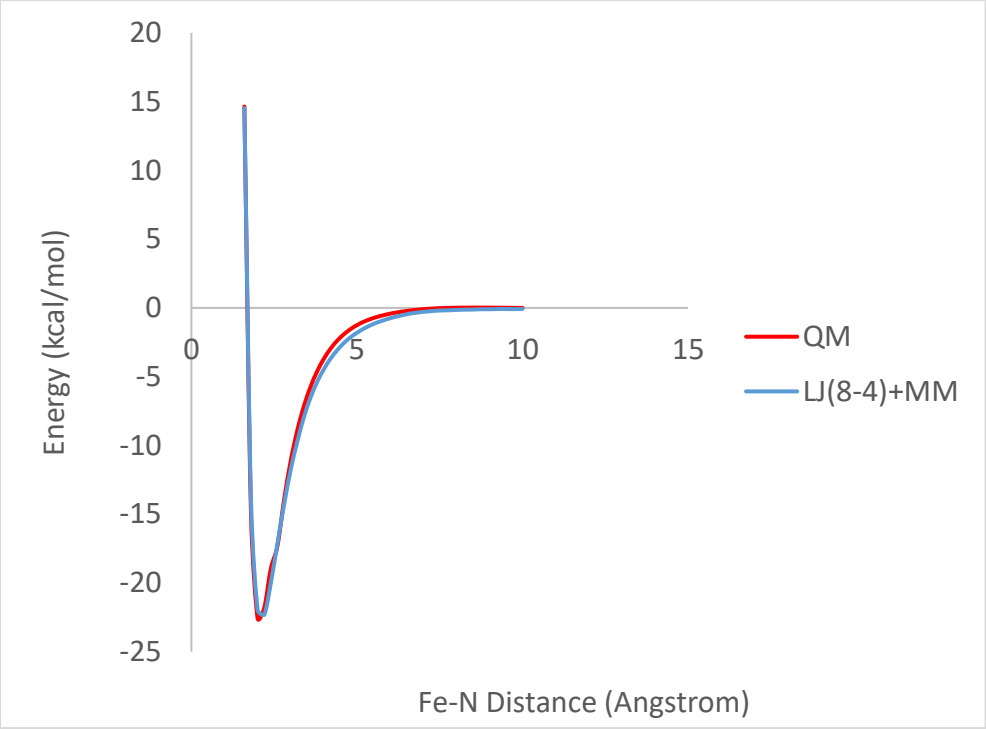

Figure C29. PES Scan for ligand 4.26. Red – QM. Blue – new potential developed in FITTED.

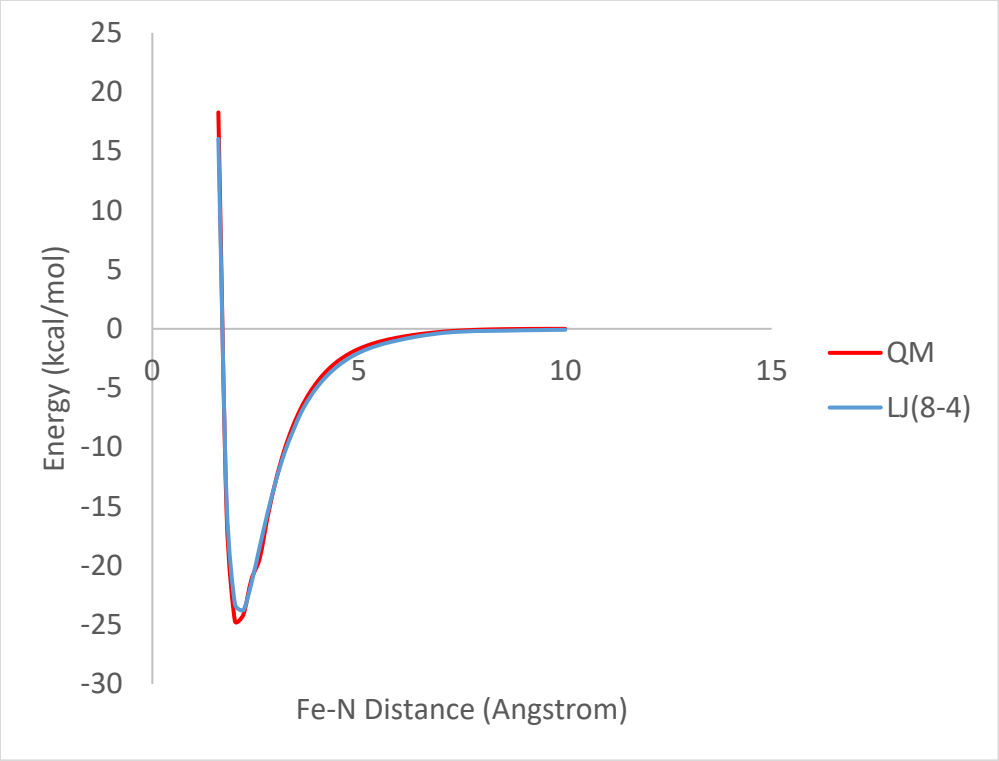

Figure C30. PES Scan for ligand 4.27. Red – QM. Blue – new potential developed in FITTED.

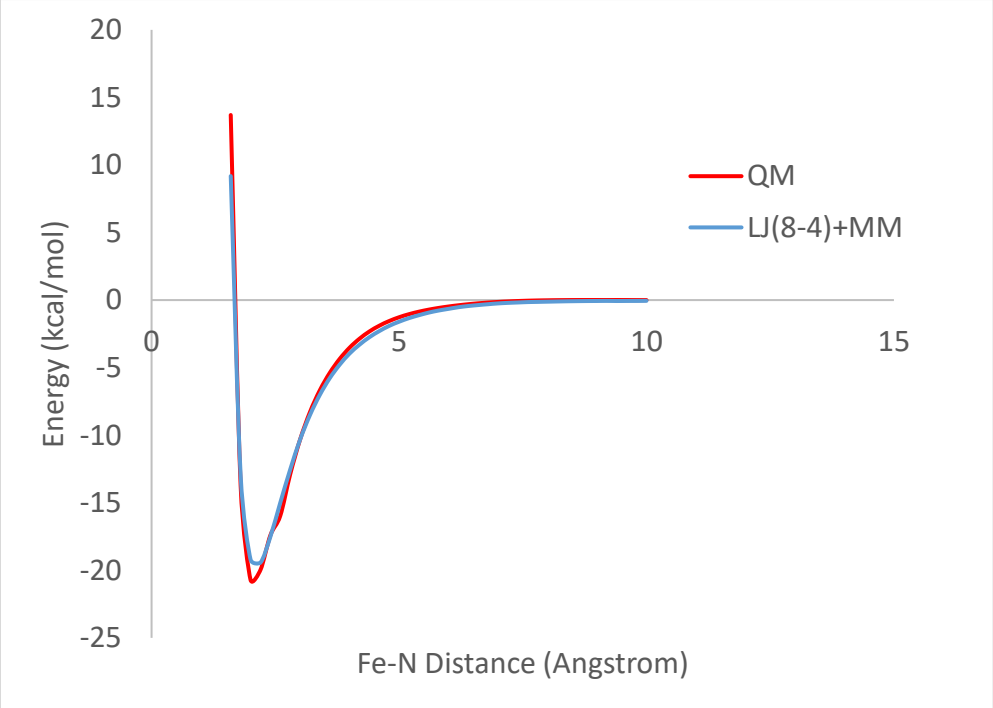

Figure C31. PES Scan for ligand 4.27a. Red – QM. Blue – new potential developed in FITTED.

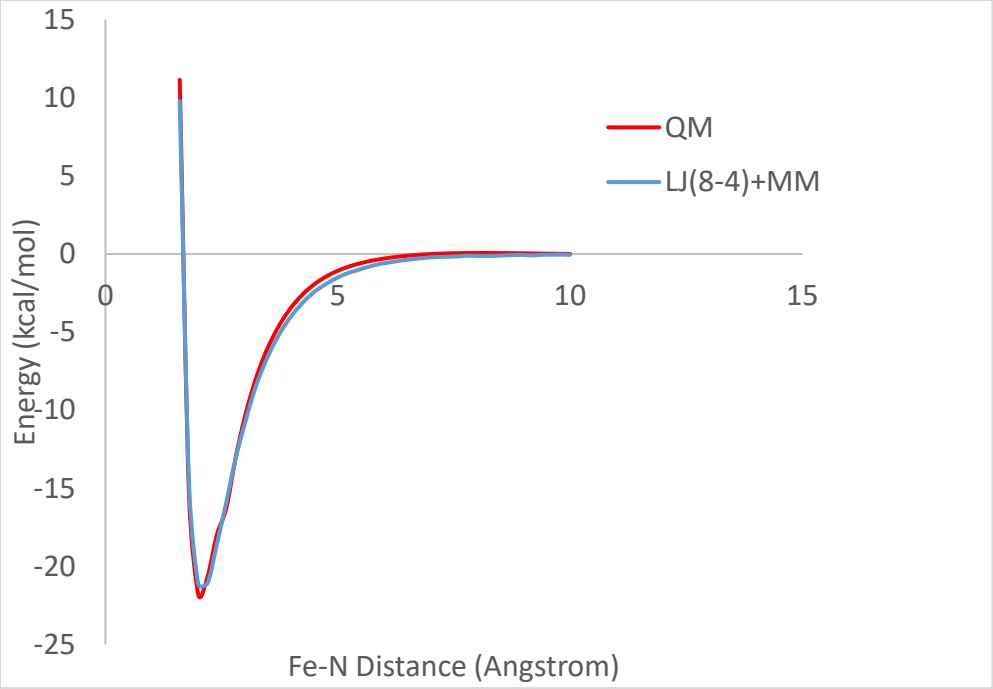

Figure C32. PES Scan for ligand 4.28. Red – QM. Blue – new potential developed in FITTED.

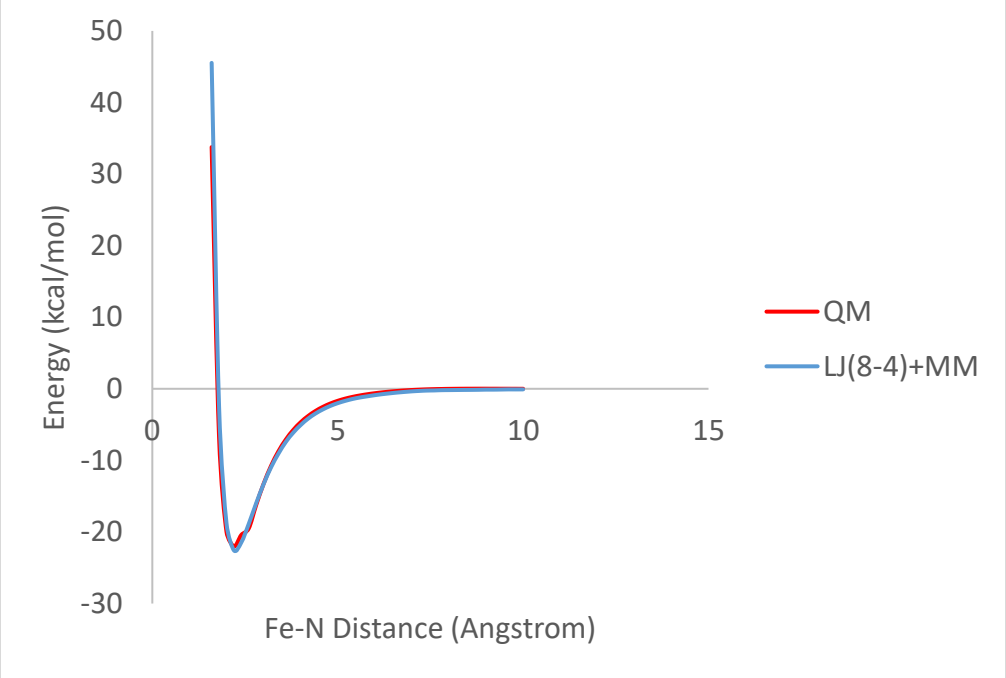

Figure C33. PES Scan for ligand 4.28a. Red – QM. Blue – new potential developed in FITTED.

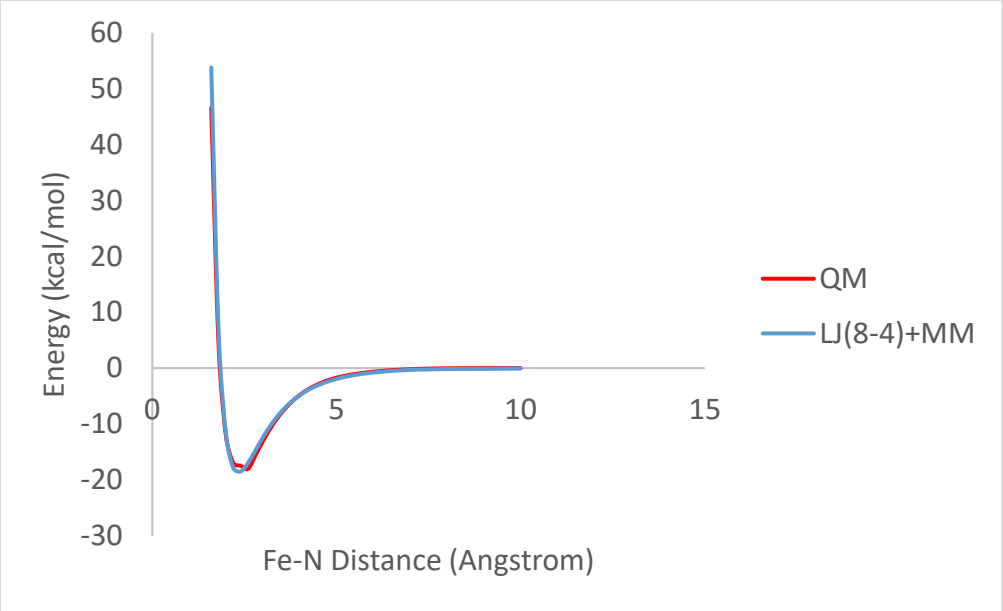

Figure C34. PES Scan for ligand 4.28b. Red – QM. Blue – new potential developed in FITTED.

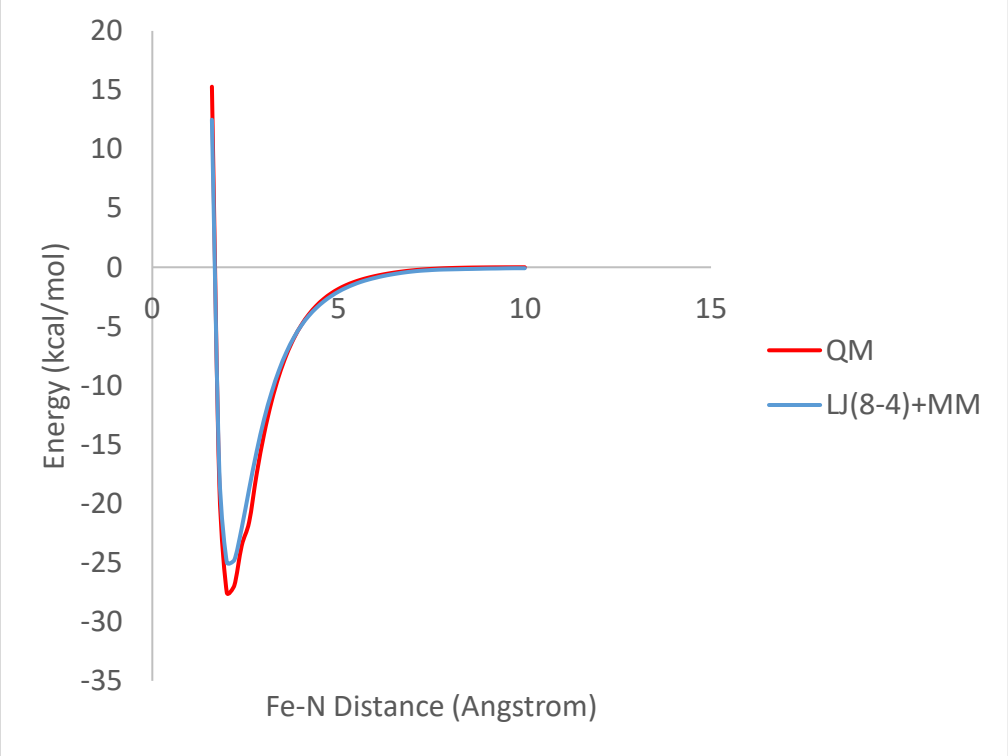

Figure C35. PES Scan for ligand 4.29. Red – QM. Blue – new potential developed in FITTED.

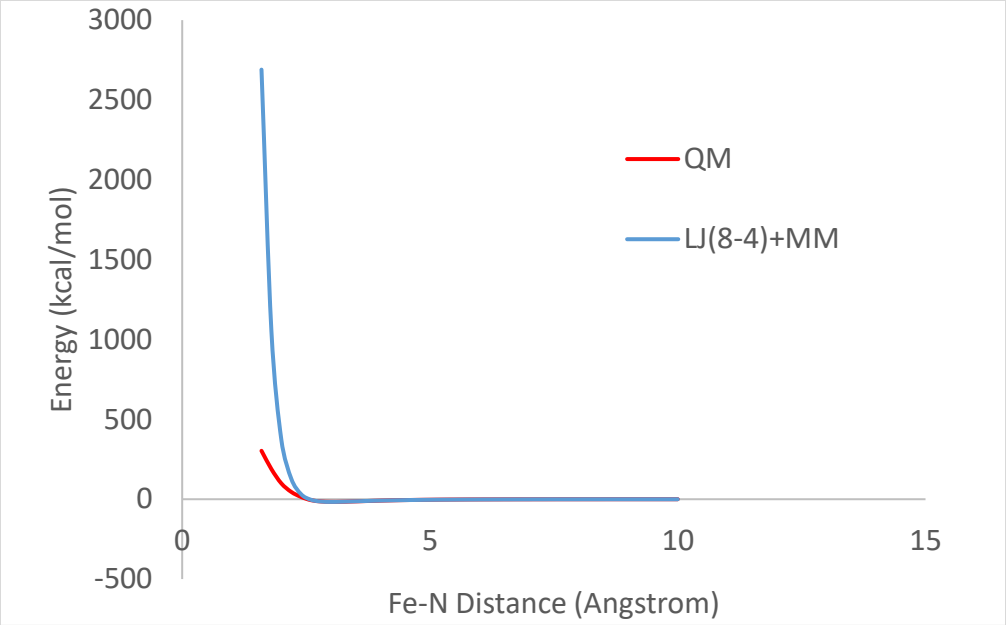

Figure C36. PES Scan for ligand 4.31. Red – QM. Blue – new potential developed in FITTED.

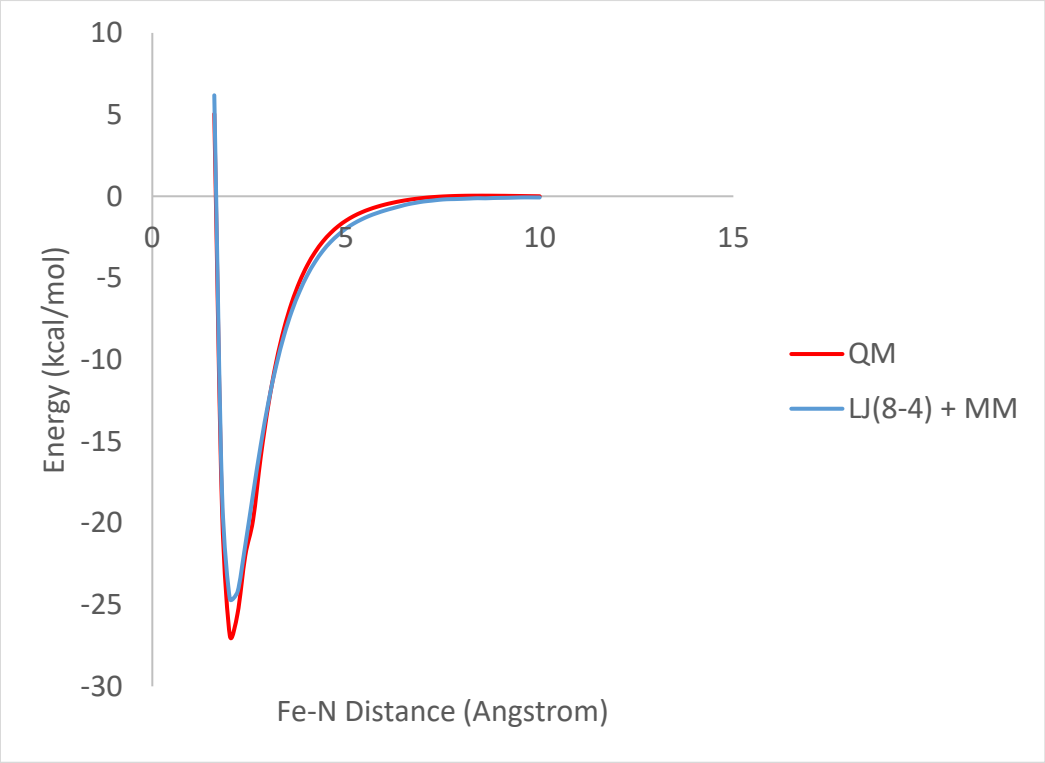

Figure C37. PES Scan for ligand 4.32. Red – QM. Blue – new potential developed in FITTED.

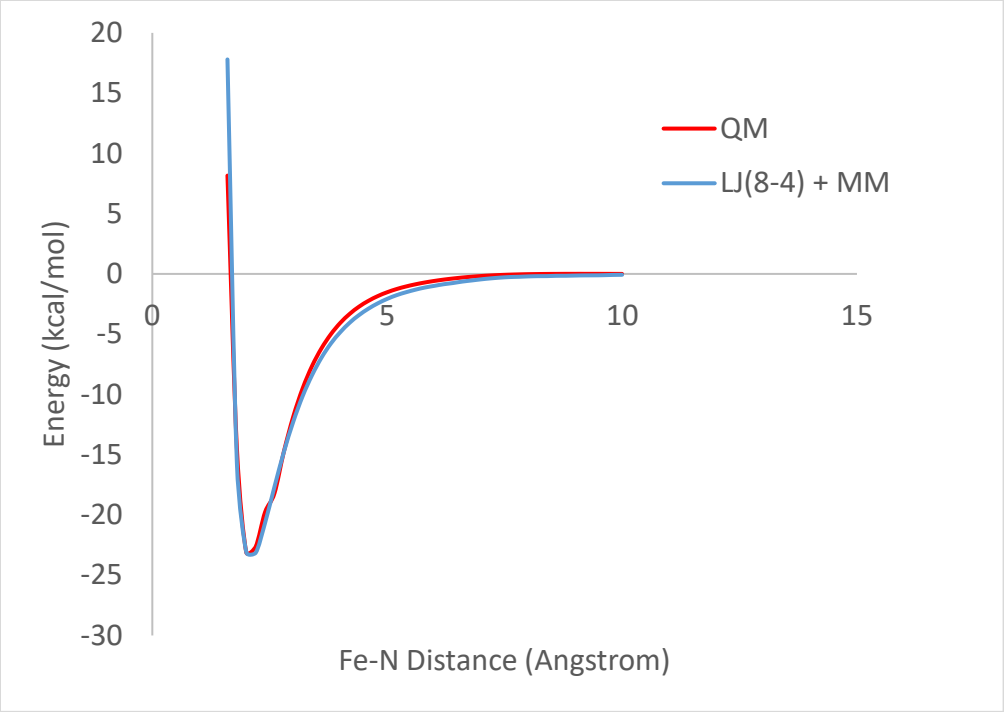

Figure C38. PES Scan for ligand 4.33. Red – QM. Blue – new potential developed in FITTED.

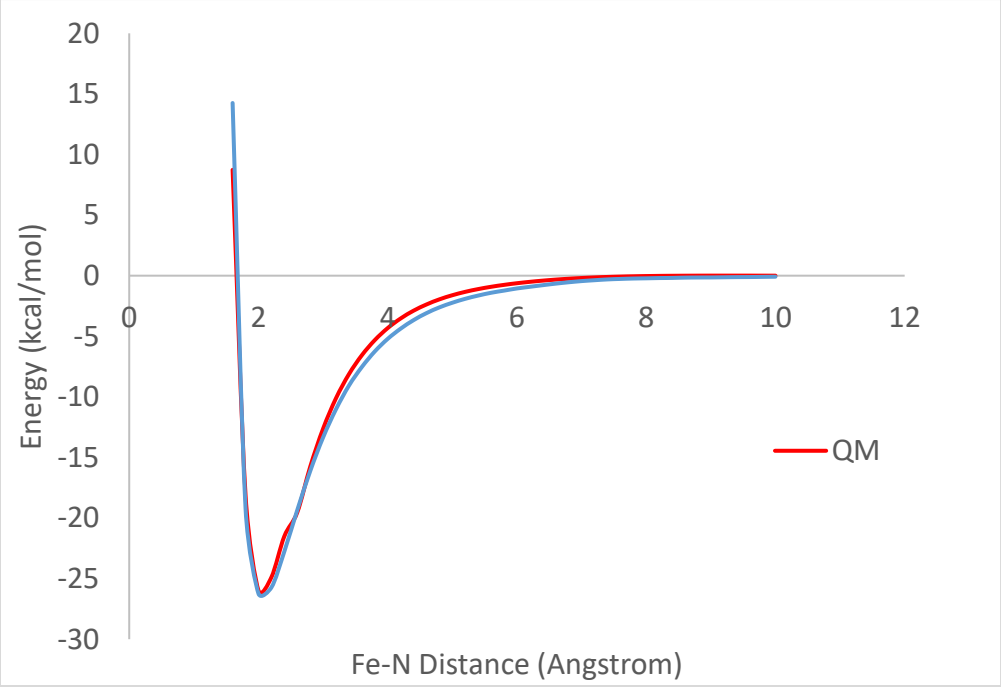

Figure C39. PES Scan for ligand 4.34. Red – QM. Blue – new potential developed in FITTED.

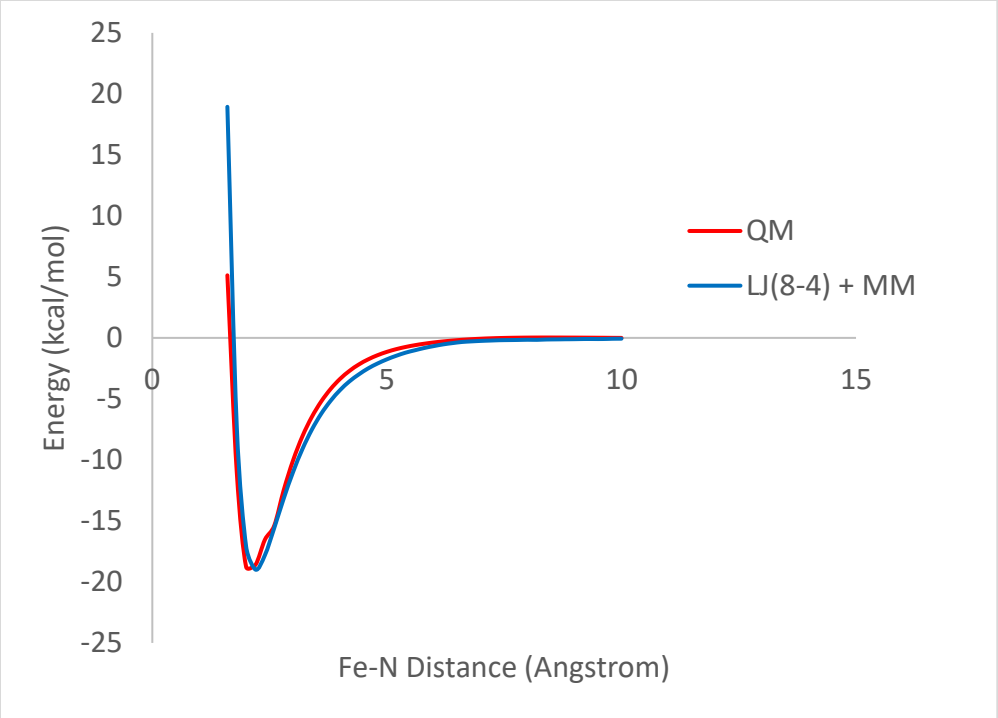

Figure C40. PES Scan for ligand 4.35. Red – QM. Blue – new potential developed in FITTED.

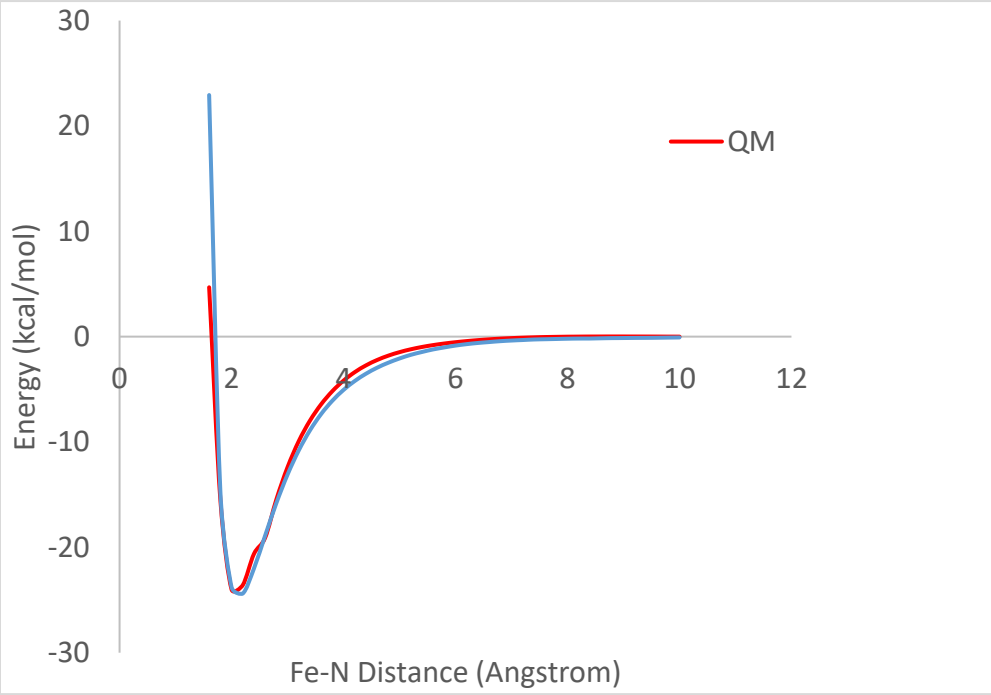

Figure C41. PES Scan for ligand 4.36. Red – QM. Blue – new potential developed in FITTED.

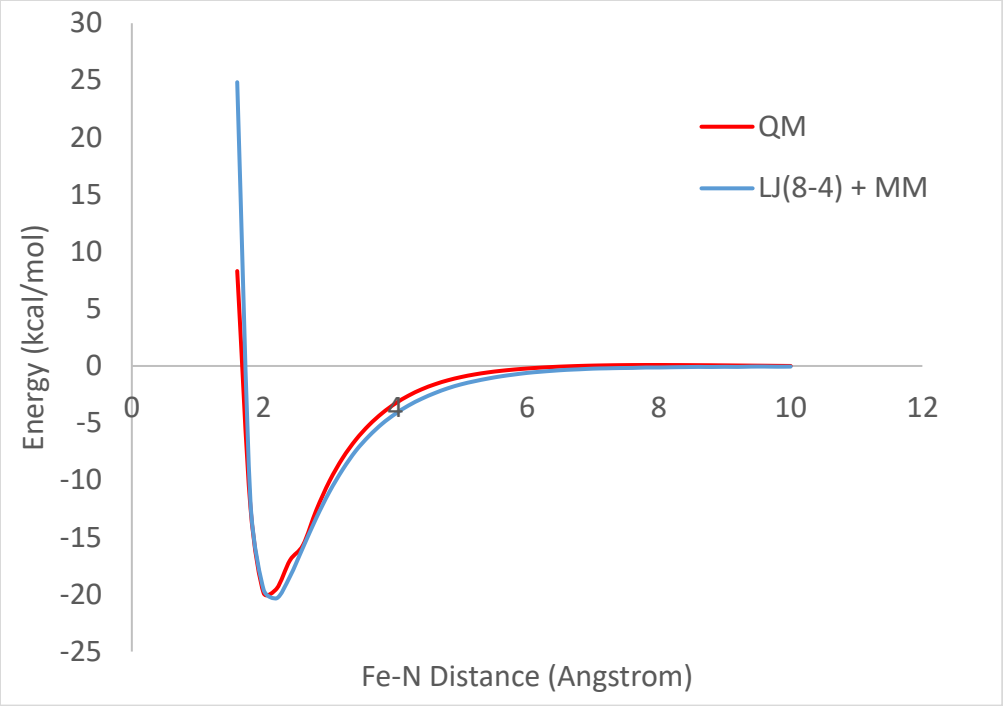

Figure C42. PES Scan for ligand 4.37. Red – QM. Blue – new potential developed in FITTED.

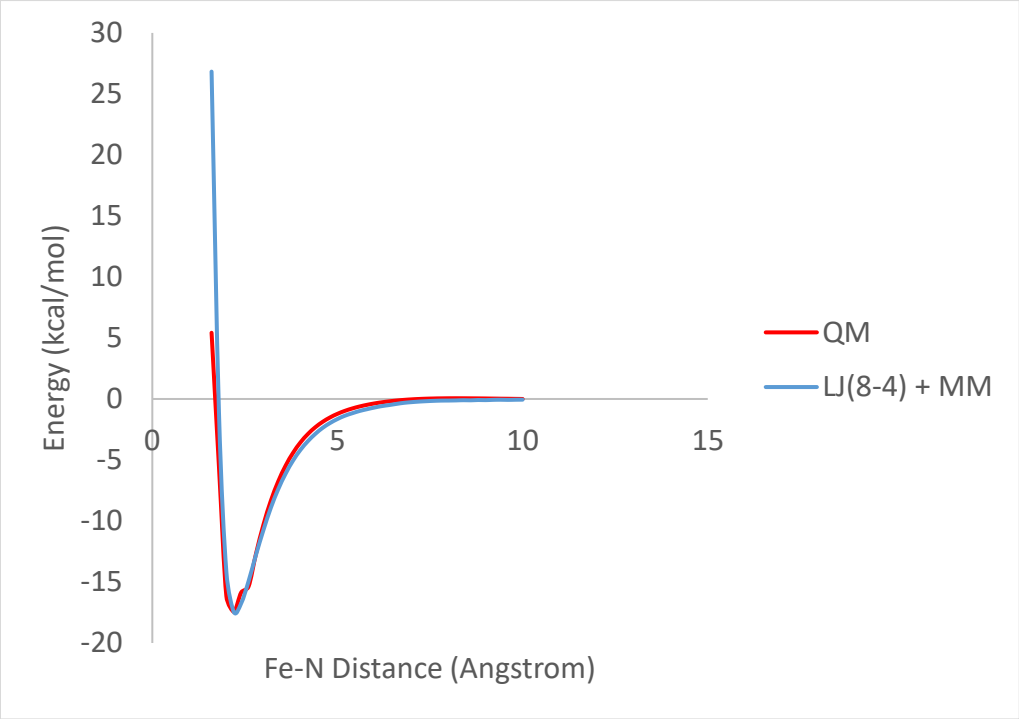

Figure C43. PES Scan for ligand 4.37a. Red – QM. Blue – new potential developed in FITTED.

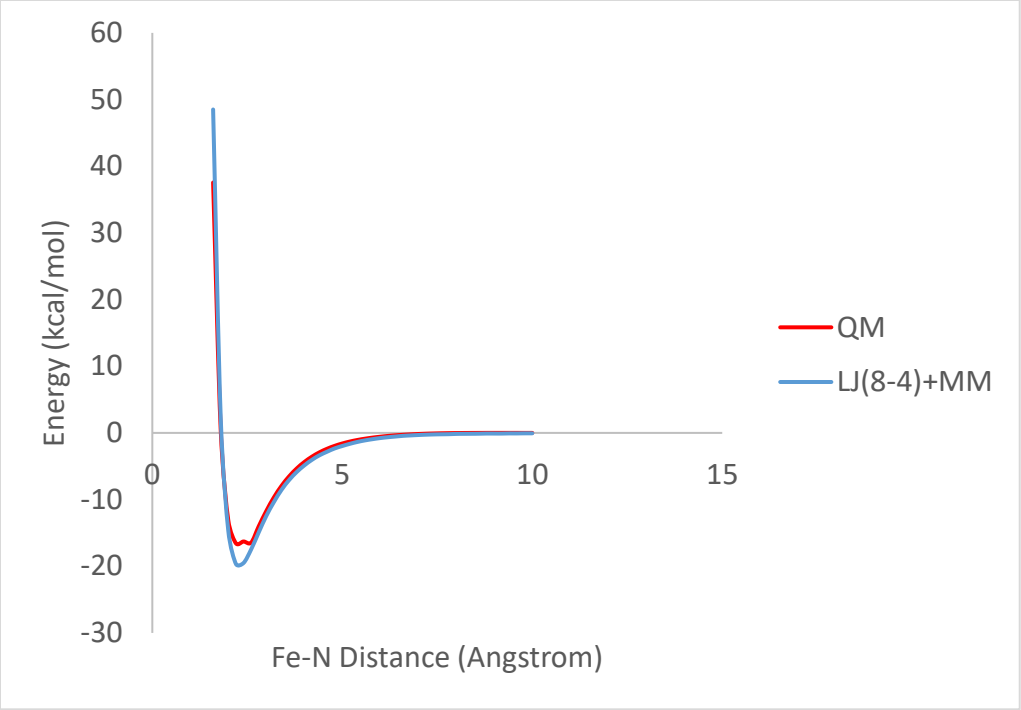

Figure C44. PES Scan for ligand 4.37b. Red – QM. Blue – new potential developed in FITTED.

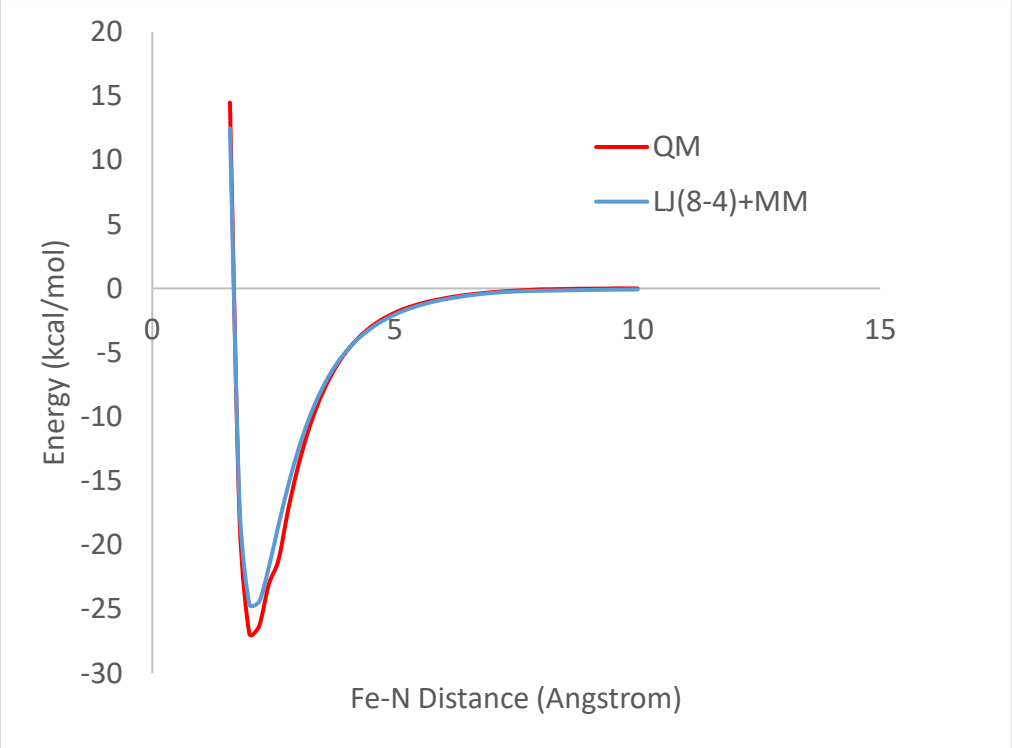

Figure C45. PES Scan for ligand 4.38. Red – QM. Blue – new potential developed in FITTED.

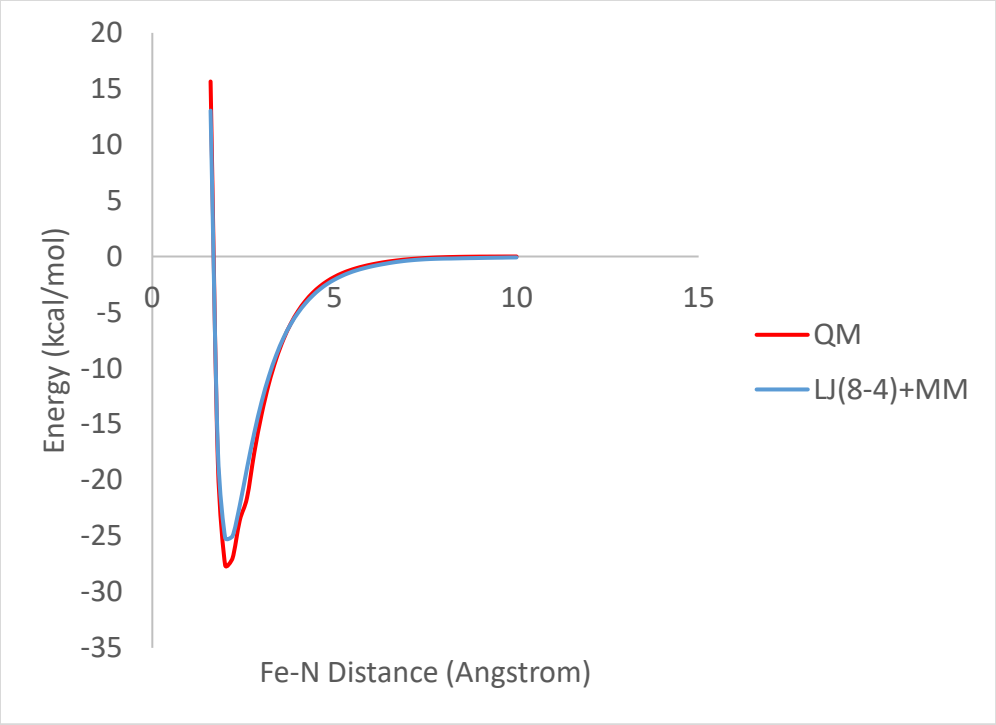

Figure C46. PES Scan for ligand 4.39. Red – QM. Blue – new potential developed in FITTED.

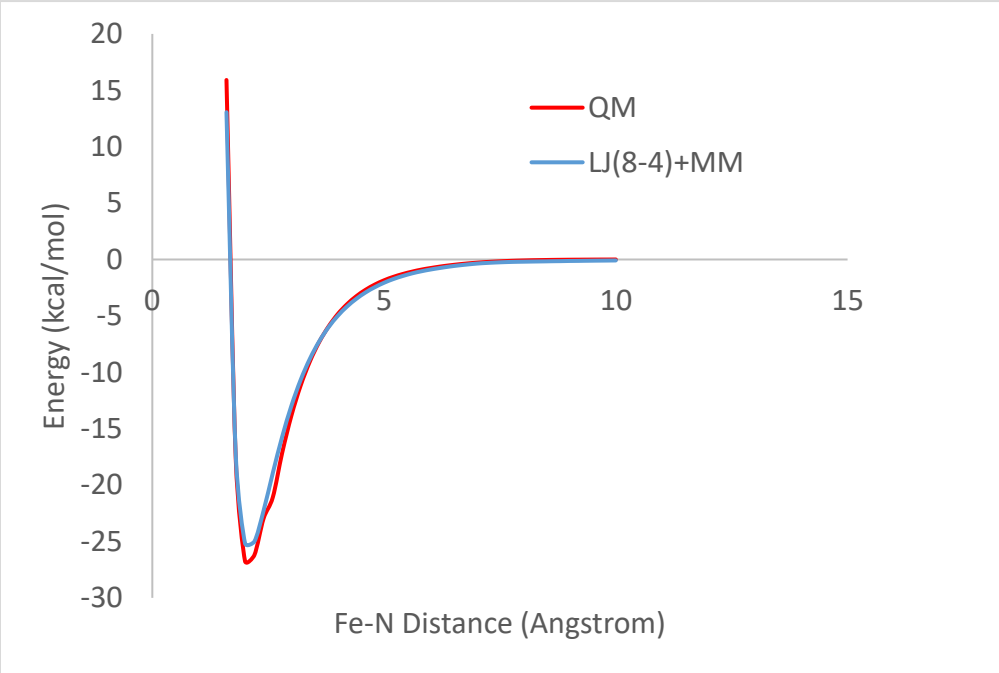

Figure C47. PES Scan for ligand 4.40. Red – QM. Blue – new potential developed in FITTED.

Table C1. Data used to build the new MM potential in FITTED (see Equation 4.1 in Chapter 4).

Inhibitor (FITTED atom type)	A	B	ε (kcal/mol)	σ (A)	Offset	QM Min. (A)	MM Min. (A)	MAE (kcal/mol)*
1(nb)	6066.2118	925.6305	35.31	1.6	+0.2	2.00	2.00	0.63
2(nb)	6323.9098	964.9521	36.81	1.6	+0.2	2.00	2.00	0.62
3(nb)	6607.3776	1008.2058	38.46	1.6	+0.2	2.00	2.00	0.74
4(nb)	6004.3642	916.1933	34.95	1.6	+0.2	2.00	2.00	0.54
5(nb)	6238.0105	951.8449	36.31	1.6	+0.2	2.00	2.00	0.61
6(nb)	6416.6811	979.1078	37.35	1.6	+0.2	2.00	2.00	0.63
9(n2)	5952.8246	908.3289	34.65	1.6	+0.2	2.00	2.00	0.43
10(n2)	6871.9476	1048.5760	40.00	1.6	+0.2	3.00	3.00	3.38
10a(n2)	4782.8756	729.8089	27.84	1.6	+0.2	2.20	2.20	0.33
11(n2)	5129.9089	782.7619	29.86	1.6	+0.2	2.20	2.20	0.48
12(n2)	6871.9476	1048.5760	40.00	1.6	+0.2	2.60	2.60	0.54
13(nb)	5576.5855	850.9194	32.46	1.6	+0.2	2.00	2.00	0.69
14(nb)	6012.9542	917.5040	35.00	1.6	+0.2	2.00	2.00	0.63
15(nb)	6294.7040	960.4956	36.64	1.6	+0.2	2.00	2.20	0.37
16(nb)	5463.1984	833.6179	31.80	1.6	+0.2	2.20	2.20	0.40
17(nb)	7038.5924	1074.0040	40.97	1.6	+0.2	2.20	2.40	0.88
18(nb)	5021.6757	766.2469	29.23	1.6	+0.2	2.40	2.40	0.86
19(nb)	5755.2561	878.1824	33.50	1.6	+0.2	2.20	2.20	0.49
20(nb)	5478.6603	835.9772	31.89	1.6	+0.2	2.20	2.20	0.54
21-ax(n3)	6871.9477	1048.5760	40.00	1.6	+0.2	2.60	2.60	0.42
21-eq(n3)	6871.9477	1048.5760	40.00	1.6	+0.2	3.00	3.00	0.48
22-ax(n3)	9105.3307	1389.3632	53.00	1.6	+0.2	2.60	2.60	0.77
22-eq(n3)	9105.3307	1389.3632	53.00	1.6	+0.2	3.00	3.00	0.87
23-ax(n3)	8589.9346	1310.7200	50.00	1.6	+0.2	2.60	2.60	0.62
23-eq(n3)	858.9935	131.0720	5.00	1.6	+0.2	3.00	2.80	2.20
24(n2)	5382.4530	821.2972	31.33	1.6	+0.2	2.00	2.20	0.36
24a(n2)	4781.1576	729.5468	27.83	1.6	+0.2	2.00	2.20	0.32
25(n2)	5081.8053	775.4220	29.58	1.6	+0.2	2.00	2.20	0.37
26(n2)	5056.0355	771.4898	29.43	1.6	+0.2	2.00	2.20	0.39
27(n2)	5567.9956	849.6087	32.41	1.6	+0.2	2.00	2.20	0.33
27a(n2)	3980.5757	607.3876	23.17	1.6	+0.2	2.00	2.20	0.36
28(n2)	4191.8881	639.6314	24.40	1.6	+0.2	2.00	2.00	0.35
28a(n2)	6012.6542	917.5040	35.00	1.6	+0.2	2.20	2.20	0.65
28b(n2)	4810.3633	734.0032	28.00	1.6	+0.2	2.60	2.40	0.46
29(nb)	6016.3902	918.0283	35.02	1.6	+0.2	2.00	2.00	0.50
31(n3)	6871.9477	1048.5760	40.00	1.6	+0.2	3.00	3.00	0.74
32(n2)	5239.8601	799.5392	30.50	1.6	+0.2	2.00	2.00	0.45
33(n2)	5325.7594	812.6464	31.00	1.6	+0.2	2.00	2.20	0.62
34(n2)	6098.8535	930.6112	35.50	1.6	+0.2	2.00	2.00	0.58
35(n2)	4552.6653	694.6816	26.50	1.6	+0.2	2.00	2.20	0.85
36(n2)	5669.3568	865.0752	33.00	1.6	+0.2	2.00	2.20	0.85
37(n2)	3951.3699	602.9312	23.00	1.6	+0.2	2.00	2.20	0.85

37a(n2)	4123.1686	629.1456	24.00	1.6	+0.2	2.20	2.20	0.95
37b(n2)	4466.7660	681.5744	26.00	1.6	+0.2	2.20	2.20	0.75
38(nb)	5904.7210	900.9889	34.37	1.6	+0.2	2.00	2.00	0.45
39(nb)	5995.7743	914.8826	34.90	1.6	+0.2	2.00	2.00	0.49
40(nb)	5995.7743	914.8826	34.90	1.6	+0.2	2.00	2.00	0.38

Table C2. Set used for self-docking along with docking results for both docking modes.

Entry	Protein	Resolution	CYP Isoform	Fe-Coordination	Nitrogen Hybridization	Reference Ligands	RMSD (Protein)	RMSD (Metalloprotein)
1	1e9x	2.1	51	yes	sp2	1	0.554	0.55
2	1ea1	2.21	51	yes	sp2	1	0.43	0.376
3	1nr6	2.1	2C5	no	x	1	0.498	0.545
4	1pha	1.63	CAM	yes	sp2	1	2.303	2.326
5	1r9o	2	2C9	no	x	1	1.237	0.269
6	1z11	2.05	2A6	no	x	1	0.299	0.303
7	2bdm	2.3	2B4	yes	sp2	1	1.025	1.006
8	2fdw	2.05	2A6	yes	sp3	1	5.464	5.453
9	2nnj	2.28	2C8	no	x	1	4.629	4.653
10	2p85	2.35	2A13	no	x	2	1.006	2.615
11	3czh	2.3	2R1	no	x	1	0.54	9.449
12	3e6i	2.2	2E1	yes	sp2	1	0.134	0.172
13	3ebs	2.15	2A6	no	x	1	1.526	1.681
14	3ibd	2	2B6	yes	sp2	1	0.257	1.401
15	3mdr	2	46A1	yes	sp3	1	0.742	0.934
16	3mdt	2.3	46A1	yes	sp2	1	0.604	2.449
17	3mdv	2.4	46A1	yes	sp2	1	0.723	0.744
18	3n9y	2.1	11A1	no	x	1	0.859	0.859
19	3n9z	2.17	11A1	no	x	1	0.44	0.431
20	3na1	2.25	11A1	no	x	1	0.527	0.354
21	3nxu	2	3A4	yes	sp2	1	4.469	3.937
22	3qoa	2.1	2B6	yes	sp2	1	1.858	1.65
23	3r9c	2.14	164A2	yes	sp2	2	1.08	0.879
24	3swz	2.4	17A1	yes	sp2	1	0.412	0.297
25	3t3q	2.1	2A6	yes	sp2	1	0.337	0.383
26	3t3r	2.4	2A6	yes	sp2	1	0.373	0.317
27	3t3z	2.35	2E1	yes	sp2	1	0.482	0.483
28	3tbg	2.1	2D6	yes	sp2	2	0.686	0.477
29	3tjs	2.25	3A4	yes	sp3	1	8.222	7.606
30	3ua1	2.15	3A4	no	x	1	0.774	0.548
31	4d75	2.25	3A4	yes	sp2	1	3.117	4.168
32	4dvq	2.49	11B2	no	x	1	0.529	0.526
33	4ejh	2.35	2A13	no	x	1	5.572	5.471
34	4eji	2.1	2A13	yes	sp2	2	6.304	0.687

35	4ejj	2.3	2A6	no	x	1	4.473	4.462
36	4fia	2.1	46A1	yes	sp	1	2.506	3.013
37	4i91	2	2B6	no	x	1	2.659	2.63
38	4k9w	2.4	3A4	yes	sp2	1	8.177	3.617
39	4key	2.05	BM3	no	x	1	0.467	0.484
40	4kpa	2	BM3	no	x	1	1.17	0.934
41	4nz2	2.45	2C9	no	x	1	0.582	1.795
42	4rql	2.1	2B6	no	x	1	3.595	1.54
43	4rrt	2.2	2B6	no	x	1	3.499	3.501
44	4tt5	2.18	119	yes	sp2	1	0.526	0.479
45	4uhi	2.05	51	yes	sp2	1	0.544	0.884
46	4wmz	2.05	51	yes	sp2	1	0.404	0.447
47	4wnu	2.26	2D6	no	x	1	0.397	0.448
48	4wnv	2.35	2D6	no	x	1	6.194	2.236
49	4wpd	2	119	yes	sp2	1	0.515	0.502
50	4xrz	2.4	2D6	yes	sp2	1	0.366	0.367
51	4zdz	2.3	51	yes	sp2	1	1.379	1.389
52	4ze0	2.2	51	yes	sp2	1	1.389	1.387
53	4ze3	2.2	51	yes	sp2	1	1.213	1.757
54	4zv8	2.24	2B6	no	x	1	2.857	2.862
55	5a1r	2.45	3A4	no	x	1	3.756	3.558
56	5a5i	2	2C9	no	x	1	1.978	2.292
57	5e58	2.4	2B35	yes	sp2	2	1.481	1.542
58	5ese	2.2	51	yes	sp2	1	0.715	0.692
59	5esf	2.25	51	yes	sp2	1	0.798	0.697
60	5esh	2.15	51	yes	sp2	1	1.185	1.355
61	5hs1	2.1	51	yes	sp2	1	1.397	1.376
62	5irq	2.2	17A1	yes	sp2	1	1.513	1.44
63	5k7k	2.3	2C9	yes	sp2	1	2.444	2.556
64	5l92	2.1	109E1	no	x	1	1.045	1.033
65	5l94	2.25	109E1	no	x	1	6.342	6.299
66	5tz1	2	51	yes	sp2	1	1.202	0.92
67	5uap	2.24	2B6	no	x	2	0.597	0.526
68	5uec	2.27	2B6	no	x	2	3.619	3.682
69	5uys	2.39	17A1	yes	sp2	1	0.484	0.368
70	5vce	2.2	3A4	yes	sp2	1	6.037	4.226
71	5vcg	2.2	3A4	no	x	1	1.045	0.964
72	5w0c	2	2C9	no	x	1	2.493	2.706
73	5x23	2	2C9	no	x	1	4.716	4.664
74	5x24	2.48	2C9	no	x	1	3.32	3.509
75	5xxi	2.3	2C9	no	x	1	3.272	3.207
76	6a16	2	90B1	yes	sp2	1	1.022	0.299
77	6a17	2.3	90B1	yes	sp2	1	0.294	0.287
78	6bcz	2.23	3A4	yes	sp2	1	2.086	3.104
79	6bd7	2.42	3A4	yes	sp2	1	2.536	5.327

80	6bd8	2.38	3A4	yes	sp2	1	6.084	3.13
81	6bdh	2.25	3A4	yes	sp2	1	4.855	4.505
82	6f85	2.05	260A1	yes	sp2	1	4.676	4.641
83	6jo1	2.1	102A1	no	x	1	0.713	0.838
84	6m7x	2.1	11B1	yes	sp2	1	0.484	0.556
85	6ung	2.3	3A4	yes	sp2	1	8.103	7.615

Rigid Docking.

Table C3. Accuracy of Impacts 2019 over 5 runs using all activation energies.

Isoform	Run 1	Run 2	Run 3	Run 4	Run 5	Overall Accuracy	Std. Dev.
1A2	77.4	77.4	77.4	73.7	74.5	76.1	1.6
2C9	76.0	80.6	79.8	80.6	78.3	79.1	1.7
2D6	70.1	74.5	73.9	71.3	75.2	73.0	2.0
3A4	74.7	74.7	74.4	73.7	73.7	74.2	0.5

Table C4. Accuracy of Impacts 2019 over 5 runs using the top 5 activation energies.

Isoform	Run 1	Run 2	Run 3	Run 4	Run 5	Overall Accuracy	Std. Dev.
1A2	77.4	78.1	77.4	74.5	78.1	77.1	1.3
2C9	76.0	79.1	78.3	79.1	76.7	77.8	1.3
2D6	70.1	72.0	71.3	70.1	72.0	71.1	0.9
3A4	72.7	72.4	70.3	71.0	72.0	71.7	0.9

Table C5. Accuracy of Impacts 2019 over 5 runs using all activation energies and FCs.

Isoform	Run 1	Run 2	Run 3	Run 4	Run 5	Overall Accuracy	Std. Dev.
1A2	73.0	72.3	70.8	75.9	72.3	72.8	1.7
2C9	70.5	72.9	70.5	73.6	73.6	72.2	1.4
2D6	63.1	68.2	61.1	61.1	63.1	63.3	2.6
3A4	67.2	67.6	66.9	68.6	67.2	67.5	0.6

Table C6. Accuracy of Impacts 2019 over 5 runs using the top 5 activation energies and FCs.

Isoform	Run 1	Run 2	Run 3	Run 4	Run 5	Overall Accuracy	Std. Dev.
1A2	73.7	74.5	70.1	71.5	70.8	72.1	1.7
2C9	74.4	72.1	70.5	73.6	72.1	72.5	1.4
2D6	56.1	56.1	56.7	58.6	58.0	57.1	1.0

3A4	67.2	66.2	67.2	68.6	70.6	68.0	1.5

Table C7. Accuracy of Impacts 2019 over 5 runs using all activation energies and SASA correction.

Isoform	Run 1	Run 2	Run 3	Run 4	Run 5	Overall Accuracy	Std. Dev.
1A2	81.0	83.9	81.8	81.0	79.6	81.5	1.4
2C9	81.4	84.5	82.2	84.5	85.3	83.6	1.5
2D6	77.1	77.7	75.8	77.1	76.4	76.8	0.7
3A4	75.4	75.4	72.2	74.4	75.8	74.6	1.3

Table C8. Accuracy of Impacts 2019 over 5 runs using the top 5 activation energies and SASA correction.

Isoform	Run 1	Run 2	Run 3	Run 4	Run 5	Overall Accuracy	Std. Dev.
1A2	82.5	83.2	84.7	86.1	83.2	83.9	1.3
2C9	84.5	86.8	83.7	86.0	83.7	84.9	1.3
2D6	75.2	76.8	75.2	75.8	74.5	75.5	0.8
3A4	76.8	75.4	76.1	77.1	77.5	76.6	0.7

Table C9. Accuracy of Impacts 2019 over 5 runs using all activation energies, SASA correction and FCs.

Isoform	Run 1	Run 2	Run 3	Run 4	Run 5	Overall Accuracy	Std. Dev.
1A2	78.8	78.1	77.4	77.4	78.1	78.0	0.5
2C9	75.2	79.8	76.0	76.7	76.0	76.7	1.6
2D6	74.5	73.9	74.5	77.1	75.2	75.0	1.1
3A4	67.2	70.3	70.0	70.4	67.9	69.2	1.3

Table C10. Accuracy of Impacts 2019 over 5 runs using the top 5 activation energies, SASA correction and FCs.

Isoform	Run 1	Run 2	Run 3	Run 4	Run 5	Overall Accuracy	Std. Dev.
1A2	81.0	81.0	81.8	81.0	80.3	81.0	0.5
2C9	79.1	80.6	80.6	79.8	80.6	80.1	0.6
2D6	70.1	68.8	70.7	69.4	70.1	69.8	0.7
3A4	71.3	71.7	71.7	72.0	72.0	71.7	0.4

Table C11. Accuracy of Impacts 2019 over 5 runs using all activation energies.

Isoform	Run 1	Run 2	Run 3	Run 4	Run 5	Overall Accuracy	Std. Dev.
1A2	66.4	68.6	69.3	68.6	65.0	67.6	1.6
2C9	70.5	69.0	67.3	67.4	69.8	68.8	1.3
2D6	47.1	48.4	49.7	45.9	51.0	48.4	1.8
3A4	67.2	67.2	65.9	66.9	66.2	66.7	0.5

Table C12. Accuracy of Impacts 2019 over 5 runs using the top 5 activation energies.

Isoform	Run 1	Run 2	Run 3	Run 4	Run 5	Overall Accuracy	Std. Dev.
1A2	63.5	63.5	65.0	63.5	63.5	63.8	0.6
2C9	64.3	65.1	65.1	65.1	66.7	65.3	0.8
2D6	43.3	43.3	42.7	42.7	43.3	43.1	0.3
3A4	63.1	63.1	64.8	62.8	64.2	63.6	0.8

Table C13. Accuracy of Impacts 2019 over 5 runs using all activation energies.

Isoform	Run 1	Run 2	Run 3	Run 4	Run 5	Overall Accuracy	Std. Dev.
1A2 (270)	78.1	79.6	80.0	79.6	78.1	79.1	0.8
2C9 (225)	72.0	73.3	74.7	75.1	73.3	73.7	1.1
2C19 (218)	69.7	69.7	70.6	70.6	71.1	70.3	0.6
2D6 (270)	70.4	68.5	70.7	67.7	68.5	69.2	1.2
2E1 (142)	65.7	66.9	70.4	66.2	66.9	67.2	1.7

Total molecules: 1125

Table C14. Accuracy of Impacts 2019 over 5 runs using the top 5 activation energies.

Isoform	Run 1	Run 2	Run 3	Run 4	Run 5	Overall Accuracy	Std. Dev.
1A2	81.1	80.7	80.0	80.6	80.4	80.6	0.4
2C9	71.6	72.4	74.2	74.2	71.1	72.7	1.3
2C19	70.6	72.9	72.9	69.3	70.6	71.3	1.4
2D6	70.4	69.6	70.0	69.3	69.3	69.7	0.4
2E1	67.6	68.3	68.3	70.0	68.3	68.5	0.8

Table C15. Accuracy of Impacts 2019 over 5 runs using all activation energies and SASA correction.

Isoform	Run 1	Run 2	Run 3	Run 4	Run 5	Overall Accuracy	Std. Dev.
1A2	80.7	78.1	80.4	81.1	80.4	80.1	1.1
2C9	73.3	76.0	74.6	73.8	73.8	74.3	0.9
2C19	76.1	75.7	75.7	77.1	76.6	76.2	0.5
2D6	75.5	74.4	77.4	77.0	74.8	75.8	1.2
2E1	70.0	70.4	70.4	72.5	70.4	70.7	0.9

Table C16. Accuracy of Impacts 2019 over 5 runs using the top 5 activation energies and SASA correction.

Isoform	Run 1	Run 2	Run 3	Run 4	Run 5	Overall Accuracy	Std. Dev.
1A2	80.4	81.9	81.9	80.7	80.7	81.1	0.6
2C9	75.1	72.4	74.2	74.2	75.1	74.2	1.0
2C19	75.7	74.8	73.9	76.6	76.6	75.5	1.0
2D6	73.3	73.7	73.0	72.2	73.0	73.0	0.5
2E1	67.6	72.5	69.0	72.5	73.2	71.0	2.2

Flexible Docking.

To run flexible docking one must ensure that the population size used for selecting suitable individuals for docking is large enough. As such, the population size used for flexible docking is increased to 200 (in comparison to rigid docking – 100) and the maximum number of generations is increased to 100 (in comparison to rigid docking – 50).

Table C17. Accuracy of Impacts 2019 over 5 runs using the top 5 activation energies, SASA correction and flexible docking – initial sets.

Isoform	Run 1	Run 2	Run 3	Run 4	Run 5	Overall Accuracy	Std. Dev.
1A2[a]	82.5	83.2	84.7	86.1	83.2	83.9	1.3
2C9[b]	77.5	76.7	77.5	76.7	77.5	77.2	0.4
2C9[c]	76.7	76.7	76.7	74.4	76.7	76.2	0.9
2D6[d]	72.6	75.2	75.8	76.4	73.9	74.8	1.4
2D6[e]	75.2	73.2	74.5	75.2	73.9	74.4	0.8
3A4	74.7	76.1	76.1	75.4	74.1	75.3	0.8

[a] results from rigid docking, isoform does not have multiple crystal structures to allow flexible docking

[b] results obtained using 5 crystal structures: 1R9O, 5K7K, 5XXI, 4NZ2, 5A5J

[c] results obtained using 3 crystal structures: 1R9O, 5K7K, 5XXI

[d] results obtained using 5 crystal structures: 3QM4, 3TBG, 4WNU, 5TFT, 2F9Q

[e] results obtained using 3 crystal structures: 3QM4, 3TBG, 4WNU

Table C18. Accuracy of Impacts 2019 over 5 runs using the top 5 activation energies, SASA correction and flexible docking – external sets.

Isoform	Run 1	Run 2	Run 3	Run 4	Run 5	Overall Accuracy	Std. Dev.
1A2[a]	80.4	81.9	81.9	80.7	80.7	81.1	0.6
2C9[b]	72.7	71.8	71.8	71.8	71.8	72.0	0.4
2C9[c]	72.9	71.6	72.0	71.1	70.7	71.7	0.8
2C19[a]	75.7	74.8	73.9	76.6	76.6	75.5	1.0
2D6[d]	74.1	74.4	75.9	74.8	74.8	74.8	0.6
2D6[e]	74.1	75.2	74.4	75.2	74.4	74.7	0.5
2E1	72.5	73.9	71.1	73.2	71.8	72.5	1.0

[a] results from rigid docking, isoform does not have multiple crystal structures to allow flexible docking

[b] results obtained using 5 crystal structures: 1R9O, 5K7K, 5XXI, 4NZ2, 5A5J

[c] results obtained using 3 crystal structures: 1R9O, 5K7K, 5XXI

[d] results obtained using 5 crystal structures: 3QM4, 3TBG, 4WNU, 5TFT, 2F9Q

[e] results obtained using 3 crystal structures: 3QM4, 3TBG, 4WNU

Flexible Docking – PDB Codes.

Flexible docking requires several crystal structures to ensure mutations across isoforms and active sites, with the aim of accurate docking. To this end we have assembled several PDB files/isoform (where available). The crystal structure PDB codes are given below:

CYP1A2

- 2HI4 (original, used in rigid docking) – 1.95Å resolution
- N/A – no other crystal structures are available for this isoform

CYP2C9

- 1R9O (original, used in rigid docking) – 2.00Å resolution
- 4NZ2 – 2.45Å resolution
- 5A5J – 2.90Å resolution
- 5K7K – 2.30Å resolution
- 5XXI – 2.30Å resolution

CYP2C19

- 4GQS (original, used in rigid docking) – 2.87Å resolution
- N/A – no other crystal structures are available for this isoform

CYP2D6

- 3QM4 (original, used in rigid docking) – 2.85Å resolution
- 3TBG – 2.10Å resolution

- 4WNU – 2.26Å resolution
- 5TFT – 2.71Å resolution
- 2F9Q – 3.00Å resolution

CYP3A4

- 3NXU (original, used in rigid docking) – 2.00Å resolution
- 1W0E – 2.80Å resolution
- 2J0D – 2.75Å resolution
- 4D78 – 2.80Å resolution
- 5TE8 – 2.70Å resolution

CYP2E1

- 3E6I (original, used in rigid docking) – 2.20Å resolution
- 3T3Z – 2.35Å resolution
- 3GPH – 2.70Å resolution
- 3E4E – 2.60Å resolution

Appendix D

All ACE and CONSTRUCTS calculations were performed with subversion 5679 of the ACE/FORECASTER platforms. The Windows/Linux/MacOS subversion can be requested from Nicolas Moitessier: nicolas.moitessier@mcgill.ca.

Single point energy calculation using QUEMIST within the HF framework– pseudocode:

```
void function quemist – single point energy calculation {
    set molecule and determine number of alpha and beta electrons
    initialize LIBINT variables (if Linux/MacOS versions used)
    create basis set as per user instructions
    compute overlap integral matrix - S
    compute kinetic integral matrix - T
    compute nuclear attraction integral matrix - V
    compute Hamiltonian = T + V
    orthogonalize basis set using canonical orthogonalization {
        compute eigenvectors and eigenvalues of overlap matrix S
        define diagonal ortho matrix = eigenvalues of S on the principal diagonal
        for (i = 0 to number of basis functions) {
            if (absolute value of ortho(i,i) less than 1e-08) {
                ortho(i, i) = 0.0
            }
            else {
                ortho(i, i) = 1.0 / square root of ortho(i, i)
            }
        }
        define unitary matrix U = eigenvectors of S
        calculate the transformation matrix:
            X = U * ortho
        calculate the transpose of the transformation matrix:
            Xp = X^T
    }
  compute initial guess density matrix using the superposition of atomic densities in the minimal basis  STO-3G
    project orbitals in actual basis set and obtain true guess density matrix
    compute Schwarz boundaries for performing the Cauchy-Schwarz inequality when computing electron repulsion integrals
    initialize DIIS
    for (iteration = 0 to max number of iterations requested by the user)
    {
        initialize Fock matrix F = Hamiltonian
```

```
        compute 2e integrals and the Coulomb (J) and exchange matrices (K) and add them to F:
                F = F + J - 0.5 * K
        compute electronic energy of the iteration
        add nuclear repulsion energy to the electronic energy
        obtain the difference in energy between iterations by subtracting the previous iteration energy from the current iteration energy
        obtain DIIS error matrix
        if (iteration larger than 2) {
                extrapolate Fock matrix using DIIS
        }

        diagonalize the Xp * F * X matrix
        obtain orbital matrix C = X * (eigenvectors of Xp * F * X matrix)
        obtain orbital energy matrix orbenergy = eigenvalues of the Xp * F * X matrix
        check if orbitals are orthonormal
        obtain new density matrix using the occupied orbitals from the orbital matrix C
        obtain convergence density matrix as the difference between the new density matrix and the previous density matrix
        compute rms and maximum absolute error of the convergence density matrix
        assign current energy to the last energy variable
        if (difference in energy less than energy threshold OR rms less than density threshold OR maximum absolute error less than density threshold OR DIIS error less than DIIS threshold) {
                convergence flag is true
                failure flag is false
        }

        if (convergence flag is true) {
                save current energy
                save current orbitals
                save current rms
                save current maximum absolute error in the density matrix
                save current DIIS error
                exit for loop
        }
        else {
                if (iteration less than 2) {
                        Current density matrix = (1 – damping factor) * new density matrix + damping factor * current density matrix;
                }
                else {
                        Current density matrix = new density matrix
                }
        }
```

```
            if (reach maximum iterations AND convergence flag is false) {
                failure flag is true
                print failure message
            }
        }
        If (failure flag is false)
        {
            print convergence details
            print orbitals and orbital energies
            print details of the convergence iteration
            print Mulliken population analysis
            print Mayer Bond Order Analysis
            print Mayer Free Valence Electrons
        }
    }
```

Geometry optimization / Hessian calculation using QUEMIST and generation of FF parameters – pseudocode:

```
    void function quemist – geometry optimization {
        set molecule and determine number of alpha and beta electrons
        initialize basis set
        determine redundant internal coordinates
        determine degrees of freedom
        determine energy at initial point (see void quemist – single point energy)
        save xyz coordinates from the initial energy evaluation to coordinate file
        initialize trust radius to 0.5
        for (i = 0 to max number of geometry optimization steps requested by user)
        {
            run single point energy of the coordinates at iteration i
            compute gradient (g) of coordinates at iteration i
            save gradient of the iteration in gradient vector
            determine norm of the gradient
            if (i equals 0) {
                initialize initial Hessian with the unit matrix
                diagonalize initial Hessian to obtain eigenvalues
                check if Hessian is positive definite based on eigenvalue values
                obtain augmented Hessian (aug.Hessian) using the gradient and initial
Hessian
                diagonalize augmented Hessian
                obtain minimum value (mvaug) in augmented Hessian
                obtain new search direction (sd) = - inverse of (aug.Hessian -  mvaug *
identity matrix) * gradient
                save new sd in sd vector
```

```
                    if (norm of sd > trust radius) {
                        scale sd components so that the norm of the sd is equal to the trust
radius
                    }
                    else {
                        accept norm of the sd as the length of the step
                    }
                    obtain new coordinates (nc) = coords. at initial point + sd
                    save current hessian in hessian vector
                }
                else {
                    update hessian at current iteration using the information from the hessian,
gradient, and sd from the previous iteration (BFGS formula)
                    diagonalize hess to obtain eigenvalues
                    check if Hessian is positive definite based on eigenvalue values
                    obtain augmented Hessian (aug.Hessian) using the gradient and initial
Hessian
                    diagonalize augmented Hessian
                    obtain minimum value (mvaug) in augmented Hessian
                    obtain new sd = - inverse of (aug.Hessian -  mvaug * identity matrix) *
gradient
                    save new sd in sd vector
                    if (norm of sd > trust radius) {
                        scale sd components so that the norm of the sd is equal to the trust
radius
                    }
                    else {
                        accept norm of the sd as the length of the step
                    }
                    obtain new coordinates (nc) = coords. at initial point + sd
                    save current hessian in hessian vector
                }
                obtain max. error (fmax) and max rms (frms) in gradient
                obtain max. error (dmax) and max rms (drms) in atomic displacements
                check if thresholds have been met:
                • If energy difference between iterations is < 0.0005
                • If fmax < 0.0003
                • If frms < 0.0001
                • If dmax < 0.0020
                • If drms < 0.0040
                if (4 of 5 conditions are met) {
                    signal convergence
                    print orbital data, Mulliken Population Analysis and Mayer Bond Order
data
                } else {
                    continue optimization until convergence is reached
```

```
                save coordinates at this step in xyz file
                if (convergence is reached and Hessian flag computation has been found) {
                        compute true Hessian numerically by using finite differences and a
step increment of 0.005
                        if (Hessian contains negative eigenvalues) {
                                print warning message that the geometry is not minimum
                        }
                        compute the force field parameters using the Hessian matrix and
Seminario algorithm
                        create parameter file named
molfilename_customized_ff_parameters.txt
                    }
                }
            }
        }
```

Datasets.

Chart and Table D1: Dienophile and dienes set used in the Diels-Alder reaction using chiral auxiliaries (*endo* adducts only).

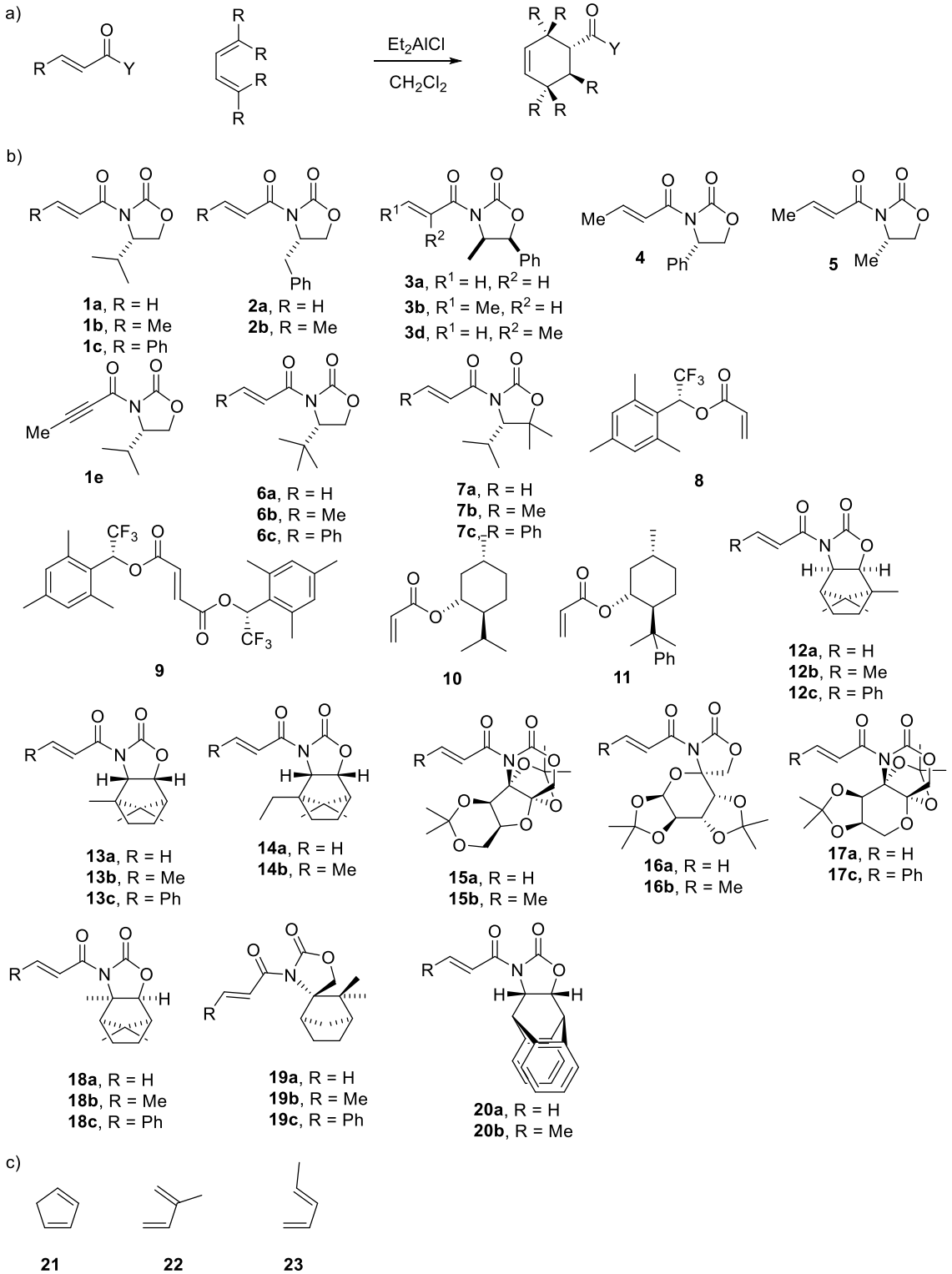

Entry	Auxiliary	Dienophile	Diene	Temp. (°C)	Observed d.e. (%)	Ref.
1	**1**	**a**	**21**	-100	86 (*R*)	326
2	**1**	**a**	**22**	-100	66 (*R*)	326
3	**1**	**b**	**21**	-100	90 (2*R*,3*S*)	326
4	**1**	**b**	**22**	-100	68 (*S*,*S*)	326
5	**1**	**c**	**21**	-22	86 (2*S*,3*S*)	326
6	**1**	**e**	**21**	-22	50 (nd)[b]	326
7	**2**	**a**	**21**	-100	90 (*R*)	326
8	**2**	**a**	**22**	-100	90 (*R*)	326
9	**2**	**a**	**23**	-100	>99 (*R*)	326
10	**2**	**b**	**21**	-100	94 (*S*,*S*)	326
11	**2**	**b**	**22**	-30	88 (*S*,*S*)	326
12	**2**	**b**	**23**	-30	98 (*S*,*S*)	326
13	**3**	**a**	**21**	-100	90 (*S*)	326
14	**3**	**b**	**21**	-100	96 (2*S*, 3*R*)	326
15	**3**	**d**	**21**	-78	64 (nd)	326
16	**4**	**b**	**22**	-100	33 (*S*,*S*)	326
17	**5**	**b**	**22**	-100	58 (*S*,*S*)	326
18	**6**	**a**	**22**	-30	98 (*S*,*S*)	326
19	**6**	**b**	**21**	-100	99 (2*R*,3*S*)	326
19	**6**	**b**	**22**	-30	>98 (*S*,*S*)	326
21	**6**	**c**	**21**	-100	>99 (*S*,*S*)	326
22	**7**	**a**	**22**	-30	94 (*S*,*S*)	326
24	**7**	**b**	**21**	-100	99 (2*R*,3*S*)	326
23	**7**	**b**	**22**	-30	94 (*S*,*S*)	326
25	**7**	**c**	**21**	-100	>99 (*S*,*S*)	326
26[a]	**8**	**a**	**21**	-78	95 (*S*)	327
27[a]	**9**	**-**	**21**	-78	97 (*R*,*R*)[b]	327
28[a]	**10**	**a**	**21**	0	47 (*R*)	328
29[a]	**11**	**a**	**21**	0	64 (*R*)	328
30	**12**	**a**	**21**	-78	96 (*S*)	329,330

32	**12**	**b**	**21**	-78	97 (2*S*,3*R*)	329,330
33	**12**	**c**	**21**	-22	98 (*R*,*R*)	329,330
34	**13**	**a**	**21**	-78	81 (*R*)	331
35	**13**	**b**	**21**	-78	>99 (2*R*,3*S*)	331
36	**13**	**c**	**21**	-22	>99 (*S*,*S*)	331
37	**14**	**a**	**21**	-78	>95 (*R*)	331
38	**14**	**b**	**21**	-78	>99 (2*R*,3*S*)	331
39	**15**	**a**	**21**	-78	82 (*S*)	332
40	**15**	**b**	**21**	-22	94 (2*S*,3*R*)	332
41	**16**	**a**	**21**	-78	80 (*R*)	333
42	**16**	**b**	**21**	-78	89 (2*R*,3*S*)	333
43	**17**	**a**	**21**	-78	87 (*S*)	334
44	**17**	**c**	**21**	-22	63 (2*S*,3*R*)	334
45	**18**	**a**	**21**	-78	92 (*S*)	330
46	**18**	**b**	**21**	-78	94 (2*S*,3*R*)	330
47	**18**	**c**	**21**	-78	94 (*R*,*R*)	330
48	**19**	**a**	**21**	-78	98 (*R*)	330
49	**19**	**b**	**21**	-78	98 (*S*,*S*)	330
50	**19**	**c**	**21**	-78	98 (2*R*,3*S*)	330
51	**20**	**a**	**21**	-78	89 (*R*)	335
52	**20**	**b**	**21**	-78	96 (*R*)	335

[a] Me_2AlCl is used in place of Et_2AlCl. [b] does not match with the template with CONSTRUCTS.

Chart and Table D2: Catalysts and alkenes set used in the epoxidation reaction.

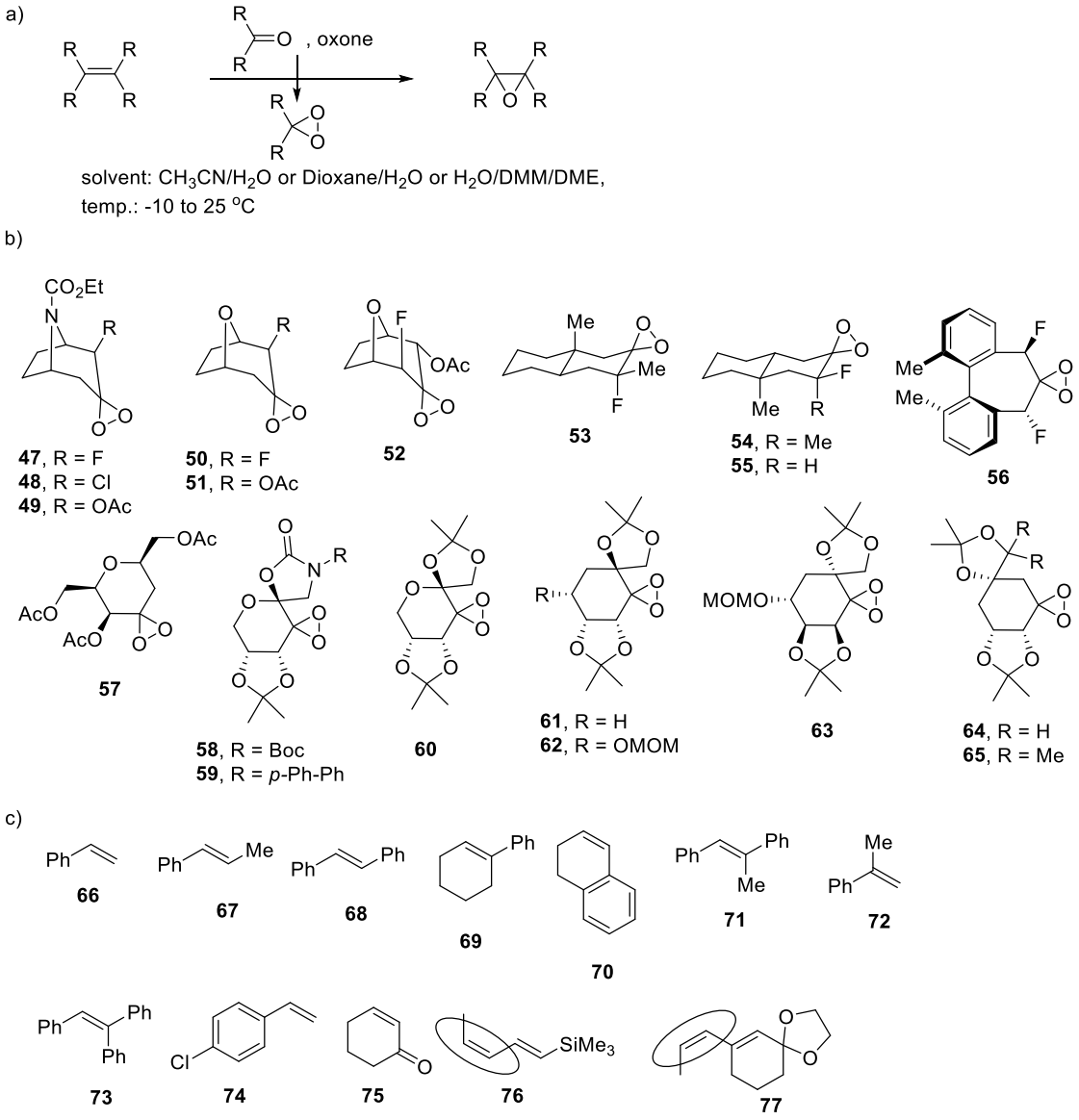

Entry	Catalyst	Substrate	Temperature (°C)	Observed e.e. (%)	Ref
1	**47**	**66**	25	29 (*R*)	336
2	**47**	**67**	25	56 (*R*,*R*)	336
3	**47**	**68**	25	76 (*R*,*R*)	336
4	**47**	**69**	25	69 (*R*,*R*)	336
5	**47**	**70**	25	18 (1*R*,2*S*)	336
6	**47**	**71**	25	73 (*R*,*R*)	336

7	**47**	**72**	25	22 (*R*)	336
8	**47**	**73**	25	83 (*R*)	336
9	**48**	**68**	25	54 (*R*,*R*)	336
10	**49**	**68**	25	86 (*R*,*R*)	336
11	**50**	**68**	25	83 (*R*,*R*)	337,338
12	**51**	**66**	25	48 (*R*)	339
13	**51**	**68**	25	93-95 (*R*,*R*)	337,339
14	**51**	**69**	25	82 (*R*,*R*)	339
15	**51**	**73**	25	98 (*R*,*R*)	339
16	**51**	**75**	25	3 (*R*,*R*)	339
17	**52**	**66**	25	2 (*S*)	338
18	**52**	**68**	25	64 (*S*,*S*)	338
-	**52**	**72**	25	8 (*S*)	338
19	**53**	**67**	25	70 (*R*,*R*)	340
20	**53**	**68**	25	86 (*R*,*R*)	340
21	**54**	**67**	25	22 (*R*,*R*)	340
22	**55**	**67**	25	0 (*R*,*R*)	340
23	**56**	**67**	0	88 (*R*,*R*)	341
24	**56**	**68**	0	94 (*R*,*R*)	341
25	**56**	**69**	0	59 (*R*,*R*)	341
26	**56**	**74**	0	43 (*R*)	341
27	**57**	**66**	25	19 (*S*)	342
-	**57**	**68**	25	81 (*S*,*S*)	342
28	**57**	**72q**	25	7 (S)	342
29	**58**	**77**	-10	93 (2*S*,3*R*)[a]	343
30	**59**	**76**	-10	92 (2*S*,3*R*)[a]	343
31	**60**	**66**	-10	15-24 (*R*)	344
32	**60**	**67**	-10	88-95 (*R*,*R*)	344,345
33	**60**	**68**	0	95-98 (*R*,*R*)	344,345
34	**60**	**69**	-	91-98 (*R*,*R*)	344,345
35	**60**	**70**	-	12-32 (1*S*,R)	344
36	**60**	**71**	-	92-95 (*R*,*R*)	344,345

37	**60**	**72**	-	20-28 (*S*)	344
38	**60**	**73**	-	92-96 (*R*)	344,345
39	**61**	**66**	-10	15 (*R*)	346
40	**61**	**67**	-10	87 (*R*,*R*)	346
41	**61**	**68**	0	88 (*R*,*R*)	346
42	**62**	**66**	-10	31 (*R*)	346
43	**62**	**67**	-10	88 (*R*,*R*)	346
44	**62**	**68**	0	89 (*R*,*R*)	346
45	**63**	**66**	-10	24 (*S*)	346
46	**63**	**67**	-10	77 (*S*,*S*)	346
47	**64**	**66**	-10	14 (*R*)	346
48	**64**	**67**	-10	46 (*R*,*R*)	346
49	**64**	**68**	0	66 (*R*,*R*)	346
50	**65**	**67**	-10	38 (*R*,*R*)	346
51	**65**	**68**	0	72 (*R*,*R*)	346

[a] Substrates containing 2 double bonds, CONSTRUCTS cannot differentiate double bonds by reactivity and will simply react the first one it finds. These substrates cannot be considered.

Chart and Table D3: Dienophile and dienes set used in the organocatalyzed Diels-Alder reactions.

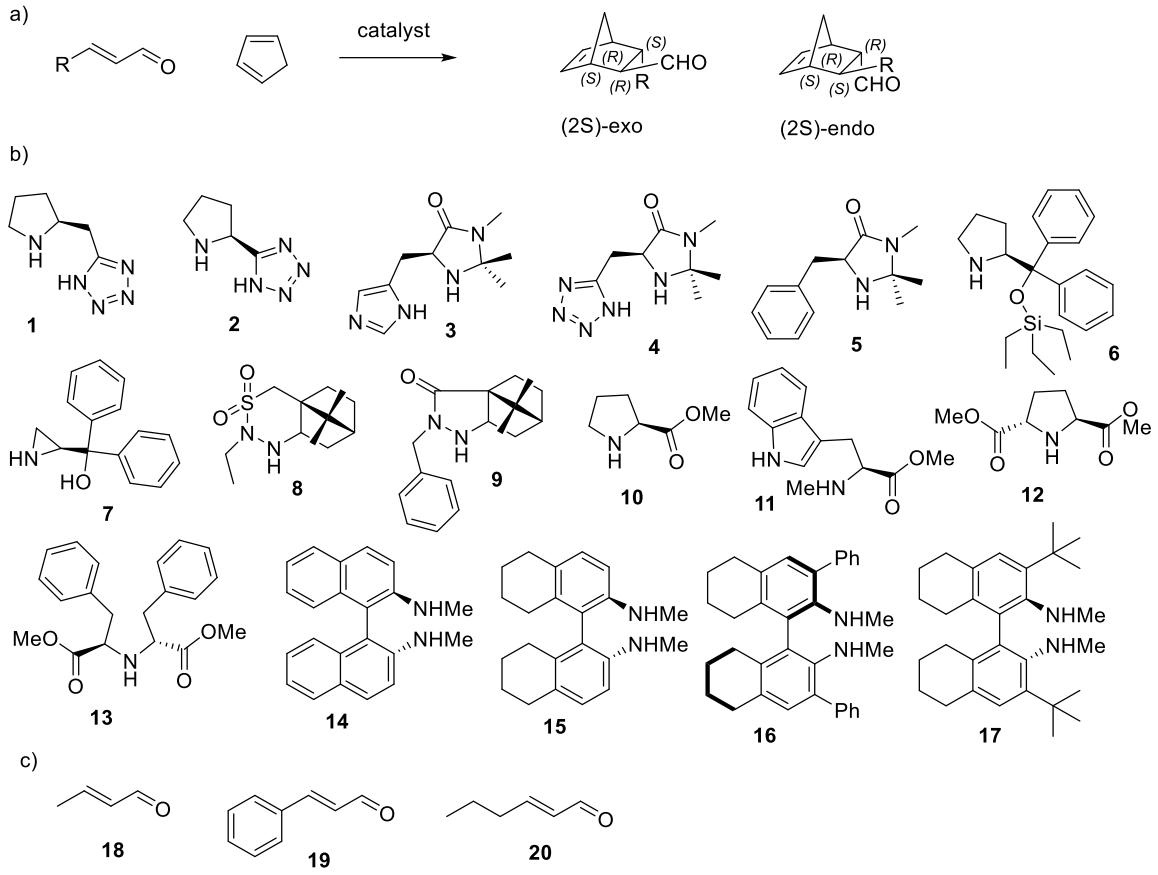

Entry	Catalyst	Substrate		Observed e.e. (%)	Ref.
1	**1**	**20**	*exo*	3-17 (2*S*)	347
2	**1**	**20**	*endo*	0-9 (2*R*)	347
3	**2**	**20**	*exo*	3-36 (2*S*)	347
4	**2**	**20**	*endo*	0-36 (2*R*)	347
5	**3**	**18**	*exo*	66-89 (2*R*)	347
6	**3**	**18**	*endo*	57-83 (2*R*)	347
7	**3**	**19**	*exo*	68-84 (2*S*)	347
8	**3**	**19**	*endo*	58-60 (2*S*)	347
9	**3**	**20**	*exo*	69-72 (2*S*)	347
10	**3**	**20**	*endo*	45-58 (2*R*)	347

11	**4**	**18**	*exo*	90 (2*R*)	347
12	**4**	**18**	*endo*	95 (2*R*)	347
13	**4**	**19**	*exo*	89 (2*S*)	347
14	**4**	**19**	*endo*	90 (2*S*)	347
15	**4**	**20**	*exo*	85 (2*S*)	347
16	**4**	**20**	*endo*	93 (2*R*)	347
17	**5**	**18**	*exo*	86 (2*R*)	347,348
18	**5**	**18**	*endo*	90 (2*R*)	347,348
19	**5**	**19**	*exo*	93 (2*S*)	347,348
20	**5**	**19**	*endo*	93 (2*S*)	347,348
21	**5**	**20**	*exo*	79-86 (2*S*)	347,348
22	**5**	**20**	*endo*	90-96 (2*R*)	347,348
23	**6**	**19**	*exo*	88 (4*S*)	349
24	**6**	**19**	*endo*	97 (4*S*)	349
25	**7**	**18**	*exo*	11-22 (nd)[a]	350
26	**7**	**18**	*endo*	10-24 (nd)[a]	350
27	**7**	**19**	*exo*	37-57 (nd)[a]	350
28	**7**	**19**	*endo*	36-66 (nd)[a]	350
29	**8**	**18**	*endo*	83 (2*S*)	351
30	**8**	**19**	*exo*	78 (2*R*)	351
31	**8**	**19**	*endo*	93 (2*R*)	351
32	**8**	**20**	*exo*	66 (2*R*)	351
33	**8**	**20**	*endo*	90 (2*R*)	351
34	**9**	**19**	*exo*	90 (2*R*)	352
35	**9**	**19**	*endo*	82-88 (2*R*)	352
36	**9**	**20**	*exo*	81 (2*R*)	352
37	**10**	**19**	*exo*	48 (2*R*)	348
38	**11**	**19**	*exo*	59 (2*S*)	348

39	**12**	**19**	*exo*	57 (2*R*)	348
40	**13**	**19**	*exo*	74 (2R)	348
41	**14**	**19**	*exo*	9 (*R*)	353
42	**14**	**19**	*endo*	15 (*R*)	353
43	**15**	**19**	*exo*	38 (*S*)	353
44	**15**	**19**	*endo*	27 (*R*)	353
45	**16**	**19**	*exo*	53 (*R*)	353
46	**16**	**19**	*endo*	39 (*R*)	353
47	**17**	**18**	*exo*	88 (*S*)	353
48	**17**	**19**	*exo*	72-92 (*R*)	353
49	**17**	**19**	*endo*	68-91 (*R*)	353

[a] Absolute stereochemistry not assigned.

Chart and Table D4: Catalysts and aldehydes set used in the organocatalyzed aldol reaction.

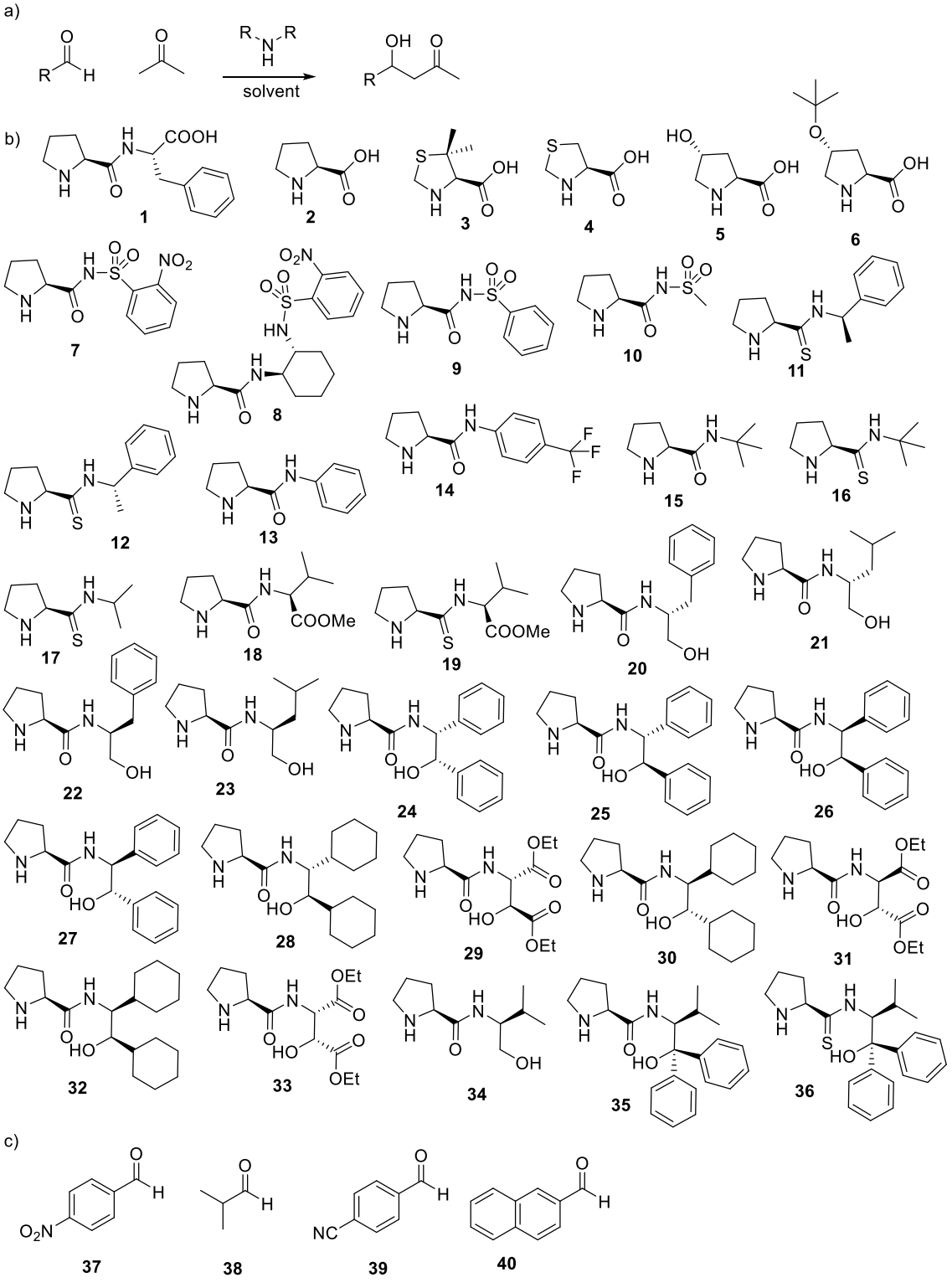

Entry	Catalyst	Substrate	Observed e.e. (%)	Ref.
1	**1**	**37**	59-73 (*R*)	354
2	**1**	**38**	77 (*R*)	354
3	**2**	**37**	76 (*R*)	355,356
4	**2**	**38**	96 (*R*)	355,356
5	**2**	**40**	77 (*R*)	355,356
6	**3**	**37**	86 (*R*)	355,356
7	**3**	**38**	94 (*R*)	355,356
8	**3**	**40**	88 (*R*)	355,356
9	**4**	**37**	73 (*R*)	355,356
10	**5**	**37**	78 (*R*)	355,356
11	**6**	**37**	62 (*R*)	355,356
12	**7**	**37**	95 (*R*)	357
13	**7**	**40**	95 (*R*)	357
14	**8**	**37**	81 (*R*)	357
15	**9**	**37**	61-92 (*R*)	358
16	**10**	**37**	44-87 (*R*)	358
17	**11**	**39**	72-93 (*R*)	359
18	**12**	**37**	84-94 (*R*)	359
19	**12**	**39**	54-93 (*R*)	359
20	**12**	**40**	81 (*R*)	359
21	**13**	**37**	37 (*R*)	360
22	**14**	**37**	45 (*R*)	360
23	**15**	**39**	15 (*R*)	360
24	**16**	**39**	27 (*R*)	361
25	**17**	**39**	75 (*R*)	361
26	**18**	**37**	22-35 (*R*)	361
27	**19**	**37**	77-85 (*R*)	361
28	**20**	**37**	46 (*R*)	362
29	**21**	**37**	33 (*R*)	362
30	**22**	**37**	48 (*R*)	362
31	**23**	**37**	52 (*R*)	362

32	**24**	**37**	49 (*R*)	362
33	**25**	**37**	44 (*R*)	362
34	**26**	**37**	64 (*R*)	362
35	**27**	**37**	69-93 (*R*)	362
36	**27**	**38**	98 (*R*)	362
37	**27**	**40**	84 (*R*)	362
38	**28**	**37**	15 (*R*)	363
39	**29**	**37**	72 (*R*)	363
40	**30**	**37**	15 (*R*)	363
41	**31**	**37**	87-99 (*R*)	363
42	**31**	**38**	>99 (*R*)	363
43	**31**	**39**	99 (*R*)	363
44	**32**	**37**	17 (*R*)	363
45	**33**	**37**	67 (*R*)	363
46	**34**	**37**	96 (*R*)	364
47	**35**	**37**	60 (*R*)	364
48	**36**	**37**	95 (*R*)	364
49	**36**	**40**	96 (*R*)	364

Chart and Table D5: Catalysts and substrates set used in the dihydroxylation reaction.

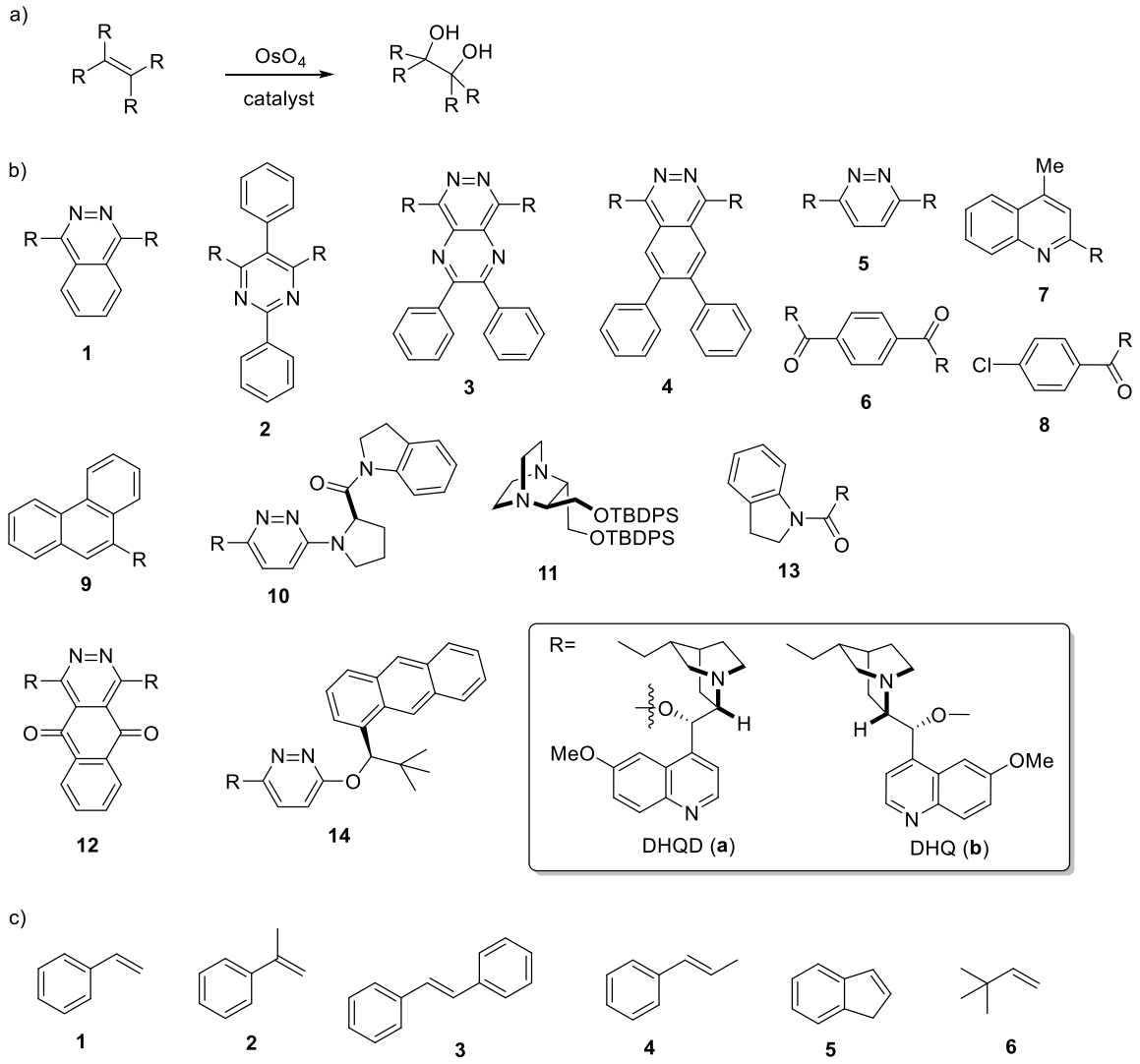

Entry	Catalyst	Substrate	Observed e.e. (%)	Ref.
1	**1a**	**1**	97 (*R*)	365,366
2	**1b**	**1**	97 (*S*)	365,366
3	**2a**	**1**	80 (*R*)	365
4	**3a**	**1**	99 (*R*)	365
5	**3b**	**1**	97 (*S*)	365
6	**4a**	**1**	98 (*R*)	365

7	**4b**	**1**	96 (*S*)	365
8	**5a**	**1**	96 (*R*)	366,367
9	**5b**	**1**	93 (*S*)	366
10	**6a**	**1**	80-92 (*R*)	366
11	**6b**	**1**	79-85 (*S*)	366
12	**7a**	**1**	87 (*R*)	368
13	**8a**	**1**	60-74 (*R*)	369 368
14	**8b**	**1**	54 (*S*)	369
15	**9a**	**1**	78 (*R*)	368
16	**10**	**1**	93 (*R*)	370
17	**11**	**1**	21 (*S*)	371
18	**12a**	**1**	89 (*R*)	372
19	**12b**	**1**	85 (*S*)	372
20	**14**	**1**	76 (*R*)	367
21	**1a**	**2**	94 (*R*)	365
22	**1b**	**2**	93 (*S*)	365
23	**2a**	**2**	69 (*R*)	365
24	**3a**	**2**	96 (*R*)	365
25	**3b**	**2**	92 (*S*)	365
26	**4a**	**2**	94 (*R*)	365
27	**4b**	**2**	94 (*S*)	365
28	**5a**	**2**	93 (*R*)	366
29	**6a**	**2**	72 (*R*)	366
30	**8a**	**2**	33 (*R*)	369
31	**12a**	**2**	82 (*R*)	372
32	**1a**	**3**	>99.5 (*R*,*R*)	373
33	**1b**	**3**	>99.5 (*S*,*S*)	373
34	**5a**	**3**	99 (*R*,*R*)	367
35	**7a**	**3**	98 (*R*,*R*)	368
36	**8a**	**3**	85-88 (*R*,*R*) 99 (*R*,*R*)	369 368

37	**8b**	**3**	78 (*S*,*S*)	369
38	**9a**	**3**	99 (*R*,*R*)	368
39	**10**	**3**	99.5 (*R*,*R*)	370
40	**11**	**3**	40 (*S*,*S*)	371
41	**14**	**3**	92 (*R*,*R*)	367
42	**8a**	**4**	65 (*R*,*R*)	369
43	**8b**	**4**	55 (*S*,*S*)	369
44	**10**	**4**	97 (*R*,*R*)	370
45	**11**	**4**	19 (*S*,*S*)	371
46	**12a**	**4**	92 (*R*,*R*)	372
47	**1a**	**5**	42 (1*R*,2*S*)	365,374
48	**2a**	**5**	35 (1*R*,2*S*)	365,374
51	**3a**	**5**	20 (1*R*,2*S*)	365
50	**4a**	**5**	53 (1*R*,2*S*)	365
51	**11**	**5**	12 (1*S* 2*R*)	371
52	**12a**	**5**	63 (1*R*,2*S*)	372
53	**1a**	**6**	64	-
54	**1b**	**6**	66	-
55	**2a**	**6**	92	-
56	**2b**	**6**	87	-
57	**3a**	**6**	59	-
58	**3b**	**6**	65	-
59	**4a**	**6**	67	-
60	**4b**	**6**	73	-
61	**7a**	**6**	79 (*R*)	-
62	**8a**	**6**	44 (*R*)	-
63	**9a**	**6**	79 (*R*)	-

Chart and Table D6: Catalysts and substrates set used in the diethylzinc addition to aldehyde reaction.

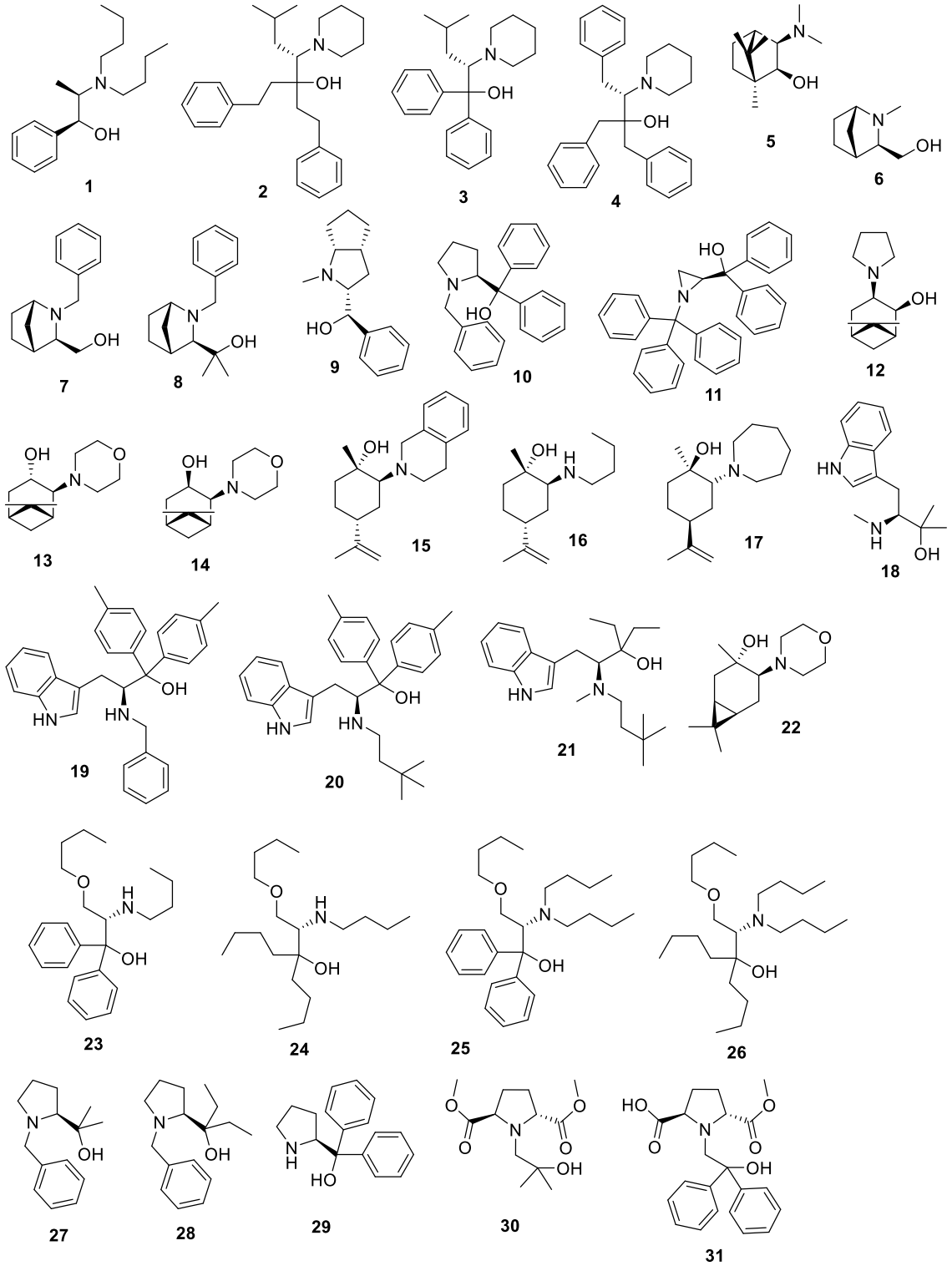

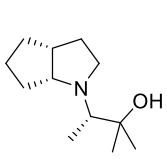

32

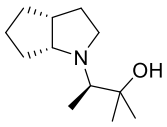

33

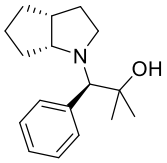

34

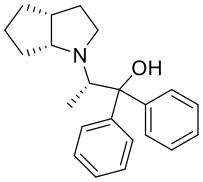

35

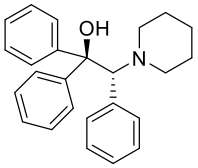

36

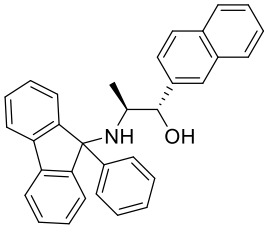

37

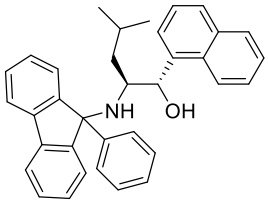

38

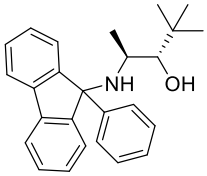

39

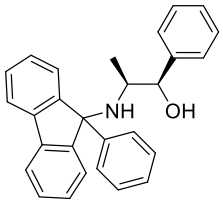

40

Entry	Catalyst	Substrate	Observed e.e. (%)	Ref.
1	**1**	**41a**	90 (*S*)	375
2	**1**	**41c**	78 (*S*)	375
3	**1**	**41d**	88 (*S*)	375
4	**2**	**41a**	97 (*R*)	376,377
5	**2**	**41c**	95 (*R*)	376,377
6	**2**	**41d**	88 (*R*)	376,377
7	**3**	**41a**	85 (*R*)	376,377
8	**3**	**41d**	78 (*R*)	376,377
9	**4**	**41a**	67 (*R*)	376
10	**5**	**41a**	98 (*S*)	378
11	**5**	**41b**	90 (*S*)	378
12	**5**	**41d**	61 (*S*)	378
13	**6**	**41a**	24 (*R*)	379
14	**7**	**41a**	75 (*S*)	379
15	**8**	**41a**	24 (*S*)	379
16	**9**	**41a**	68 (*R*)	380
17	**10**	**41a**	81.8 (*S*)	320
18	**11**	**41a**	99 (*S*)[a]	381
19	**11**	**41c**	99 (*S*)[a]	381
20	**11**	**41d**	80 (*S*)[a]	381
21	**12**	**41a**	84 (*S*)	382

22	**13**	**41a**	58 (*R*)	382
23	**14**	**41a**	99 (*R*)	382
24	**15**	**41a**	78 (*R*)	383
25	**16**	**41a**	48 (*R*)	383
26	**17**	**41a**	80 (*S*)	383
27	**18**	**41a**	31 (*R*)	384
28	**19**	**41a**	36.7 (*S*)	384
29	**20**	**41a**	57.9 (*R*)	384
30	**21**	**41a**	87.5 (*R*)	384
31	**22**	**41a**	81 (*R*)	385
32	**22**	**41c**	93 (*R*)	385
33	**23**	**41a**	66 (*S*)	386
34	**23**	**41b**	70 (*S*)	386
35	**24**	**41a**	28 (*R*)	386
36	**25**	**41a**	26 (*R*)	386
37	**26**	**41a**	79 (*R*)	386
38	**26**	**41b**	69 (*R*)	386
39	**27**	**41a**	96.7 (*R*)	320
40	**28**	**41a**	95.9 (*R*)	320
41	**29**	**41a**	36.1 (*R*)	320
42	**30**	**41a**	61 (*R*)	387
43	**31**	**41a**	91 (*R*)	387
44	**32**	**41a**	36 (*R*)	388
45	**33**	**41a**	80 (*S*)	388
46	**34**	**41a**	80 (*S*)	388
47	**35**	**41a**	86 (*R*)	388
48	**36**	**41a**	98 (*S*)	389
49	**36**	**41b**	93 (*S*)	389
50	**36**	**41c**	98 (*S*)	389
51	**36**	**41d**	92 (*S*)	389
52	**37**	**41a**	50 (*S*)	390
53	**38**	**41a**	24 (*S*)	390

54	**39**	**41a**	97 (*S*)	390
55	**40**	**41a**	29 (*R*)	390

[a] This catalyst features an aziridine which does not match with the template used in Constructs.

Chart and Table D7: Ruthenium ligands and substrates set used in the hydrogenation reaction.

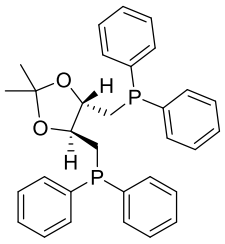

1. (S,S)-diop

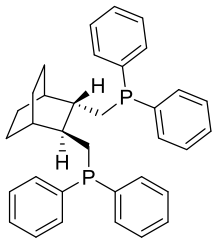

2. (S,S)-bcop

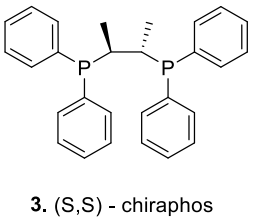

3. (S,S) - chiraphos

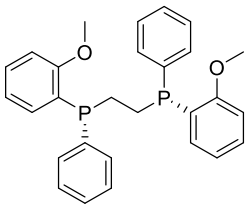

4. (R,R) - dipamp

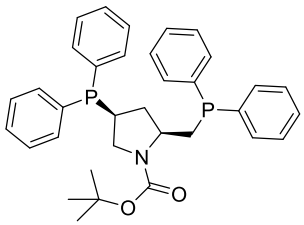

5. (S,S) - bppm

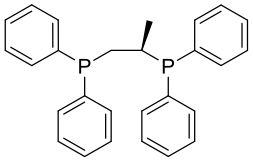

6. (R) - prophos

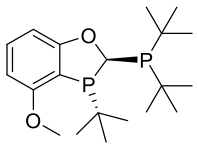

7. (S,S)-CatMeOPOP

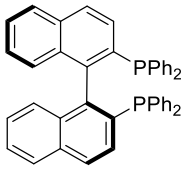

8. (S)-BINAP

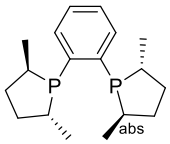

9. (R,R)-Me-Duphos

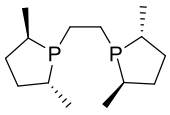

10. (R,R)-Me-BPE

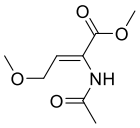

11

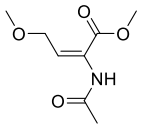

12

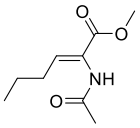

13

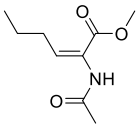

14

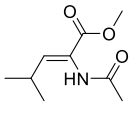

15

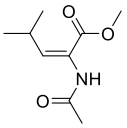

16

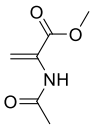

17

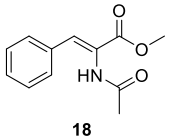

18

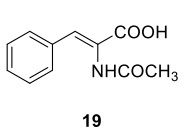

19

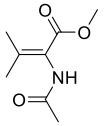

20

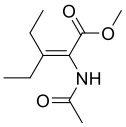

21

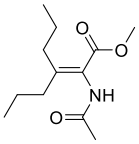

22

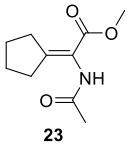

23

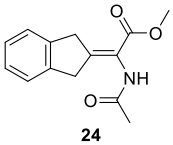

24

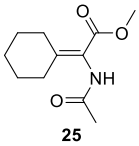

25

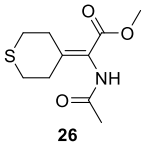

26

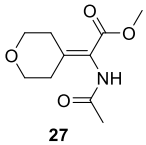

27

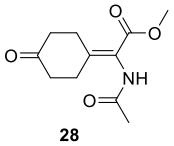

28

Entry	Catalyst	Substrate	Observed e.e. (%)[a]	Ref.
1	**1**	**11**	29 (*S*)	391
2	**2**	**11**	30 (*S*)	391
3	**3**	**11**	87 (*R*)	391
4	**4**	**11**	86 (*S*)	391
5	**5**	**11**	37 (*R*)	391
6	**6**	**11**	74 (*S*)	391
7	**1**	**12**	67 (*S*)	391
8	**2**	**12**	78 (*S*)	391
9	**3**	**12**	36 (*R*)	391
10	**4**	**12**	94 (*S*)	391
11	**5**	**12**	82 (*R*)	391
12	**6**	**12**	60 (*S*)	391
13	**1**	**13**	30 (*S*)	391
14	**2**	**13**	17 (*S*)	391
15	**3**	**13**	82 (*R*)	391
16	**4**	**13**	96 (*S*)	391
17	**5**	**13**	80 (*R*)	391
18	**6**	**13**	88 (*S*)	391
19	**1**	**14**	49 (*S*)	391
20	**2**	**14**	55 (*S*)	391
21	**3**	**14**	22 (*R*)	391
22	**4**	**14**	95 (*S*)	391
23	**5**	**14**	75 (*R*)	391
24	**6**	**14**	53 (*S*)	391
25	**1**	**15**	18 (*S*)	391
26	**2**	**15**	8 (*S*)	391
27	**3**	**15**	71 (*R*)	391
28	**4**	**15**	65 (*S*)	391
29	**5**	**15**	57 (*R*)	391
30	**6**	**15**	81 (*S*)	391
31	**1**	**16**	54 (*S*)	391

32	**2**	**16**	24 (*S*)	391
33	**3**	**16**	24 (*R*)	391
34	**4**	**16**	78 (*S*)	391
35	**5**	**16**	72 (*R*)	391
36	**6**	**16**	67 (*S*)	391
37	**1**	**17**	56 (*S*)	391
38	**2**	**17**	45 (*S*)	391
39	**3**	**17**	79 (*R*)	391
40	**4**	**17**	95 (*S*)	391
41	**5**	**17**	82 (*R*)	391
42	**6**	**17**	80 (*S*)	391
43	**7**	**17**	98 (*S*)[b]	392
44	**1**	**18**	49 (*S*)	391
45	**4**	**18**	96 (*S*)	391,393
46	**5**	**18**	95 (*R*)	391
47	**7**	**18**	99 (*S*)[b]	392
48	**8**	**18**	21 (*R*)[b]	394
49	**1**	**19**	83 (*S*)	393
50	**3**	**19**	95 +(*R*)	393
51	**4**	**19**	95 (*S*)	393
52	**5**	**19**	91 (*R*)	393
53	**7**	**19**	99 (*S*)[b]	392
54	**8**	**19**	15 (*R*)[b]	394
55	**4**	**20**	55 (*S*)	391
56	**5**	**20**	0	391
57	**9**	**20**	96 (*R*)	310
58	**10**	**20**	98.2 (*R*)	310
59	**9**	**21**	96.2 (*R*)	310
60	**10**	**21**	97.5 (*R*)	310
61	**9**	**22**	85.1 (*R*)	310
62	**10**	**22**	96.8 (*R*)	310
63	**9**	**23**	96.8 (*R*)	310

64	**10**	**23**	97.2 (*R*)	310
65	**9**	**24**	99.0 (*R*)	310
66	**10**	**24**	98.6 (*R*)	310
67	**9**	**25**	96.2 (*R*)	310
68	**10**	**25**	98.6 (*R*)	310
69	**9**	**26**	95.0 (*R*)	310
70	**10**	**26**	98.4 (*R*)	310
71	**9**	**27**	98.2 (*R*)	310
72	**10**	**27**	98.6 (*R*)	310
73	**9**	**28**	93.7 (*R*)	310
74	**10**	**28**	98.0 (*R*)	310

[a] Stereochemistry inverted when assigned by CONSTRUCTS. This results from the presence of Rhodium in the TS where the product will have a hydrogen. [b] These substrates do not match with the template used in CONSTRUCTS.

Chart and Table D8: Substrates set used in the substrate scope study with $(DHQD)_2PHAL$.[a]

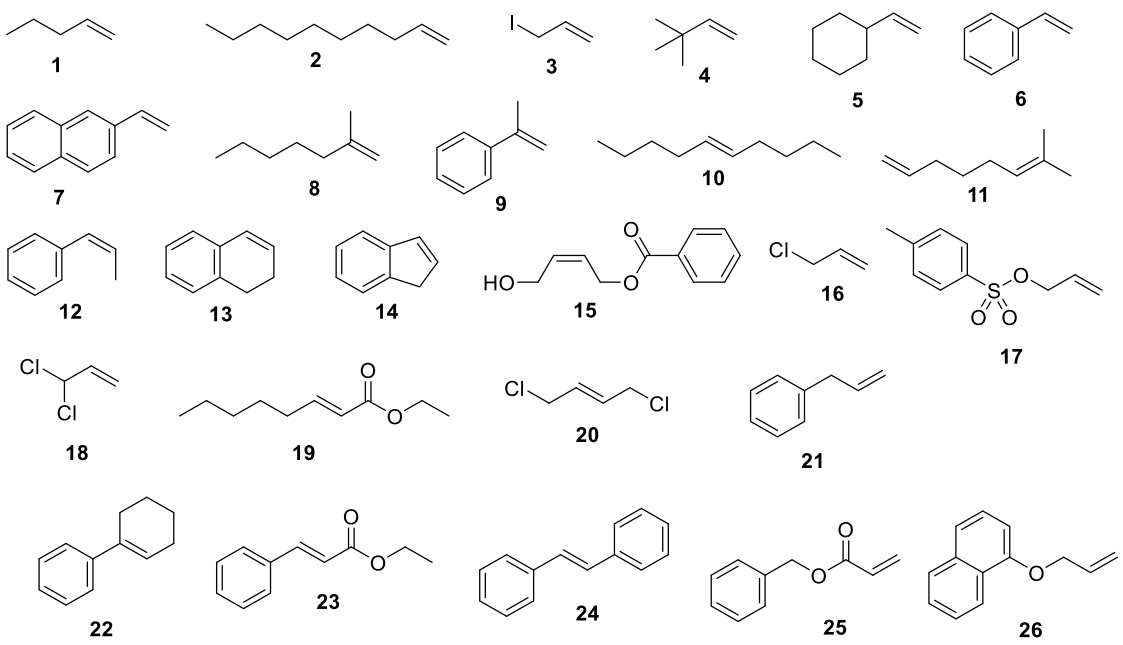

Entry	Substrate	Observed e.e. (%)	Ref.
1	**1**	79 (*R*)	365
2	**2**	84 (*R*)	365
3	**3**	63 (*S*)	365
4	**4**	64 (*R*)	365
5	**5**	88 (*R*)	365
6	**6**	97 (*R*)	365
7	**7**	99 (*R*)	365
8	**8**	78 (*R*)	365
9	**9**	94 (*R*)	365
10	**10**	97 (*R*,*R*)	365
11	**11**[b]	98 (*R*)	365
12	**12**	35 (1*R*,2*S*)	365
13	**13**	15 (1*R*,2*S*)	365
14	**14**	42 (1*R*,2*S*)	365
15	**15**	64 (1*S*,2*R*)	365
16	**16**	63 (*S*)	372
17	**17**	40 (*S*)	372
18	**18**	63 (*S*)	372
19	**19**	99 (2*S*,3*R*)	372
20	**20**	94 (*S*,*S*)	372
21	**21**	44 (*R*)	372
22	**22**	99 (*R*,*R*)	373
23	**23**	97 (2*S*, 2*R*)	373
24	**24**	>99.5 (*R*,*R*)	373
25	**25**	77 (*S*)	373
26	**26**	91 (*S*)	373

[a] $(DHQD)_2PHAL$ is catalyst **1a** in Table D5. [b] the two double bonds cannot be distinguished by CONSTRUCTS. This substrate was discarded.

Chapter 7 – References

(1) Council, N. R.: *Mathematical Challenges from Theoretical/Computational Chemistry*; The National Academies Press: Washington, DC, 1995.

(2) Lipkowitz, K. B.; Boyd, D. B.: *Reviews in Computational Chemistry - Volume 1*, 1990.

(3) W. J. Hehre; W. A. Lathan; R. Ditchfield; M. D. Newton, a.; Pople, J. A. Gaussian 70 (Quantum Chemistry Program Exchange, Program No. 237, 1970). **1970**.

(4) DelMonte, A. J.; Haller, J.; Houk, K. N.; Sharpless, K. B.; Singleton, D. A.; Strassner, T.; Thomas, A. A. Experimental and Theoretical Kinetic Isotope Effects for Asymmetric Dihydroxylation. Evidence Supporting a Rate-Limiting "(3 + 2)" Cycloaddition. *Journal of the American Chemical Society* **1997**, *119*, 9907-9908.

(5) McCammon, J. A.; Gelin, B. R.; Karplus, M. Dynamics of folded proteins. *Nature* **1977**, *267*, 585-590.

(6) The Nobel Prize in Chemistry 1998. (accessed January 21 2020).

(7) The Nobel Prize in Chemistry 2013. (accessed January 21 2020).

(8) Cornell, W. D.; Cieplak, P.; Bayly, C. I.; Gould, I. R.; Merz, K. M.; Ferguson, D. M.; Spellmeyer, D. C.; Fox, T.; Caldwell, J. W.; Kollman, P. A. A Second Generation Force Field for the Simulation of Proteins, Nucleic Acids, and Organic Molecules J. Am. Chem. Soc. 1995, 117, 5179−5197. *Journal of the American Chemical Society* **1996**, *118*, 2309-2309.

(9) Wang, J.; Wolf, R. M.; Caldwell, J. W.; Kollman, P. A.; Case, D. A. Development and testing of a general amber force field. *Journal of Computational Chemistry* **2004**, *25*, 1157-1174.

(10) Harder, E.; Damm, W.; Maple, J.; Wu, C.; Reboul, M.; Xiang, J. Y.; Wang, L.; Lupyan, D.; Dahlgren, M. K.; Knight, J. L.; Kaus, J. W.; Cerutti, D. S.; Krilov, G.; Jorgensen, W. L.; Abel, R.; Friesner, R. A. OPLS3: A Force Field Providing Broad Coverage of Drug-like Small Molecules and Proteins. *Journal of Chemical Theory and Computation* **2016**, *12*, 281-296.

(11) Champion, C.; Barigye, S. J.; Wei, W.; Liu, Z.; Labute, P.; Moitessier, N. Atom Type Independent Modeling of the Conformational Energy of Benzylic, Allylic, and Other Bonds Adjacent to Conjugated Systems. *Journal of Chemical Information and Modeling* **2019**, *59*, 4750-4763.

(12) Vanommeslaeghe, K.; Guvench, O.; MacKerell, A. D., Jr. Molecular mechanics. *Curr Pharm Des* **2014**, *20*, 3281-3292.

(13) Clobazam in Treatment of Refractory Epilepsy: The Canadian Experience. A Retrospecti. *Epilepsia* **1991**, *32*, 407-416.

(14) Mobley, D. L.; Bannan, C. C.; Rizzi, A.; Bayly, C. I.; Chodera, J. D.; Lim, V. T.; Lim, N. M.; Beauchamp, K. A.; Shirts, M. R.; Gilson, M. K.; Eastman, P. K. Open Force Field Consortium: Escaping atom types using direct chemical perception with SMIRNOFF v0.1. *bioRxiv* **2018**, 286542.

(15) Lengauer, T.; Rarey, M. Computational methods for biomolecular docking. *Current Opinion in Structural Biology* **1996**, *6*, 402-406.

(16) Khanna, V.; Ranganathan, S.; Petrovsky, N.: Rational Structure-Based Drug Design. In *Encyclopedia of Bioinformatics and Computational Biology*; Ranganathan, S., Gribskov, M., Nakai, K., Schönbach, C., Eds.; Academic Press: Oxford, 2019; pp 585-600.

(17) Voelz, V. A.; Bowman, G. R.; Beauchamp, K.; Pande, V. S. Molecular simulation of ab initio protein folding for a millisecond folder NTL9(1-39). *Journal of the American Chemical Society* **2010**, *132*, 1526-1528.

(18) Burai Patrascu, M.; Pottel, J.; Pinus, S.; Bezanson, M.; Norrby, P.-O.; Moitessier, N. From Desktop to Benchtop – A Paradigm Shift in Asymmetric Synthesis. *ChemRxiv* **2019**.

(19) Ren, P.; Wu, C.; Ponder, J. W. Polarizable Atomic Multipole-Based Molecular Mechanics for Organic Molecules. *Journal of Chemical Theory and Computation* **2011**, *7*, 3143-3161.

(20) Roothaan, C. C. J. New Developments in Molecular Orbital Theory. *Reviews of Modern Physics* **1951**, *23*, 69-89.

(21) Kohn, W.; Sham, L. J. Self-Consistent Equations Including Exchange and Correlation Effects. *Physical Review* **1965**, *140*, A1133-A1138.

(22) Pople, J. A.; Beveridge, D. L.; Dobosh, P. A. Approximate Self-Consistent Molecular-Orbital Theory. V. Intermediate Neglect of Differential Overlap. *The Journal of Chemical Physics* **1967**, *47*, 2026-2033.

(23) Szabo, A.; Ostlund, N. S.: *Modern quantum chemistry : introduction to advanced electronic structure theory*; 1st ed., Rev. ed.; McGraw-Hill: New York, 1989. pp. xiv, 466 pages : illustrations ; 24 cm.

(24) Christensen, A. S.; Kubař, T.; Cui, Q.; Elstner, M. Semiempirical Quantum Mechanical Methods for Noncovalent Interactions for Chemical and Biochemical Applications. *Chemical Reviews* **2016**, *116*, 5301-5337.

(25) Barone, V.; Arnaud, R. Study of prototypical Diels-Alder reactions by a hybrid density functional/Hartree-Fock approach. *Chemical Physics Letters* **1996**, *251*, 393-399.

(26) Barone, V.; Adamo, C. A theoretical investigation of potential energy surfaces governing the photochemical tautomerization of 2-pyridone. *Chemical Physics Letters* **1994**, *226*, 399-404.

(27) Burai Patrascu, M.; Plescia, J.; Kalgutkar, A.; Mascitti, V.; Moitessier, N. Computational methods for prediction of drug properties - application to Cytochrome P450 metabolism prediction. *Arkivoc* **2019**, *2019*, 280-298.

(28) Dewar, M. J. S.; Zoebisch, E. G.; Healy, E. F.; Stewart, J. J. P. Development and use of quantum mechanical molecular models. 76. AM1: a new general purpose quantum mechanical molecular model. *Journal of the American Chemical Society* **1985**, *107*, 3902-3909.

(29) Stewart, J. J. P. Optimization of parameters for semiempirical methods II. Applications. *Journal of Computational Chemistry* **1989**, *10*, 221-264.

(30) Stewart, J. J. P. Optimization of parameters for semiempirical methods V: Modification of NDDO approximations and application to 70 elements. *Journal of Molecular Modeling* **2007**, *13*, 1173-1213.

(31) Rocha, G. B.; Freire, R. O.; Simas, A. M.; Stewart, J. J. P. RM1: A reparameterization of AM1 for H, C, N, O, P, S, F, Cl, Br, and I. *Journal of Computational Chemistry* **2006**, *27*, 1101-1111.

(32) Bikadi, Z.; Hazai, E. Application of the PM6 semi-empirical method to modeling proteins enhances docking accuracy of AutoDock. *Journal of Cheminformatics* **2009**, *1*, 15.

(33) Matsuzawa, N.; Dixon, D. A. Semiempirical calculations of hyperpolarizabilities for donor-acceptor molecules: comparison to experiment. *The Journal of Physical Chemistry* **1992**, *96*, 6232-6241.

(34) Stewart, J. J. P. Application of the PM6 method to modeling proteins. *Journal of Molecular Modeling* **2009**, *15*, 765-805.

(35) Muddana, H. S.; Gilson, M. K. Calculation of Host–Guest Binding Affinities Using a Quantum-Mechanical Energy Model. *Journal of Chemical Theory and Computation* **2012**, *8*, 2023-2033.

(36) Korth, M. Third-Generation Hydrogen-Bonding Corrections for Semiempirical QM Methods and Force Fields. *Journal of Chemical Theory and Computation* **2010**, *6*, 3808-3816.

(37) Becke, A. D. Density-functional thermochemistry. III. The role of exact exchange. *The Journal of Chemical Physics* **1993**, *98*, 5648-5652.

(38) Lee, C.; Yang, W.; Parr, R. G. Development of the Colle-Salvetti correlation-energy formula into a functional of the electron density. *Physical Review B* **1988**, *37*, 785-789.

(39) Becke, A. D. Perspective: Fifty years of density-functional theory in chemical physics. *The Journal of Chemical Physics* **2014**, *140*, 18A301.

(40) Neese, F. Software update: the ORCA program system, version 4.0. *WIREs Computational Molecular Science* **2018**, *8*, e1327.

(41) Schmidt, M. W.; Baldridge, K. K.; Boatz, J. A.; Elbert, S. T.; Gordon, M. S.; Jensen, J. H.; Koseki, S.; Matsunaga, N.; Nguyen, K. A.; Su, S.; Windus, T. L.; Dupuis, M.; Montgomery, J. A. General atomic and molecular electronic structure system. *J. Comp. Chem.* **1993**, *14*, 1347-1363.

(42) Gordon, M. S.; Schmidt, M. W.: Advances in electronic structure theory: GAMESS a decade later. In *Theory and Applications of Computational Chemistry: the first forty years*; Dykstra, C. E., Frenking, G., Kim, K. S., Scuseria, G. E., Eds.; Elsevier, 2005; pp 1167-1189.

(43) Vondrášek, J.; Bendová, L.; Klusák, V.; Hobza, P. Unexpectedly Strong Energy Stabilization Inside the Hydrophobic Core of Small Protein Rubredoxin Mediated by Aromatic Residues: Correlated Ab Initio Quantum Chemical Calculations. *Journal of the American Chemical Society* **2005**, *127*, 2615-2619.

(44) Grimme, S. Density functional theory with London dispersion corrections. *WIREs Computational Molecular Science* **2011**, *1*, 211-228.

(45) Grimme, S.; Brandenburg, J. G.; Bannwarth, C.; Hansen, A. Consistent structures and interactions by density functional theory with small atomic orbital basis sets. *The Journal of Chemical Physics* **2015**, *143*, 054107.

(46) Brandenburg, J. G.; Bannwarth, C.; Hansen, A.; Grimme, S. B97-3c: A revised low-cost variant of the B97-D density functional method. *The Journal of Chemical Physics* **2018**, *148*, 064104.

(47) Lundberg, M.; Siegbahn, P. E. M. Quantifying the effects of the self-interaction error in DFT: When do the delocalized states appear? *The Journal of Chemical Physics* **2005**, *122*, 224103.

(48) Harvey, J. N. On the accuracy of density functional theory in transition metal chemistry. *Annual Reports Section "C" (Physical Chemistry)* **2006**, *102*, 203-226.

(49) Marques, A. N. L.; Mendes Filho, J.; Freire, P. T. C.; Santos, H. S.; Albuquerque, M. R. J. R.; Bandeira, P. N.; Leite, R. V.; Braz-Filho, R.; Gusmão, G. O. M.; Nogueira, C. E. S.; Teixeira, A. M. R. Vibrational spectroscopy and DFT calculations of flavonoid derriobtusone A. *Journal of Molecular Structure* **2017**, *1130*, 231-237.

(50) Cresswell, A. J.; Eey, S. T. C.; Denmark, S. E. Catalytic, stereospecific syn-dichlorination of alkenes. *Nature Chemistry* **2015**, *7*, 146-152.

(51) Fu, L.; Mu, X.; Li, B. Reaction mechanism of organoselenium-catalyzed syn-dichlorination of alkenes: a DFT study. *Journal of Molecular Modeling* **2018**, *24*, 91.

(52) Fleming, E. M.; Quigley, C.; Rozas, I.; Connon, S. J. Computational Study-Led Organocatalyst Design: A Novel, Highly Active Urea-Based Catalyst for Addition Reactions to Epoxides. *The Journal of Organic Chemistry* **2008**, *73*, 948-956.

(53) Ainsley, J.; Lodola, A.; Mulholland, A. J.; Christov, C. Z.; Karabencheva-Christova, T. G.: Chapter One - Combined Quantum Mechanics and Molecular Mechanics Studies of Enzymatic Reaction Mechanisms. In *Advances in Protein Chemistry and Structural Biology*; Karabencheva-Christova, T. G., Christov, C. Z., Eds.; Academic Press, 2018; Vol. 113; pp 1-32.

(54) Karabencheva-Christova, T. G.; Torras, J.; Mulholland, A. J.; Lodola, A.; Christov, C. Z. Mechanistic Insights into the Reaction of Chlorination of Tryptophan Catalyzed by Tryptophan 7-Halogenase. *Scientific Reports* **2017**, *7*, 17395.

(55) Chaskar, P.; Zoete, V.; Röhrig, U. F. On-the-Fly QM/MM Docking with Attracting Cavities. *Journal of Chemical Information and Modeling* **2017**, *57*, 73-84.

(56) Senn, H. M.; Thiel, W.: QM/MM Methods for Biological Systems. In *Atomistic Approaches in Modern Biology: From Quantum Chemistry to Molecular Simulations*; Reiher, M., Ed.; Springer Berlin Heidelberg: Berlin, Heidelberg, 2007; pp 173-290.

(57) Ibragimova, G. T.; Wade, R. C. Importance of Explicit Salt Ions for Protein Stability in Molecular Dynamics Simulation. *Biophysical Journal* **1998**, *74*, 2906-2911.

(58) Cova, T. F. G. G.; Pais, A. A. C. C. Deep Learning for Deep Chemistry: Optimizing the Prediction of Chemical Patterns. *Frontiers in Chemistry* **2019**, *7*, 809.

(59) Hirohara, M.; Saito, Y.; Koda, Y.; Sato, K.; Sakakibara, Y. Convolutional neural network based on SMILES representation of compounds for detecting chemical motif. *BMC Bioinformatics* **2018**, *19*, 526.

(60) Hiller, S. A.; Golender, V. E.; Rosenblit, A. B.; Rastrigin, L. A.; Glaz, A. B. Cybernetic methods of drug design. I. Statement of the problem—The perceptron approach. *Computers and Biomedical Research* **1973**, *6*, 411-421.

(61) Jaén-Oltra, J.; Salabert-Salvador, M. T.; García-March, F. J.; Pérez-Giménez, F.; Tomás-Vert, F. Artificial Neural Network Applied to Prediction of Fluorquinolone Antibacterial Activity by Topological Methods. *Journal of Medicinal Chemistry* **2000**, *43*, 1143-1148.

(62) Zhou, Y.; Cahya, S.; Combs, S. A.; Nicolaou, C. A.; Wang, J.; Desai, P. V.; Shen, J. Exploring Tunable Hyperparameters for Deep Neural Networks with Industrial ADME Data Sets. *Journal of Chemical Information and Modeling* **2019**, *59*, 1005-1016.

(63) Zaretzki, J.; Matlock, M.; Swamidass, S. J. XenoSite: Accurately Predicting CYP-Mediated Sites of Metabolism with Neural Networks. *Journal of Chemical Information and Modeling* **2013**, *53*, 3373-3383.

(64) Svetnik, V.; Liaw, A.; Tong, C.; Culberson, J. C.; Sheridan, R. P.; Feuston, B. P. Random Forest: A Classification and Regression Tool for Compound Classification and QSAR Modeling. *Journal of Chemical Information and Computer Sciences* **2003**, *43*, 1947-1958.

(65) Wang, C.; Zhang, Y. Improving scoring-docking-screening powers of protein–ligand scoring functions using random forest. *Journal of Computational Chemistry* **2017**, *38*, 169-177.

(66) Finkelmann, A. R.; Göller, A. H.; Schneider, G. Site of Metabolism Prediction Based on ab initio Derived Atom Representations. *ChemMedChem* **2017**, *12*, 606-612.

(67) Dalvie, D.; Kalgutkar, A. S.; Chen, W. Practical approaches to resolving reactive metabolite liabilities in early discovery. *Drug Metabolism Reviews* **2015**, *47*, 56-70.

(68) Kaitin, K. I. Deconstructing the Drug Development Process: The New Face of Innovation. *Clinical Pharmacology & Therapeutics* **2010**, *87*, 356-361.

(69) Taft, C. A.; da Silva, V. B.; da Silva, C. H. T. d. P. Current topics in computer-aided drug design. *Journal of Pharmaceutical Sciences* **2008**, *97*, 1089-1098.

(70) Aparoy, P.; Reddy, K. K.; Reddanna, P. Structure and ligand based drug design strategies in the development of novel 5- LOX inhibitors. *Curr Med Chem* **2012**, *19*, 3763-3778.

(71) Corbeil, C. R.; Englebienne, P.; Moitessier, N. Docking Ligands into Flexible and Solvated Macromolecules. 1. Development and Validation of FITTED 1.0. *Journal of Chemical Information and Modeling* **2007**, *47*, 435-449.

(72) Pagadala, N. S.; Syed, K.; Tuszynski, J. Software for molecular docking: a review. *Biophys Rev* **2017**, *9*, 91-102.

(73) Koshland Jr, D. E. The Key–Lock Theory and the Induced Fit Theory. *Angewandte Chemie International Edition in English* **1995**, *33*, 2375-2378.

(74) Forli, S.; Huey, R.; Pique, M. E.; Sanner, M. F.; Goodsell, D. S.; Olson, A. J. Computational protein-ligand docking and virtual drug screening with the AutoDock suite. *Nat Protoc* **2016**, *11*, 905-919.

(75) Friesner, R. A.; Banks, J. L.; Murphy, R. B.; Halgren, T. A.; Klicic, J. J.; Mainz, D. T.; Repasky, M. P.; Knoll, E. H.; Shelley, M.; Perry, J. K.; Shaw, D. E.; Francis, P.; Shenkin, P. S. Glide: A New Approach for Rapid, Accurate Docking and Scoring. 1. Method and Assessment of Docking Accuracy. *Journal of Medicinal Chemistry* **2004**, *47*, 1739-1749.

(76) Jones, G.; Willett, P.; Glen, R. C.; Leach, A. R.; Taylor, R. Development and validation of a genetic algorithm for flexible docking11Edited by F. E. Cohen. *Journal of Molecular Biology* **1997**, *267*, 727-748.

(77) von Itzstein, M.; Wu, W.-Y.; Kok, G. B.; Pegg, M. S.; Dyason, J. C.; Jin, B.; Van Phan, T.; Smythe, M. L.; White, H. F.; Oliver, S. W.; Colman, P. M.; Varghese, J. N.; Ryan, D. M.; Woods, J. M.; Bethell, R. C.; Hotham, V. J.; Cameron, J. M.; Penn, C. R. Rational design of potent sialidase-based inhibitors of influenza virus replication. *Nature* **1993**, *363*, 418-423.

(78) Jenwitheesuk, E.; Samudrala, R. Improved prediction of HIV-1 protease-inhibitor binding energies by molecular dynamics simulations. *BMC Struct Biol* **2003**, *3*, 2-2.

(79) Irwin, J. J.; Shoichet, B. K. ZINC--a free database of commercially available compounds for virtual screening. *Journal of chemical information and modeling* **2005**, *45*, 177-182.

(80) Hoffmann, T.; Gastreich, M. The next level in chemical space navigation: going far beyond enumerable compound libraries. *Drug Discovery Today* **2019**, *24*, 1148-1156.

(81) Therrien, E.; Englebienne, P.; Arrowsmith, A. G.; Mendoza-Sanchez, R.; Corbeil, C. R.; Weill, N.; Campagna-Slater, V.; Moitessier, N. Integrating Medicinal Chemistry, Organic/Combinatorial Chemistry, and Computational Chemistry for the Discovery of Selective Estrogen Receptor Modulators with Forecaster, a Novel Platform for Drug Discovery. *Journal of Chemical Information and Modeling* **2012**, *52*, 210-224.

(82) Kuck, D.; Singh, N.; Lyko, F.; Medina-Franco, J. L. Novel and selective DNA methyltransferase inhibitors: Docking-based virtual screening and experimental evaluation. *Bioorganic & Medicinal Chemistry* **2010**, *18*, 822-829.

(83) Wang, D.; Wang, F.; Tan, Y.; Dong, L.; Chen, L.; Zhu, W.; Wang, H. Discovery of potent small molecule inhibitors of DYRK1A by structure-based virtual screening and bioassay. *Bioorganic & Medicinal Chemistry Letters* **2012**, *22*, 168-171.

(84) Hospital, A.; Goñi, J. R.; Orozco, M.; Gelpí, J. L. Molecular dynamics simulations: advances and applications. *Adv Appl Bioinform Chem* **2015**, *8*, 37-47.

(85) Kmiecik, S.; Gront, D.; Kolinski, M.; Wieteska, L.; Dawid, A. E.; Kolinski, A. Coarse-Grained Protein Models and Their Applications. *Chemical Reviews* **2016**, *116*, 7898-7936.

(86) Nelson, M. T.; Humphrey, W.; Gursoy, A.; Dalke, A.; Kalé, L. V.; Skeel, R. D.; Schulten, K. NAMD: a Parallel, Object-Oriented Molecular Dynamics Program. *The International Journal of Supercomputer Applications and High Performance Computing* **1996**, *10*, 251-268.

(87) Schames, J. R.; Henchman, R. H.; Siegel, J. S.; Sotriffer, C. A.; Ni, H.; McCammon, J. A. Discovery of a Novel Binding Trench in HIV Integrase. *Journal of Medicinal Chemistry* **2004**, *47*, 1879-1881.

(88) Durrant, J. D.; McCammon, J. A. Molecular dynamics simulations and drug discovery. *BMC Biology* **2011**, *9*, 71.

(89) Zeevaart, J. G.; Wang, L.; Thakur, V. V.; Leung, C. S.; Tirado-Rives, J.; Bailey, C. M.; Domaoal, R. A.; Anderson, K. S.; Jorgensen, W. L. Optimization of Azoles as Anti-Human Immunodeficiency Virus Agents Guided by Free-Energy Calculations. *Journal of the American Chemical Society* **2008**, *130*, 9492-9499.

(90) Acharya, C.; Coop, A.; Polli, J. E.; Mackerell, A. D., Jr. Recent advances in ligand-based drug design: relevance and utility of the conformationally sampled pharmacophore approach. *Curr Comput Aided Drug Des* **2011**, *7*, 10-22.

(91) Cramer, R. D.; Patterson, D. E.; Bunce, J. D. Comparative molecular field analysis (CoMFA). 1. Effect of shape on binding of steroids to carrier proteins. *Journal of the American Chemical Society* **1988**, *110*, 5959-5967.

(92) Klebe, G.; Abraham, U.; Mietzner, T. Molecular Similarity Indices in a Comparative Analysis (CoMSIA) of Drug Molecules to Correlate and Predict Their Biological Activity. *Journal of Medicinal Chemistry* **1994**, *37*, 4130-4146.

(93) Kuo, C.-L.; Assefa, H.; Kamath, S.; Brzozowski, Z.; Slawinski, J.; Saczewski, F.; Buolamwini, J. K.; Neamati, N. Application of CoMFA and CoMSIA 3D-QSAR and Docking Studies in Optimization of Mercaptobenzenesulfonamides as HIV-1 Integrase Inhibitors. *Journal of Medicinal Chemistry* **2004**, *47*, 385-399.

(94) Shaldam, M.; Tawfik, H.; El-Bastawissy, E.; El-Moselhy, T. The Application of CoMFA Approach for the Design of 1,4-Dihydropyridines as Calcium Channel Blockers. *CHEMISTRY and BIOLOGY INTERFACE* **2016**, *6*, 350-356.

(95) Ehrlich, P. Über den jetzigen Stand der Chemotherapie. *Berichte der deutschen chemischen Gesellschaft* **1909**, *42*, 17-47.

(96) Schueler, F. W. Chemobiodynamics and Drug Design. *Journal of Pharmaceutical Sciences* **1961**, *50*.

(97) Wermuth, C.-G.; Robin Ganellin, C.; Lindberg, P.; Mitscher, L. A.: Chapter 36 - Glossary of Terms Used in Medicinal Chemistry (IUPAC Recommendations 1997). In *Annual Reports in Medicinal Chemistry*; Bristol, J. A., Ed.; Academic Press, 1998; Vol. 33; pp 385-395.

(98) Yang, S.-Y. Pharmacophore modeling and applications in drug discovery: challenges and recent advances. *Drug Discovery Today* **2010**, *15*, 444-450.

(99) Toba, S.; Srinivasan, J.; Maynard, A. J.; Sutter, J. Using Pharmacophore Models To Gain Insight into Structural Binding and Virtual Screening: An Application Study with CDK2 and Human DHFR. *Journal of Chemical Information and Modeling* **2006**, *46*, 728-735.

(100) Hecker, E. A.; Duraiswami, C.; Andrea, T. A.; Diller, D. J. Use of Catalyst Pharmacophore Models for Screening of Large Combinatorial Libraries. *Journal of Chemical Information and Computer Sciences* **2002**, *42*, 1204-1211.

(101) Vadivelan, S.; Sinha, B. N.; Irudayam, S. J.; Jagarlapudi, S. A. R. P. Virtual Screening Studies to Design Potent CDK2-Cyclin A Inhibitors. *Journal of Chemical Information and Modeling* **2007**, *47*, 1526-1535.

(102) Ren, J.-X.; Li, L.-L.; Zou, J.; Yang, L.; Yang, J.-L.; Yang, S.-Y. Pharmacophore modeling and virtual screening for the discovery of new transforming growth factor-β type I receptor (ALK5) inhibitors. *European Journal of Medicinal Chemistry* **2009**, *44*, 4259-4265.

(103) Wei, D.; Jiang, X.; Zhou, L.; Chen, J.; Chen, Z.; He, C.; Yang, K.; Liu, Y.; Pei, J.; Lai, L. Discovery of Multitarget Inhibitors by Combining Molecular Docking with Common Pharmacophore Matching. *Journal of Medicinal Chemistry* **2008**, *51*, 7882-7888.

(104) Steindl, T. M.; Schuster, D.; Laggner, C.; Langer, T. Parallel Screening: A Novel Concept in Pharmacophore Modeling and Virtual Screening. *Journal of Chemical Information and Modeling* **2006**, *46*, 2146-2157.

(105) Law, J.; Zsoldos, Z.; Simon, A.; Reid, D.; Liu, Y.; Khew, S. Y.; Johnson, A. P.; Major, S.; Wade, R. A.; Ando, H. Y. Route Designer: A Retrosynthetic Analysis Tool Utilizing Automated Retrosynthetic Rule Generation. *Journal of Chemical Information and Modeling* **2009**, *49*, 593-602.

(106) Blurock, E. S. Computer-aided synthesis design at RISC-Linz: automatic extraction and use of reaction classes. *Journal of Chemical Information and Computer Sciences* **1990**, *30*, 505-510.

(107) Kayala, M. A.; Baldi, P. ReactionPredictor: Prediction of Complex Chemical Reactions at the Mechanistic Level Using Machine Learning. *Journal of Chemical Information and Modeling* **2012**, *52*, 2526-2540.

(108) Feng, F.; Lai, L.; Pei, J. Computational Chemical Synthesis Analysis and Pathway Design. *Frontiers in Chemistry* **2018**, *6*, 199.

(109) Wu, J.; Magrakvelidze, M.; Schmidt, L. P. H.; Kunitski, M.; Pfeifer, T.; Schöffler, M.; Pitzer, M.; Richter, M.; Voss, S.; Sann, H.; Kim, H.; Lower, J.; Jahnke, T.; Czasch, A.; Thumm, U.; Dörner, R. Understanding the role of phase in chemical bond breaking with coincidence angular streaking. *Nature Communications* **2013**, *4*, 2177.

(110) Cheng, G.-J.; Zhang, X.; Chung, L. W.; Xu, L.; Wu, Y.-D. Computational Organic Chemistry: Bridging Theory and Experiment in Establishing the Mechanisms of Chemical Reactions. *Journal of the American Chemical Society* **2015**, *137*, 1706-1725.

(111) Heravi, M. M.; Zadsirjan, V.; Esfandyari, M.; Lashaki, T. B. Applications of sharpless asymmetric dihydroxylation in the total synthesis of natural products. *Tetrahedron: Asymmetry* **2017**, *28*, 987-1043.

(112) Hentges, S. G.; Sharpless, K. B. Asymmetric induction in the reaction of osmium tetroxide with olefins. *Journal of the American Chemical Society* **1980**, *102*, 4263-4265.

(113) Corey, E. J.; Jardine, P. D.; Virgil, S.; Yuen, P. W.; Connell, R. D. Enantioselective vicinal hydroxylation of terminal and E-1,2-disubstituted olefins by a chiral complex of osmium tetroxide. An effective controller system and a rational mechanistic model. *Journal of the American Chemical Society* **1989**, *111*, 9243-9244.

(114) Tomberg, A.; Pottel, J.; Liu, Z.; Labute, P.; Moitessier, N. Understanding P450-mediated Bio-transformations into Epoxide and Phenolic Metabolites. *Angewandte Chemie International Edition* **2015**, *54*, 13743-13747.

(115) Chattaraj, P. K.; Roy, D. R.: Chapter 9 - Conceptual Density Functional Theory of Chemical Reactivity. In *Advances in Mathematical Chemistry and Applications*; Basak, S. C., Restrepo, G., Villaveces, J. L., Eds.; Bentham Science Publishers, 2015; pp 196-221.

(116) Kohn, W.; Becke, A. D.; Parr, R. G. Density Functional Theory of Electronic Structure. *The Journal of Physical Chemistry* **1996**, *100*, 12974-12980.

(117) Pearson, R. G. Hard and soft acids and bases—the evolution of a chemical concept. *Coordination Chemistry Reviews* **1990**, *100*, 403-425.

(118) Parr, R. G.; Szentpály, L. v.; Liu, S. Electrophilicity Index. *Journal of the American Chemical Society* **1999**, *121*, 1922-1924.

(119) Parr, R. G.; Yang, W. Density functional approach to the frontier-electron theory of chemical reactivity. *Journal of the American Chemical Society* **1984**, *106*, 4049-4050.

(120) Fukui, K. Role of Frontier Orbitals in Chemical Reactions. *Science* **1982**, *218*, 747.

(121) Martinez, C.; Rivera, J. L.; Herrera, R.; Rico, J. L.; Flores, N.; Rutiaga, J. G.; López, P. Evaluation of the chemical reactivity in lignin precursors using the Fukui function. *Journal of Molecular Modeling* **2007**, *14*, 77.

(122) Mendez, F.; Gazquez, J. L. Chemical Reactivity of Enolate Ions: The Local Hard and Soft Acids and Bases Principle Viewpoint. *Journal of the American Chemical Society* **1994**, *116*, 9298-9301.

(123) Corbeil, C. R.; Thielges, S.; Schwartzentruber, J. A.; Moitessier, N. Toward a Computational Tool Predicting the Stereochemical Outcome of Asymmetric Reactions: Development and Application of a Rapid and Accurate Program Based on Organic Principles. *Angewandte Chemie International Edition* **2008**, *47*, 2635-2638.

(124) Rosales, A. R.; Quinn, T. R.; Wahlers, J.; Tomberg, A.; Zhang, X.; Helquist, P.; Wiest, O.; Norrby, P.-O. Application of Q2MM to predictions in stereoselective synthesis. *Chemical Communications* **2018**, *54*, 8294-8311.

(125) Houk, K. N.; Cheong, P. H.-Y. Computational prediction of small-molecule catalysts. *Nature* **2008**, *455*, 309-313.

(126) Du, X.; Gao, X.; Hu, W.; Yu, J.; Luo, Z.; Cen, K. Catalyst Design Based on DFT Calculations: Metal Oxide Catalysts for Gas Phase NO Reduction. *The Journal of Physical Chemistry C* **2014**, *118*, 13617-13622.

(127) Wheeler, S. E.; Seguin, T. J.; Guan, Y.; Doney, A. C. Noncovalent Interactions in Organocatalysis and the Prospect of Computational Catalyst Design. *Accounts of Chemical Research* **2016**, *49*, 1061-1069.

(128) Reid, J. P.; Simón, L.; Goodman, J. M. A Practical Guide for Predicting the Stereochemistry of Bifunctional Phosphoric Acid Catalyzed Reactions of Imines. *Accounts of Chemical Research* **2016**, *49*, 1029-1041.

(129) Andrea N., B.; Steven, W.: *Popular Integration Grids Can Result in Large Errors in DFT-Computed Free Energies*, 2019.

(130) Rosales, A. R.; Wahlers, J.; Limé, E.; Meadows, R. E.; Leslie, K. W.; Savin, R.; Bell, F.; Hansen, E.; Helquist, P.; Munday, R. H.; Wiest, O.; Norrby, P.-O. Rapid virtual screening of enantioselective catalysts using CatVS. *Nature Catalysis* **2019**, *2*, 41-45.

(131) Hansen, E.; Rosales, A. R.; Tutkowski, B.; Norrby, P.-O.; Wiest, O. Prediction of Stereochemistry using Q2MM. *Accounts of Chemical Research* **2016**, *49*, 996-1005.

(132) Eksterowicz, J. E.; Houk, K. N. Transition-state modeling with empirical force fields. *Chemical Reviews* **1993**, *93*, 2439-2461.

(133) Schrödinger Suite v.2017-2.

(134) Nagata, S.; Tsuchiya, M.; Asano, S.; Kaziro, Y.; Yamazaki, T.; Yamamoto, O.; Hirata, Y.; Kubota, N.; Oheda, M.; Nomura, H.; Ono, M. Molecular cloning and expression of cDNA for human granulocyte colony-stimulating factor. *Nature* **1986**, *319*, 415-418.

(135) Stein, C. A.; Castanotto, D. FDA-Approved Oligonucleotide Therapies in 2017. *Mol. Ther.* **2017**, *25*, 1069-1075.

(136) Dolgin, E. Spinal muscular atrophy approval boosts antisense drugs. *Nat. Biotech.* **2017**, *35*, 99-100.

(137) Broder, S. The development of antiretroviral therapy and its impact on the HIV-1/AIDS pandemic. *Antiviral Res.* **2010**, *85*, 1.

(138) Soudeyns, H.; Yao, X. I.; Gao, Q.; Belleau, B.; Kraus, J. L.; Nguyen-Ba, N.; Spira, B.; Wainberg, M. A. Anti-human immunodeficiency virus type 1 activity and in vitro toxicity of 2'-deoxy-3'-thiacytidine (BCH-189), a novel heterocyclic nucleoside analog. *Antimicrob. Agents and Chemother.* **1991**, *35*, 1386-1390.

(139) Liotta, D. C.; Painter, G. R. Discovery and Development of the Anti-Human Immunodeficiency Virus Drug, Emtricitabine (Emtriva, FTC). *Acc. Chem. Res.* **2016**, *49*, 2091-2098.

(140) Dienstag, J.; Easley, C.; Kirkpatrick, P. Telbivudine. *Nat. Rev. Drug Discov.* **2007**, *6*, 267-268.

(141) Warren, T. K.; Wells, J.; Panchal, R. G.; Stuthman, K. S.; Garza, N. L.; Van Tongeren, S. A.; Dong, L.; Retterer, C. J.; Eaton, B. P.; Pegoraro, G.; Honnold, S.; Bantia, S.; Kotian, P.; Chen, X.; Taubenheim, B. R.; Welch, L. S.; Minning, D. M.; Babu, Y. S.; Sheridan, W. P.; Bavari, S. Protection against filovirus diseases by a novel broad-spectrum nucleoside analogue BCX4430. *Nature* **2014**, *508*, 402-405.

(142) Whitley , R.; Arvin , A.; Prober , C.; Burchett , S.; Corey , L.; Powell , D.; Plotkin , S.; Starr , S.; Alford , C.; Connor , J.; Jacobs , R.; Nahmias , A.; Soong , S.-J. A Controlled Trial Comparing Vidarabine with Acyclovir in Neonatal Herpes Simplex Virus Infection. *New Engl. J. Med.* **1991**, *324*, 444-449.

(143) Plunkett, W.; Huang, P.; Gandhi, V. Preclinical characteristics of gemcitabine. *Anti-Cancer Drugs* **1995**, *6*, 7-13.

(144) Moitessier, N.; Englebienne, P.; Lee, D.; Lawandi, J.; Corbeil, C. R. Towards the development of universal, fast and highly accurate docking/scoring methods: A long way to go. *Br. J. Pharmacol.* **2008**, *153*, S7-S26.

(145) Yurenko, Y. P.; Zhurakivsky, R. O.; Ghomi, M.; Samijlenko, S. P.; Hovorun, D. M. How Many Conformers Determine the Thymidine Low-Temperature Matrix Infrared Spectrum? DFT and MP2 Quantum Chemical Study. *J. Phys. Chem. B* **2007**, *111*, 9655-9663.

(146) Deleavey, G. F.; Damha, M. J. Designing chemically modified oligonucleotides for targeted gene silencing. *Chem. Biol.* **2012**, *19*, 937-954.

(147) Altona, C. T.; Sundaralingam, M. Conformational analysis of the sugar ring in nucleosides and nucleotides. New description using the concept of pseudorotation. *Journal of the American Chemical Society* **1972**, *94*, 8205-8212.

(148) Kawasaki, A. M.; Casper, M. D.; Freier, S. M.; Lesnik, E. A.; Zounes, M. C.; Cummins, L. L.; Gonzalez, C.; Cook, P. D. Uniformly modified 2'-deoxy-2'-fluoro-phosphorothioate oligonucleotides as nuclease-resistant antisense compounds with high affinity and specificity for RNA targets. *J. Med. Chem.* **1993**, *36*, 831-841.

(149) Obika, S.; Nanbu, D.; Hari, Y.; Andoh, J.-i.; Morio, K.-i.; Doi, T.; Imanishi, T. Stability and structural features of the duplexes containing nucleoside analogues with a fixed N-type conformation, 2′-O,4′-C-methyleneribonucleosides. *Tetrahedron Lett.* **1998**, *39*, 5401-5404.

(150) Koshkin, A. A.; Singh, S. K.; Nielsen, P.; Rajwanshi, V. K.; Kumar, R.; Meldgaard, M.; Olsen, C. E.; Wengel, J. LNA (Locked Nucleic Acids): Synthesis of the adenine, cytosine, guanine, 5-methylcytosine, thymine and uracil bicyclonucleoside monomers, oligomerisation, and unprecedented nucleic acid recognition. *Tetrahedron* **1998**, *54*, 3607-3630.

(151) Li, F.; Sarkhel, S.; Wilds, C. J.; Wawrzak, Z.; Prakash, T. P.; Manoharan, M.; Egli, M. 2′-Fluoroarabino- and Arabinonucleic Acid Show Different Conformations, Resulting in Deviating RNA Affinities and Processing of Their Heteroduplexes with RNA by RNase H. *Biochemistry* **2006**, *45*, 4141-4152.

(152) Malek-Adamian, E.; Guenther, D. C.; Matsuda, S.; Martinez-Montero, S.; Zlatev, I.; Harp, J.; Burai Patrascu, M.; Foster, D.; Fakhoury, J.; Perkins, L.; Manoharan, R. M.; Taneja, N.; Bisbe, A.; Charisse, K.; Maier, M.; Kallanthottathil, R. G.; Egli, M.; Manoharan, M.; Damha, M. J. 4′-C-Methoxy-2′-Deoxy-2′-Fluoro Modified Ribonucleotides Improve Metabolic Stability and Elicit Efficient siRNA-Mediated Gene Silencing. *J. Am. Chem. Soc.* **2017**, *139*, 14542-14555.

(153) Sander, J. D.; Joung, J. K. CRISPR-Cas systems for editing, regulating and targeting genomes. *Nat. Biotech.* **2014**, *32*, 347-355.

(154) Monia, B. P.; Lesnik, E. A.; Gonzalez, C.; Lima, W. F.; McGee, D.; Guinosso, C. J.; Kawasaki, A. M.; Cook, P. D.; Freier, S. M. Evaluation of 2'-modified oligonucleotides containing 2'-deoxy gaps as antisense inhibitors of gene expression. *J. Biol. Chem.* **1993**, *268*, 14514-14522.

(155) Trempe, J.-F.; Wilds, C. J.; Denisov, A. Y.; Pon, R. T.; Damha, M. J.; Gehring, K. NMR Solution Structure of an Oligonucleotide Hairpin with a 2‘F-ANA/RNA Stem: Implications for RNase H Specificity toward DNA/RNA Hybrid Duplexes. *J. Am. Chem. Soc.* **2001**, *123*, 4896-4903.

(156) Damha, M. J.; Wilds, C. J.; Noronha, A.; Brukner, I.; Borkow, G.; Arion, D.; Parniak, M. A. Hybrids of RNA and Arabinonucleic Acids (ANA and 2‘F-ANA) Are Substrates of Ribonuclease H. *J. Am. Chem. Soc.* **1998**, *120*, 12976-12977.

(157) Kalota, A.; Karabon, L.; Swider, C. R.; Viazovkina, E.; Elzagheid, M.; Damha, M. J.; Gewirtz, A. M. 2′-Deoxy-2′-fluoro-β- d -arabinonucleic acid (2′F-ANA) modified oligonucleotides (ON) effect highly efficient, and persistent, gene silencing. *Nucl. Acids Res.* **2006**, *34*, 451-461.

(158) Martínez-Montero, S.; Deleavey, G. F.; Kulkarni, A.; Martín-Pintado, N.; Lindovska, P.; Thomson, M.; González, C.; Götte, M.; Damha, M. J. Rigid 2′,4′-Difluororibonucleosides: Synthesis, Conformational Analysis, and Incorporation into Nascent RNA by HCV Polymerase. *J. Org. Chem.* **2014**, *79*, 5627-5635.

(159) Marquez, V. E.; Siddiqui, M. A.; Ezzitouni, A.; Russ, P.; Wang, J.; Wagner, R. W.; Matteucci, M. D. Nucleosides with a Twist. Can Fixed Forms of Sugar Ring Pucker Influence Biological Activity in Nucleosides and Oligonucleotides? *J. Med. Chem.* **1996**, *39*, 3739-3747.

(160) Marquez, V. E.; Ben-Kasus, T.; Barchi, J. J.; Green, K. M.; Nicklaus, M. C.; Agbaria, R. Experimental and Structural Evidence that Herpes 1 Kinase and Cellular DNA Polymerase(s) Discriminate on the Basis of Sugar Pucker. *J. Am. Chem. Soc.* **2004**, *126*, 543-549.

(161) Liu, Z.; Pottel, J.; Shahamat, M.; Tomberg, A.; Labute, P.; Moitessier, N. Elucidating Hyperconjugation from Electronegativity to Predict Drug Conformational Energy in a High Throughput Manner. *J. Chem. Inf. Model.* **2016**, *56*, 788-801.

(162) Houseknecht, J. B.; Lowary, T. L.; Hadad, C. M. Gas-and Solution-Phase Energetics of the Methyl α-and β-d-Aldopentofuranosides. *J. Phys. Chem. A* **2003**, *107*, 5763-5777.

(163) Islam, S. M.; Richards, M. R.; Taha, H. A.; Byrns, S. C.; Lowary, T. L.; Roy, P.-N. Conformational analysis of oligoarabinofuranosides: Overcoming torsional barriers with umbrella sampling. *J. Chem. Theor. Comput.* **2011**, *7*, 2989-3000.

(164) Islam, S. M.; Roy, P.-N. Performance of the SCC-DFTB Model for Description of Five-Membered Ring Carbohydrate Conformations: Comparison to Force Fields, High-Level Electronic Structure Methods, and Experiment. *J. Chem. Theor. Comput.* **2012**, *8*, 2412-2423.

(165) Kirschner K.N.; Yongye A.B.; Tschampel S.M.; González-Outeiriño J.; Daniels C.R.; Foley B.L.; R.J., W. GLYCAM06: a generalizable biomolecular force field. Carbohydrates. *J. Comp. Chem.* **2008**, *29*, 622-655.

(166) Barnett, C. B.; Naidoo, K. J. Ring Puckering: A Metric for Evaluating the Accuracy of AM1, PM3, PM3CARB-1, and SCC-DFTB Carbohydrate QM/MM Simulations. *J. Phys. Chem. B* **2010**, *114*, 17142-17154.

(167) Huang, M.; Giese, T. J.; Lee, T.-S.; York, D. M. Improvement of DNA and RNA Sugar Pucker Profiles from Semiempirical Quantum Methods. *J. Chem. Theor. Comput.* **2014**, *10*, 1538-1545.

(168) McNamara, J. P.; Muslim, A.-M.; Abdel-Aal, H.; Wang, H.; Mohr, M.; Hillier, I. H.; Bryce, R. A. Towards a quantum mechanical force field for carbohydrates: a reparametrized semi-empirical MO approach. *Chem. Phys. Lett.* **2004**, *394*, 429-436.

(169) Elstner, M.; Porezag, D.; Jungnickel, G.; Elsner, J.; Haugk, M.; Frauenheim, T.; Suhai, S.; Seifert, G. Self-consistent-charge density-functional tight-binding method for simulations of complex materials properties. *Phys. Rev. B* **1998**, *58*.

(170) Fischl, M. A.; Richman, D. D.; Grieco, M. H.; Gottlieb, M. S.; Volberding, P. A.; Laskin, O. L.; Leedom, J. M.; Groopman, J. E.; Mildvan, D.; Schooley, R. T.; et al. The efficacy of azidothymidine (AZT) in the treatment of patients with AIDS and AIDS-related complex. A double-blind, placebo-controlled trial. *New Engl. J. Med.* **1987**, *317*, 185-191.

(171) Evdokimov, A.; Gilboa, A. J.; Koetzle, T. F.; Klooster, W. T.; Schultz, A. J.; Mason, S. A.; Albinati, A.; Frolow, F. Structures of furanosides: geometrical analysis of low-temperature X-ray and neutron crystal structures of five crystalline methyl pentofuranosides. *Acta Cryst. Sec. B* **2001**, *57*, 213-220.

(172) Evdokimov, A. G.; Martin, J. M. L.; Kalb, A. J. Structures of Furanosides: A Study of the Conformational Space of Methyl α-d-Lyxofuranoside by Density Functional Methods. *J. Phys. Chem. A* **2000**, *104*, 5291-5297.

(173) Evdokimov, A.; Gilboa, A. J.; Koetzle, T. F.; Klooster, W. T.; Martin, J. M. L. Structures of Furanosides: Density Functional Calculations and High-Resolution X-ray and Neutron Diffraction Crystal Structures. *J. Phys. Chem. A* **1999**, *103*.

(174) De Leeuw, F. A. A. M.; Altona, C. Computer-assisted pseudorotation analysis of five-membered rings by means of proton spin–spin coupling constants: Program PSEUROT. *J. Comp. Chem.* **1983**, *4*, 428-437.

(175) Yamada, K.; Wahba, A. S.; Bernatchez, J. A.; Ilina, T.; Martínez-Montero, S.; Habibian, M.; Deleavey, G. F.; Götte, M.; Parniak, M. A.; Damha, M. J. Nucleotide Sugar Pucker Preference Mitigates Excision by HIV-1 RT. *ACS Chem. Biol.* **2015**, *10*, 2024-2033.

(176) Martínez-Montero, S.; Deleavey, G. F.; Dierker-Viik, A.; Lindovska, P.; Ilina, T.; Portella, G.; Orozco, M.; Parniak, M. A.; González, C.; Damha, M. J. Synthesis and Properties of 2′-Deoxy-2′,4′-difluoroarabinose-Modified Nucleic Acids. *J. Org. Chem.* **2015**, *80*, 3083-3091.

(177) Morita, K.; Takagi, M.; Hasegawa, C.; Kaneko, M.; Tsutsumi, S.; Sone, J.; Ishikawa, T.; Imanishi, T.; Koizumi, M. Synthesis and properties of 2′-O,4′-C-Ethylene-Bridged nucleic acids (ENA) as effective antisense oligonucleotides. *Bioorg. Med. Chem.* **2003**, *11*, 2211-2226.

(178) Lipnick, R. L.; Fissekis, J. D. A comparative conformational study of certain 2'-deoxy-2'-fluoro-arabinofuranosylcytosine nucleosides. *Biochim. Biophys. Acta Nucl. Acids Prot. Synth.* **1980**, *608*, 96-102.

(179) Watts, J. K.; Sadalapure, K.; Choubdar, N.; Pinto, B. M.; Damha, M. J. Synthesis and Conformational Analysis of 2‘-Fluoro-5-methyl-4‘-thioarabinouridine (4‘S-FMAU). *J. Org. Chem.* **2006**, *71*, 921-925.

(180) Petrová, M.; Páv, O.; Buděšínský, M.; Zborníková, E.; Novák, P.; Rosenbergová, Š.; Pačes, O.; Liboska, R.; Dvořáková, I.; Šimák, O.; Rosenberg, I. Straightforward Synthesis of Purine 4′-Alkoxy-2′-deoxynucleosides: First Report of Mixed Purine–Pyrimidine 4′-Alkoxyoligodeoxynucleotides as New RNA Mimics. *Org. Lett.* **2015**, *17*, 3426-3429.

(181) Gaus, M.; Cui, Q.; Elstner, M. DFTB3: Extension of the Self-Consistent-Charge Density-Functional Tight-Binding Method (SCC-DFTB). *J. Chem. Theor. Comput.* **2011**, *7*, 931-948.

(182) Yang; Yu, H.; York, D.; Cui, Q.; Elstner, M. Extension of the Self-Consistent-Charge Density-Functional Tight-Binding Method: Third-Order Expansion of the Density Functional Theory Total Energy and Introduction of a Modified Effective Coulomb Interaction. *J. Phys. Chem. A* **2007**, *111*, 10861-10873.

(183) Watts, J. K.; Damha, M. J. 2′F-Arabinonucleic acids (2′F-ANA) — History, properties, and new frontiers. *Can. J. Chem.* **2008**, *86*, 641-656.

(184) Petraglia, R.; Corminboeuf, C. A Caveat on SCC-DFTB and Noncovalent Interactions Involving Sulfur Atoms. *J. Chem. Theor. Comput.* **2013**, *9*, 3020-3025.

(185) Klamt, A.; Schüürmann, G. COSMO: a new approach to dielectric screening in solvents with explicit expressions for the screening energy and its gradient. *J. Chem. Soc. Perkin Trans 2* **1993**, 799-805.

(186) Zhao, Y.; Truhlar, D. G. The M06 suite of density functionals for main group thermochemistry, thermochemical kinetics, noncovalent interactions, excited states, and transition elements: two new functionals and systematic testing of four M06-class functionals and 12 other functionals. *Theor. Chem. Acc.* **2008**, *120*, 215-241.

(187) Weigend, F.; Ahlrichs, R. Balanced basis sets of split valence, triple zeta valence and quadruple zeta valence quality for H to Rn: Design and assessment of accuracy. . *Phys. Chem. Chem. Phys.* **2005**, *7*, 3297-3305.

(188) Neese, F. The ORCA program system. *Wiley Interdisc. Rev. Comp. Mol. Sci.* **2012**, *2*, 73-78.

(189) Sun, G.; Voigt, J. H.; Filippov, I. V.; Marquez, V. E.; Nicklaus, M. C. PROSIT: pseudo-rotational online service and interactive tool, applied to a conformational survey of nucleosides and nucleotides. *J. Chem. Inf. Comput. Sci.* **2004**, *35*, 1752-1762.

(190) Case, D.; Darden, T.; Cheatham III, T.; Simmerling, C.; Wang, J.; Duke, R.; Luo, R.; Walker, R.; Zhang, W.; Merz, K. AMBER 12. *University of California: San Francisco* **2012**.

(191) Lindorff-Larsen, K.; Piana, S.; Palmo, K.; Maragakis, P.; Klepeis, J. L.; Dror, R. O.; Shaw, D. E. Improved side-chain torsion potentials for the Amber ff99SB protein force field. *Proteins* **2010**, *78*, 1950-1958.

(192) Jorgensen, W. L.; Chandrasekhar, J.; Madura, J. D.; Impey, R. W.; Klein, M. L. Comparison of simple potential functions for simulating liquid water. *J. Chem. Phys.* **1983**, *79*, 926-935.

(193) Adelman, S.; Doll, J. Generalized Langevin equation approach for atom/solid-surface scattering: General formulation for classical scattering off harmonic solids. *J. Chem. Phys.* **1976**, *64*, 2375-2388.

(194) Ryckaert, J.-P.; Ciccotti, G.; Berendsen, H. J. Numerical integration of the cartesian equations of motion of a system with constraints: molecular dynamics of n-alkanes. *J. Comp. Phys.* **1977**, *23*, 327-341.

(195) Darden, T.; York, D.; Pedersen, L. An N log (N) method for Ewald sums in large systems. *J. Chem. Phys.* **1993**, *98*, 10089-10092.

(196) Essmann, U.; Perera, L.; Berkowitz, M. L.; Darden, T.; Lee, H.; Pedersen, L. G. A smooth particle mesh Ewald method. *J. Chem. Phys.* **1995**, *103*, 8577-8593.

(197) Kumar, S.; Rosenberg, J. M.; Bouzida, D.; Swendsen, R. H.; Kollman, P. A. The weighted histogram analysis method for free-energy calculations on biomolecules. I. The method. *J. Comp. Chem.* **1992**, *13*, 1011-1021.

(198) Grossfield, A., WHAM: the weighted histogram analysis method, version 2.0.2. **2008.**

(199) Weinhold, F. Natural bond orbital analysis: a critical overview of relationships to alternative bonding perspectives. *J. Comp. Chem.* **2012**, *33*, 2363-2379.

(200) Glendening, E.; Badenhoop, J.; Reed, A.; Carpenter, J.; Bohmann, J.; Morales, C.; Landis, C.; Weinhold, F. Natural bond orbital analysis program: NBO 6.0. *Theoretical Chemistry Institute, University of Wisconsin, Madison, WI* **2013**.

(201) Varetto, U., Molekel 5.4. 0.8. Swiss National Supercomputing Centre, Manno, Switzerland. **2009**.

(202) Khvorova, A.; Watts, J. K. The chemical evolution of oligonucleotide therapies of clinical utility. *Nature Biotechnology* **2017**, *35*, 238-248.

(203) Hendel, A.; Bak, R. O.; Clark, J. T.; Kennedy, A. B.; Ryan, D. E.; Roy, S.; Steinfeld, I.; Lunstad, B. D.; Kaiser, R. J.; Wilkens, A. B.; Bacchetta, R.; Tsalenko, A.; Dellinger, D.; Bruhn, L.; Porteus, M. H. Chemically modified guide RNAs enhance CRISPR-Cas genome editing in human primary cells. *Nature Biotechnology* **2015**, *33*, 985-989.

(204) Plavec, J.; Tong, W.; Chattopadhyaya, J. How do the gauche and anomeric effects drive the pseudorotational equilibrium of the pentofuranose moiety of nucleosides? *Journal of the American Chemical Society* **1993**, *115*, 9734-9746.

(205) Nishizaki, T.; Iwai, S.; Ohtsuka, E.; Nakamura, H. Solution Structure of an RNA·2‘-O-Methylated RNA Hybrid Duplex Containing an RNA·DNA Hybrid Segment at the Center. *Biochemistry* **1997**, *36*, 2577-2585.

(206) Teplova, M.; Minasov, G.; Tereshko, V.; Inamati, G. B.; Cook, P. D.; Manoharan, M.; Egli, M. Crystal structure and improved antisense properties of 2'-O-(2-methoxyethyl)-RNA. *Nature Structural Biology* **1999**, *6*, 535-539.

(207) Pallan, P. S.; Greene, E. M.; Jicman, P. A.; Pandey, R. K.; Manoharan, M.; Rozners, E.; Egli, M. Unexpected origins of the enhanced pairing affinity of 2'-fluoro-modified RNA. *Nucleic acids research* **2011**, *39*, 3482-3495.

(208) Berger, I.; Tereshko, V.; Ikeda, H.; Marquez, V. E.; Egli, M. Crystal structures of B-DNA with incorporated 2'-deoxy-2'-fluoro-arabino-furanosyl thymines: implications of conformational preorganization for duplex stability. *Nucleic acids research* **1998**, *26*, 2473-2480.

(209) Erande, N.; Gunjal, A. D.; Fernandes, M.; Gonnade, R.; Kumar, V. A. Synthesis and structural studies of S-type/N-type-locked/frozen nucleoside analogues and their incorporation in RNA-selective, nuclease resistant 2′–5′ linked oligonucleotides. *Organic & Biomolecular Chemistry* **2013**, *11*, 746-757.

(210) Martínez-Montero, S.; Deleavey, G. F.; Martín-Pintado, N.; Fakhoury, J. F.; González, C.; Damha, M. J. Locked 2′-Deoxy-2′,4′-Difluororibo Modified Nucleic Acids: Thermal Stability, Structural Studies, and siRNA Activity. *ACS Chemical Biology* **2015**, *10*, 2016-2023.

(211) Alabugin, I. V.; Zeidan, T. A. Stereoelectronic Effects and General Trends in Hyperconjugative Acceptor Ability of σ Bonds. *Journal of the American Chemical Society* **2002**, *124*, 3175-3185.

(212) Burai Patrascu, M.; Malek-Adamian, E.; Damha, M. J.; Moitessier, N. Accurately Modeling the Conformational Preferences of Nucleosides. *Journal of the American Chemical Society* **2017**, *139*, 13620-13623.

(213) Thompson, H. P. G.; Day, G. M. Which conformations make stable crystal structures? Mapping crystalline molecular geometries to the conformational energy landscape. *Chemical Science* **2014**, *5*, 3173-3182.

(214) Martins, F. A.; Freitas, M. P. The Fluorine gauche Effect and a Comparison with Other Halogens in 2-Halofluoroethanes and 2-Haloethanols. *European Journal of Organic Chemistry* **2019**, *2019*, 6401-6406.

(215) Hunter, L. The C-F bond as a conformational tool in organic and biological chemistry. *Beilstein J Org Chem* **2010**, *6*, 38-38.

(216) Dunitz, J. D.; Taylor, R. Organic Fluorine Hardly Ever Accepts Hydrogen Bonds. *Chemistry – A European Journal* **1997**, *3*, 89-98.

(217) Klein, R. A. Electron Density Topological Analysis of Hydrogen Bonding in Glucopyranose and Hydrated Glucopyranose. *Journal of the American Chemical Society* **2002**, *124*, 13931-13937.

(218) Isaacs, E. D.; Shukla, A.; Platzman, P. M.; Hamann, D. R.; Barbiellini, B.; Tulk, C. A. Covalency of the Hydrogen Bond in Ice: A Direct X-Ray Measurement. *Physical Review Letters* **1999**, *82*, 600-603.

(219) Masunov, A.; Dannenberg, J. J. Theoretical Study of Urea. I. Monomers and Dimers. *The Journal of Physical Chemistry A* **1999**, *103*, 178-184.

(220) Dalvit, C.; Invernizzi, C.; Vulpetti, A. Fluorine as a Hydrogen-Bond Acceptor: Experimental Evidence and Computational Calculations. *Chemistry – A European Journal* **2014**, *20*, 11058-11068.

(221) Dalvit, C.; Piotto, M.; Vulpetti, A. Fluorine NMR spectroscopy and computational calculations for assessing intramolecular hydrogen bond involving fluorine and for characterizing the dynamic of a fluorinated molecule. *Journal of Fluorine Chemistry* **2017**, *202*, 34-40.

(222) Parsch, J.; Engels, J. W. C−F···H−C Hydrogen Bonds in Ribonucleic Acids. *Journal of the American Chemical Society* **2002**, *124*, 5664-5672.

(223) Champagne, P. A.; Descroches, J.; Paquin, J.-F. Organic Fluorine as a Hydrogen-Bond Acceptor: Recent Examples and Applications. *Synthesis* **2015**, *47*, 306-322.

(224) Anzahaee, M. Y.; Watts, J. K.; Alla, N. R.; Nicholson, A. W.; Damha, M. J. Energetically Important C−H···F−C Pseudohydrogen Bonding in Water: Evidence and

Application to Rational Design of Oligonucleotides with High Binding Affinity. *Journal of the American Chemical Society* **2011**, *133*, 728-731.

(225) Watts, J. K.; Martín-Pintado, N.; Gómez-Pinto, I.; Schwartzentruber, J.; Portella, G.; Orozco, M.; González, C.; Damha, M. J. Differential stability of 2'F-ANA*RNA and ANA*RNA hybrid duplexes: roles of structure, pseudohydrogen bonding, hydration, ion uptake and flexibility. *Nucleic acids research* **2010**, *38*, 2498-2511.

(226) Wilds, C. J.; Damha, M. J. 2′-Deoxy-2′-fluoro-β-d-arabinonucleosides and oligonucleotides (2′F-ANA): synthesis and physicochemical studies. *Nucleic Acids Research* **2000**, *28*, 3625-3635.

(227) Jenkins, I. D.; Verheyden, J. P. H.; Moffatt, J. G. 4'-Substituted nucleosides. 2. Synthesis of the nucleoside antibiotic nucleocidin. *Journal of the American Chemical Society* **1976**, *98*, 3346-3357.

(228) Dugovic, B.; Leumann, C. J. A 6′-Fluoro-Substituent in Bicyclo-DNA Increases Affinity to Complementary RNA Presumably by CF–HC Pseudohydrogen Bonds. *The Journal of Organic Chemistry* **2014**, *79*, 1271-1279.

(229) Dickerhoff, J.; Weisz, K. Nonconventional C–H···F Hydrogen Bonds Support a Tetrad Flip in Modified G-Quadruplexes. *The Journal of Physical Chemistry Letters* **2017**, *8*, 5148-5152.

(230) Gillis, E. P.; Eastman, K. J.; Hill, M. D.; Donnelly, D. J.; Meanwell, N. A. Applications of Fluorine in Medicinal Chemistry. *Journal of Medicinal Chemistry* **2015**, *58*, 8315-8359.

(231) Gore, K. R.; Harikrishna, S.; Pradeepkumar, P. I. Influence of 2′-Fluoro versus 2′-O-Methyl Substituent on the Sugar Puckering of 4′-C-Aminomethyluridine. *The Journal of Organic Chemistry* **2013**, *78*, 9956-9962.

(232) Bader, R. F. W. Definition of Molecular Structure: By Choice or by Appeal to Observation? *The Journal of Physical Chemistry A* **2010**, *114*, 7431-7444.

(233) Koch, U.; Popelier, P. L. A. Characterization of C-H-O Hydrogen Bonds on the Basis of the Charge Density. *The Journal of Physical Chemistry* **1995**, *99*, 9747-9754.

(234) Fonseca, T. A. O.; Freitas, M. P.; Cormanich, R. A.; Ramalho, T. C.; Tormena, C. F.; Rittner, R. Computational evidence for intramolecular hydrogen bonding and nonbonding X···O interactions in 2'-haloflavonols. *Beilstein J Org Chem* **2012**, *8*, 112-117.

(235) Hanwell, M. D.; Curtis, D. E.; Lonie, D. C.; Vandermeersch, T.; Zurek, E.; Hutchison, G. R. Avogadro: an advanced semantic chemical editor, visualization, and analysis platform. *Journal of Cheminformatics* **2012**, *4*, 17.

(236) Frisch, M. J.; Trucks, G. W.; Schlegel, H. B.; Scuseria, G. E.; Robb, M. A.; Cheeseman, J. R.; Scalmani, G.; Barone, V.; Petersson, G. A.; Nakatsuji, H.; Li, X.; Caricato, M.; Marenich, A. V.; Bloino, J.; Janesko, B. G.; Gomperts, R.; Mennucci, B.; Hratchian, H. P.; Ortiz, J. V.; Izmaylov, A. F.; Sonnenberg, J. L.; Williams; Ding, F.; Lipparini, F.; Egidi, F.; Goings, J.; Peng, B.; Petrone, A.; Henderson, T.; Ranasinghe, D.; Zakrzewski, V. G.; Gao, J.; Rega, N.; Zheng, G.; Liang, W.; Hada, M.; Ehara, M.; Toyota, K.; Fukuda, R.; Hasegawa, J.; Ishida, M.; Nakajima, T.; Honda, Y.; Kitao, O.; Nakai, H.; Vreven, T.; Throssell, K.; Montgomery Jr., J. A.; Peralta, J. E.; Ogliaro, F.; Bearpark, M. J.; Heyd, J. J.; Brothers, E. N.; Kudin, K. N.; Staroverov, V. N.; Keith, T. A.; Kobayashi, R.; Normand, J.; Raghavachari, K.; Rendell, A. P.; Burant, J. C.; Iyengar, S. S.; Tomasi, J.; Cossi, M.; Millam, J. M.; Klene, M.; Adamo, C.; Cammi, R.; Ochterski, J. W.; Martin, R. L.; Morokuma, K.; Farkas, O.; Foresman, J. B.; Fox, D. J.: Gaussian 16 Rev. C.01. Wallingford, CT, 2016.

(237) T. A. Keith: AIMAll (Version 17.11. 14). In *TK Gristmill Software*, 2017.

(238) Systemes, D.: Discovery Studio v.4.5. San Diego, 2018.

(239) Guengerich, F. P. Cytochrome P450 and Chemical Toxicology. *Chemical Research in Toxicology* **2008**, *21*, 70-83.

(240) Stjernschantz, E.; Vermeulen, N. P. E.; Oostenbrink, C. Computational prediction of drug binding and rationalisation of selectivity towards cytochromes P450. *Expert Opinion on Drug Metabolism & Toxicology* **2008**, *4*, 513-527.

(241) Ivanov, S. M.; Lagunin, A. A.; Poroikov, V. V. In silico assessment of adverse drug reactions and associated mechanisms. *Drug Discovery Today* **2016**, *21*, 58-71.

(242) Wong, Y. C.; Qian, S.; Zuo, Z. Regioselective biotransformation of CNS drugs and its clinical impact on adverse drug reactions. *Expert Opinion on Drug Metabolism & Toxicology* **2012**, *8*, 833-854.

(243) Kato, H. Computational prediction of cytochrome P450 inhibition and induction. *Drug Metabolism and Pharmacokinetics* **2020**, *35*, 30-44.

(244) He, S. M.; Zhou, Z. W.; Li, X. T.; Zhou, S. F. Clinical Drugs Undergoing Polymorphic Metabolism by Human Cytochrome P450 2C9 and the Implication in Drug Development. *Curr Med Chem* **2011**, *18*, 667-713.

(245) Jones, J. P.; Mysinger, M.; Korzekwa, K. R. Computational Models for Cytochrome P450: A Predictive Electronic Model for Aromatic Oxidation and Hydrogen Atom Abstraction. *Drug Metabolism and Disposition* **2002**, *30*, 7.

(246) Hennemann, M.; Friedl, A.; Lobell, M.; Keldenich, J.; Hillisch, A.; Clark, T.; Göller, A. H. CypScore: Quantitative Prediction of Reactivity toward Cytochromes P450 Based on Semiempirical Molecular Orbital Theory. *ChemMedChem* **2009**, *4*, 657-669

(247) Naven, R. T.; Louise-May, S. Computational toxicology: Its essential role in reducing drug attrition. *Human & Experimental Toxicology* **2015**, *34*, 1304-1309.

(248) Campagna-Slater, V.; Pottel, J.; Therrien, E.; Cantin, L. D.; Moitessier, N. Development of a computational tool to rival experts in the prediction of sites of metabolism of xenobiotics by p450s. *J Chem Inf Model* **2012**, *52*, 2471-2483.

(249) Lin, J. H.; Lu, A. Y. H. Inhibition and Induction of Cytochrome P450 and the Clinical Implications. *Clinical Pharmacokinetics* **1998**, *35*, 361-390.

(250) Ahlström, M. M.; Zamora, I. Characterization of Type II Ligands in CYP2C9 and CYP3A4. *Journal of Medicinal Chemistry* **2008**, *51*, 1755-1763.

(251) Orlando, R.; Piccoli, P.; De Martin, S.; Padrini, R.; Palatini, P. Effect of the CYP3A4 inhibitor erythromycin on the pharmacokinetics of lignocaine and its pharmacologically active metabolites in subjects with normal and impaired liver function. *Br J Clin Pharmacol* **2003**, *55*, 86-93.

(252) Takakusa, H.; Wahlin, M. D.; Zhao, C.; Hanson, K. L.; New, L. S.; Chan, E. C. Y.; Nelson, S. D. Metabolic intermediate complex formation of human cytochrome P450 3A4 by lapatinib. *Drug Metab Dispos* **2011**, *39*, 1022-1030.

(253) Ortiz de Montellano, P. R.: Cytochrome P450 : structure, mechanism, and biochemistry. 4th edition. ed.; Springer: Cham, 2015.

(254) Vitaku, E.; Smith, D. T.; Njardarson, J. T. Analysis of the Structural Diversity, Substitution Patterns, and Frequency of Nitrogen Heterocycles among U.S. FDA Approved Pharmaceuticals. *Journal of Medicinal Chemistry* **2014**, *57*, 10257-10274.

(255) Rostkowski, M.; Spjuth, O.; Rydberg, P. WhichCyp: prediction of cytochromes P450 inhibition. *Bioinformatics* **2013**, *29*, 2051-2052.

(256) Terfloth, L.; Bienfait, B.; Gasteiger, J. Ligand-Based Models for the Isoform Specificity of Cytochrome P450 3A4, 2D6, and 2C9 Substrates. *Journal of Chemical Information and Modeling* **2007**, *47*, 1688-1701.

(257) Röhrig, U. F.; Grosdidier, A.; Zoete, V.; Michielin, O. Docking to heme proteins. *Journal of Computational Chemistry* **2009**, *30*, 2305-2315.

(258) Rydberg, P.; Olsen, L. The Accuracy of Geometries for Iron Porphyrin Complexes from Density Functional Theory. *The Journal of Physical Chemistry A* **2009**, *113*, 11949-11953.

(259) Pottel, J.; Therrien, E.; Gleason, J. L.; Moitessier, N. Docking Ligands into Flexible and Solvated Macromolecules. 6. Development and Application to the Docking of HDACs and other Zinc Metalloenzymes Inhibitors. *Journal of Chemical Information and Modeling* **2014**, *54*, 254-265.

(260) Cali, J. J.; Ma, D.; Sobol, M.; Simpson, D. J.; Frackman, S.; Good, T. D.; Daily, W. J.; Liu, D. Luminogenic cytochrome P450 assays. *Expert Opinion on Drug Metabolism & Toxicology* **2006**, *2*, 629-645.

(261) Serenella, Z.; Stefano, F.; Mahmud, K. Evaluation of Cytochrome P450 Inhibition Assays Using Human Liver Microsomes by a Cassette Analysis /LC-MS/MS. *Drug Metabolism Letters* **2010**, *4*, 120-128.

(262) NCATS: Cytochrome panel assay with activity outcomes. NCBI, Ed.: PubChem, 2009.

(263) Gasteiger, J.; Zupan, J. Neural Networks in Chemistry. *Angewandte Chemie International Edition in English* **1993**, *32*, 503-527.

(264) Rumelhart, D. E.; Hinton, G. E.; Williams, R. J. Learning representations by back-propagating errors. *Nature* **1986**, *323*, 533-536.

(265) Englebienne, P.; Moitessier, N. Docking Ligands into Flexible and Solvated Macromolecules. 4. Are Popular Scoring Functions Accurate for this Class of Proteins? *Journal of Chemical Information and Modeling* **2009**, *49*, 1568-1580.

(266) Englebienne, P.; Moitessier, N. Docking Ligands into Flexible and Solvated Macromolecules. 5. Force-Field-Based Prediction of Binding Affinities of Ligands to Proteins. *Journal of Chemical Information and Modeling* **2009**, *49*, 2564-2571.

(267) Sun, H.; Veith, H.; Xia, M.; Austin, C. P.; Huang, R. Predictive Models for Cytochrome P450 Isozymes Based on Quantitative High Throughput Screening Data. *Journal of Chemical Information and Modeling* **2011**, *51*, 2474-2481.

(268) Cheng, F.; Yu, Y.; Shen, J.; Yang, L.; Li, W.; Liu, G.; Lee, P. W.; Tang, Y. Classification of Cytochrome P450 Inhibitors and Noninhibitors Using Combined Classifiers. *Journal of Chemical Information and Modeling* **2011**, *51*, 996-1011.

(269) Li, X.; Xu, Y.; Lai, L.; Pei, J. Prediction of Human Cytochrome P450 Inhibition Using a Multitask Deep Autoencoder Neural Network. *Molecular Pharmaceutics* **2018**, *15*, 4336-4345.

(270) Gomez-Jeria, J. S. A New Set of Local Reactivity Indices within the Hartree-Fock-Roothaan and Density Functional Theory Frameworks. *Canadian Chemical Transactions* **2013**, *1*, 25-55.

(271) Tomberg, A. Towards Virtual Biocatalysis: Computational Methods Development for Organometallic Catalysts and Enzyme Engineering. McGill University, 2017.

(272) Contreras, R. R.; Fuentealba, P.; Galván, M.; Pérez, P. A direct evaluation of regional Fukui functions in molecules. *Chemical Physics Letters* **1999**, *304*, 405-413.

(273) Pino-Rios, R.; Yañez, O.; Inostroza, D.; Ruiz, L.; Cardenas, C.; Fuentealba, P.; Tiznado, W. Proposal of a simple and effective local reactivity descriptor through a topological analysis of an orbital-weighted fukui function. *Journal of Computational Chemistry* **2017**, *38*, 481-488.

(274) Olsen, L.; Montefiori, M.; Tran, K. P.; Jørgensen, F. S. SMARTCyp 3.0: enhanced cytochrome P450 site-of-metabolism prediction server. *Bioinformatics* **2019**.

(275) Mardirossian, N.; Head-Gordon, M. Thirty years of density functional theory in computational chemistry: an overview and extensive assessment of 200 density functionals. *Molecular Physics* **2017**, *115*, 2315-2372.

(276) Olsen, L.; Rydberg, P.; Rod, T. H.; Ryde, U. Prediction of Activation Energies for Hydrogen Abstraction by Cytochrome P450. *Journal of Medicinal Chemistry* **2006**, *49*, 6489-6499.

(277) Shrake, A.; Rupley, J. A. Environment and exposure to solvent of protein atoms. Lysozyme and insulin. *Journal of Molecular Biology* **1973**, *79*, 351-371.

(278) Wang, A.; Chen, Y.; Walter, E. D.; Washton, N. M.; Mei, D.; Varga, T.; Wang, Y.; Szanyi, J.; Wang, Y.; Peden, C. H. F.; Gao, F. Unraveling the mysterious failure of Cu/SAPO-34 selective catalytic reduction catalysts. *Nat. Commun.* **2019**, *10*, 1137.

(279) Wang, X.-G.; Li, Y.; Liu, H.-C.; Zhang, B.-S.; Gou, X.-Y.; Wang, Q.; Ma, J.-w.; Liang, Y.-M. Three-Component Ruthenium-Catalyzed Direct meta-Selective C-H Activation of Arenes: A New Approach to The Alkylarylation of Alkenes. *J. Am. Chem. Soc.* **2019**.

(280) Meucci, E. A.; Nguyen, S. N.; Camasso, N. M.; Chong, E.; Ariafard, A.; Canty, A. J.; Sanford, M. S. Nickel(IV)-Catalyzed C–H Trifluoromethylation of (Hetero)arenes. *J. Am. Chem. Soc.* **2019**, *141*, 12872-12879.

(281) Borhani, D. W.; Shaw, D. E. The future of molecular dynamics simulations in drug discovery. *J Comput Aid Mol Des* **2012**, *26*, 15-26.

(282) Liu, X.; Shi, D.; Zhou, S.; Liu, H.; Liu, H.; Yao, X. Molecular dynamics simulations and novel drug discovery. *Expert Opinion on Drug Discovery* **2018**, *13*, 23-37.

(283) Wang, G.; Zhu, W. Molecular docking for drug discovery and development: a widely used approach but far from perfect. *Future Medicinal Chemistry* **2016**, *8*, 1707-1710.

(284) Santosh, A. K.; Alpeshkumar, K. M.; Evans, C. C.; Sudha, S. Pharmacophore Modeling in Drug Discovery and Development: An Overview. *Medicinal Chemistry* **2007**, *3*, 187-197.

(285) Sanderson, K. Automation: Chemistry shoots for the Moon. *Nature* **2019**, *568*, 577-579.

(286) Segler, M. H. S.; Preuss, M.; Waller, M. P. Planning chemical syntheses with deep neural networks and symbolic AI. *Nature* **2018**, *555*, 604.

(287) Zheng, S.; Rao, J.; Zhang, Z.; Xu, J.; Yang, Y. Predicting Retrosynthetic Reaction using Self-Corrected Transformer Neural Networks. *chemRxiv* **2019**, *preprint*.

(288) Marques-Lopez, E.; Herrera, R. P.; Christmann, M. Asymmetric organocatalysis in total synthesis--a trial by fire. *Nat Prod Rep* **2010**, *27*, 1138-1167.

(289) Maldonado, A. G.; Rothenberg, G. Predictive modeling in homogeneous catalysis: a tutorial. *Chem Soc Rev* **2010**, *39*, 1891-1902.

(290) Brown, J. M.; Deeth, R. J. Is enantioselectivity predictable in asymmetric catalysis. *Angewandte Chemie - International Edition* **2009**, *48*, 4476-4479.

(291) Harper, K. C.; Sigman, M. S. Predicting and optimizing asymmetric catalyst performance using the principles of experimental design and steric parameters. *Proc. Natl. Acad. Sci. USA* **2011**, *108*, 2179-2183.

(292) Reid, J. P.; Sigman, M. S. Holistic prediction of enantioselectivity in asymmetric catalysis. *Nature* **2019**, *571*, 343-348.

(293) Norrby, P. O. Holistic models of reaction selectivity. *Nature* **2019**, *571*, 332-333.

(294) Beker, W.; Gajewska, E. P.; Badowski, T.; Grzybowski, B. A. Prediction of Major Regio-, Site-, and Diastereoisomers in Diels–Alder Reactions by Using Machine-Learning: The Importance of Physically Meaningful Descriptors. *Angew. Chem. Int. Ed.* **2019**, *58*, 4515-4519.

(295) Zahrt, A. F.; Henle, J. J.; Rose, B. T.; Wang, Y.; Darrow, W. T.; Denmark, S. E. Prediction of higher-selectivity catalysts by computer-driven workflow and machine learning. *Science* **2019**, *363*, eaau5631.

(296) Reid, J. P.; Sigman, M. S. Comparing quantitative prediction methods for the discovery of small-molecule chiral catalysts. *Nature Reviews Chemistry* **2018**, *2*, 290-305.

(297) Bahmanyar, S.; Houk, K. N. The origin of stereoselectivity in proline-catalyzed intramolecular aldol reactions. *Journal of the American Chemical Society* **2001**, *123*, 12911-12912 Aldol Reaction

Proline.

(298) Gordillo, R.; Houk, K. N. Origins of stereoselectivity in Diels-Alder cycloadditions catalyzed by chiral imidazolidinones. *Journal of the American Chemical Society* **2006**, *128*, 3543-3553.

(299) Ford, D. D.; Nielsen, L. P. C.; Zuend, S. J.; Musgrave, C. B.; Jacobsen, E. N. Mechanistic Basis for High Stereoselectivity and Broad Substrate Scope in the (salen)Co(III)-Catalyzed Hydrolytic Kinetic Resolution. *J. Am. Chem. Soc.* **2013**, *135*, 15595-15608.

(300) Lin, H.; Pei, W.; Wang, H.; Houk, K. N.; Krauss, I. J. Enantioselective Homocrotylboration of Aliphatic Aldehydes. *J. Am. Chem. Soc.* **2013**, *135*, 82-85.

(301) Lam, Y.-h.; Houk, K. N. How Cinchona Alkaloid-Derived Primary Amines Control Asymmetric Electrophilic Fluorination of Cyclic Ketones. *J. Am. Chem. Soc.* **2014**, *136*, 9556-9559.

(302) Lam, Y.-h.; Houk, K. N. Origins of Stereoselectivity in Intramolecular Aldol Reactions Catalyzed by Cinchona Amines. *J. Am. Chem. Soc.* **2015**, *137*, 2116-2127.

(303) Wolf, L. M.; Denmark, S. E. A Theoretical Investigation on the Mechanism and Stereochemical Course of the Addition of (E)-2-Butenyltrimethylsilane to Acetaldehyde by Electrophilic and Nucleophilic Activation. *J. Am. Chem. Soc.* **2013**, *135*, 4743-4756.

(304) Weill, N.; Corbeil, C. R.; De Schutter, J. W.; Moitessier, N. Toward a computational tool predicting the stereochemical outcome of asymmetric reactions: Development of the molecular mechanics-based program ACE and application to asymmetric epoxidation reactions. *Journal of Computational Chemistry* **2011**, *32*, 2878-2889.

(305) Schneebeli, S. T.; Hall, M. L.; Breslow, R.; Friesner, R. A. Quantitative DFT Modeling of the Enantiomeric Excess for Dioxirane-Catalyzed Epoxidations. *J. Am. Chem. Soc.* **2009**, *131*, 3965-3973

(306) Pottel, J.; Moitessier, N. Customizable Generation of Synthetically Accessible, Local Chemical Subspaces. *J. Chem. Inf. Model.* **2017**, *57*, 454-467.

(307) van Hilten, N.; Chevillard, F.; Kolb, P. Virtual Compound Libraries in Computer-Assisted Drug Discovery. *J. Chem. Inf. Model.* **2019**, *59*, 644-651.

(308) Rasmussen, T.; Norrby, P. O. Modeling the stereoselectivity of the beta-amino alcohol-promoted addition of dialkylzinc to aldehydes. *J. Am. Chem. Soc.* **2003**, *125*, 5130-5138

(309) Norrby, P. O.; Rasmussen, T.; Haller, J.; Strassner, T.; Houk, K. N. Rationalizing the stereoselectivity of osmium tetroxide asymmetric dihydroxylations with transition state modeling using quantum mechanics- guided molecular mechanics. *J. Am. Chem. Soc.* **1999**, *121*, 10186-10192

(310) Donoghue, P. J.; Helquist, P.; Norrby, P.-O.; Wiest, O. Prediction of Enantioselectivity in Rhodium Catalyzed Hydrogenations. *J. Am. Chem. Soc.* **2009**, *131*, 410-411

(311) Pritchard, B. P.; Altarawy, D.; Didier, B.; Gibson, T. D.; Windus, T. L. New Basis Set Exchange: An Open, Up-to-Date Resource for the Molecular Sciences Community. *Journal of Chemical Information and Modeling* **2019**, *59*, 4814-4820.

(312) Guennebaud, G.; Jacob, B.; others. Eigen v3. **2010**.

(313) Valeev, E. F. Libint: A library for the evaluation of molecular integrals of many-body operators over Gaussian functions. *http://libint.valeyev.net/* **2019**, *version 2.5.0-beta.2*.

(314) Marques, M. A. L.; Oliveira, M. J. T.; Burnus, T. Libxc: A library of exchange and correlation functionals for density functional theory. *Computer Physics Communications* **2012**, *183*, 2272-2281.

(315) Seminario, J. M. Calculation of intramolecular force fields from second-derivative tensors. *International Journal of Quantum Chemistry* **1996**, *60*, 1271-1277.

(316) Allen, A. E. A.; Payne, M. C.; Cole, D. J. Harmonic Force Constants for Molecular Mechanics Force Fields via Hessian Matrix Projection. *Journal of Chemical Theory and Computation* **2018**, *14*, 274-281.

(317) Tiznado, W.; Chamorro, E.; Contreras, R.; Fuentealba, P. Comparison among Four Different Ways to Condense the Fukui Function. *The Journal of Physical Chemistry A* **2005**, *109*, 3220-3224.

(318) Chattaraj, P. K.; Maiti, B.; Sarkar, U. Philicity: A Unified Treatment of Chemical Reactivity and Selectivity. *The Journal of Physical Chemistry A* **2003**, *107*, 4973-4975.

(319) Harvey, J. N.; Himo, F.; Maseras, F.; Perrin, L. Scope and Challenge of Computational Methods for Studying Mechanism and Reactivity in Homogeneous Catalysis. *ACS Cat.* **2019**, *9*, 6803-6813.

(320) Yang, X.; Shen, J.; Da, C.; Wang, R.; Choi, M. C. K.; Yang, L.; Wong, K.-y. Chiral pyrrolidine derivatives as catalysts in the enantioselective addition of diethylzinc to aldehydes. *Tetrahedron Asym.* **1999**, *10*, 133-138.

(321) Liang, G.; Bays, J. P.; Bowen, J. P. Ab initio calculations and molecular mechanics (MM3) force field development for sulfonamide and its alkyl derivatives. *J. Mol. Struct. THEOCHEM* **1997**, *401*, 165-179.

(322) Immirzi, A.; Musco, A. A method to measure the size of phosphorus ligands in coordination complexes. *Inorg. Chim. Acta* **1977**, *25*, L41-L42.

(323) Sterling, T.; Irwin, J. J. ZINC 15 – Ligand Discovery for Everyone. *J. Chem. Inf. Model.* **2015**, *55*, 2324-2337.

(324) Hall, H. K. Correlation of the Base Strengths of Amines. *J. Am. Chem. Soc.* **1957**, *79*, 5441-5444.

(325) Gerosa, G. G.; Spanevello, R. A.; Suárez, A. G.; Sarotti, A. M. Joint Experimental, in Silico, and NMR Studies toward the Rational Design of Iminium-Based Organocatalyst Derived from Renewable Sources. *J. Org. Chem.* **2015**, *80*, 7626-7634.

(326) Evans, D. A.; Chapman, K. T.; Bisaha, J. Asymmetric Diels-Alder cycloaddition reactions with chiral .alpha.,.beta.-unsaturated N-acyloxazolidinones. *J. Am. Chem. Soc.1* **1988**, *110*, 1238-1256

(327) Corey, E. J.; Cheng, X.-M.; Cimprich, K. A. 1-Mesityl-2,2,2-trifluoroethanol, an outstanding new chiral controller for catalyzed diels-alder reactions. *Tetrahedron Lett.1* **1991**, *32*, 6839-6842

(328) Oppolzer, W.; Kurth, M.; Reichlin, D.; Moffatt, F. A reinvestigation of asymmetric induction in diels-alder reactions to chiral acrylates. *Tetrahedron Lett.* **1981**, *22*, 2545-2548

(329) Banks, M. R.; Blake, A. J.; Cadogan, J. I. G.; Dawson, I. M.; Gosney, I.; Grant, K. J.; Gaur, S.; Hodgson, P. K. G.; Knight, K. S.; Smith, G. W.; Stevenson, D. E. Enantiospecific preparation of [(2,6)-endo]-5-aza-1,10,10-trimethyl-3-oxatricyclo[5.2.1.02,6]decan-4-one by a nitrene-mediated route from [(1)-endo]-(-)-borneol and its utility as a chiral auxiliary in some asymmetric transformations. *Tetrahedron* **1992**, *48*, 7979-8006

(330) Banks, M. R.; Blake, A. J.; Brown, A. R.; Cadogan, J. I. G.; Gaur, S.; Gosney, I.; Hodgson, P. K. G.; Thorburn, P. Exploiting steric shielding: Tuning terpenoid-derived oxazolidin-2-ones as chiral auxiliaries for the Diels-Alder reaction. *Tetrahedron Lett.* **1994**, *35*, 489-492

(331) Banks, M. R.; Blake, A. J.; Cadogan, J. I. G.; Doyle, A. A.; Gosney, I.; Hodgson, P. K. G.; Thorburn, P. Asymmetric Diels-Alder reactions employing modified camphor-derived oxazolidin-2-one chiral auxiliaries. *Tetrahedron* **1996**, *52*, 4079-4094

(332) Banks, M. R.; Cadogan, J. I. G.; Gosney, I.; Gaur, S.; Hodgson, P. K. G. Highly regio- and stereo-specific preparation of a new carbohydrate-based 1,3-oxazin-2-one by the INIR method and its applications in some asymmetric transformations. *Tetrahedron Asym.* **1994**, *5*, 2447-2458

(333) Banks, M. R.; Blake, A. J.; Cadogan, J. I. G.; Dawson, I. M.; Gaur, S.; Gosney, I.; Gould, R. O.; Grant, K. J.; Hodgson, P. K. G. (5R)-7,8:9,10-Di-O-isopropylidene-2,6-dioxa-4-azaspiro[4,5]decan-3-one: A new chiral spirooxazolidin-2-one derived from D-(+)-galactose for use in asymmetric transformations. *J. Chem. Soc. Chem. Commun.* **1993**, 1146-1148

(334) Banks, M. R.; Cadogan, J. I. G.; Gosney, I.; Gould, R. O.; Hodgson, P. K. G.; McDougall, D. Preparation of enantiomerically pure fructose-derived 1,3-oxazin-2-one by INIR methodology and its application as a chiral auxiliary in some model asymmetric reactions. *Tetrahedron* **1998**, *54*, 9765-9784

(335) Matsunaga, H.; Kimura, K.; lshizuka, T.; Haratake, M.; Kunleda, T. Conformationally rigid chiral [4+2]cycloadduct-based 2-oxazolidinones as new auxiliairies. *Tetrahedron Lett.* **1991**, *32*, 7715-7718.

(336) Armstrong, A.; Ahmed, G.; Dominguez-Fernandez, B.; Hayter, B. R.; Wailes, J. S. Enantioselective Epoxidation of Alkenes Catalyzed by 2-Fluoro-N-Carbethoxytropinone and Related Tropinone Derivatives. *J. Org. Chem.* **2002**, *67*, 8610-8617

(337) Armstrong, A.; Hayter, B. R.; Moss, W. O.; Reeves, J. R.; Wailes, J. S. Alkene epoxidation catalyzed by bicyclo[3.2.1]octan-3-ones: effects of structural modifications on catalyst efficiency and epoxidation enantioselectivity. *Tetrahedron Asym.* **2000**, *11*, 2057-2061

(338) Armstrong, A.; Dominguez-Fernandez, B.; Tsuchiya, T. Bicyclo[3.2.1]octanone catalysts for asymmetric alkene epoxidation: the effect of disubstitution. *Tetrahedron* **2006**, *62*, 6614-6620.

(339) Armstrong, A.; Moss, W. O.; Reeves, J. R. Asymmetric epoxidation catalyzed by esters of [alpha]-hydroxy-8-oxabicyclo[3.2.1]octan-3-one. *Tetrahedron Asym.* **2001**, *12*, 2779-2781

(340) Solladié-Cavallo, A.; Jierry, L.; Klein, A.; Schmitt, M.; Welter, R. [alpha]-Fluoro decalones as chiral epoxidation catalysts: fluorine effect. *Tetrahedron Asym.* **2004**, *15*, 3891-3898

(341) Denmark, S. E.; Matsuhashi, H. Chiral Fluoro Ketones for Catalytic Asymmetric Epoxidation of Alkenes with Oxone. *J. Org. Chem.* **2002**, *67*, 3479-3486

(342) Armstrong, A.; Tsuchiya, T. A new class of chiral tetrahydropyran-4-one catalyst for asymmetric epoxidation of alkenes. *Tetrahedron* **2006**, *62*, 257-263.

(343) Burke, C. P.; Shi, Y. Regio- and Enantioselective Epoxidation of Dienes by a Chiral Dioxirane: Synthesis of Optically Active Vinyl cis-Epoxides. *Angew. Chem. Int. Ed.* **2006**, *45*, 4475-4478

(344) Wang, Z. X.; Tu, Y.; Frohn, M.; Zhang, J. R.; Shi, Y. An Efficient Catalytic Asymmetric Epoxidation Method. *J. Am. Chem. Soc.* **1997**, *119*, 11224-11235

(345) Tu, Y.; Wang, Z.-X.; Shi, Y. An Efficient Asymmetric Epoxidation Method for trans-Olefins Mediated by a Fructose-Derived Ketone. *J. Am. Chem. Soc.* **1996**, *118*, 9806-9807.

(346) Wang, Z. X.; Miller, S. M.; Anderson, O. P.; Shi, Y. Asymmetric Epoxidation by Chiral Ketones Derived from Carbocyclic Analogues of Fructose. *J. Org. Chem.* **2001**, *66*, 521-530

(347) Hartikka, A.; Hojabri, L.; Bose, P. P.; Arvidsson, P. I. Synthesis and application of novel imidazole and 1H-tetrazolic acid containing catalysts in enantioselective organocatalyzed Diels-Alder reactions. *Tetrahedron Asym.* **2009**, *20*, 1871-1876.

(348) Ahrendt, K. A.; Borths, C. J.; MacMillan, D. W. C. New strategies for organic catalysis: The first highly enantioselective organocatalytic diels - Alder reaction [16]. *J. Am. Chem. Soc.* **2000**, *122*, 4243-4244.

(349) Gotoh, H.; Hayashi, Y. Diarylprolinol silyl ether as catalyst of an exo-selective, enantioselective diels-alder reaction. *Org. Lett.* **2007**, *9*, 2859-2862.

(350) Bonini, B. F.; Capitò, E.; Comes-Franchini, M.; Fochi, M.; Ricci, A.; Zwanenburg, B. Aziridin-2-yl methanols as organocatalysts in Diels-Alder reactions and Friedel-Crafts alkylations of N-methyl-pyrrole and N-methyl-indole. *Tetrahedron Asym.* **2006**, *17*, 3135-3143.

(351) He, H.; Pei, B. J.; Chou, H. H.; Tian, T.; Chan, W. H.; Lee, A. W. M. Camphor sulfonyl hydrazines (CaSH) as organocatalysts in enantioselective Diels-Alder reactions. *Org. Lett.* **2008**, *10*, 2421-2424.

(352) Lemay, M.; Ogilvie, W. W. Aqueous enantioselective organocatalytic Diels-Alder reactions employing hydrazide catalysts. A new scaffold for organic acceleration. *Org. Lett.* **2005**, *7*, 4141-4144.

(353) Kano, T.; Tanaka, Y.; Maruoka, K. exo-selective asymmetric Diels-Alder reaction catalyzed by diamine salts as organocatalysts. *Org. Lett.* **2006**, *8*, 2687-2689.

(354) Shi, L. X.; Sun, Q.; Ge, Z. M.; Zhu, Y. Q.; Cheng, T. M.; Li, R. T. Dipeptide-catalyzed direct asymmetric aldol reaction. *Synlett* **2004**, 2215-2217

(355) List, B.; Lerner, R. A.; Barbas III, C. F. Proline-catalyzed direct asymmetric aldol reactions [13]. *J. Am. Chem. Soc.* **2000**, *122*, 2395-2396.

(356) Sakthivel, K.; Notz, W.; Bui, T.; Barbas III, C. F. Amino acid catalyzed direct asymmetric aldol reactions: A bioorganic approach to catalytic asymmetric carbon-carbon bond-forming reactions. *J. Am. Chem. Soc.* **2001**, *123*, 5260-5267.

(357) Wagner, M.; Contie, Y.; Ferroud, C.; Revial, G. Enantioselective Aldol Reactions and Michael Additions Using Proline Derivatives as Organocatalysts. *Int. J. Org. Chem.* **2014**, *4*, 55-67.

(358) Cobb, A. J. A.; Shaw, D. M.; Longbottom, D. A.; Gold, J. B.; Ley, S. V. Organocatalysis with proline derivatives: Improved catalysts for the asymmetric Mannich, nitro-Michael and aldol reactions. *Org. Biomol. Chem.* **2005**, *3*, 84-96.

(359) Gryko, D.; Lipiński, R. L-prolinethioamides - Efficient organocatalysts for the direct asymmetric aldol reaction. *Adv. Synth. Cat.* **2005**, *347*, 1948-1952.

(360) Tang, Z.; Jiang, F.; Cui, X.; Gong, L. Z.; Mi, A. Q.; Jiang, Y. Z.; Wu, Y. D. Enantioselective direct aldol reactions catalyzed by L-prolinamide derivatives. *Proc. Natl Acad. Sci. USA* **2004**, *101*, 5755-5760.

(361) Gryko, D.; Chromiński, M.; Pielacińska, D. J. Prolinethioamides versus Prolinamides in Organocatalyzed Aldol Reactions—A Comparative Study. *Symmetry* **2011**, *3*, 265-282.

(362) Tang, Z.; Jiang, F.; Yu, L. T.; Cui, X.; Gong, L. Z.; Mi, A. Q.; Jiang, Y. Z.; Wu, Y. D. Novel small organic molecules for a highly enantioselective direct aldol reaction. *J. Am. Chem. Soc.* **2003**, *125*, 5262-5263

(363) Tang, Z.; Yang, Z. H.; Chen, X. H.; Cun, L. F.; Mi, A. Q.; Jiang, Y. Z.; Gong, L. Z. A highly efficient organocatalyst for direct Aldol reactions of ketones with aldedydes. *J. Am. Chem. Soc.* **2005**, *127*, 9285-9289

(364) Wang, B.; Liu, X. W.; Liu, L. Y.; Chang, W. X.; Li, J. Highly efficient direct asymmetric aldol reactions catalyzed by a prolinethioamide derivative in aqueous media. *Eur. J. Org. Chem.* **2010**, 5951-5954.

(365) Becker, H.; King, S. B.; Taniguchi, M.; Vanhessche, K. P. M.; Sharpless, K. B. New ligands and improved enantioselectivities for the asymmetric dihydroxylation of olefins. *J. Org. Chem.* **1995**, *60*, 3940-3941

(366) Crispino, G. A.; Makita, A.; Wang, Z. M.; Sharpless, K. B. A comparison of ligands proposed for the asymmetric dihydroxylation. *Tetrahedron Lett.* **1994**, *35*, 543-546

(367) Corey, E. J.; Noe, M. C.; Grogan, M. J. A mechanistically designed mono-cinchona alkaloid is an excellent catalyst for the enantioselective dihydroxylation of olefins. *Tetrahedron Lett.* **1994**, *35*, 6427-6430

(368) Sharpless, K. B.; Amberg, W.; Beller, M.; Chen, H.; Hartung, J.; Kawanami, Y.; Labben, D.; Manoury, E.; Ogino, Y.; Shibata, T.; Ukita, T. New ligands double the scope of the catalytic asymmetric dihydroxylation of olefins. *J. Org. Chem.* **1991**, *56*, 4585-4588

(369) Jacobsen, E. N.; Marko, I.; Mungall, W. S.; Schroder, G.; Sharpless, K. B. Asymmetric Dihydroxylation via Ligand-Accelerated Catalysis. *J. Am. Chem. Soc.* **1988**, *110*, 1968-1970.

(370) Huang, J.; Corey, E. J. A Mechanistically Guided Design Leads to the Synthesis of an Efficient and Practical New Reagent for the Highly Enantioselective, Catalytic Dihydroxylation of Olefins. *Org. Lett.* **2003**, *5*, 3455-3458

(371) Oishi, T.; Hirama, M. Synthesis of chiral 2,3-disubstituted 1,4-diazabicyclo[2.2.2]octane. New ligand for the osmium-catalyzed asymmetric dihydroxylation of olefins. *Tetrahedron Lett.* **1992**, *33*, 639-642.

(372) Becker, H.; Barry Sharpless, K. A New Ligand Class for the Asymmetric Dihydroxylation of Olefins. *Angew. Chem. Int. Ed.* **1996**, *35*, 448-451

(373) Sharpless, K. B.; Amberg, W.; Bennani, Y. L.; Crispino, G. A.; Hartung, J.; Jeong, K. S.; Kwong, H. L.; Morikawa, K.; Wang, Z. M.; Xu, D.; Zhang, X. L. The osmium-catalyzed asymmetric dihydroxylation: A new Ligand class and a process improvement. *J. Org. Chem.* **1992**, *57*, 2768-2771

(374) Wang, Z. M.; Kakiuchi, K.; Sharpless, K. B. Osmium-catalyzed asymmetric dihydroxylation of cyclic cis-disubstituted olefins. *J. Org. Chem.* **1994**, *59*, 6895-6897

(375) Soai, K.; Yokoyama, S.; Ebihara, K.; Hayasaka, T. A new chiral catalyst for the highly enantioselective addition of dialkylzinc reagents to aliphatic aldehydes. *J. Chem. Soc. Chem. Commun.* **1987**, 1690-1691.

(376) Ohga, T.; Umeda, S.; Kawanami, Y. Enantioselective addition of diethylzinc to aldehydes catalyzed by chiral amino alcohols. Substituent effect and nonlinear effect. *Tetrahedron* **2001**, *57*, 4825-4829.

(377) Kawanami, Y.; Mitsuie, T.; Miki, M.; Sakamoto, T.; Nishitani, K. New Chiral Ligands Derived from (S)-Leucine for the Enantioselective Addition of Diethylzinc to Aldehydes. *Tetrahedron* **2000**, *56*, 175-178.

(378) Kitamura, M.; Suga, S.; Kawai, K.; Noyori, R. Catalytic asymmetric induction. Highly enantioselective addition of dialkylzincs to aldehydes. *J. Am. Chem. Soc.* **1986**, *108*, 6071-6072.

(379) Guijarro, D.; Pinho, P.; Andersson, P. G. Enantioselective Addition of Dialkylzinc Reagents to N-(Diphenylphosphinoyl) Imines Promoted by 2-Azanorbornylmethanols. *J. Org. Chem.* **1998**, *63*, 2530-2535.

(380) Wassmann, S.; Wilken, J.; Martens, J. Synthesis and application of C2-symmetrical bis-β-amino alcohols based on the octahydro-cyclopenta[b]pyrrole system in the catalytic enantioselective addition of diethylzinc to benzaldehyde. *Tetrahedron Asym.* **1999**, *10*, 4437-4445.

(381) Lawrence, C. F.; Nayak, S. K.; Thijs, L.; Zwanenburg, B. N-Trityl-Aziridinyl(diphenyl)methanol as an Effective Catalyst in the Enantioselective Addition of Diethylzinc to Aldehydes. *Synlett* **1999**, *10*, 1571-1572.

(382) Binder, C. M.; Bautista, A.; Zaidlewicz, M.; Krzemiński, M. P.; Oliver, A.; Singaram, B. Dual Stereoselectivity in the Dialkylzinc Reaction Using (−)-β-Pinene Derived Amino Alcohol Chiral Auxiliaries. *J. Org. Chem.* **2009**, *74*, 2337-2343.

(383) Steiner, D.; Sethofer, S. G.; Goralski, C. T.; Singaram, B. Asymmetric addition of diethylzinc to aldehydes catalyzed by β-amino alcohols derived from limonene oxide. *Tetrahedron Asym.* **2002**, *13*, 1477-1483.

(384) Dai, W.-M.; Zhu, H.-J.; Hao, X.-J. Chiral ligands derived from abrine. Part 6: Importance of a bulky N-alkyl group in indole-containing chiral β-tertiary amino alcohols for controlling enantioselectivity in addition of diethylzinc toward aldehydes. *Tetrahedron Asym.* **2000**, *11*, 2315-2337.

(385) Joshi, S. N.; Malhotra, S. V. Enantioselective addition of diethylzinc to aldehydes catalyzed by a β-amino alcohol derived from (+)-3-carene. *Tetrahedron Asym.* **2003**, *14*, 1763-1766.

(386) Sibi, M. P.; Chen, J.-x.; Cook, G. R. Reversal of stereochemistry in diethylzinc addition to aldehydes by a simple change of the backbone substituent in L-serine derived ligands. *Tetrahedron Lett.* **1999**, *40*, 3301-3304.

(387) Shi, M.; Satoh, Y.; Masaki, Y. Chiral C2-symmetric 2,5-disubstituted pyrrolidine derivatives as catalytic chiral ligands in the reactions of diethylzinc with aryl aldehydes. *J. Chem. Soc. Perkin Trans 1* **1998**, 2547-2552.

(388) Kossenjans, M.; Soeberdt, M.; Wallbaum, S.; Harms, K.; Martens, J.; Gunter Aurich, H. Utilization of industrial waste materials. Part 14.[dagger] Synthesis of [small beta]-amino alcohols and thiols with a 2-azabicyclo[3.3.0]octane backbone and their application in enantioselective catalysis. *J. Chem. Soc. Perkin Trans 1* **1999**, 2353-2365.

(389) Solà, L.; Reddy, K. S.; Vidal-Ferran, A.; Moyano, A.; Pericàs, M. A.; Riera, A.; Alvarez-Larena, A.; Piniella, J.-F. A Superior, Readily Available Enantiopure Ligand for the Catalytic Enantioselective Addition of Diethylzinc to α-Substituted Aldehydes. *J. Org. Chem.* **1998**, *63*, 7078-7082.

(390) Paleo, M. R.; Cabeza, I.; Sardina, F. J. Enantioselective Addition of Diethylzinc to Aldehydes Catalyzed by N-(9-Phenylfluoren-9-yl) β-Amino Alcohols. *J. Org. Chem.* **2000**, *65*, 2108-2113.

(391) Scott, J. W.; Keith, D. D.; Nix, G.; Parrish, D. R.; Remington, S.; Roth, G. R.; Townsend, J. M.; Valentine, D.; Yang, R. Catalytic asymmetric hydrogenation of methyl (E)- and (Z)-2-acetamido-3-alkylacrylates. *The Journal of Organic Chemistry* **1981**, *46*, 5086-5093.

(392) Tang, W.; Capacci, A. G.; White, A.; Ma, S.; Rodriguez, S.; Qu, B.; Savoie, J.; Patel, N. D.; Wei, X.; Haddad, N.; Grinberg, N.; Yee, N. K.; Krishnamurthy, D.; Senanayake, C. H. Novel and Efficient Chiral Bisphosphorus Ligands for Rhodium-Catalyzed Asymmetric Hydrogenation. *Org. Lett.* **2010**, *12*, 1104-1107.

(393) Knowles, W. S. Asymmetric hydrogenation. *Acc. Chem. Res.* **1983**, *16*, 106-112.

(394) Hopkins, J. M.; Dalrymple, S. A.; Parvez, M.; Keay, B. A. 3,3‘-Disubstituted BINAP Ligands: Synthesis, Resolution, and Applications in Asymmetric Hydrogenation. *Org. Lett.* **2005**, *7*, 3765-3768.